



DOCTORAL THESIS IN ENGINEERING MECHANICS  
STOCKHOLM, SWEDEN 2018

# Of Pipes and Bends

JACOPO CANTON



KTH ROYAL INSTITUTE OF TECHNOLOGY  
SCHOOL OF ENGINEERING SCIENCES

# **Of Pipes and Bends**

by

Jacopo Canton

May 2018  
Technical Reports  
Royal Institute of Technology  
Department of Mechanics  
SE-100 44 Stockholm, Sweden

Akademisk avhandling som med tillstånd av Kungliga Tekniska Högskolan i Stockholm framlägges till offentlig granskning för avläggande av teknologie doktorsexamen fredagen den 15 juni 2018 kl 10:15 i sal F2, Kungliga Tekniska Högskolan, Lindstedtsvägen 26, Stockholm.

TRITA-SCI-FOU 2018:25  
ISBN 978-91-7729-823-6

*Cover:* Chaos running after order: turbulent slug coexisting with a nonlinear travelling wave. The flow is in a toroidal pipe with curvature 0.022 and Reynolds number  $Re = 5050$ . The travelling wave is the result of a Hopf bifurcation at  $Re = 5032$ ; it is stable and has a finite basin of attraction. The slug is a symptom of subcritical transition, it expands and suppresses the wave, but it eventually dissipates and the wave is restored. Isocontours of opposite values of streamwise velocity are depicted in red and blue, while the white isocontours are of negative  $\lambda_2$ . The fluid is flowing from right to left: ↘ .

©Jacopo Canton 2018  
Universitetsservice US–AB, Stockholm 2018

*“Well, we ain’t got any,” George exploded.  
“Whatever we ain’t got, that’s what you want.  
God a’mighty.”*

— John Steinbeck  
Of Mice and Men



# Of Pipes and Bends

Jacopo Canton

Linné FLOW Centre, KTH Mechanics, Royal Institute of Technology  
SE-100 44 Stockholm, Sweden

## Abstract

This work is concerned with the transition to turbulence of the flow in bent pipes, but it also includes an analysis of large-scale turbulent structures and their use for flow control.

The flow in a toroidal pipe is selected as it represents the common asymptotic limit between spatially developing and helical pipes. The study starts with a characterisation of the laminar flow as a function of curvature and the Reynolds number  $Re$ , since the so-called Dean number is found to be of little use except for infinitesimally low curvatures. It is found that the flow is modally unstable and undergoes a Hopf bifurcation for any curvature greater than zero. The bifurcation is studied in detail, and an effort to connect this modal instability with the linearly stable straight pipe is also presented.

This flow is not only modally unstable, but undergoes subcritical transition at low curvatures. This scenario is found to bear similarities to straight pipes, but also fundamental differences such as weaker turbulent structures and the apparent absence of puff splitting. Toroidal pipe flow is peculiar, in that it is one of the few fluid flows presenting both sub- and supercritical transition to turbulence; the critical point where the two scenarios meet is therefore of utmost interest. It is found that a bifurcation cascade and featureless turbulence actually coexist for a range of curvature and  $Re$ , and the attractors of the respective structures have a small but finite basin of attraction.

In  $90^\circ$  bent pipes at higher  $Re$  large-scale flow structures cause an oscillatory motion known as swirl-switching. Three-dimensional proper orthogonal decomposition is used to determine the cause of this phenomenon: a wave-like structure which is generated in the bent section, and is possibly a remnant of a low- $Re$  instability.

The final part of the thesis has a different objective: to reduce the turbulent frictional drag on the walls of a channel by employing a control strategy independent of  $Re$ -dependent turbulent scales, initially proposed by Schoppa & Hussain [Phys. Fluids **10**:1049–1051 (1998)]. Results show that the original method only gives rise to transient drag reduction while a revised version is capable of sustained drag reduction of up to 18%. However, the effectiveness of this control decreases rapidly as the Reynolds number is increased, and the only possibility for high- $Re$  applications is to use impractically small actuators.

**Key words:** nonlinear instability, bifurcation, flow control

# Rör och krökningar

Jacopo Canton

Linné FLOW Centre, KTH Mekanik, Kungliga Tekniska Högskolan  
SE-100 44 Stockholm, Sverige

## Sammanfattning

Detta arbete behandlar omslaget till turbulens hos strömningen i krökta rör, men det inkluderar även en analys av storskaliga turbulenta strukturer samt dess användning inom strömningskontroll.

Strömningen i ett torusformat rör är valt eftersom det representerar den vanliga asymptotiska gränsen mellan rumsutvecklade och helixformade rör. Studien inleds med en karakterisering av den laminära strömningen som en funktion av Reynoldstalet  $Re$ , eftersom det så kallade Deantalet konstateras vara av liten nytta förutom vid infinitesimalt små krökningar. Det konstateras även att strömningen är modalt instabil och genomgår en Hopf-bifurkation för alla krökningar större än noll. Bifurkationen är studeras i detalj, och ett försök att sammankoppla denna modala instabilitet med det linjärt stabila raka röret presenteras också.

Strömningen är inte bara modalt instabil, utan genomgår även ett subkritiskt omslag för låga kurvaturer. Detta scenario visar sig ha likheter med raka rör, men även fundamentala skillnader såsom svagare turbulent strukturer samt en till synes frånvarande delning av turbulent puffar. Strömningen i torusformade rör är besynnerlig i det avseendet att det är en av de få strömningar som uppvisar så väl sub- som superkritiskt omslag till turbulens; den kritiska punkten där de två scenarierna möts är därför av ytterst intresse. Det konstateras att en bifurkationskaskad faktiskt samexisterar med turbulens utan särdrag för ett spann av  $Re$ -tal, och att attraktorerna av de respektive strukturerna har en liten men ändlig attraktionsbassäng.

I  $90^\circ$  böjda rör vid högre  $Re$ -tal orsakar storskaliga strömningsstrukturer ett fenomen känt som virvelväxling (eng. *swirl switching*). Tredimensionell *proper orthogonal decomposition* används för att bestämma orsaken till detta fenomen: en våglik struktur som genereras i den krökta delen, och är en möjlig kvarleva av en instabilitet vid låga  $Re$ -tal.

Den sista delen av avhandlingen har en annan målsättning: att minska det turbulentna friktionsmotståndet på väggarna i en kanal genom att använda en kontrollstrategi som är oberoende av  $Re$ -beroende turbulent strukturer, och som först föreslogs av Schoppa & Hussain [Phys. Fluids **10**:1049–1051 (1998)]. Resultaten visar att den ursprungliga metoden endast ger upphov till tillfällig motståndsminskning, medan en reviderad version är kapabel till upprätthållen motståndsminskning på upp till 18%. Emellertid minskar effektiviteten för denna kontrollteknik hastigt med stigande Reynoldstal, och den enda möjligheten att tillämpa tekniken vid höga  $Re$ -tal är att använda opraktiskt små manöverdon.

**Nyckelord:** icke-linjär instabilitet, bifurkation, strömningskontroll

## Preface

This thesis deals with transition to turbulence and skin-friction-drag reduction. A brief introduction and summary of the results is presented in the first part. The second part contains the journal articles written during this work. The papers are adjusted to comply with the present thesis format for consistency, but their contents have not been altered as compared with their original counterparts.

**Paper 1.** J. CANTON, R. ÖRLÜ & P. SCHLATTER, 2017. *Characterisation of the steady, laminar incompressible flow in toroidal pipes covering the entire curvature range.* Int. J. Heat Fluid Fl. **66**, 95–107.

**Paper 2.** J. CANTON, P. SCHLATTER & R. ÖRLÜ, 2016. *Modal instability of the flow in a toroidal pipe.* J. Fluid Mech. **792**, 894–909.

**Paper 3.** J. CANTON, E. RINALDI & P. SCHLATTER, 2018. *Approaching zero curvature: modal instability in a bent pipe.* Technical report.

**Paper 4.** E. RINALDI, J. CANTON & P. SCHLATTER, 2018. *The collapse of strong turbulent fronts in bent pipes.* Submitted.

**Paper 5.** J. CANTON, E. RINALDI, R. ÖRLÜ, & P. SCHLATTER, 2018. *A critical point for bifurcation cascades and intermittency.* To be submitted.

**Paper 6.** L. HUFNAGEL, J. CANTON, R. ÖRLÜ, O. MARIN, E. MERZARI & P. SCHLATTER, 2018. *The three-dimensional structure of swirl-switching in bent pipe flow.* J. Fluid Mech. **835**, 86–101.

**Paper 7.** J. CANTON, R. ÖRLÜ, C. CHIN, N. HUTCHINS, J. MONTY AND P. SCHLATTER, 2016. *On large-scale friction control in turbulent wall flow in low Reynolds number channels.* Flow Turbul. Combust. **97**, 811–827.

**Paper 8.** J. CANTON, R. ÖRLÜ, C. CHIN & P. SCHLATTER, 2016. *Reynolds number dependence of large-scale friction control in turbulent channel flow.* Phys. Rev. Fluids **1**, 081501.

May 2018, Stockholm  
Jacopo Canton

## **Division of work between authors**

The main advisor for the project is Dr. Philipp Schlatter (PS). Dr. Ramis Örlü (RÖ) acts as co-advisor.

**Paper 1.** The code was developed by Jacopo Canton (JC) who also performed the computations. The paper was written by JC with feedback from PS and RÖ.

**Paper 2.** The stability code was developed by JC, the nonlinear simulation code by Azad Noorani and JC. All computations were performed by JC. The paper was written by JC with feedback from PS and RÖ.

**Paper 3.** The second stability code was developed by JC with help from Enrico Rinaldi (ER) and PS. The computations were done by JC, who wrote the paper with feedback from PS.

**Paper 4.** The codes were developed by JC and ER, the code for the nonlinear adjoints was based on a code written by Oana Marin (OM) and Michel Schanen. ER and JC also performed the computations and wrote the paper, with feedback from PS.

**Paper 5.** The codes were written by JC who also did the computations. The paper was written by JC with feedback from ER, PS and RÖ.

**Paper 6.** This work was started during the Master's Thesis of Lorenz Hufnagel (LH) who was supervised by JC and PS. The code was developed by LH and JC starting from a code written by OM; LH and JC performed the simulations. The paper was written by JC with feedback from LH, OM, EM, PS and RÖ.

**Paper 7.** The code was developed by PS and JC, JC performed the simulations. The paper was written by JC with feedback from PS, RÖ and the external co-authors.

**Paper 8.** JC performed the simulations using the code developed by PS and JC. The paper was written by JC with feedback from Cheng Chin, PS and RÖ.

## Other publications

The following papers, although related, are not included in this thesis.

J. CANTON, M. CARINI & F. AUTERI, 2017. *Global stability of axisymmetric coaxial jets*. J. Fluid Mech. **824**, 886–911.

P. SCHLATTER, L. HUFNAGEL, J. CANTON, E. MERZARI, O. MARIN & R. ÖRLÜ, 2017. *Swirl switching in bent pipes studied by numerical simulation*. Proceedings of TSFP-10. Chicago, USA.

P. SCHLATTER, A. NOORANI, J. CANTON, L. HUFNAGEL, R. ÖRLÜ, O. MARIN & E. MERZARI, 2017. *Transitional and turbulent bent pipes*. Proceedings of iTi Conference in turbulence. Bertinoro, Italy, 81–87.

J. CANTON, R. ÖRLÜ & P. SCHLATTER, 2017. *On stability and transition in bent pipes*. Proceedings of DLES11. Pisa, Italy.

J. CANTON, P. SCHLATTER & R. ÖRLÜ, 2015. *Linear stability of the flow in a toroidal pipe*. Proceedings of TSFP-9. Melbourne, Australia.

## Conferences

Part of the work in this thesis has been presented at the following international conferences. The presenting author is underlined.

J. CANTON, R. ÖRLÜ, C. CHIN & P. SCHLATTER. “*Large*”- vs *Small-scale friction control in turbulent channel flow*. 70<sup>th</sup> Annual meeting of the APS Division of Fluid Dynamics. Denver, USA, November 2017.

E. RINALDI, J. CANTON, O. MARIN, M. SCHANEN & P. SCHLATTER. *Non-linear optimal perturbations in a curved pipe*. 70<sup>th</sup> Annual meeting of the APS Division of Fluid Dynamics. Denver, USA, November 2017.

J. CANTON, R. ÖRLÜ & P. SCHLATTER. *Subcritical and supercritical transition in curved pipes*. Euromech Symposium 591: 3D Instability mechanisms in transitional and turbulent flows. Bari, Italy, September 2017.

J. CANTON, R. ÖRLÜ & P. SCHLATTER. *Subcritical transition in bent pipes*. 16<sup>th</sup> European Turbulence Conference (ETC 16). Stockholm, Sweden, August 2017.

J. CANTON, R. ÖRLÜ, C. CHIN & P. SCHLATTER. *The effect of large-scale vortices on frictional drag in channel flow*. Euromech Colloquium 586: Turbulent superstructures in closed and open flows. Erfurt, Germany, July 2017.

J. CANTON. *Modal instability of the flow in a toroidal pipe*. 25<sup>th</sup> Svenska Mekanikdagarna. Uppsala, Sweden, June 2017.

J. CANTON, R. ÖRLÜ & P. SCHLATTER. *On stability and transition in bent pipes*. 11<sup>th</sup> ERCOFTAC Workshop on Direct and Large-Eddy Simulation. Pisa, Italy, May 2017.

J. CANTON, R. ÖRLÜ, C. CHIN & P. SCHLATTER. *Reynolds number dependence of large-scale friction control in turbulent channel flow*. ERCOFTAC

European Drag Reduction and Flow Control Meeting (EDRFCM). Rome, Italy, April 2017.

J. CANTON, R. ÖRLÜ, C. CHIN, N. HUTCHINS, J. MONTY & P. SCHLATTER. *Reynolds number dependence of large-scale friction control in turbulent channel flow*. 69<sup>th</sup> Annual meeting of the APS Division of Fluid Dynamics. Portland, USA, November 2016.

P. SCHLATTER, L. HUFNAGEL, J. CANTON, R. ÖRLÜ, O. MARIN & E. MERZARI. *Unravelling the mechanism behind swirl-switching in turbulent bent pipes*. 69<sup>th</sup> Annual meeting of the APS Division of Fluid Dynamics. Portland, USA, November 2016.

P. SCHLATTER, A. NOORANI, J. CANTON, L. HUFNAGEL & R. ÖRLÜ. *Transitional and turbulent bent pipes*. iTi Conference on Turbulence VII. Bertinoro, Italy, September 2016.

J. CANTON, R. ÖRLÜ & P. SCHLATTER. *Neutral stability of the flow in a toroidal pipe*. 15<sup>th</sup> European Turbulence Conference (ETC 15). Delft, The Netherlands, August 2015.

J. CANTON, P. SCHLATTER & R. ÖRLÜ. *Linear stability of the flow in a toroidal pipe*. 9<sup>th</sup> Turbulence Shear Flow Phenomena (TSFP-9). Melbourne, Australia, July 2015.

J. CANTON, R. ÖRLÜ & P. SCHLATTER. *Tracking the first bifurcation of the flow inside a toroidal pipe*. 11<sup>th</sup> ERCOFTAC SIG 33 Workshop. St. Helier, Jersey, UK, April 2015.

P. SCHLATTER, J. CANTON & R. ÖRLÜ. *Linear stability of the flow in a toroidal pipe*. 67<sup>th</sup> Annual Meeting of the APS Division of Fluid Dynamics. San Francisco, USA, November 2014.

# Contents

<b>Abstract</b>	v
<b>Sammanfattning</b>	vi
<b>Preface</b>	vii
 <b>Part I - Overview and summary</b>	
<b>Chapter 1. Introduction</b>	1
1.1. Supercritical transition and hydrodynamic stability	3
1.2. Subcritical transition and intermittency	5
1.3. A description of the flow	6
<b>Chapter 2. Hydrodynamic stability</b>	10
2.1. Investigation methods	10
2.2. The Hopf bifurcation and the neutral curve	12
<b>Chapter 3. Subcritical transition</b>	16
3.1. Investigation methods	17
3.2. The collapse of strong fronts	18
<b>Chapter 4. The critical point</b>	21
4.1. Investigation methods	22
4.2. Bifurcation cascades and intermittency	22
<b>Chapter 5. Large-scale structures in turbulent flow</b>	25
5.1. Investigation methods	26
5.2. Swirl-switching is a wave-like structure	27
<b>Chapter 6. Friction control in turbulent channel flows</b>	30
6.1. Prelude	30
6.2. A description of the flow	31

6.3.	Investigation methods	33
6.4.	Large-scale friction control	33
6.5.	Reynolds number dependence of the control method	34
6.6.	Large- vs Small-scale control	36
<b>Chapter 7.</b>	<b>Summary of the papers</b>	39
<b>Chapter 8.</b>	<b>Conclusions and outlook</b>	43
<b>Acknowledgements</b>		46
<b>Bibliography</b>		47

## Part II - Papers

<b>Paper 1.</b>	<b>Characterisation of the steady, laminar incompressible flow in toroidal pipes covering the entire curvature range</b>	55
<b>Paper 2.</b>	<b>Modal instability of the flow in a toroidal pipe</b>	85
<b>Paper 3.</b>	<b>Approaching zero curvature: modal instability in a bent pipe</b>	105
<b>Paper 4.</b>	<b>The collapse of strong turbulent fronts in bent pipes</b>	121
<b>Paper 5.</b>	<b>A critical point for bifurcation cascades and intermittency</b>	139
<b>Paper 6.</b>	<b>The three-dimensional structure of swirl-switching in bent pipe flow</b>	149
<b>Paper 7.</b>	<b>On large-scale friction control in turbulent wall flow in low Reynolds number channels</b>	169
<b>Paper 8.</b>	<b>Reynolds number dependence of large-scale friction control in turbulent channel flow</b>	191

# **Part I**

## **Overview and summary**



## CHAPTER 1

# Introduction

Fluid mechanics is a vast and fascinating subject and ultimately a field of classical physics. Differently from other branches of classical mechanics, though, it still presents unanswered questions and open problems. Some are of fundamental nature such as *why and how does a flow transition from a laminar to a turbulent state*, while others echo in everyday life: *how can an aeroplane fly or fluid be transported while consuming less energy?*

Owing to the inherent difficulty of describing the complex motion of a continuum, fluid mechanics is approached from different routes depending on the nature of the problem at hand. Analytical, *i.e.* exact, solutions can, in fact, be computed only for particularly simple cases while most problems require a numerical solution or experimental approach. Fluid mechanics itself is subdivided into branches: fluids can be regarded as Newtonian or non-Newtonian, viscous or inviscid, compressible or incompressible; flows can also be categorised as wall-bounded or unbounded, laminar or turbulent; and these are but a few examples. The present work deals with Newtonian, viscous, incompressible fluids in wall-bounded flows and sheds some light on the laminar, transitional and the turbulent regimes.

A flow is deemed laminar when it is either steady, *i.e.* time-invariant, or its unsteady motion appears to be ordered, easily described; conversely, turbulent flows are chaotic and comprise a wide range of spatial and temporal scales which interact with each other and render the description of the motion much more complicated. Traditionally, two different methodologies are employed to approach each regime: laminar flows are considered ‘simple enough’ to be described from a deterministic point of view and dynamical system theory is often used to analyse this regime. Turbulent flows, on the other hand, are too complex for a deterministic description, hence they are treated as a random process and are usually studied with tools developed by probability theory.

Figure 1.1 illustrates the difference between laminar and turbulent regimes: the plume of smoke rising from a pipe is initially laminar and rises in a quasi-rectilinear direction, it then becomes unstable and forms a couple of vortex rings before transitioning towards a turbulent state.



Figure 1.1: Plume of smoke rising from a pipe. The picture illustrates different flow regimes: laminar (close to the pipe), transitional (at the height of the vortex rings), and turbulent (towards the top of the frame). Own photograph.

The equations describing the motion of a Newtonian, viscous, incompressible fluid, be it in the laminar or turbulent regime, are the incompressible Navier–Stokes equations, written here in non-dimensional form:

$$\frac{\partial \mathbf{u}}{\partial t} + (\mathbf{u} \cdot \nabla) \mathbf{u} - \frac{1}{Re} \nabla^2 \mathbf{u} + \nabla p = \mathbf{f}, \quad (1.1a)$$

$$\nabla \cdot \mathbf{u} = 0. \quad (1.1b)$$

The unknowns are the velocity and pressure fields  $(\mathbf{u}, p)$ ,  $\mathbf{f}$  represents a force field and  $Re$  is a non-dimensional group named Reynolds number. Clearly, the equations also need to be provided with appropriate initial and boundary conditions, which depend on the geometry and the flow being examined.

The Reynolds number can be interpreted as the ratio between the orders of magnitude of the nonlinear (inertial) and viscous terms; this explains how this system of equations can describe both kinds of flows: the laminar regime, dominated by viscosity, and the turbulent regime, where nonlinear effects are prevalent (see, for example, Batchelor 2000).

The Navier–Stokes equations represent a nonlinear dynamical system describing the evolution of  $(\mathbf{u}, p)$ . As it often happens with nonlinear dynamical systems, the qualitative nature of the solution can be significantly altered by the parameters that describe the system. Moreover, although the equations describe a deterministic phenomenon, *i.e.* one where any subsequent state can be exactly determined provided the knowledge of an initial state, the evolution of the solution can be highly sensitive to the initial condition. This is another qualitative difference between laminar and turbulent regimes: while the former is unaffected by this problem, the smallest uncertainty on the initial datum for a turbulent flow entails the impossibility of the exact knowledge of its evolution (see, for example, Strogatz 1994; Kuznetsov 2004).

The chapters that follow present a summary of the thesis, where these concepts are applied to the flow in bent pipes (chapters 2–5) and the turbulent flow in a channel (chapter 6). Chapter 7 presents a summary of the journal articles included in Part II. Finally, this overview concludes in chapter 8 which includes a summary and an outlook on future work. Part II of this manuscript forms a collection of the journal articles written on these subjects.

## 1.1. Supercritical transition and hydrodynamic stability

Hydrodynamic stability is concerned with the discovery and analysis of the mechanisms that lead a flow from a laminar state through the first stages of transition towards turbulence. This section provides a brief overview on some key concepts used in chapter 2. Exhaustive discussions on the subject and on dynamical systems in general can be found, for instance, in the books by Strogatz (1994) and Schmid & Henningson (2001).

In a very schematic way, and considering the Reynolds number as the sole parameter for the Navier–Stokes equations, the initial evolution of some fluid mechanical systems can be described as follows:

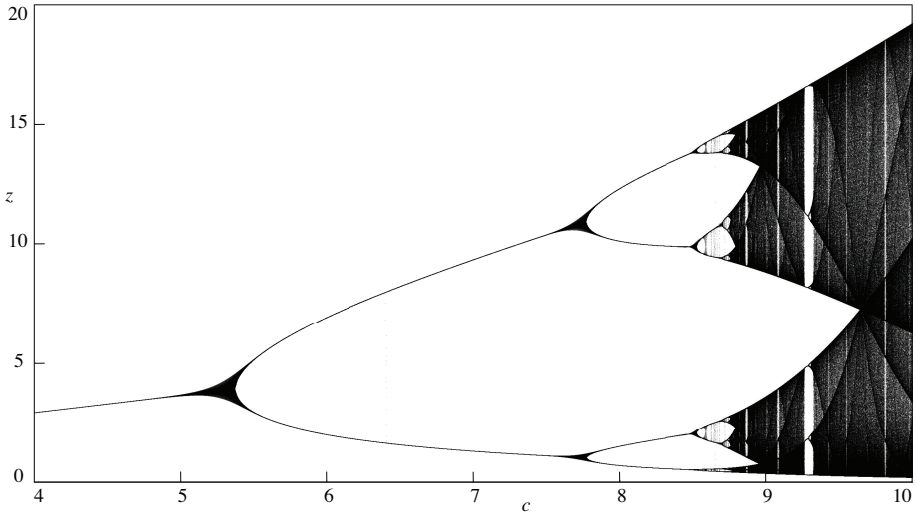


Figure 1.2: Bifurcation diagram for the Rössler system (Rössler 1976) as a function of  $c$ , one of its parameters.  $\dot{x} = -y - z$ ,  $\dot{y} = x + ay$ ,  $\dot{z} = b + z(x - c)$ .

For a small enough  $Re$  there exists only one steady, stable solution. Here *stable* means that any perturbation to this solution will, eventually, disappear, either due to convection or to diffusion. These steady states comprise most of the solutions to the Navier–Stokes equations that can be computed analytically. When the solution cannot be obtained analytically, as is the case for the flow in a toroidal pipe presented in this thesis, the equations have to be solved numerically. Two common approaches in this case are employing Newton’s method or integrating the equations in time until convergence to the steady state is reached. In some simple cases, for very low Reynolds numbers, the nonlinear term in the equations has such a small influence that it can be completely neglected; the flows belonging to this category are called Stokes flows.

For larger values of  $Re$  the initial steady state becomes unstable and another solution (or more than one) appears.

If this new solution is a steady state, then a steady state bifurcation has occurred. This scenario, with the Reynolds number replaced by the curvature, occurs in bent pipes: for low  $Re$  the flow in a straight pipe is described by the axisymmetric Poiseuille solution (Batchelor 2000), when the pipe is bent into a torus this solution becomes unstable and is substituted by a different steady state, described analytically by Dean (1927), and provided with only a mirror symmetry.

Instead of a steady state a time-periodic solution can appear, in this case a Hopf bifurcation has occurred. When the bifurcation is supercritical the flow settles onto a stable limit cycle where it oscillates at one determined

frequency. Toroidal pipes present this scenario as well: when the Reynolds number is increased the steady state becomes unstable and the flow undergoes a Hopf bifurcation. The nature of this bifurcation and the exact values of the parameters involved are discussed in chapter 2.

Typically these systems then undergo a period-doubling cascade (see, e.g. Strogatz 1994; Kuznetsov 2004) or follow a Ruelle–Takens–Newhouse route to chaos (Ruelle & Takens 1971; Newhouse *et al.* 1978). A period-doubling cascade is a succession of bifurcations where the system moves to new periodic attractors with twice the period of the previous limit cycle. An example of period-doubling is illustrated in figure 1.2 which presents the bifurcation diagram for the Rössler system (Rössler 1976). This is a system of three differential equations, with just one nonlinear term, designed by Otto Rössler to exhibit the simplest possible strange attractor. The flow inside of a torus, instead, undergoes a Ruelle–Takens–Newhouse route to turbulence (Ruelle & Takens 1971; Newhouse *et al.* 1978), where a succession of Hopf bifurcations moves the system to quasi-periodic attractors with one additional period per each bifurcation. This is the main topic in chapter 2 and papers 2, 3 and 5.

## 1.2. Subcritical transition and intermittency

The occurrence of a bifurcation can be predicted by a linear stability analysis, which allows the determination of the bifurcation point and a description of the flow following the instability. In some cases, though, a different scenario can occur: the stable solution may not undergo any bifurcation, and the steady state, which was the only solution for low  $Re$ , can remain stable for any Reynolds number. In these cases other solutions can appear in the form of more complicated, at times chaotic, attractors. Separating the steady solution from this new attractor there can be a saddle boundary, so-called edge of chaos (Skufca *et al.* 2006). This is the scenario observed in many wall-bounded shear flows such as straight pipes (see, among others, Wygnanski & Champagne 1973; Wygnanski *et al.* 1975; Hof *et al.* 2004; Avila *et al.* 2011; Barkley *et al.* 2015; Barkley 2016), channel flow, plane Couette flow (for a review see Manneville 2016).

Straight pipe flow, for example, has a linearly stable laminar velocity profile (Meseguer & Trefethen 2003), *i.e.* all small perturbations decay and no critical Reynolds number can be defined using linear theory. However, experiments and simulations show that subcritical transition to turbulence can occur for  $Re \gtrsim 1700$  if perturbations are sufficiently large. Several experimental studies have detailed the transition scenario and found a distinction between turbulent patches that do not grow in size, so-called *puffs*, and patches that expand in the surrounding laminar flow, *slugs* (see, e.g. Lindgren 1969; Wygnanski & Champagne 1973; Wygnanski *et al.* 1975; and the review by Mullin 2011). Only recently a statistical description of the intermittent flow in pipes has provided an accurate estimate of a critical Reynolds number,  $Re \approx 2040$  (Avila *et al.* 2011). Below this threshold, the probability of a puff decaying outweighs

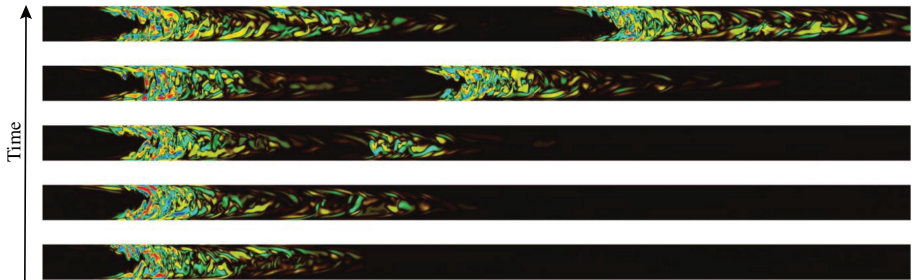


Figure 1.3: Visualisation of a puff splitting on a cross-section of a straight pipe. Colours represent streamwise vorticity, with blue as negative and red as positive. From Avila *et al.* (2011). Reprinted with permission from AAAS.

the probability of a new puff being generated through a splitting mechanism, depicted in figure 1.3. On the other hand, if the Reynolds number is higher than 2040, the probability of splitting rapidly increases and puffs proliferate. If  $Re \gtrsim 2300$  puffs turn into slugs, which rapidly fill the pipe thereby marking the onset of sustained turbulence.

A similar transition scenario takes place in toroidal pipes for low curvatures, this is the main topic of chapter 3 and papers 4 and 5.

### 1.3. A description of the flow

As a first step in the investigation of the flow inside bent pipes, the focus is on an idealised toroidal setup, depicted in figure 1.4. This shape, albeit rarely encountered in industrial applications, is representative of a canonical flow. This makes it relevant for the research on the onset of turbulence since it deviates from a straight pipe by the addition of one parameter only: the curvature. Moreover, the torus constitutes the common asymptotic limit of two flow cases: the curved (spatially developing) pipe and the helical pipe. Analysing a toroidal pipe allows us to identify the effect that the curvature has on the flow, separating it from that of the torsion (as in helical coils) and the developing length (as in spatially developing curved pipes).

Following the first experimental investigations by Eustice (1910, 1911), Dean (1927, 1928) analysed this flow analytically. In both of his papers the curvature of the pipe, defined as the ratio between pipe and torus radii ( $\delta = R_p/R_t$ , see figure 1.4), was assumed to be very small. By means of this and successive approximations Dean was able to derive a solution to the incompressible Navier–Stokes equations. Dean’s approximate solution depends on a single parameter, called Dean number and defined as  $De = Re\sqrt{\delta}$ . Dean was also the first to demonstrate the presence of secondary motion and found it to be in the form of two counter-rotating vortices that were then given his name (see Kalpakli Vester *et al.* 2016, for an extensive review with an historical perspective).

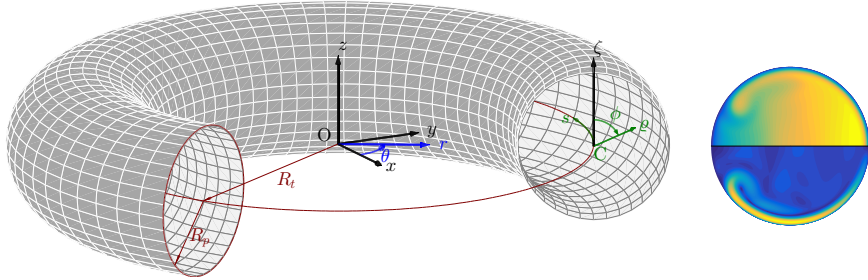


Figure 1.4: *Left:* Sketch of the toroidal pipe with curvature  $\delta = R_p/R_t = 0.3$ . The ‘equatorial’ plane of the torus corresponds to the  $x - y$  plane. *Right:* Corresponding base flow for  $Re = 3379$ , streamwise (top) and in-plane (bottom) velocity magnitude. Reprinted from Canton *et al.* (2017) with permission from Elsevier.

Later, Adler (1934), Keulegan & Beij (1937) and other experimentalists proceeded to measure the frictional resistance offered by the fluid when flowing through a curved pipe. The most notable of these works were included in a seminal paper by Ito (1959). One of the major findings presented in this paper is that the Fanning friction factor for the laminar flow scales with the Dean number up to  $De = 2 \times 10^3$ . As it will be shown in paper 1, this is actually not entirely correct.

Di Piazza & Ciofalo (2011) were the first to present an analysis on instability encountered by this flow. These authors investigated two values of curvature (0.1 and 0.3) by direct numerical simulation and observed, in both cases, a transition from stationary to periodic, quasi-periodic and then chaotic flow. However, as indicated by Kühnen *et al.* (2015) and as will be shown in chapter 2 and paper 2, their results were inaccurate, with the exception of the symmetry characteristics observed in the flow. The only experiments employing toroidal pipes in the context of the present work are those by Kühnen *et al.* (2014, 2015). The experimental difficulty to impose a bulk flow in the torus, led these authors to sacrifice the  $2\pi$  (streamwise) periodicity and the mirror symmetry of the system by introducing a steel sphere in the tube to drive the fluid. Their results for  $0.028 < \delta < 0.1$  confirmed the findings of Webster & Humphrey (1993), *i.e.* that the first instability leads the flow to a periodic regime, while for  $\delta < 0.028$  subcritical transition was observed, as in Sreenivasan & Strykowski (1983).

One of the most relevant quantities for the flow through curved pipes is the friction encountered by the fluid. Ito (1959) and Cieślicki & Piechna (2012) report friction factors ( $f$ ) measured in experiments (the former) and numerical computations (the latter), along with theoretical and empirical regression lines. Their conclusion is that the data collapse onto one line, confirming Dean’s finding of a single non-dimensional number governing the flow. The actual

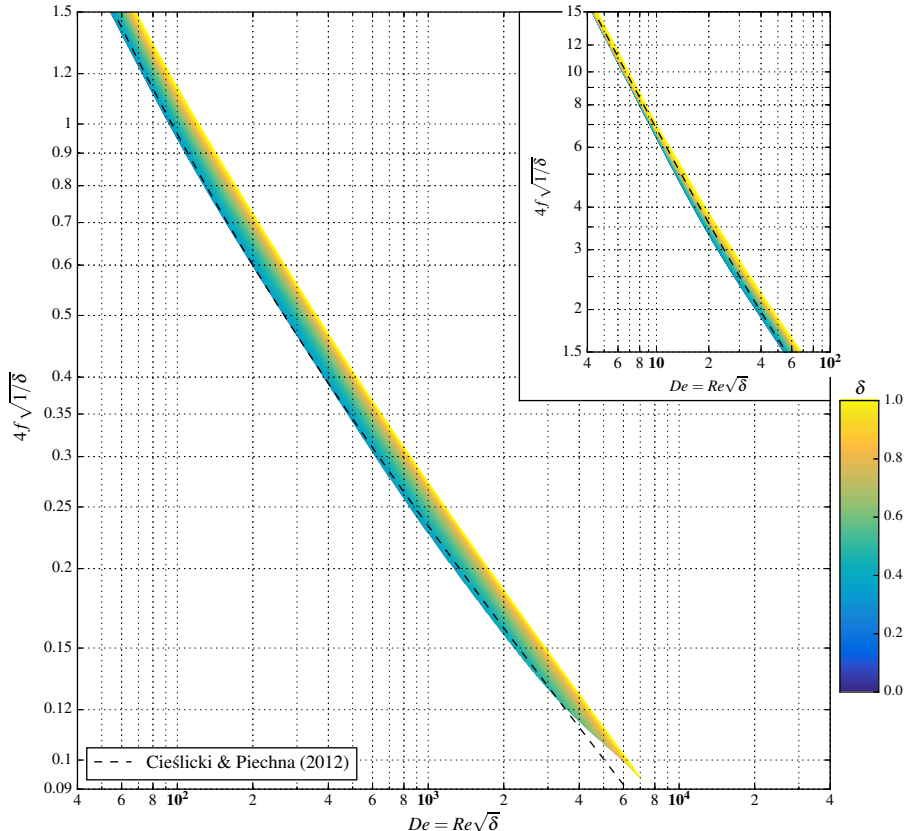


Figure 1.5: Fanning friction factor as a function of Dean number, with same scaling and axes as in figure 6 in Ito (1959). Individual lines are coloured by the corresponding curvature. The ‘band’ of lines becomes thinner for high  $De$  because the maximum  $Re$  was limited to 7000 for all values of  $\delta$ , resulting in a different maximum  $De$  dependent on the curvature. Reprinted from Canton *et al.* (2017) with permission from Elsevier.

picture is, however, different: as can be seen in figure 1.5 the lines do indeed show a common trend, but do not scale with  $De$ . The data represent a wide band, where the value of  $f$  changes with curvature. Even at  $De = 10$  the friction range is still quite wide, with  $0.004 \leq f \leq 1.74$  and a relative difference with respect to Cieślicki & Piechna’s formula ( $f \approx 0.50$ ) of -100% and 290% respectively. From this and other results, presented in paper 1, it can be concluded that the Dean number is not suitable as a scaling parameter for this flow: Reynolds number and curvature need to be considered as separate parameters.

As was mentioned before, the curvature is the only parameter that differentiates a toroidal pipe from a straight one. It therefore appears natural to

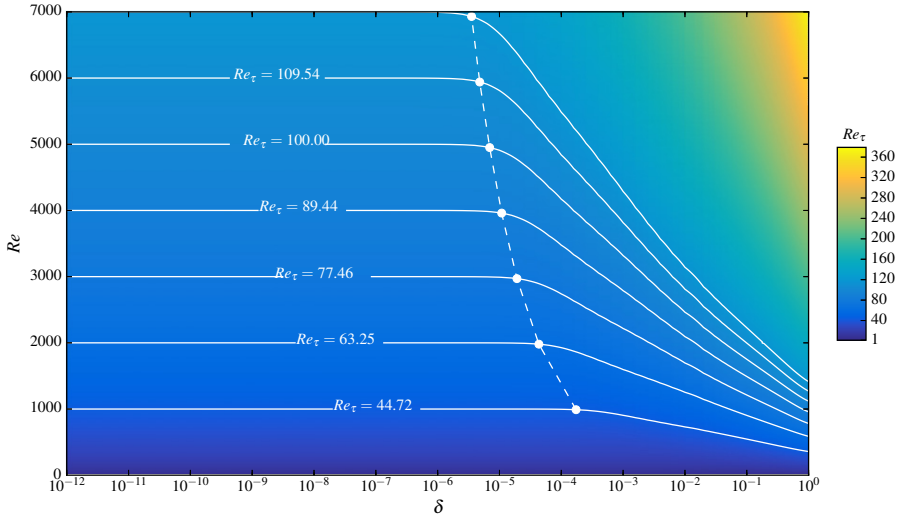


Figure 1.6: Friction Reynolds number as a function of curvature and bulk Reynolds number. The continuous white lines represent isocontours of  $Re_\tau$  corresponding to the friction Reynolds number of a straight pipe with fluid flowing at the bulk Reynolds number indicated by the  $y$ -labels, *i.e.* 1 000, 2 000, ..., 7 000. The markers and dashed white line indicate a departure of more than 1% from the straight pipe  $Re_\tau$ . Reprinted from Canton *et al.* (2017) with permission from Elsevier.

ask the question of “when can  $\delta$  be considered *low enough* that it does not influence the flow?”. It can be demonstrated analytically that the secondary motion characterising this flow is always present, for any Reynolds number and curvature larger than zero (see paper 1, § 3.3). Hence, the mathematical answer to the question is that the two flows can never be considered similar, but how would a physicist or engineer answer the same question?

Figure 1.6 shows the friction Reynolds number ( $Re_\tau$ ) of the laminar flow as a function of  $\delta$  and  $Re$ . The white lines represent isocontours of  $Re_\tau$  corresponding to the friction Reynolds number of a straight pipe with fluid flowing at the bulk Reynolds number indicated by the  $y$ -labels, *i.e.* 1 000, 2 000, ..., 7 000. It can be noticed that below a certain curvature, which depends on the Reynolds number, these lines become horizontal. The dashed white line marks a 1% departure from the values in a straight pipe; below these curvatures a toroidal pipe has approximately the same friction of a straight pipe for the same fluid and flow speed. As friction is concerned, below  $Re = 7\,000$  a torus can be approximated with a straight pipe for  $\delta \lesssim 10^{-5}$ . This is but one of the quantities that can be used to answer the question, paper 1 presents a more in-depth discussion.

## CHAPTER 2

# Hydrodynamic stability

While hydrodynamic stability and transition to turbulence in straight pipes — being one of the classical problems in fluid mechanics — has been studied extensively, the stability of curved pipe flow has received less attention. The technical relevance of this flow case is apparent from its prevalence in industrial applications: bent pipes are found, for example, in power production facilities, air conditioning systems, and chemical and food processing plants. Vashisth *et al.* (2008) presents a comprehensive review on the applications of curved pipes in industry. A second fundamental area of research where bent pipes are relevant is the medical field. Curved pipes are, in fact, an integral part of vascular and respiratory systems. Understanding the behaviour of the flow in this case can aid the prevention of several cardiovascular problems (Berger *et al.* 1983; Bulusu *et al.* 2014).

### 2.1. Investigation methods

The flow is driven at a constant volume rate by a force field directed along the streamwise direction. The steady solution, which is stable for low Reynolds numbers, inherits from the geometry the invariance with respect to  $s$  and the symmetry with respect to the equatorial plane of the torus (see figure 1.4). This allows the solution to be computed on a two dimensional section (retaining three velocity components) sensibly reducing the computational cost.

The steady states and the stability analysis are computed with **PaStA**, an in-house developed Fortran90 code written using primitive variables in cylindrical coordinates and based on the finite element method (Canton 2013; Canton *et al.* 2017a).

The steady solutions to the Navier–Stokes equations (1.1) are computed via Newton’s method. Introducing  $\mathcal{N}(\mathbf{x})$  as a shorthand for the terms without time derivative, with  $\mathbf{x} = (\mathbf{u}, p)$ , and separating the linear and quadratic parts, the equations can be written as:

$$\mathcal{N}(\mathbf{x}) = \mathcal{Q}(\mathbf{x}, \mathbf{x}) + \mathcal{L}(\mathbf{x}) - \mathbf{f} = 0, \quad (2.1)$$

where

$$\mathcal{Q}(\mathbf{x}, \mathbf{y}) = \begin{pmatrix} (\mathbf{u} \cdot \nabla) \mathbf{v} \\ 0 \end{pmatrix}, \quad \mathcal{L}(\mathbf{x}) = \begin{pmatrix} -\frac{1}{Re} \nabla^2 \mathbf{u} + \nabla p \\ \nabla \cdot \mathbf{u} \end{pmatrix}, \quad (2.2)$$

and  $\mathbf{y} = (\mathbf{v}, q)$ . The non-incremental formulation of Newton's method reads:

$$\mathcal{J}|_{\mathbf{x}_n}(\mathbf{x}_{n+1}) = \mathcal{Q}(\mathbf{x}_n, \mathbf{x}_n) + \mathbf{f}, \quad (2.3)$$

where  $\mathcal{J}|_{\mathbf{x}_n}$  is the Fréchet derivative of  $\mathcal{N}(\mathbf{x})$  evaluated at  $\mathbf{x}_n$  corresponding, after spatial discretisation, to the Jacobian matrix  $J$ . The convergence criterion is based on the infinity norm of the residual, *i.e.*  $\|\mathcal{N}(\mathbf{x}_n)\|_{L^\infty}$ , and the tolerance is set to  $10^{-15}$  for all computations.

Once a steady state has been computed, its stability properties are investigated by modal stability analysis. Employing a normal modes ansatz, the perturbation fields are defined as:

$$\mathbf{u}'(r, \theta, z, t) = \hat{\mathbf{u}}(r, z) \exp\{\mathrm{i}(k\theta - \omega t)\}, \quad (2.4a)$$

$$p'(r, \theta, z, t) = \hat{p}(r, z) \exp\{\mathrm{i}(k\theta - \omega t)\}, \quad (2.4b)$$

where  $k \in \mathbb{Z}$  is the streamwise wave number,  $\omega = \omega_r + \mathrm{i}\omega_i \in \mathbb{C}$  is the eigenvalue and  $\hat{\mathbf{x}} = (\hat{\mathbf{u}}, \hat{p}) \in \mathbb{C}$  the corresponding eigenvector. Although  $k$  is in principle a real number, the  $2\pi$ -periodicity of the torus restricts it to integer values.

The (spatially discretised) linearised Navier–Stokes equations are then reduced to a generalised eigenvalue problem of the form

$$\mathrm{i}\omega M\hat{\mathbf{x}} = L_k \hat{\mathbf{x}}, \quad (2.5)$$

where  $\hat{\mathbf{x}}$  is the discretised eigenvector,  $M \in \mathbb{R}^{\text{dof} \times \text{dof}}$  is the (singular) generalised mass matrix, and  $L_k \in \mathbb{C}^{\text{dof} \times \text{dof}}$  represents the discretisation of the linearised Navier–Stokes operator, parametrised by  $k$ . Finally, ‘dof’ is a shorthand for the total number of degrees of freedom, accounting for both velocity and pressure nodes. The eigensolutions are computed to machine precision through an interface to the ARPACK library (Lehoucq *et al.* 1998).

Once a bifurcation is identified, its neutral curve can be traced in parameter space, separating the stable and unstable regions. In order to track a bifurcation, an augmented set of equations describing the system at the bifurcation point needs to be solved. Equation (2.6) presents this system in the case of a Hopf bifurcation, which is the type of bifurcation encountered in toroidal pipe flows:

$$N\mathbf{x} = 0, \quad (2.6a)$$

$$\mathrm{i}\omega_r M\hat{\mathbf{x}} = L_k \hat{\mathbf{x}}, \quad (2.6b)$$

$$\phi \cdot \hat{\mathbf{x}} = 1, \quad (2.6c)$$

with  $N = N(Re, \delta, x)$ ,  $M = M(\delta)$ , and  $L_k = L_k(Re, \delta, x)$ . The unknowns for this system are: the base flow  $\mathbf{x} = (u, p) \in \mathbb{R}^{\text{dof}}$ , the frequency of the critical eigenmode  $\omega_r \in \mathbb{R}$ , and the corresponding eigenvector  $\hat{\mathbf{x}} = (\hat{\mathbf{u}}, \hat{p}) \in \mathbb{C}^{\text{dof}}$ . The roles of  $Re$  and  $\delta$  can be interchanged: one is given while the other is obtained as part of the solution. Equation (2.6a) is a real equation determining that  $x$  is a steady state. Equation (2.6b) is a complex equation which represents the eigenvalue problem (2.5) when a pair of complex conjugate eigenvalues has zero growth rate. This equation forces the solution of the system to be on the

neutral curve. Equation (2.6c) is a complex equation as well, it fixes the phase and amplitude of the eigenvector. The constant vector  $\phi$  is chosen as the real part of the initial guess for  $\hat{x}$ , such that (2.6c) mimics an  $L^2$  norm.

Newton's method is employed for this system as well, without assembling the Jacobian matrix. Instead, a block Gauss factorisation and linear algebra are used to split the resulting system into five dof  $\times$  dof linear systems, two real and three complex, presented in (2.7a–e). Beside reducing memory requirements, these systems have matrices with the same sparsity pattern as those already used for the solution of the steady state and the eigenvalue problem. Vectors  $\alpha$  through  $\epsilon$  are then used to compute the updates for the unknowns (2.7f–i). The tolerance for the solution of this system is chosen as to have an uncertainty on  $Re$  on the neutral curve of  $\pm 10^{-4}\%$ .

$$\alpha = -J^{-1}N, \quad (2.7a)$$

$$\beta = -J^{-1} \frac{\partial N}{\partial \delta}, \quad (2.7b)$$

$$\gamma = -[L_k + i\omega_r M]^{-1} iM\hat{x}, \quad (2.7c)$$

$$\delta = -[L_k + i\omega_r M]^{-1} \left( \frac{\partial L_k \hat{x}}{\partial x} + i\omega_r \frac{\partial M \hat{x}}{\partial x} \right) \alpha, \quad (2.7d)$$

$$\epsilon = -[L_k + i\omega_r M]^{-1} \left( \frac{\partial L_k \hat{x}}{\partial \delta} + i\omega_r \frac{\partial M \hat{x}}{\partial \delta} + \left( \frac{\partial L_k \hat{x}}{\partial x} + i\omega_r \frac{\partial M \hat{x}}{\partial x} \right) \beta \right); \quad (2.7e)$$

$$\Delta\delta = \frac{-\Re(\phi \cdot \gamma)\Im(\phi \cdot \delta) - \Im(\phi \cdot \gamma)(1 - \Re(\phi \cdot \delta))}{\Re(\phi \cdot \gamma)\Im(\phi \cdot \epsilon) - \Im(\phi \cdot \gamma)\Re(\phi \cdot \epsilon)}, \quad (2.7f)$$

$$\Delta\omega_r = \frac{\Im(\phi \cdot \delta)\Re(\phi \cdot \epsilon) - \Im(\phi \cdot \epsilon)(1 - \Re(\phi \cdot \delta))}{\Re(\phi \cdot \gamma)\Im(\phi \cdot \epsilon) - \Im(\phi \cdot \gamma)\Re(\phi \cdot \epsilon)}, \quad (2.7g)$$

$$\Delta\hat{x} = -\hat{x} + \gamma + \Delta\omega_r \delta + \Delta\delta \epsilon, \quad (2.7h)$$

$$\Delta x = \alpha + \Delta\delta \beta. \quad (2.7i)$$

## 2.2. The Hopf bifurcation and the neutral curve

Preliminary eigenvalue computations reveal the presence of unstable pairs of complex-conjugate eigenmodes, indicating the presence of a Hopf bifurcation. Employing the method described in §2.1, the neutral curve of each critical mode has been traced in the parameter space as a function of curvature and Reynolds number. The result is a complex picture, depicted in figure 2.1. It presents five *families* and three *isolated* modes, and their envelope constitutes the global neutral curve for the flow. All eigenmodes represent a travelling wave, but their properties are modified along the neutral curve. A family comprises eigenmodes that share common characteristics, while the eigenvalues designated as isolated are those which contribute to the global neutral curve while being dissimilar to the modes belonging to the neighbouring neutral curves. In more detail, all modes belonging to a given family display the same

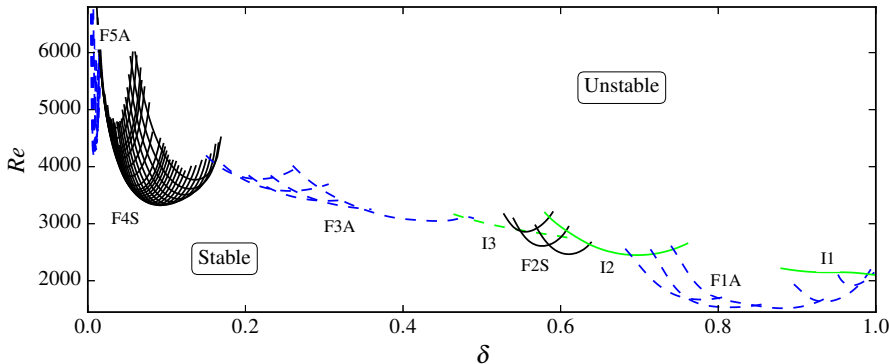


Figure 2.1: Neutral curve in the  $\delta - Re$  plane. Each line corresponds to the neutral curve of one mode. Five families (black and blue) and three isolated modes (green) are marked by labels. Continuous lines correspond to symmetric modes while antisymmetric modes are represented with dashed lines. Canton *et al.*, Modal instability of the flow in a toroidal pipe, *J. Fluid Mech.* 792:894–909 (2016), reproduced with permission.

spatial structure and symmetry properties, they have approximately equal phase speed and comparable wavelength. In addition, while the wavenumber does not vary monotonically along the global neutral curve, it does so inside families. Furthermore, eigenvalues in the same family lie on the same branch and, possibly even more characteristic, the eigenmodes forming a family have neutral curves with a very similar trend  $(\delta, Re(\delta))$ . This can readily be observed in figure 2.1 where each neutral curve is purposely plotted beyond the envelope line to illustrate this feature. Nonlinear direct numerical simulations were also performed and show excellent agreement with these results: all of the characteristics of the bifurcation are observed in the nonlinear flow and the accuracy on the critical Reynolds number is confirmed as well.

Given that straight pipe flow is linearly stable at least up to  $Re = 10^7$  (Mesequer & Trefethen 2003), it appears natural to ask how the neutral curve behaves when the curvature tends to zero. It is hard to see with the  $\delta$ -axis in linear scale, but the leftmost line in figure 2.1 ends at curvature 0.002. As was mentioned in chapter 1, there actually is a limit for  $\delta$ , depending on  $Re$ , below which the flow in a toroidal pipe can be well approximated by that in a straight pipe (see figure 1.6). Paper 3 provides a description of this problem, some of the solutions that were adopted, and preliminary results.

Studying the behaviour of the flow in a torus becomes more complicated after the first Hopf bifurcation: linear stability tools can still be used, but the flow is now periodic. Instead of eigenvalues, Floquet multipliers of the periodic orbit need to be computed, and these, in general, can only be found by numerical

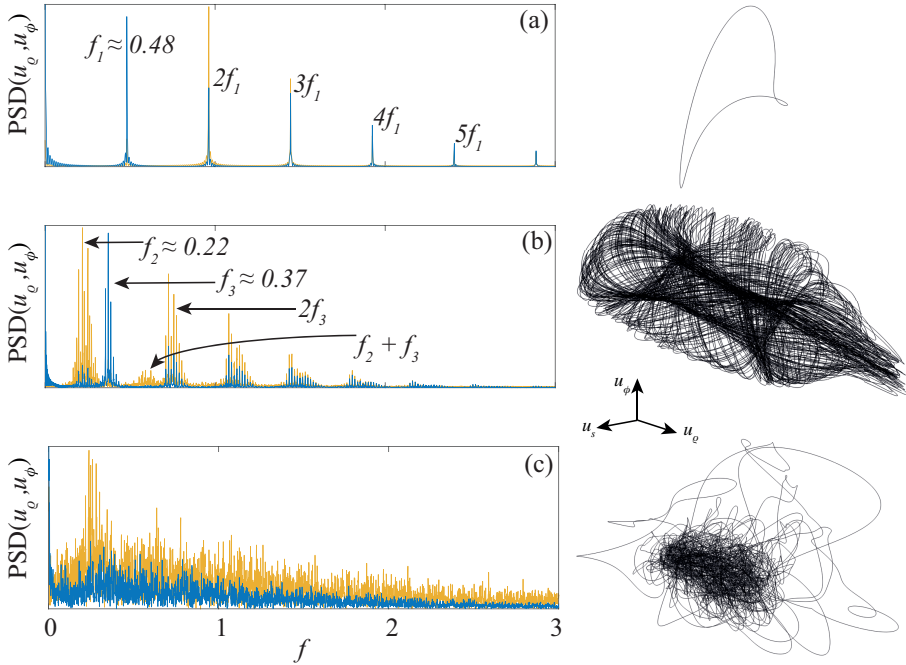


Figure 2.2: Power spectral densities (PSD) and corresponding phase spaces for point velocity measurements at  $\delta = 0.05$  and  $Re = 4000$  (a),  $Re = 4500$  (b), and  $Re = 6000$  (c). The velocity is measured in a point close to the wall of the pipe ( $\varrho = 0.48R_p, \phi = \pi/2$ ). Yellow lines represent PSD of  $u_\varrho$ , while blue lines are PSD of  $u_\phi$ .

integration (Strogatz 1994). This method only allows to find a possible second Hopf bifurcation, beyond which the trajectories of the system are on a toroidal orbit, *i.e.* there are now two incommensurable frequencies, resp. periods. To study the stability of this torus and find successive bifurcations, Lyapunov exponents have to be computed, to know if neighbouring orbits remain close together or separate exponentially fast. This is a very expensive analysis to carry out on a large system such as a fluid flow, where the number of degrees of freedom is typically very large.

An alternative is to simply “observe” the flow, either experimentally or via numerical simulations, and measure quantities that are good indicators of the state of the system which can be used for a reduced-order analysis of the flow. Examples of these quantities include the kinetic energy, dissipation, or even simply velocity components in a selection of points of the domain. This is the procedure that was followed to analyse the flow inside a torus. After the first bifurcation, this system undergoes what appears to be a Ruelle–Takens–Newhouse route to chaos (Ruelle & Takens 1971; Newhouse *et al.* 1978),

with new, incommensurable frequencies appearing as the Reynolds number is increased. Figure 2.2 provides an overview of the results, which are further detailed in paper 5. The figure depicts power spectral densities (PSD), and the corresponding phase space trajectories, for the flow at  $\delta = 0.05$  and  $Re = 4000$ , 4500 and 6000. Figure 2.2(a) highlights the importance of the neutral curve for the nonlinear flow: after the first bifurcation there is a single, stable limit cycle which attracts all initial conditions. The 2-periodic, toroidal attractor in figure 2.2(b), instead, is indicative of a second Hopf bifurcation following the first one identified by the neutral curve. The corresponding PSD also highlights two incommensurable frequencies measured in the flow. This particular value of curvature is selected in paper 2 to verify the accuracy of the neutral curve and provide more details on the relevance of the linear analysis for the nonlinear flow.

## CHAPTER 3

# Subcritical transition

In chapter 2 it was shown that the flow inside a toroidal pipe is linearly unstable for all curvatures greater than zero. However, this is not the only transition mechanism in bent pipes.

White (1929) was the first to observe that the flow in a bent pipe at low curvatures can be maintained in a laminar state for higher Reynolds numbers than in a straight pipe. Later, Sreenivasan & Strykowski (1983) showed that even a turbulent flow coming from a straight pipe can be fully relaminarised after entering a coiled pipe section. Besides reporting this observation, made possible by the injection of a dye streak, Sreenivasan & Strykowski (1983) also provided estimates for the critical Reynolds number for transition to turbulence for curvatures up to  $\delta = 0.12$ . Since the transition mechanism was unknown at the time, these authors reported critical Reynolds numbers based on three different criteria. They defined a “conservative lower” critical  $Re$  for the appearance of the first ‘burst’ of turbulence near the outer wall of the pipe, a “liberal lower” transitional  $Re$  corresponding to the first appearance of turbulence on the whole cross-section of the pipe under investigation, and finally an “upper” limit as the lowest  $Re$  at which the flow becomes fully turbulent. The reason for these three distinct limits is that the transitional flow at low curvatures displays a degree of intermittency, depending both on the Reynolds number and the curvature, which made it difficult to define a precise limit for transition to turbulence.

Straight pipes present a similar problem. The Hagen-Poiseuille velocity profile is linearly stable at least up to  $Re = 10^7$  (Meseguer & Trefethen 2003), *i.e.* all small perturbations decay and no critical Reynolds number can be defined using linear theory. However, experiments and simulations show that subcritical transition to turbulence can occur for  $Re \gtrsim 1700$  if perturbations are sufficiently large. Different structures have been observed at transitional Reynolds numbers: turbulent patches that do not grow in size and are now known as *puffs*, and structures that expand in the surrounding laminar flow, so-called *slugs* (see, e.g. Lindgren 1969; Wygnanski & Champagne 1973; Wygnanski *et al.* 1975; and the review by Mullin 2011). Only in recent years a statistical description of the flow in straight pipes has provided an accurate estimate of a critical Reynolds number,  $Re \approx 2040$  (Avila *et al.* 2011). Below this threshold, the probability of a puff decaying outweighs the probability of a new puff being generated through a

splitting mechanism. On the other hand, if the Reynolds number is higher than the threshold, the probability of splitting increases superexponentially and puffs proliferate. Theoretical models have been proposed and quantitatively capture this subcritical transition scenario, which falls into the directed percolation universality class (Barkley 2011; Barkley *et al.* 2015; Shih *et al.* 2015; Barkley 2016).

Building on top of this knowledge, Kühnen *et al.* (2015) repeated the analysis by Sreenivasan & Strykowski (1983) and reported that subcritical transition dominates in bent pipes for  $\delta \lesssim 0.028$ , while above this value transition to turbulence is supercritical. Subcritical transition in bent pipes was described as being “very similar as in straight pipes, where laminar and turbulent flows can coexist” (Kühnen *et al.* 2015). However, an in-depth analysis of this regime is still missing.

### 3.1. Investigation methods

Subcritical transition is more expensive to study than supercritical transition: linearisation cannot be used and the flow has to be simulated by solving the full time-dependent Navier–Stokes equations (1.1). For this reason only one value of curvature was chosen to investigate this regime. In order to ensure that the nature of transition investigated is subcritical, the curvature was set to  $\delta = 0.01$ . This value is sufficiently smaller than the threshold for the onset of supercritical transition,  $\delta \approx 0.028$  according to Kühnen *et al.* (2015). At the same time, it introduces a significant deviation of the laminar flow from the one of a straight pipe (see chapter 1 and paper 1), which for this curvature becomes linearly unstable for  $Re = 4257$  (see chapter 2 and paper 2).

The study is again fully numerical, and direct numerical simulations (DNS) are performed using the spectral element solver Nek5000 (Fischer *et al.* 2008), which was previously validated on turbulent straight and bent pipes (El Khoury *et al.* 2013; Noorani *et al.* 2013) and in transitional regimes (chapter 2 and paper 2). In order to observe the large scale evolution of puffs and slugs, the length of the computational domain is  $L_s = 100D$  and  $L_s = \pi d/3 \simeq 105D$  for straight and bent pipes, respectively (the subscript  $s$  indicates the streamwise direction). The spatial resolution satisfies typical DNS requirements for fully turbulent flows at Reynolds numbers slightly higher than the ones considered here, for details see paper 4.

The scalar quantity  $q$  is used as an indicator of the level of turbulence in accordance with the literature on transitional straight pipes (see, e.g. Barkley 2011), and its definition is adapted to the case of bent pipes as:

$$q(s, t) = \sqrt{\int_0^{2\pi} \int_0^R \left( (u_r - U_r)^2 + (u_\theta - U_\theta)^2 \right) r dr d\theta}. \quad (3.1)$$

Here  $s$ ,  $r$  and  $\theta$  indicate the streamwise, radial and azimuthal directions in toroidal coordinates. The instantaneous velocity components are  $u_s = u_s(s, r, \theta, t)$ ,  $u_r = u_r(s, r, \theta, t)$  and  $u_\theta = u_\theta(s, r, \theta, t)$ ; capital letters denote the

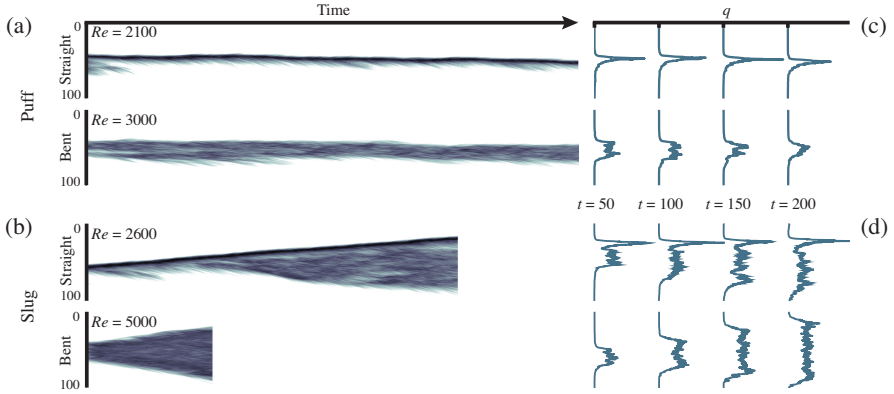


Figure 3.1: Space-time evolution of the cross-flow velocity fluctuations  $q$ , defined by equation (3.1), for exemplary puffs (a) and slugs (b) in straight and curved pipes. Colours represent  $\log_{10} q$ , white corresponds to laminar flow, dark colours to high fluctuations. Panels (c,d) report the spatial distribution of  $q$  sampled at four time instants. The (horizontal) scale used to indicate the magnitude of  $q$  is the same for the straight and curved pipes.

laminar flow at a given curvature and Reynolds number.  $U_r = U_r(r, \theta; \delta, Re)$  and  $U_\theta = U_\theta(r, \theta; \delta, Re)$  are zero in a straight pipe but not in a curved one, where the Dean vortices (Dean 1927) constitute a secondary motion that can exhibit intensities comparable to that of the streamwise flow (see chapter 1 and paper 1).

### 3.2. The collapse of strong fronts

Figure 3.1 illustrates one of the most relevant findings of this analysis. It depicts the evolution of the cross-flow velocity fluctuations,  $q$ , for puffs (figure 3.1(a)) and slugs (figure 3.1(b)) in both straight and bent pipes. The turbulence intensity  $q = q(s - u_f t, t)$  is computed in a frame of reference that moves with a constant streamwise velocity  $u_f$ , and the same range of colour levels is used for straight and bent pipes to allow for a direct visual comparison. One-dimensional profiles of  $q$ , sampled at several subsequent times, are reported in figure 3.1(c) and (d), and help the comparison between the two flows.

Localised turbulent structures in bent pipes bear qualitative similarities to those in straight pipes in that they appear in the form of puffs and slugs that are sustained by an instability at their upstream front. However, a clear and distinctive feature differentiates puffs and slugs between the two pipes: the absence of a strong upstream front if the pipe is bent. The space–time diagrams show the well-known concentration of turbulent fluctuations, indicated by the dark tone of the colour, at the upstream front in straight pipes (Barkley 2011,

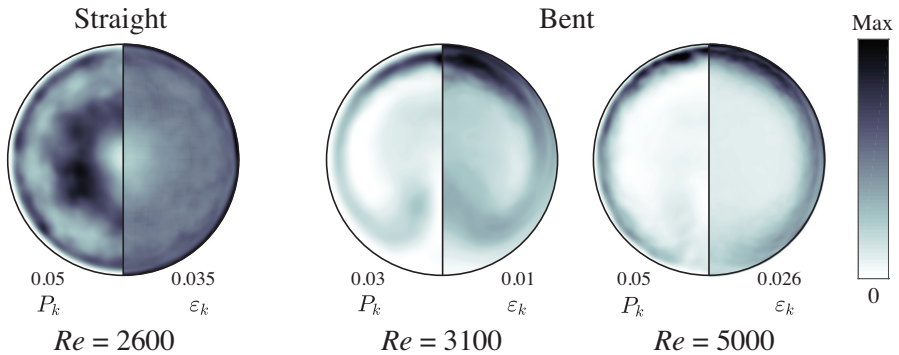


Figure 3.2: Turbulent kinetic energy production (left halves) and dissipation (right halves) at the front of slugs in straight and bent pipes. All quantities are averaged over time by tracking the slug, and over the cross-section taking into account the mirror symmetry of the torus, the axial invariance of the pipe has not been used in order not to alter the comparison. The text labels on the bottom report the maxima of  $P_k$  and  $\varepsilon_k$  on each section.

2016; Song *et al.* 2017). Conversely, the flow in bent pipes shows no evidence of this strong front and is characterised by a somewhat uniform distribution of  $q$ .

As reported by Sreenivasan & Strykowski (1983), turbulent fluctuations in bent pipes appear first in the outer portion of the bend, while they pervade the whole cross-section only for higher Reynolds numbers. To investigate the connection between this observation and localised structures, figure 3.2 presents the time averaged distributions of production and dissipation over a cross-section of the pipe. The panels in figure 3.2 are computed at the upstream front of slugs for different Reynolds numbers. In a straight pipe  $P_k$  and  $\varepsilon_k$  are mainly concentrated in the near-wall region and in a ring around the centre of the pipe. Conversely, the budget in a bent pipe shows a high localisation towards the outside of the bend and lower peak values. The spatial localisation and lower local values of  $P_k$  and  $\varepsilon_k$  also suggest that an additional mechanism must come into play in sustaining localised turbulent structures, and this is likely to simply be the secondary motion created by the Dean vortices. As the curvature is increased from a straight to a bent pipe, the linear and nonlinear optimal perturbations (see paper 4) become increasingly localised in the same region where the peaks of  $P_k$  and  $\varepsilon_k$  are located. It therefore appears that this region, where the recirculating flow impinges on the wall of the pipe, is highly receptive to flow perturbations and is responsible for their amplification. The fluctuations are then transported around the walls of the pipe and lifted up towards the inner section.

Paper 4 provides more details of this study, but there is a fundamental difference between straight and bent pipes worth mentioning here: the apparent

absence of puff splitting when the pipe is bent, at least for the choice of parameters investigated. The absence of puff splitting appears to be connected to the weak and localised upstream fronts. Turbulent structures that leave a mother puff have a low probability of entering the small region of high amplification located near the outer wall, which would trigger the instability that sustains a puff. Moreover, due to the secondary motion, the few vortical structures that visit this region do not linger for long enough to generate a new puff.

## CHAPTER 4

# The critical point

The flow inside of a toroidal pipe presents both sub- and supercritical transition to turbulence, as discussed in chapters 2 and 3, and detailed in papers 2–5. The number of fluid flows with this characteristics is quite small.

There are some flows which are modally stable for all Reynolds numbers, meaning that according to a linear analysis they should never become turbulent. This is the case, for example, of straight pipe flow, which is modally stable at least up to  $Re = 10^7$  (Meseguer & Trefethen 2003) but undergoes subcritical transition for  $Re \gtrsim 1700$  (see, e.g. Barkley 2016, and references therein). For these flows a linearised analysis fails entirely.

Other flows, instead, are actually linearly unstable but still undergo subcritical transition for lower Reynolds numbers. One of the most famous examples is plane Poiseuille flow, which has a critical Reynolds number of 5772 but actually becomes naturally turbulent for  $Re \approx 3300$  (Kim *et al.* 1987), and can even be partially turbulent for Reynolds numbers as low as 1200 (Kleiser & Zang 1991; Tsukahara *et al.* 2005). For these flows a linearised analysis fails in the sense that it provides results which are “irrelevant” in a nonlinear simulation or experiment. This is what happens to the flow in the torus for low curvatures: there is a linear instability, as for all other curvatures, but in experiments and DNS the flow undergoes transition to turbulence at lower Reynolds numbers. Even when above the neutral curve, nonlinear simulations do not show any trace of the modes that should be unstable according to linear analysis.

What makes the flow inside of a torus peculiar is that for curvature above approximately 0.025 a linear analysis does actually provide the correct results, as was discussed in chapter 2. For curvatures above this value the nonlinear flow undergoes a Hopf bifurcation, exactly as predicted by a modal analysis.

To the best of our knowledge, there are not many other flows that undergo both transition scenarios by changing only one parameter, examples are Taylor-Couette flow (Coles 1965; Andereck *et al.* 1986) and rotating Couette flow (Tsukahara *et al.* 2010; Tsukahara 2011). There still is one important difference between Taylor-Couette, rotating Couette, and the flow in a torus: the first two do indeed present both subcritical and supercritical transition, but the regimes are well separated. Subcritical transition is present if the outer cylinder is rotated in anti-clockwise direction, while supercritical transition appears when

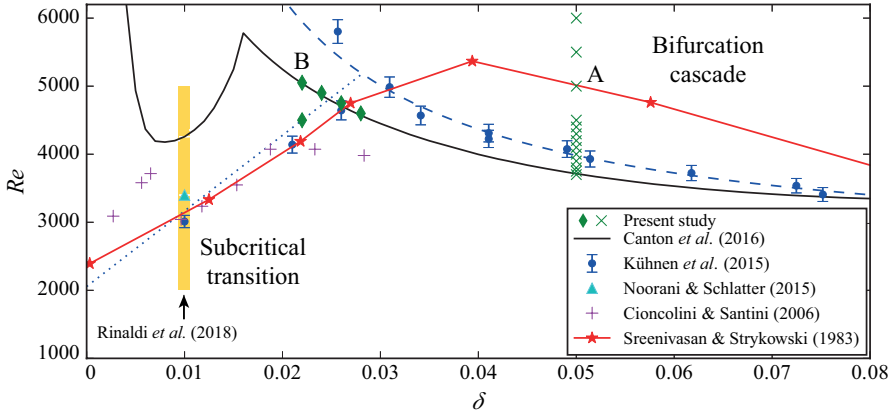


Figure 4.1: Portion of the  $\delta - Re$  parameter space of the flow in a toroidal pipe. Experimental and numerical data from the literature are reported as well as the location of the present computations. The data by Cioncolini & Santini (2006) refers to the first discontinuity in their friction measurements, while the data by Sreenivasan & Strykowski (1983) is the curve they refer to as the “conservative lower critical limit”. Point A is supercritical, and illustrated in figure 2.2(b), while point B is critical and is detailed in figure 4.2.

the outer cylinder rotates in clockwise direction. The two scenarios do not actually coexist, either one or the other is observed, depending on the rotation direction. The flow in a torus, instead, presents one critical point where the two scenarios intersect: to the left of this point subcritical transition dominates, while to the right the transition is supercritical.

The questions are several, chief among which is “what happens when the two scenarios meet?”, and “why does one scenario dominate for low curvatures while the other is dominant for higher curvatures?”. This is the topic of this chapter, which provides an insight into this new critical regime.

#### 4.1. Investigation methods

In this region of parameter space the flow has to be studied in its full nonlinear regime, since linear and nonlinear mechanisms coexist. The neutral curve was computed with PaStA, as detailed in chapter 2, while the nonlinear simulations are all performed with Nek5000, as in chapter 3. The same meshes and degree of spatial accuracy, validated in the previous chapters, are also employed.

#### 4.2. Bifurcation cascades and intermittency

We now turn our attention to the region of parameter space where the neutral curve meets the lines indicating subcritical transition, *i.e.*  $\delta \approx 0.025$  and

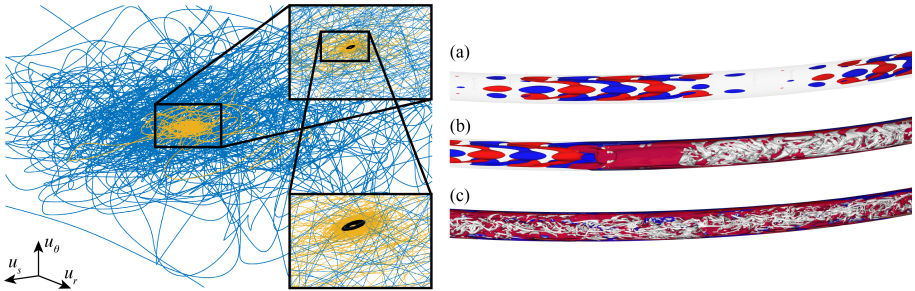


Figure 4.2: Left: phase space for  $\delta = 0.022$  and  $Re = 5050$  (point B in figure 4.1). All trajectories start in the neighbourhood of the travelling wave, the closest being the black line (panel (a)). The yellow trajectory is turbulent for  $t \approx 100D/U$  and then slowly returns to the stable limit cycle (panel (b)), while the blue trajectory remains turbulent for  $t > 1000D/U$  (panel (c)). Right: snapshots of the flow field along the three phase space trajectories. Red and blue colours are isocontours of streamwise velocity for two opposite values, *i.e.*  $u_s = \pm 0.005$ ; white isocontours are of negative  $\lambda_2$  (Jeong & Hussain 1995).

$4000 < Re < 5000$ . As a first step it is necessary to verify that both sub- and supercritical behaviours can still be isolated. We therefore perform nonlinear simulations for  $\delta = 0.022$  and  $Re = 4500$ , with two domains of different length, about  $10D$  and  $20D$ , respectively. The simulations are initialised with puffs computed by Rinaldi *et al.* (2018) which, for both domains, grow in length in the form of slugs and turn the whole domain to turbulent flow, confirming once more the subcritical transition lines by Sreenivasan & Strykowski (1983); Kühnen *et al.* (2015) and the findings by Rinaldi *et al.* (2018). The second verification is at  $\delta = 0.028$  and  $Re = 4600$ , just above the neutral curve, which for this curvature marks the linear instability at  $Re = 4570$ , and below the subcritical transition thresholds. Here the flow is initialised with a paraboloidal profile perturbed with random noise, and converges to the nonlinear travelling wave created by the Hopf bifurcation, as previously explained for  $\delta = 0.05$ .

We therefore proceed by lowering the curvature, while remaining above the neutral curve, and investigate three more pairs of  $(\delta, Re)$ , *i.e.*  $(0.026, 4750)$ ,  $(0.024, 4900)$ , and  $(0.022, 5050)$ . The last pair of values corresponds to point B in figure 4.1, and is illustrated in figure 4.2. In this region of parameter space the two transition scenarios coexist. The beginning of the Ruelle–Takens–Newhouse route to chaos can be observed in the form of stable, nonlinear travelling waves, while subcritical transition is found in the form of expanding slugs. In point B, for example, a simulation initialised with a randomly perturbed parabolic velocity profile slowly converges to a nonlinear travelling wave, as predicted by the modal analysis. This process is illustrated by the black trajectory in the phase space of figure 4.2 and with a snapshot of the flow field in figure 4.2(a). On the other hand, if the simulation is initialised with a localised disturbance,

the disturbance grows and invades the whole pipe, turning the flow into a fully turbulent state; in agreement with the location of the lines indicating subcritical transition.

The intermediate cases are what makes this flow unique. When the travelling wave is perturbed with a *highly* energetic puff the subcritical transition scenario dominates: the puff expands and creates a fully turbulent flow. For this particular combination of  $\delta$  and  $Re$ , *highly* energetic means that the kinetic energy of the puff,  $E_{k,\text{puff}}$ , has to be more than approximately 6.3 times that of the travelling wave,  $E_{k,\text{wave}}$ . This is the case represented by the blue trajectory in figure 4.2 and the corresponding flow field in panel (c), where the white  $\lambda_2$  isocontours (Jeong & Hussain 1995) illustrate the spatially chaotic nature of turbulence, while the temporal disorder is visualised by the trajectory. Conversely, if the puff has lower energy, *i.e.*  $E_{k,\text{puff}} < 6.3E_{k,\text{wave}}$ , it will grow in size but only transiently, before diffusing and disappearing completely. The yellow trajectory in figure 4.2 illustrates this process: it starts from an initial condition close to that represented in panel (b), then travels through the turbulent region of phase space (main panel and upper insert), and finally returns to the attracting limit cycle of the travelling wave (lower insert). It can therefore be concluded that both transition mechanisms, sub- and supercritical, can be observed in this critical region of parameter space. The structures corresponding to these processes are all stable, and their basins of attraction are complementary and finite.

## CHAPTER 5

# Large-scale structures in turbulent flow

After investigating transition to turbulence, the attention is now moved to a different problem: the presence of large-scale, low-frequency structures in fully turbulent curved pipe flow, known as *swirl-switching*. The focus is now in understanding the nature of these structures, similarly to what was done with puffs and slugs in low-curvature pipes. A study on the origin of these oscillations is still underway and is outlined towards the end of this chapter.

Swirl-switching is a low-frequency oscillatory phenomenon which affects the Dean vortices in bent pipes and may cause fatigue in piping systems (Kalpakli Vester *et al.* 2016). Despite thirty years worth of research, the mechanism that causes these oscillations and the frequencies that characterise them remain unclear. The Dean vortex alternation was initially, and unexpectedly, observed by Tunstall & Harvey (1968), who experimentally studied the turbulent flow through a sharp, L-shaped bend ( $\delta = 1$ ). These authors measured “low random-frequency” switches between two distinct states, and were able to identify an either clockwise or anti-clockwise predominance of the swirling flow following the bent section. Tunstall & Harvey attributed the origin of the switching to the presence of a separation bubble in the bend and to the “occasional existence of turbulent circulation entering the bend”. It was Brücker (1998) who coined the term “swirl-switching”, and identified the oscillations as a continuous transition between two mirror-symmetric states with one Dean cell larger than the other.

Rütten *et al.* (2001, 2005) were the first to numerically study the phenomenon and showed that the switching takes place even without flow separation. Moreover, Rütten and co-workers found that the structure of the switching is more complex than just the alternation between two distinct symmetric states, since the outer stagnation point “can be found at any angular position within  $\pm 40^\circ$ ”. Rütten *et al.* attributed the switching to a shear-layer instability. However, their simulations were performed by using a “recycling” method, where the results from a straight pipe simulation were used as inflow condition for the bent pipe. These periodic straight pipes likely introduced a forcing with frequency comparable to that of the switching. Sakakibara *et al.* (2010) were the first to analyse the flow by means of two-dimensional proper orthogonal decomposition (2D POD). In a subsequent work (Sakakibara & Machida 2012) they conjectured that the swirl-switching is caused by very large-scale motions (VLSM) formed

in the straight pipe preceding the bend. Hellström *et al.* (2013) and Kalpakli & Örlü (2013); Kalpakli Vester *et al.* (2015) also presented results based on 2D POD. The former found non-symmetric modes resembling a tilted variant of the Dean vortices corresponding to the shear-layer instabilities found by Rütten *et al.* (2005). Kalpakli & Örlü (2013); Kalpakli Vester *et al.* (2015) also found antisymmetric modes as most dominant structures. Carlsson *et al.* (2015) performed LES in a geometry similar to that of Kalpakli & Örlü (2013), namely, with a short straight section following the bend, for four different curvatures. The inflow boundary condition was generated by means of a recycling method, as in Rütten *et al.* (2001, 2005). The three lower curvatures were therefore dominated by the spurious frequencies artificially created in the straight pipe by the recycling method, while the frequencies measured for  $\delta = 1$  were in the same range identified by Hellström *et al.* (2013) but were found to be mesh dependent. Noorani & Schlatter (2016) were the first to investigate the swirl-switching by means of direct numerical simulations (DNS). By using a toroidal pipe they showed that swirl-switching is not caused by structures coming from the straight pipe preceding the bend, but is a phenomenon inherent to the curved section.

### 5.1. Investigation methods

The present analysis is performed by means of direct numerical simulations, where the equations are discretised with the spectral-element code NEK5000 (Fischer *et al.* 2008). Figure 5.1 shows the computational domain, which is a  $90^\circ$  bent pipe with curvature  $\delta = 0.3$ . A straight pipe of length  $L_i = 7D$  precedes the bent section and a second straight segment of length  $L_o = 15D$  follows it. The Reynolds number is fixed to  $Re = 11\,700$ , corresponding to a friction Reynolds number  $Re_\tau \approx 360$  (referred to the straight pipe sections). In order to avoid the excitation of unphysical phenomena or a modification of the frequencies inherent to the swirl-switching, the velocity field at the inlet boundary of the straight pipe preceding the bend is prescribed via a divergence-free synthetic eddy method (DFSEM). This method, introduced by Poletto *et al.* (2011) and based on the original work by Jarrin *et al.* (2006), works by prescribing a mean flow modulated in time by fluctuations in the vorticity field. Details are provided in paper 6.

Snapshot POD (Lumley 1967; Sirovich 1987) is used to extract coherent structures from the DNS flow fields and identify the mechanism responsible for swirl-switching. POD decomposes the flow into a set of orthogonal spatial modes and corresponding time coefficients ranked by kinetic energy content in decreasing order. The most energetic structure extracted by POD corresponds to the mean flow and will be herein named “zeroth mode”, while the term “first mode” will be reserved for the first time-dependent structure. The symmetry of the pipe about the  $I - O$  plane, which results into a statistical symmetry for the flow, is used to improve the convergence of the decomposition by storing an additional mirror image for each snapshot (Berkooz *et al.* 1993).

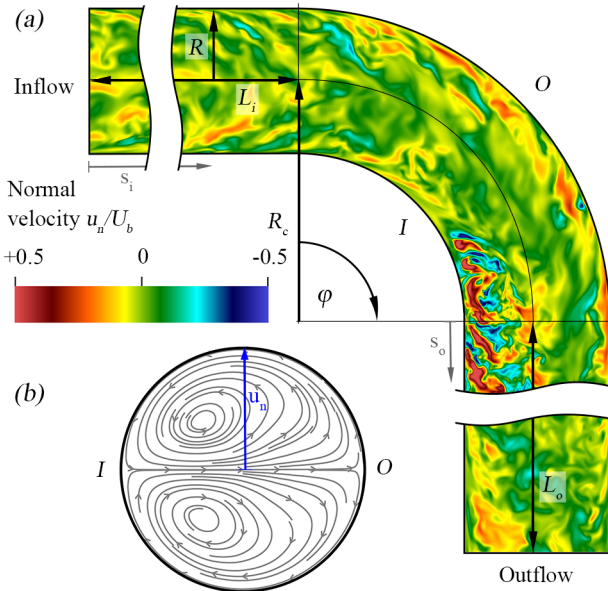


Figure 5.1: Schematic of the computational domain. (a) A section of the pipe with curvature  $\delta = R/R_c = 0.3$ , including the definition of the geometrical parameters and an instantaneous flow field coloured by normal velocity, *i.e.* normal to the bend symmetry plane. (b) Streamlines of the mean cross-flow showing the Dean vortices on a cross-section extracted at  $s_o = 0$ . Hufnagel *et al.*, The three-dimensional structure of swirl-switching in bent pipe flow, *J. Fluid Mech.* 835:86–101 (2017), reproduced with permission.

## 5.2. Swirl-switching is a wave-like structure

The four most energetic modes are depicted in figure 5.2 by means of pseudo-colors of normal and streamwise velocity components, as well as streamlines of the in-plane velocity. It can be observed that the modes come in pairs: 1-2 and 3-4, as is usual for POD modes and their time coefficients in a convective flow. The first coherent structure extracted by the POD is formed by modes 1 and 2 and constitutes a damped wave-like structure that is convected by the mean flow. The spatial structure of these modes is qualitatively sinusoidal along the streamwise direction  $s_o$ , with a wavelength of about 7 pipe diameters. This wave-like structure is formed by two counter-rotating swirls, visible in the 2D cross-sections in figure 5.2, which are advected in the streamwise direction while decaying in intensity and, at the same time, move from the inside of the bend towards the outside, as can be seen in the longitudinal cuts in figure 5.2

As can be observed from figure 5.2, the modes do not present any connection to the straight pipe section preceding the bend. This is in direct contrast with

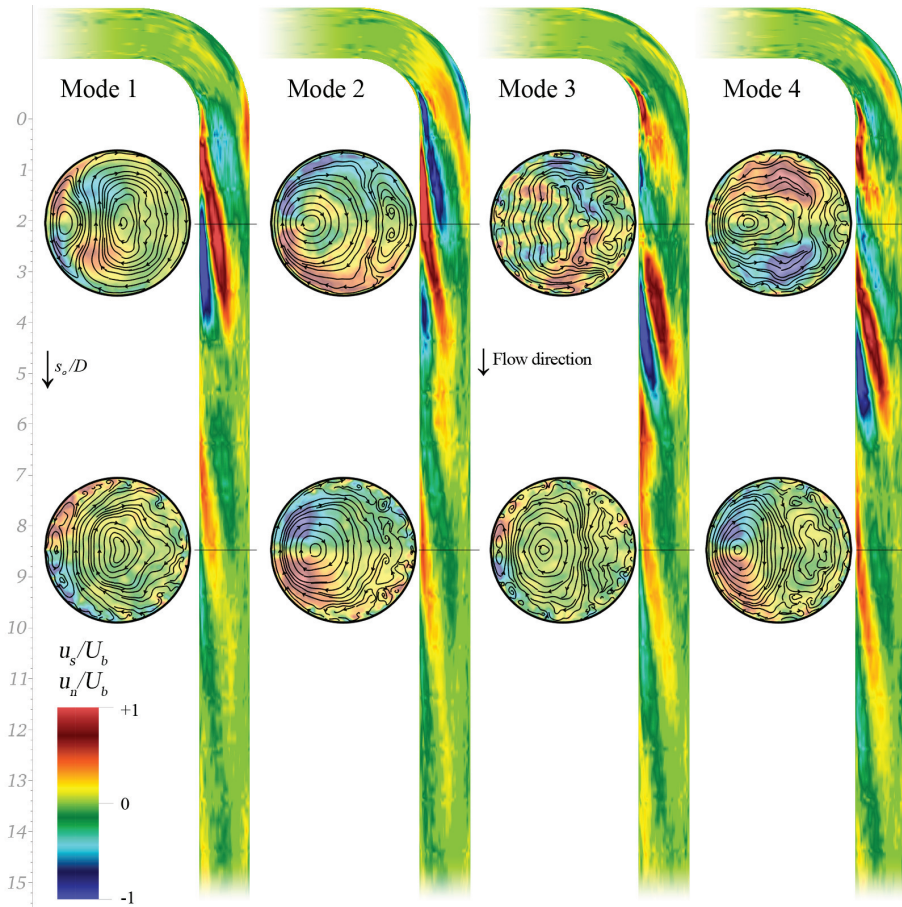


Figure 5.2: Four most energetic three-dimensional POD modes. The four longitudinal cuts show pseudocolours of the normal velocity component  $u_n$ , while the eight cross-sections display the in-plane streamlines and are coloured by streamwise velocity  $u_s$ . Hufnagel *et al.*, The three-dimensional structure of swirl-switching in bent pipe flow, *J. Fluid Mech.* 835:86–101 (2017), reproduced with permission.

the findings of Carlsson *et al.* (2015), whose results were likely altered by the use of a recycling inflow.

The present findings are also in contrast with previous conclusions drawn from flow reconstructions based on 2D POD modes that invoke Taylor's frozen turbulence hypothesis (see, *e.g.*, Hellström *et al.* 2013). This is due to the fact that the 2D analysis mixes convection and true temporal variation, and thus cannot reveal the full three-dimensional structure of travelling modes. This does

not only apply to the present flow case, but to any streamwise inhomogeneous flow in which 2D POD is utilised in the cross-flow direction.

A final comment is that the wave-like structure found in the present study is different from those observed in transitional flows (see, *e.g.* Hof *et al.* 2004). It is simply a coherent structure extracted by POD from a turbulent background flow, as opposed to an exact coherent state or an eigenmode. Nevertheless, this wavy structure may be a surviving remnant of a global instability caused by the bend, as discussed in chapter 2.

## CHAPTER 6

# Friction control in turbulent channel flows

Turbulent flows are massively present in engineering applications which require fast and effective solutions. As an example the energy and transport industries have seen a steady development over the years. The naval shipping and aeronautical industries alone consume a combined 572 billion liters of fuel per year (Kim & Bewley 2007). The shear size of this figure indicates that even marginal improvements aimed at fuel saving have an enormous impact on the economy and the environment.

The turbulent flow in a channel, similarly to that inside of a straight pipe, is one of the most studied internal flows in fluid mechanics (Moser *et al.* 1999). This is because, despite its simplicity, it presents most of the features found in wall-bounded turbulent flows, it can therefore be used as a model for more complex geometries and, among other things, as a test case for control and drag reduction strategies. In fact, a large number of numerical and experimental studies have been performed in channel flows to find effective control mechanisms for wall-shear-stress modifications (see, for example, Gad-el Hak 2007). Most of these control strategies, though, have only been tested for relatively low Reynolds numbers.

### 6.1. Prelude

Turbulent flows are studied with a different approach: these flows are chaotic and it is nearly impossible to accurately describe the kinematics and dynamics of each of the numerous structures that constitute them.

When analysing turbulent flows it is customary to decompose the velocity field into its mean and fluctuating components (see, for example, Pope 2000). Each of these satisfies a ‘modified version’ of the Navier–Stokes equations, where different terms can be identified as contributing to the production, transport and dissipation of turbulent kinetic energy. It is by analysing the time averaged effect of these terms, and the action of the fluid on solid surfaces, that turbulent flows are commonly studied. A different but complementary approach is to analyse what is known as *coherent structures*. These are structures, first identified by flow visualisation (Kline *et al.* 1967) or other eduction techniques, which can interact between each other in a self-sustaining process (Waleffe 1997) and regulate the turbulence intensity close to the wall.

In the present chapter the goal is not only to analyse the flow, but also to find a way to modify it and reduce the viscous drag that affects the surfaces in contact with the fluid. Different approaches to this problem have been proposed in the past decades. A first major distinction can be made between *active* and *passive* strategies: the former class comprises solutions that require an input of energy, while methods pertaining to the latter category are based on modifications of the geometry of the flow (Gad-el Hak 2007).

A few examples of effective active techniques comprise blowing and/or suction of fluid on the wetted surface (Kametani *et al.* 2015; Stroh *et al.* 2015), applying volume forces to modify the velocity field (Choi *et al.* 1994), and introducing spanwise oscillations (Jung *et al.* 1992) or travelling waves (Quadrio *et al.* 2009) at the wall. Passive techniques, instead, usually involve the addition of surface elements such as riblets (Choi *et al.* 1993; García-Mayoral & Jiménez 2011) or a non-uniform distribution of roughness (Vanderwel & Ganapathisubramani 2015).

The drag on a moving object can be divided into two major contributions: one caused by pressure differences between the front and backward facing parts of the body, and the other due to friction generated by the relative movement between the object and the surrounding fluid. The second part of the present thesis, and all of the flow control techniques mentioned above, deal with the second cause, also known as *skin-friction drag*. It has been long known, though, that turbulent flows for relatively low Reynolds numbers are affected by phenomena which disappear when  $Re$  is increased (Moser *et al.* 1999), so called low- $Re$  effects. It is then very important to verify the effectiveness of the proposed control strategies at higher  $Re$  and/or as a function of  $Re$  (Iwamoto *et al.* 2002; Gatti & Quadrio 2013).

## 6.2. A description of the flow

This chapter is concerned with the ideal flow through a channel of height  $2h$ , and ‘infinite’ length and width. This infinitely large channel is numerically simulated with a box periodic in the streamwise and spanwise directions (see figure 6.1). In the uncontrolled case the mean flow has only one component ( $U$ ) in the streamwise ( $x$ ) direction and most of the turbulent production takes place close to the channel walls, in an area known as viscous wall region.

Following the initial idea by Schoppa & Hussain (1998) (sometimes referred to as SH in the following), a series of streamwise-invariant, counter-rotating vortices are superposed on the flow. In the original implementation by these authors, the vortices were introduced by performing numerical simulations with the shape of the streamwise mean flow fixed in time. This strategy, referred to as “frozen vortices” in the following, can only provide transient drag reduction and required re-thinking, as will be shown in paper 7. In the present implementation, the large-scale vortices are introduced via a volume forcing provided with variable intensity and spanwise wavelength. Applying a volume

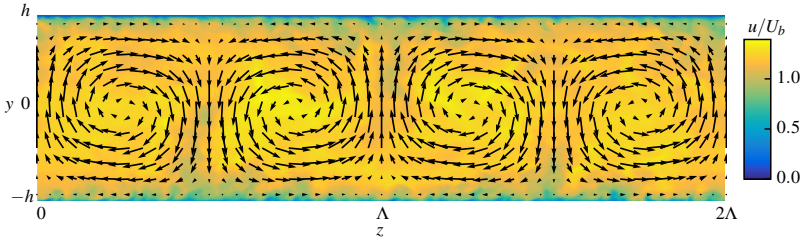


Figure 6.1: Instantaneous flow field of a controlled simulation for  $Re_\tau = 550$  illustrating the large-scale vortices (equation (6.1)). The figure depicts two vortex wavelengths, with  $\Lambda = 3.3h$ , on a cross-stream channel plane coloured by streamwise velocity magnitude. The control amplitude is  $\max |\langle v \rangle_{x,t}| \approx 0.07U_b$ . Reprinted with permission from Canton *et al.*, Phys. Rev. Fluids, 1, 081501, 2016. Copyright by the American Physical Society.

force is less intrusive than fixing the mean, and allows the fluid to freely adapt to the control mechanism.

The force field that generates the large-scale vortices is defined as:

$$\begin{aligned} f_x &= 0, \\ f_y(y, z) &= A\beta \cos(\beta z)(1 + \cos(\pi y/h)), \\ f_z(y, z) &= A\pi/h \sin(\beta z) \sin(\pi y/h), \end{aligned} \quad (6.1)$$

where  $A$  is the forcing amplitude and  $\beta$  the wavenumber along  $z$ . A sketch of the control vortices is depicted in figure 6.1. The wavenumber is chosen such as to have vortex periods  $\Lambda = 2\pi/\beta$  between  $1.1h$  and  $9.9h$ , corresponding to inner-scaled wavelengths  $\Lambda^+$  between 120 and 3630. Since  $A$  does not correspond to a measurable flow quantity, the rescaled maximum wall-normal mean velocity is used to characterise the strength of the vortices, *i.e.*  $\max |\langle v \rangle_{x,t}|/U_b$ , where  $\langle \cdot \rangle_{x,t}$  denotes the average in the streamwise direction and time.

The objective of this study is to achieve drag reduction DR. This is measured as the relative reduction in the streamwise pressure gradient  $p_x$  necessary to achieve a certain bulk flow. This index can be related to the ratio of the wall-integrated strain rate  $\Omega_w$  between the controlled and uncontrolled cases, employed by Schoppa & Hussain (1998), with the following expression:

$$DR = \frac{p_{x,\text{unc}} - p_{x,\text{con}}}{p_{x,\text{unc}}} = 1 - \frac{p_{x,\text{con}}}{p_{x,\text{unc}}} = 1 - \frac{\Omega_{w,\text{con}}}{\Omega_{w,\text{unc}}}; \quad (6.2)$$

$$\Omega_w = \frac{1}{L_x(z_2 - z_1)} \int_0^{L_x} \int_{z_1}^{z_2} \frac{\partial u}{\partial y} \Big|_{y=0} dx dz. \quad (6.3)$$

Clearly, positive values of DR correspond to a favourable effect while negative ones indicates drag increase.

The uncertainty on DR is quantified as (Tropea *et al.* 2007):

$$\sigma_{\langle \text{DR} \rangle}^2 = \frac{1}{T} \int_{-T}^T \left(1 - \frac{|\tau|}{T}\right) C_{\text{DR DR}}(\tau) d\tau \quad (6.4)$$

where  $C_{\text{DR DR}}(\tau)$  is the autocovariance of DR,  $\tau$  the signal time, and  $T$  is the length of the integration time (see table 6.1).

### 6.3. Investigation methods

All simulations are performed using the fully spectral code **SIMSON** (Chevalier *et al.* 2007), where periodicity in the wall-parallel directions  $x$  (streamwise) and  $z$  (spanwise) is imposed, and the no-slip condition is applied on the two channel walls. The wall-parallel directions are discretised using Fourier series, where aliasing errors are removed by using 1.5 times the number of modes prescribed, while a Chebyshev series is employed in the wall-normal direction. The temporal discretisation is carried out by a combination of a third order, four stage Runge–Kutta scheme for the nonlinear term, and a second order Crank–Nicolson scheme for the linear terms. The time step is chosen such that the Courant number is always below 0.8.

Four values of the bulk Reynolds number, based on bulk velocity  $U_b$ , channel half-height  $h$  and fluid viscosity  $\nu$ , are employed:  $Re = 1518, 2800, 6240$  and  $10000$ , such as to result in a friction Reynolds number, based on friction velocity  $u_\tau$ ,  $h$  and  $\nu$ , corresponding to  $Re_\tau \approx 104, 180, 360$  and  $550$ . The lowest Reynolds number, corresponding to a barely turbulent flow, is the value employed in the original study by Schoppa & Hussain (1998). Details of the domain sizes and spatial resolution employed for the four sets of simulations are reported in table 6.1.

### 6.4. Large-scale friction control

As a first step, the forcing method is applied to a channel flow for the same Reynolds number as employed by Schoppa & Hussain (1998), *i.e.*  $Re_\tau = 104$ , to compare the two methods. Six different spanwise wavelengths were chosen, including the wavelength identified by SH as the best performing for the frozen vortices, *i.e.*  $\Lambda^+ = 400$ . For each vortex size the amplitude was varied in order to determine an optimum value. Figure 6.2(b) shows that the friction on the channel walls is unchanged for very low amplitudes of the imposed vortices (approximately below 0.5%). Negative results are also obtained for strong amplitudes: above 8% of the bulk velocity all cases show significant negative DR, *i.e.* drag increase. An inspection of the flow fields, presented in paper 7, clearly shows that negative DR is caused by the strong shear created by the vortices in the near-wall region, rather than increased turbulence. In fact, for the strongest amplitude of the forcing, turbulence disappears altogether, but the frictional drag is sensibly increased. Relevant for the present study is the intermediate region of amplitudes, for which all vortex sizes (except  $\Lambda = 1.1h$ ) show at least a 10% reduction of the drag. The maximum efficiency for this Reynolds number is reached for the case with  $\Lambda = 2.2h$ , which yields  $DR \approx 16\%$ .

$Re_\tau$	Integration time $T [h/U_b]$	Domain size $L_x/h, L_z/h$	Grid points $N_x, N_y, N_z$
104	10500	8, 3.832	48, 65, 48
		8, 6.6	48, 65, 60
		8, 9.9	48, 65, 96
180	1500	12, 6.6	128, 97, 96
		12, 9.9	128, 97, 144
360	1000	12, 6.6	300, 151, 200
		12, 9.9	300, 151, 300
550	400	12, 6.6	432, 193, 300

Table 6.1: Details of the numerical discretisation employed for the simulations.  $T$  corresponds to the duration of the controlled simulations;  $N_x$  and  $N_z$  represent the number of Fourier modes employed in the wall-parallel directions (values before dealiasing), while  $N_y$  is the order of the Chebyshev series used for the wall-normal direction.

## 6.5. Reynolds number dependence of the control method

The same analysis is repeated for  $Re_\tau = 180, 360$  and  $550$ . The results for  $Re_\tau = 180$ , presented in figure 6.2(c), are similar to those for  $Re_\tau = 104$ , presenting approximately the same range of effective wavelengths and forcing amplitudes. An even greater reduction in drag, corresponding to  $DR \approx 18\%$ , is achieved for  $\Lambda = 6.6h$  and a forcing amplitude of just  $0.04U_b$ .

Although the large-scale vortices can provide a good level of drag reduction for  $Re_\tau = 104$  and  $180$ , their performance degrades rapidly with Reynolds number. For  $Re_\tau = 360$  the maximum DR is only  $8\%$ , and for  $Re_\tau = 550$  no more than  $0.4\%$  can be obtained for any of the wavelengths investigated. This is illustrated in figure 6.2(a) which shows, in semi-log scale, the maximum achievable value of DR as a function of  $Re_\tau$ .

Valuable insight on the effect that the Reynolds number has on the large-scale vortices can be obtained by analysing the wall-shear stress  $\tau_w$  as a function of  $Re_\tau$ . Figure 6.3 presents the profiles of  $\tau_w$  measured at the lower channel wall ( $y = -1$ ) for the four values of  $Re_\tau$  investigated. The analysis is conducted on vortices with  $\Lambda = 6.6h$  which better highlight the Reynolds-number dependence, but the same trend is observed for all other wavelengths. Two phenomena are clearly observable as the Reynolds number is increased: a reduction in the variation in  $\tau_w$  and a modification of the profiles as a function of  $z$ .

The first phenomenon is most probably a direct consequence of the increase in  $Re$ : as the Reynolds number increases the height of the viscous sublayer, measured in outer units, decreases as  $1/Re_\tau$ . The maximum variation in  $\tau_w$  (for a positive DR) at the centre of two vortices, where the fluid is pushed towards the wall, does also decrease monotonically with  $Re_\tau$ . This appears

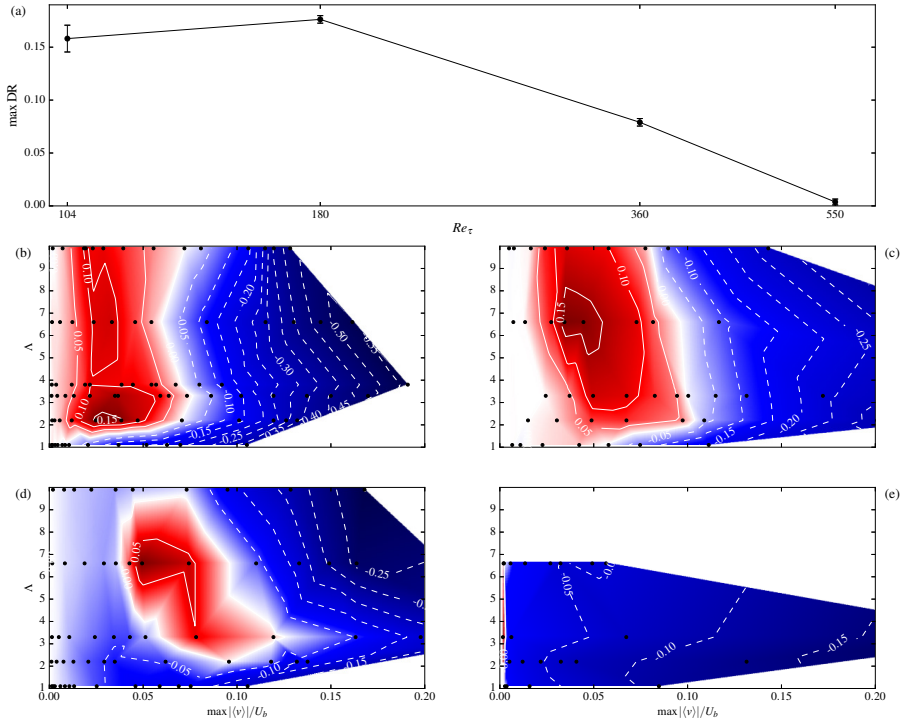


Figure 6.2: Panel (a): maximum achievable drag reduction as a function of friction Reynolds number. The uncertainty on DR is quantified by equation (6.4); the  $x$ -axis is in logarithmic scale. Panels (b) to (e) depict DR as a function of control strength,  $\max |\langle v \rangle_{x,t}|/U_b$ , and wavelength of the vortices,  $\Lambda$ .  $Re_\tau = 104, 180, 360$  and  $550$  are reported in (b), (c), (d) and (e), respectively. In (b–e) red and blue colors correspond to positive, resp. negative, values of DR; values are reported on the isocontours; black points correspond to simulations. Reprinted with permission from Canton *et al.*, Phys. Rev. Fluids, 1, 081501, 2016. Copyright by the American Physical Society.

to indicate that the large-scale vortices cannot penetrate the viscous sublayer as its height decreases, and thus cannot affect the near-wall region as  $Re_\tau$  is increased beyond a limit value. Such a result is unfortunate as the idea behind this method was to use large, Reynolds number-independent, scales to control the flow.

The second phenomenon is well illustrated by comparing figures 6.3a,b with 6.3c,d. For controlled flows at low Reynolds numbers the minimum in  $\tau_w$  is achieved close to the vertical vortex axes (located at  $1/4$  and  $3/4$  of  $\Lambda$ ) at  $z/\Lambda \approx 0.16$  and  $0.84$ ; in this area the vortices are pushing the fluid in the spanwise direction only. As the Reynolds number is increased this minimum is moved to the extrema of the period, where the vortices are lifting the fluid

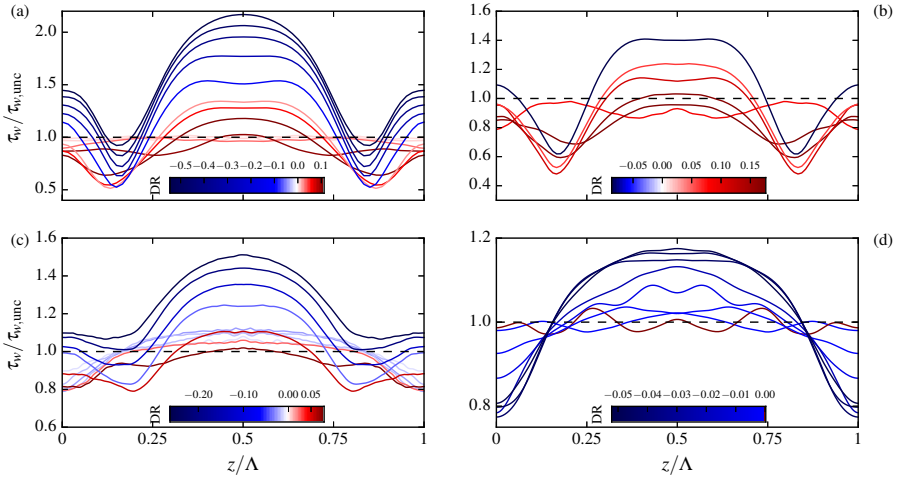


Figure 6.3: Wall shear stress at the lower channel wall ( $y = -1$ ) normalised by the value assumed in the uncontrolled case ( $\tau_w = 1$ ). The four panels (a–d) correspond to increasing Reynolds numbers,  $Re_\tau = 104, 180, 360$  and  $550$ , and show the measurements for control vortices with  $\Lambda = 6.6h$ , each line corresponding to a different forcing amplitude. A similar picture is observed for the other wavelengths investigated. The curves are colour-coded with their value of DR, reported in the legends. The dark red line in (d) corresponds to a drag reduction of only  $0.02\%$ , the highest achievable value for  $Re_\tau = 550$  for vortices with  $\Lambda = 6.6h$ . Reprinted with permission from Canton *et al.*, Phys. Rev. Fluids, 1, 081501, 2016. Copyright by the American Physical Society.

away from the wall. Concurrently, the area where the wall-shear stress is increased becomes wider than  $\Lambda/2$ , extending over the vertical vortex axes. This modification is clear at the intermediate  $Re_\tau = 360$  (figure 6.3c) where both low- and high-Reynolds profiles of  $\tau_w$  can be observed.

If the first of these phenomena can be easily attributed to an increase of  $Re_\tau$  alone, and simply results in a decrease in amplitude, the modification of the  $\tau_w$  profiles is an indication of a more fundamental change in the flow mechanics affected by the large-scale vortices. Clearly, low Reynolds number effects are still present for  $Re_\tau = 104$  and  $180$  (see also Moser *et al.* 1999) and the present large-scale control is able to affect the low- $Re$  wall cycle and thereby reduce the turbulence intensity. For higher Reynolds numbers these low  $Re$  effects disappear and the present control strategy cannot provide any drag reduction.

## 6.6. Large- vs Small-scale control

At the end of paper 8 we suggested that “a technique capable of generating fluid lift up directly at the wall, differently from the present one based on motion

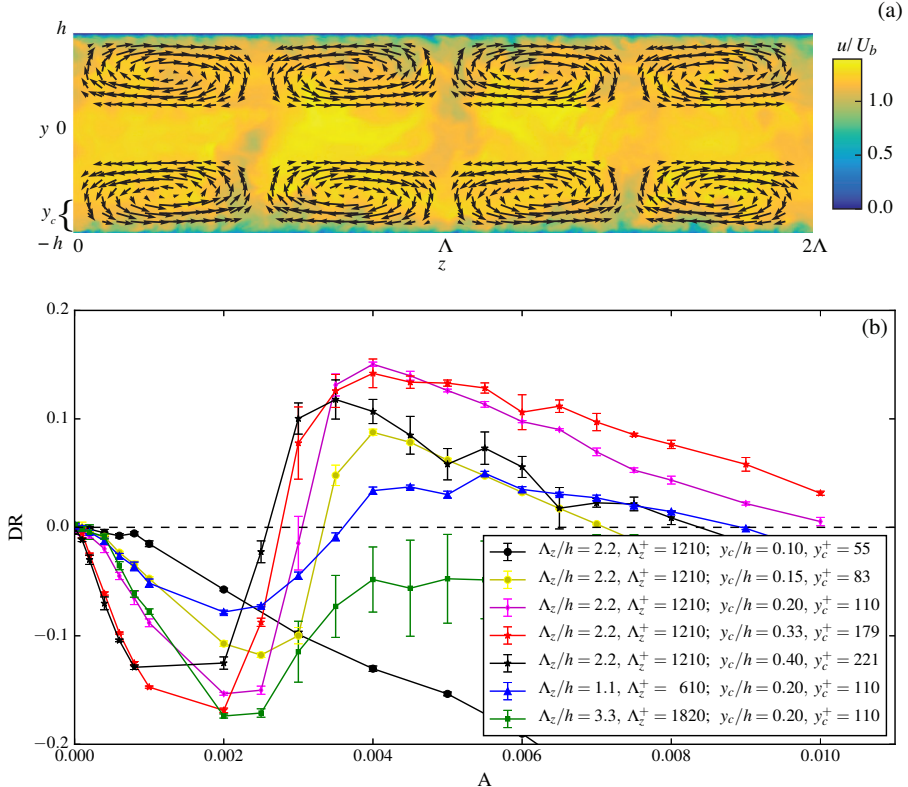


Figure 6.4: Small scale version of the control method applied at  $Re_\tau = 550$ . Besides the amplitude  $A$  and the spanwise wavelength  $\Lambda_z$ , the vortices are now controlled by one more parameter: the distance of their centre of rotation from the wall,  $y_c$ . Panel (b) presents the drag reduction provided by seven size combinations for different amplitudes. The best performing vortices for this  $Re_\tau$  have the same viscous scales of the best vortices for  $Re_\tau = 180$ .

created outside of the viscous layer, would probably be more successful for high Reynolds numbers".

We tested our idea by performing simulations at  $Re_\tau = 550$  and controlling the flow with small vortices close to the wall. Figure 6.4(a) depicts a sketch of the small-scale vortices, while preliminary results are presented in figure 6.4(b). As we expected, the small-scale vortices perform quite well for  $Re_\tau = 550$ , with a maximum DR of about 15%, while the large-scale version of the method could not provide any drag reduction. In particular, figure 6.4(b) reports results for three values of the streamwise wavelength  $\Lambda_z/h$ , and for the best of the three,  $\Lambda_z/h = 2.2$ , different vortex heights. Even without doing a thorough

optimisation of the control scheme, it can be observed that the best performance is obtained for  $\Lambda_z^+ \approx 1200$  and  $100 \lesssim y_c^+ \lesssim 180$ . These are the same values that provide the best performance for  $Re_\tau = 180$ . We can therefore conclude that this control scheme does not scale in outer units, as observed in section 6.5, but in viscous units. Therefore, this is clearly a small-scale control, and not – as labelled by others (Yao *et al.* 2017) – a large-scale control.

To make a numerical example, the experimental data and empirical relation by Dean (1978) can be used to estimate the friction coefficient as a function of Reynolds number:  $Re_\tau \approx 0.09 Re^{0.88}$ . By using this approximation, we can estimate the size that the actuators would need to have for practical applications knowing that

$$\Lambda_z = \Lambda_z^+ \delta_\nu = \frac{\Lambda_z^+ \delta}{Re_\tau}, \quad \text{and} \quad y_c = y_c^+ \delta_\nu = \frac{y_c^+ \delta}{Re_\tau}, \quad (6.5)$$

where  $\delta_\nu$  denotes the viscous length scale. If, for example, one wanted to employ this control scheme on the wings of a plane (typical cruising  $Re$  of about  $10^7$ ), substituting numerical values for optimal performance in equation (6.5), results in a spanwise wavelength  $\Lambda_z = \mathcal{O}(10^{-4})$  m and distance from the wall  $y_c = \mathcal{O}(10^{-5})$  m. It is clear that actuators of this size are utterly impractical.

## CHAPTER 7

# Summary of the papers

### Paper 1

*Characterisation of the steady, laminar incompressible flow in toroidal pipes covering the entire curvature range*

This paper presents an in-depth analysis of the steady solution in curved pipe flows. A large database of numerical solutions, computed without any approximation, is presented spanning, for the first time, the entire curvature range and for Reynolds numbers ranging from 10 to 7000, where the flow is known to be unsteady. The analysis shows that by increasing the curvature the flow is fundamentally changed. Moderate to high curvature solutions are not only quantitatively, but also qualitatively different from low curvature solutions. It is therefore concluded that the Dean number and the Dean similarity are only relevant for infinitesimally low curvature. A complete description of some of the most relevant flow quantities is provided. Most notably Ito's [J. Basic Eng. **81**:123–134 (1959)] plot of the friction factor for laminar flow in curved pipes is reproduced, the influence of the curvature on the friction factor is quantified and the scaling is discussed at length.

### Paper 2

*Modal instability of the flow in a toroidal pipe*

This paper presents a study of the first instability encountered by the incompressible flow in a toroidal pipe. It is found that, differently from the flow inside a straight pipe, this flow is modally unstable for all curvatures, the lowest investigated being 0.002, and that the steady solution undergoes a Hopf bifurcation leading to a limit cycle for a bulk Reynolds number of about 4000. The instability is therefore studied by means of linear stability analysis with classical eigenvalue computations and a novel bifurcation tracking algorithm. The analysis reveals that several families and isolated modes contribute to the neutral curve corresponding to the Hopf bifurcation. Comparison to nonlinear DNS shows excellent agreement, confirming the linear analysis and proving its significance for the nonlinear flow. Experimental data from the literature are also shown to be in considerable agreement with the present results.

## Paper 3

### *Approaching zero curvature: modal instability in a bent pipe*

The objective of the present work to investigate the behaviour of the linear instability as the curvature of the pipe tends to zero. In order to do so, a stability code solving the equations in toroidal coordinates is presented. Results indicate that the toroidal pipe remains linearly unstable for curvatures as low as  $10^{-7}$ . While the critical Reynolds number  $Re$  necessary for the instability grows with an approximately algebraic trend below  $\delta = 0.002$ , the neutral curve also closes in onto the limit of negligible curvature. It therefore appears that there could be values of  $\delta$  and  $Re$  where a linearly unstable toroidal flow could be connected to the linearly stable straight pipe flow.

## Paper 4

### *The collapse of strong turbulent fronts in bent pipes*

Isolated patches of turbulence in transitional straight pipes are sustained by a strong instability at their upstream front, where the production of turbulent kinetic energy (TKE) is up to five times higher than in the core. Direct numerical simulations presented in this paper show no evidence of such strong fronts if the pipe is bent. This paper details the temporal and spatial evolution of puffs and slugs in a toroidal pipe with pipe-to-torus diameter ratio  $\delta = D/d = 0.01$  at several subcritical Reynolds numbers. Results show that the upstream overshoot of TKE production is at most one-and-a-half times the value in the core and that the average cross-flow fluctuations at the front are up to three times lower if compared to a straight pipe, while attaining similar values in the core. Localised turbulence can be sustained at smaller energies through a redistribution of turbulent fluctuations and vortical structures by the in-plane Dean motion of the mean flow. This asymmetry determines a strong localisation of TKE production near the outer bend, where linear and nonlinear mechanisms optimally amplify perturbations. A substantial reduction of the range of Reynolds numbers for long-lived intermittent turbulence is also observed, in agreement with experimental data from the literature. Moreover, no occurrence of nucleation of spots through splitting are detected in the range of parameters considered. Based on the present results, we argue that this mechanism gradually becomes marginal as the curvature of the pipe increases and the transition scenario approaches a dynamical switch from subcritical to supercritical.

**Paper 5***A critical point for bifurcation cascades and intermittency*

Transition to turbulence in straight pipe flow is a subcritical process, dominated by the proliferation of isolated patches of turbulence. However, experiments and computations suggest that when the pipe is bent above a pipe-to-coiling diameter ratio  $\delta \gtrsim 0.028$  a supercritical Hopf bifurcation initiates a cascade, leading through increasing flow complexity and, ultimately, to a fully turbulent state. This paper proves this speculation correct by presenting the reconstruction, from nonlinear simulations at  $\delta = 0.05$ , of a stable two-periodic attractor and measurements of incommensurable frequencies in the flow. We also report evidence, in a limited region of the  $\delta - Re$  parameter space, of the coexistence of fully turbulent flow and of a stable supercritical limit cycle; both being attracting states with finite and complementary basins. This is the first time that a fluid flow is shown to be stable in both turbulent and laminar states (other than the steady solution) for a fixed combination of flow parameters.

**Paper 6***The three-dimensional structure of swirl-switching in bent pipe flow*

Swirl-switching is a low-frequency oscillatory phenomenon which affects the Dean vortices in bent pipes and may cause fatigue in piping systems. Despite thirty years worth of research, the mechanism that causes these oscillations and the frequencies that characterise them remain unclear. This paper shows that a three-dimensional wave-like structure is responsible for the low-frequency switching of the dominant Dean vortex. The present study, performed via direct numerical simulation, focuses on the turbulent flow through a  $90^\circ$  pipe bend preceded and followed by straight pipe segments. A pipe with curvature 0.3 (defined as ratio between pipe radius and bend radius) is studied for a bulk Reynolds number  $Re = 11\,700$ , corresponding to a friction Reynolds number  $Re_\tau \approx 360$ . Synthetic turbulence is generated at the inflow section and used instead of the classical recycling method in order to avoid the interference between recycling and swirl-switching frequencies. The flow field is analysed by three-dimensional proper orthogonal decomposition (POD) which for the first time allows the identification of the source of swirl-switching: a wave-like structure that originates in the pipe bend. Contrary to some previous studies, the flow in the upstream pipe does not show any direct influence on the swirl-switching modes. It is also shown that a three-dimensional characterisation of the modes is crucial to understand the mechanism, and that reconstructions based on 2D POD modes are incomplete.

## Paper 7

*On large-scale friction control in turbulent wall flow in low Reynolds number channels*

This is the first of two papers on turbulent skin-friction control via large-scale, counter-rotating vortices. The idea of a control strategy not involving viscous, and thus Reynolds number-dependent, flow scales was advanced in a paper by Schoppa & Hussain [Phys Fluids **10**:1049–1051 (1998)]. The original implementation of the vortices consisted in the numerical imposition of the mean flow in the simulations. This approach is revisited in the present paper where the vortices are re-implemented as a volume force since the original implementation was found to be unphysical and lead only to transient drag-reduction at most. The control is tested in turbulent channel flows for friction Reynolds numbers  $Re_\tau$  of 104 (as in the original study) and 180. A parameter study involving forcing amplitude and wavelength are performed for both Reynolds numbers, in search for optimal values. The vortices prove to be effective, providing a drag reduction of up to 18% for a viscous-scaled wavelength of 1200 and a forcing strength of only about 4% of the bulk velocity. An analysis of the flow quantities altered by the control is presented in an effort to elucidate the mechanics of operation of the vortices.

## Paper 8

*Reynolds number dependence of large-scale friction control in turbulent channel flow*

This paper is concerned with the Reynolds-number dependence of the large scale vortex control scheme proposed by Schoppa & Hussain [Phys Fluids **10**:1049–1051 (1998)] and is a natural extension of Paper 3. Two new sets of Direct Numerical Simulations have been performed for friction Reynolds numbers  $Re_\tau$  of 360 and 550. These simulations, along with the ones carried out for lower  $Re_\tau$ , constitute an extensive database that allows an in-depth analysis of the method as a function of the control parameters (amplitude and wavelength) and the Reynolds number. Results show that the effectiveness of the method is reduced as the Reynolds number increases above  $Re_\tau = 180$  and no drag reduction can be achieved for  $Re_\tau = 550$  for any combination of the parameters controlling the vortices. An analysis of the effects of  $Re_\tau$  on the mechanics of the control is presented as a function of both outer and inner (viscous) scaling.

## CHAPTER 8

# Conclusions and outlook

Stability and transition to turbulence in bent pipes have been studied with linear and nonlinear methods. Regarding lower Reynolds numbers, the focus is on the flow in a toroidal pipe, as it represents the common asymptotic limit between spatially developing and helical pipes. It is shown that a Dean number ( $De$ )-based analysis is inadequate even for the laminar flow where quantities that were believed to scale with  $De$ , e.g. the friction factor, are actually a function of curvature and Reynolds number separately.

The flow inside a toroidal pipe is analysed close to its first instability for the complete range of curvatures. The results of the stability analysis show that an infinitesimal curvature is sufficient to make this flow linearly unstable. It is found that a Hopf bifurcation leads the flow to a periodic regime for all curvatures. A novel bifurcation tracking algorithm is introduced and employed to trace the neutral curve associated to this bifurcation. Several different modes are found, with differing properties and eigenfunction shapes. Some eigenmodes are observed to belong to groups with common characteristics, deemed families, while others appear as isolated. These findings show excellent agreement with nonlinear simulations and previous experimental results. As the curvature tends to zero, towards the straight pipe limit, the flow remains linearly unstable, but the critical Reynolds number grows nearly exponentially.

A different kind of analysis is performed in the low curvature range, where subcritical transition precedes the modal instability. Here the flow becomes turbulent while being linearly stable, with laminar and turbulent flows coexisting in an intermittent fashion. Localised turbulent structures in bent pipes bear qualitative similarities to those in straight pipes in that they appear in the form of puffs and slugs that are sustained by an instability at their upstream front. However, the most striking difference is a substantial weakening of the front if the pipe is bent. Furthermore, there appears to be no puff splitting, at least for the choice of parameters investigated. The absence of puff splitting is likely to be connected to the weak and localised upstream fronts: turbulent structures that leave a mother puff have a low probability of entering the small region of high amplification located near the outer wall, which would trigger the instability that sustains a puff.

The phenomenon of swirl-switching in turbulent bent pipe flow is also studied in the present work. The method of choice is three-dimensional proper orthogonal decomposition, performed on snapshots extracted from nonlinear simulations, where synthetic turbulence is prescribed at the inflow. Results show that the switching is caused by the presence of a wave-like structure with a wave length of about 7 pipe diameters. Differently from results reported in the literature, this mode does not present any connection to the straight pipe preceding the bend. Moreover, it is concluded that it is due to the three-dimensional, travelling structure of this single mode that this phenomenon was confused with multiple two-dimensional modes in previous studies.

Finally, a study on drag reduction via large-scale vortices in turbulent channel flow is also presented. It is shown that, for low Reynolds numbers, substantial skin-friction drag reduction can be achieved by imposing counter-rotating, streamwise-invariant vortices as a volume force. Drag reduction is achieved via a delicate balance between the region where the vortices lift turbulence away from the wall, reducing the wall-shear stress, and the region where, despite causing relaminarisation, the vortices induce a higher skin-friction drag. It is also found that the performance of this control strategy rapidly decreases with Reynolds number, since the large-scale vortices are only effective in flows where low- $Re$  effects are still present, and cannot induce any drag reduction for  $Re_\tau \geq 550$ . For high values of  $Re_\tau$  the control scheme can still work, but only if the size of the vortices and their distance from the wall are scaled in viscous units. This renders the method Reynolds number-dependent, and necessitates small and impractical actuators for typical industry applications.

## Outlook on future work

As it is often the case, some rather interesting questions remain unanswered.

It is still not entirely clear how the neutral curve of the flow in a toroidal pipe connects to the  $Re$ -independent stability of the flow in a straight pipe. Present results indicate that zero curvature is an asymptotic limit for the neutral curve, which approaches  $\delta = 0$  with  $Re \rightarrow \infty$  algebraically. However, the number of data points currently available is not sufficient to draw firm conclusions. An additional analysis could also be performed by separating the effects that the curvature has on the base flow and on the perturbation fields. Moreover, the code written in toroidal coordinates can be readily adapted to solve the equations in helical coordinates, allowing the study of helically coiled pipes and of the effect of torsion on the transition scenario.

No puff splitting was observed in our simulations of the subcritical regime at low curvatures. We conjectured that this phenomenon is actually absent, and provided a possible explanation. Our claim should be verified by repeating our simulations for longer times or, even better, experimentally, as done in straight pipes. An experimental apparatus with a helically coiled pipe could also be used, since low torsion does not affect the transition scenario; this could

be built using a very long pipe, therefore allowing the observation of puffs for long times and the possibility of numerous repetitions with different initial perturbations. It is also important to understand whether puff splitting is absent for any curvature greater than zero, confining it to a purely straight pipe phenomenon, or if instead, and more likely, it is gradually affected by the introduction of curvature.

The critical point where sub- and supercritical transition intersect also requires additional investigations. We documented the coexistence of a bifurcation cascade and featureless turbulence, but an in-depth explanation of the dynamics of the system in the neighbourhood of this point could shed new light on both transition processes. Here as well the code written in toroidal coordinates could help, by reducing the computational cost of the many simulations required.

Regarding swirl-switching, we could determine the nature of these oscillations, but the origin of this wave-like structure remains, at the moment of writing, unknown. We conjectured that this structure, until now observed in relatively turbulent flows, could actually appear at lower Reynolds numbers and be caused by a modal instability of the flow; this is currently under active investigation.

## Acknowledgements

I would like to thank my advisors, Philipp Schlatter and Ramis Örlü for choosing me as a PhD student. During the past four years they have taught me a lot, not only about fluid mechanics; they have also provided me with constant support and helped me whenever I needed it, in and out of the office. Lastly, they have also sent me around the globe to conferences and workshops which greatly enriched me as a researcher and as a person. Special thanks to Shervin Bagheri who reviewed both my theses, providing helpful suggestions, and took me twice to Montestigliano workshops. Lastly, Henrik Alfredsson who, with the help of Ramis and Antonio Segalini, did his best to bring me back to the real world, and asked to be chairman at my defence.

I am grateful to my many friends and colleagues at the department, past and present, to all the people who lent me their couch in times of need, to the Royal Technicians for the distraction, and to the graphic designers for helping with the cover page. And, in no particular order, to Enrico, with whom it was nice to work and exchange opinions in the past year, Mattias, who translated all the Swedish things that needed translation and accepted only gelato as form of payment, Prabal, Giandomenico, Elektra, Nicolas, Pierluigi, Luca, Marco, Walter, Nicolò, Mehdi, Ali, Kristina, Ning, Francesco, Marco, Pedro, Ricardo, Evelyn, Lorenz, Velibor, Matteo, Emanuele, Ekaterina, Uğis, Erik, Azad, Daniel, Ellinor, Iman, Jean Cristophe, Luis.

I would like to thank my family, for the support you always give me and for teaching me how to become who I am. Last, but not least, thank you Agnese, always with me even when two thousand kilometers away, for the love and the infinite patience.

This study has been supported by the *Swedish Research Council* (VR; Diarienummer: 621-2013-5788). Parts of the thesis have also been funded by the Knut and Alice Wallenberg Foundation via the Wallenberg Academy Fellow Programme. Computer time was provided by the Swedish National Infrastructure for Computing (SNIC) and PRACE. The Petersohns Minne Foundation is acknowledged for travel stipends. GKN Aerospace is acknowledged for awarding the prize in mechanics at the 25<sup>th</sup> Svenska Mekanikdagarna.

## Bibliography

- ADLER, M. 1934 Strömung in gekrümmten Rohren. *ZAMM-Z. Angew. Math. Mech.* **14**, 257–275.
- ANDERECK, C. D., LIU, S. S. & SWINNEY, H. L. 1986 Flow regimes in a circular Couette system with independently rotating cylinders. *J. Fluid Mech.* **164**, 155–183.
- AVILA, K., MOXEY, D., DE LOZAR, A., AVILA, M., BARKLEY, D. & HOF, B. 2011 The onset of turbulence in pipe flow. *Science* **333** (6039), 192–196.
- BARKLEY, D. 2011 Simplifying the complexity of pipe flow. *Phys. Rev. E* **84** (1), 016309.
- BARKLEY, D. 2016 Theoretical perspective on the route to turbulence in a pipe. *J. Fluid Mech.* **803**, P1.
- BARKLEY, D., SONG, B., MUKUND, V., LEMOULT, G., AVILA, M. & HOF, B. 2015 The rise of fully turbulent flow. *Nature* **526** (7574), 550–553.
- BATCHELOR, G. K. 2000 *An Introduction to Fluid Dynamics*. Cambridge University Press.
- BERGER, S. A., TALBOT, L. & YAO, L. S. 1983 Flow in curved pipes. *Annu. Rev. Fluid Mech.* **15**, 461–512.
- BERKOOZ, G., HOLMES, P. & LUMLEY, J. L. 1993 The proper orthogonal decomposition in the analysis of turbulent flows. *Annu. Rev. Fluid Mech.* **25**, 539–575.
- BRÜCKER, C. 1998 A time-recording DPIV-study of the swirl switching effect in a 90° bend flow. *Proc. 8th Int. Symp. Flow Vis. Sorrento (NA), Italy* pp. 171.1–171.6.
- BULUSU, K. V., HUSSAIN, S. & PLESNIAK, M. W. 2014 Determination of secondary flow morphologies by wavelet analysis in a curved artery model with physiological inflow. *Exp. Fluids* **55**, 1832.
- CANTON, J. 2013 Global linear stability of axisymmetric coaxial jets. Master's thesis, Politecnico di Milano, Italy, <https://www.politesi.polimi.it/handle/10589/87827>.
- CANTON, J., AUTERI, F. & CARINI, M. 2017a Linear global stability of two incompressible coaxial jets. *J. Fluid Mech.* **824**, 886–911.
- CANTON, J., ÖRLÜ, R. & SCHLATTER, P. 2017b Characterisation of the steady, laminar incompressible flow in toroidal pipes covering the entire curvature range. *Int. J. Heat Fluid Flow* **66**, 95–107.
- CARLSSON, C., ALENIUS, E. & FUCHS, L. 2015 Swirl switching in turbulent flow through 90° pipe bends. *Phys. Fluids* **27**, 085112.
- CHEVALIER, M., SCHLATTER, P., LUNDBLADH, A. & HENNINGSON, D. S. 2007 SIMSON

- A pseudo-spectral solver for incompressible boundary layer flows. *Tech. Rep.* TRITA-MEK 2007:07. KTH Mechanics, Stockholm, Sweden.
- CHOI, H., MOIN, P. & KIM, J. 1993 Direct numerical simulation of turbulent flow over riblets. *J. Fluid Mech.* **255**, 503–539.
- CHOI, H., MOIN, P. & KIM, J. 1994 Active turbulence control for drag reduction in wall-bounded flows. *J. Fluid Mech.* **262**, 75–110.
- CIEŚLICKI, K. & PIECHNA, A. 2012 Can the Dean number alone characterize flow similarity in differently bent tubes? *J. Fluids Eng.* **134**, 051205.
- CIONCOLINI, A. & SANTINI, L. 2006 An experimental investigation regarding the laminar to turbulent flow transition in helically coiled pipes. *Exp. Therm. Fluid Sci.* **30**, 367–380.
- COLES, D. 1965 Transition in circular Couette flow. *J. Fluid Mech.* **21** (3), 385–425.
- DEAN, R. B. 1978 Reynolds number dependence of skin friction and other bulk flow variables in two-dimensional rectangular duct flow. *J. Fluids Eng.* **100** (2), 215–223.
- DEAN, W. R. 1927 XVI. Note on the motion of fluid in a curved pipe. *London, Edinburgh, Dublin Philos. Mag. J. Sci.* **4**, 208–223.
- DEAN, W. R. 1928 The streamline motion of fluid in a curved pipe. *Phil. Mag.* **5**, 673–693.
- EL KHOURY, G. K., SCHLATTER, P., NOORANI, A., FISCHER, P. F., BRETHOUWER, G. & JOHANSSON, A. V. 2013 Direct numerical simulation of turbulent pipe flow at moderately high reynolds numbers. *Flow Turbul. Combust.* **91** (3), 475–495.
- EUSTICE, J. 1910 Flow of water in curved pipes. *Proc. R. Soc. London, Ser. A* **84**, 107–118.
- EUSTICE, J. 1911 Experiments on stream-line motion in curved pipes. *Proc. R. Soc. A Math. Phys. Eng. Sci.* **85**, 119–131.
- FISCHER, P. F., LOTTES, J. W. & KERKEMEIR, S. G. 2008 Nek5000 Web page.
- GARCÍA-MAYORAL, R. & JIMÉNEZ, J. 2011 Drag reduction by riblets. *Philos. Trans. A. Math. Phys. Eng. Sci.* **369**, 1412–1427.
- GATTI, D. & QUADRI, M. 2013 Performance losses of drag-reducing spanwise forcing at moderate values of the Reynolds number. *Phys. Fluids* **25**, 125109.
- GAD-EL HAK, M. 2007 *Flow Control: Passive, Active, and Reactive Flow Management*. Cambridge University Press.
- HELLSTRÖM, L. H. O., ZLATINOV, M. B., CAO, G. & SMITS, A. J. 2013 Turbulent pipe flow downstream of a 90° bend. *J. Fluid Mech.* **735**, R7.
- HOF, B., VAN DOORNE, C. W. H., WESTERWEEL, J., NIEUWSTADT, F. T. M., FAISST, H., ECKHARDT, B., WEDIN, H., KERSWELL, R. R. & WALEFFE, F. 2004 Experimental observation of nonlinear traveling waves in turbulent pipe flow. *Science* **305**, 1594–1598.
- ITO, H. 1959 Friction factors for turbulent flow in curved pipes. *J. Basic Eng.* **81**, 123–134.
- IWAMOTO, K., SUZUKI, Y. & KASAGI, N. 2002 Reynolds number effect on wall turbulence: toward effective feedback control. *Int. J. Heat Fluid Flow* **23**, 678–689.
- JARRIN, N., BENHAMADOUCHE, S., LAURENCE, D. & PROSSER, R. 2006 A synthetic-eddy-method for generating inflow conditions for large-eddy simulations. *Int. J. Heat Fluid Flow* **27**, 585–593.

- JEONG, J. & HUSSAIN, F. 1995 On the identification of a vortex. *J. Fluid Mech.* **285**, 69–94.
- JUNG, W., MANGIAVACCHI, N. & AKHAVAN, R. 1992 Suppression of turbulence in wall-bounded flows by high-frequency spanwise oscillations. *Phys. Fluids* **4**, 1605–1607.
- KALPAKLI, A. & ÖRLÜ, R. 2013 Turbulent pipe flow downstream a 90° pipe bend with and without superimposed swirl. *Int. J. Heat Fluid Flow* **41**, 103–111.
- KALPAKLI VESTER, A., ÖRLÜ, R. & ALFREDSSON, P. H. 2015 POD analysis of the turbulent flow downstream a mild and sharp bend. *Exp. Fluids* **56**, 57.
- KALPAKLI VESTER, A., ÖRLÜ, R. & ALFREDSSON, P. H. 2016 Turbulent flows in curved pipes: recent advances in experiments and simulations. *Appl. Mech. Rev.* **68**, 050802.
- KAMETANI, Y., FUKAGATA, K., ÖRLÜ, R. & SCHLATTER, P. 2015 Effect of uniform blowing/suction in a turbulent boundary layer at moderate Reynolds number. *Int. J. Heat Fluid Flow* **55**, 132–142.
- KEULEGAN, G. H. & BEIJ, K. H. 1937 Pressure losses for fluid flow in curved pipes. *J. Res. Nat. Bur. Stand.* **18**, 89–114.
- KIM, J. & BEWLEY, T. R. 2007 A linear systems approach to flow control. *Annu. Rev. Fluid Mech.* **39**, 383–417.
- KIM, J., MOIN, P. & MOSER, R. 1987 Turbulence statistics in fully developed channel flow at low Reynolds number. *J. Fluid Mech.* **177**, 133–166.
- KLEISER, L. & ZANG, T. A. 1991 Numerical-simulation of transition in wall-bounded shear flows. *Annu. Rev. Fluid Mech.* **23**, 495–537.
- KLINE, S. J., REYNOLDS, W. C., SCHRAUB, F. A. & RUNSTADLER, P. W. 1967 The structure of turbulent boundary layers. *J. Fluid Mech.* **30**, 741–773.
- KÜHNEN, J., BRAUNSHIER, P., SCHWEGEL, M., KUHLMANN, H. C. & HOF, B. 2015 Subcritical versus supercritical transition to turbulence in curved pipes. *J. Fluid Mech.* **770**, R3.
- KÜHNEN, J., HOLZNER, M., HOF, B. & KUHLMANN, H. C. 2014 Experimental investigation of transitional flow in a toroidal pipe. *J. Fluid Mech.* **738**, 463–491.
- KUZNETSOV, Y. A. 2004 *Elements of Applied Bifurcation Theory*. Springer–Verlag.
- LEHOUCQ, R. B., SORENSEN, D. C. & YANG, C. 1998 ARPACK users guide: solution of large-scale eigenvalue problems with implicitly restarted Arnoldi methods.
- LINDGREN, E. R. 1969 Propagation velocity of turbulent slugs and streaks in transition pipe flow. *Phys. Fluids* **12** (2), 418–425.
- LUMLEY, J. L. 1967 The structure of inhomogeneous turbulent flows. In *Atmos. Turbul. Radio Wave Propag.* (ed. A. M. Yaglom & V. I. Tatarski), pp. 166–178. Moscow.
- MANNEVILLE, P. 2016 Transition to turbulence in wall-bounded flows: Where do we stand? *B. JSME* **3** (2), 15–00684–15–00684.
- MESEGUR, Á. & TREFETHEN, L. N. 2003 Linearized pipe flow to Reynolds number 107. *J. Comput. Phys.* **186** (1), 178–197.
- MOSER, R. D., KIM, J. & MANSOUR, N. N. 1999 Direct numerical simulation of turbulent channel flow up to  $Re_\tau = 590$ . *Phys. Fluids* **11**, 943–945.
- MULLIN, T. 2011 Experimental studies on transition to turbulence in a pipe. *Annu. Rev. Fluid Mech.* **43**, 1–24.
- NEWHOUSE, S., RUELLE, D. & TAKENS, F. 1978 Occurrence of strange axiom A

- attractors near quasi periodic flows on  $T^m$ ,  $m \geq 3$ . *Commun. Math. Phys.* **64**, 35–40.
- NOORANI, A., EL KHOURY, G. K. & SCHLATTER, P. 2013 Evolution of turbulence characteristics from straight to curved pipes. *Int. J. Heat Fluid Flow* **41**, 16–26.
- NOORANI, A. & SCHLATTER, P. 2016 Swirl-switching phenomenon in turbulent flow through toroidal pipes. *Int. J. Heat Fluid Flow* **61**, 108–116.
- DI PIAZZA, I. & CIOFALO, M. 2011 Transition to turbulence in toroidal pipes. *J. Fluid Mech.* **687**, 72–117.
- POLETTI, R., REVELL, A., CRAFT, T. J. & JARRIN, N. 2011 Divergence free synthetic eddy method for embedded LES inflow boundary conditions. In *7th Int. Symp. Turbul. Shear Flow Phenom.*.. Ottawa.
- POPE, S. B. 2000 *Turbulent Flows*. Cambridge University Press.
- QUADRI, M., RICCO, P. & VIOTTI, C. 2009 Streamwise-traveling waves of spanwise wall velocity for turbulent drag reduction. *J. Fluid Mech.* **627**, 161–178.
- RINALDI, E., CANTON, J. & SCHLATTER, P. 2018 The collapse of strong turbulent fronts in bent pipes. *Submitted*.
- RÖSSLER, O. E. 1976 An equation for continuous chaos. *Phys. Lett. A* **57** (5), 397–398.
- RUELLE, D. & TAKENS, F. 1971 On the nature of turbulence. *Commun. Math. Phys.* **20** (3), 167–192.
- RÜTTEN, F., MEINKE, M. & SCHRÖDER, W. 2001 Large-eddy simulations of 90° pipe bend flows. *J. Turbul.* **2**, N3.
- RÜTTEN, F., SCHRÖDER, W. & MEINKE, M. 2005 Large-eddy simulation of low frequency oscillations of the Dean vortices in turbulent pipe bend flows. *Phys. Fluids* **17**, 035107.
- SAKAKIBARA, J. & MACHIDA, N. 2012 Measurement of turbulent flow upstream and downstream of a circular pipe bend. *Phys. Fluids* **24**, 041702.
- SAKAKIBARA, J., SONOBE, R., GOTO, H., TEZUKA, H., TADA, H. & TEZUKA, K. 2010 Stereo-PIV study of turbulent flow downstream of a bend in a round pipe. In *14th Int. Symp. Flow Vis.*.. EXCO Daegu, Korea.
- SCHMID, P. J. & HENNINGSON, D. S. 2001 *Stability and Transition in Shear Flows*. Springer.
- SCHOPPA, W. & HUSSAIN, F. 1998 A large-scale control strategy for drag reduction in turbulent boundary layers. *Phys. Fluids* **10**, 1049.
- SHIH, H.-Y., HSIEH, T.-L. & GOLDENFELD, N. 2015 Ecological collapse and the emergence of travelling waves at the onset of shear turbulence. *Nature Physics* **12**, 245–248.
- SIROVICH, L. 1987 Turbulence and the dynamics of coherent structures. Part I: coherent structures. *Q. Appl. Math.* **45**, 561–571.
- SKUFCA, J. D., YORKE, J. A. & ECKHARDT, B. 2006 Edge of chaos in a parallel shear flow. *Phys. Rev. Lett.* **96**, 5–8.
- SONG, B., BARKLEY, D., HOF, B. & AVILA, M. 2017 Speed and structure of turbulent fronts in pipe flow. *J. Fluid Mech.* **813**, 1045–1059.
- SREENIVASAN, K. R. & STRYKOWSKI, P. J. 1983 Stabilization effects in flow through helically coiled pipes. *Exp. Fluids* **1**, 31–36.
- STROGATZ, S. H. 1994 *Nonlinear Dynamics and Chaos*. Westview Press.
- STROH, A., FROHNAPFEL, B., SCHLATTER, P. & HASEGAWA, Y. 2015 A comparison

- of opposition control in turbulent boundary layer and turbulent channel flow. *Phys. Fluids* **27**, 075101.
- TROPEA, C., YARIN, A. L. & FOSS, J. F. 2007 *Springer Handbook of Experimental Fluid Mechanics*. Springer Science & Business Media.
- TSUKAHARA, T. 2011 Structures and turbulent statistics in a rotating plane Couette flow. *J. Phys.: Conf. Ser.* **318** (2), 022024.
- TSUKAHARA, T., SEKI, Y., KAWAMURA, H. & TOCHIO, D. 2005 DNS of turbulent channel flow at very low Reynolds numbers. In *In Proc. of the Forth Int. Symp. on Turbulence and Shear Flow Phenomena*, pp. 935–940. Williamsburg, USA.
- TSUKAHARA, T., TILLMARK, N. & ALFREDSSON, P. H. 2010 Flow regimes in a plane Couette flow with system rotation. *J. Fluid Mech.* **648**, 5–33.
- TUNSTALL, M. J. & HARVEY, J. K. 1968 On the effect of a sharp bend in a fully developed turbulent pipe-flow. *J. Fluid Mech.* **34**, 595–608.
- VANDERWEL, C. & GANAPATHISUBRAMANI, B. 2015 Effects of spanwise spacing on large-scale secondary flows in rough-wall turbulent boundary layers. *J. Fluid Mech.* **774**, R2.
- VASHISTH, S., KUMAR, V. & NIGAM, K. D. P. 2008 A review on the potential applications of curved geometries in process industry. *Ind. Eng. Chem. Res.* **47**, 3291–3337.
- WALEFFE, F. 1997 On a self-sustaining process in shear flows. *Phys. Fluids* **9**, 883–900.
- WEBSTER, D. R. & HUMPHREY, J. A. C. 1993 Experimental observations of flow instability in a helical coil (Data bank contribution). *J. Fluid Eng.-T. ASME* **115**, 436–443.
- WHITE, C. M. 1929 Streamline flow through curved pipes. *Proc. R. Soc. London Ser. A* **123**, 645–663.
- WYGNANSKI, I. J. & CHAMPAGNE, F. H. 1973 On transition in a pipe. Part 1. The origin of puffs and slugs and the flow in a turbulent slug. *J. Fluid Mech.* **59** (2), 281–335.
- WYGNANSKI, I. J., SOKOLOV, M. & FRIEDMAN, D. 1975 On transition in a pipe. Part 2. The equilibrium puff. *J. Fluid Mech.* **69** (2), 283–304.
- YAO, J., CHEN, X., THOMAS, F. O. & HUSSAIN, F. 2017 Large-scale control strategy for drag reduction in turbulent channel flows. *Phys. Rev. Fluids* **2** (6).



## **Part II**

## **Papers**



1

Paper 1



# Characterisation of the steady, laminar incompressible flow in toroidal pipes covering the entire curvature range

Jacopo Canton<sup>1,2</sup>, Ramis Örlü<sup>1</sup> and Philipp Schlatter<sup>1,2</sup>

<sup>1</sup>Linné FLOW Centre, KTH Mechanics, Royal Institute of Technology, SE-100 44 Stockholm, Sweden

<sup>2</sup>Swedish e-Science Research Centre (SeRC), Royal Institute of Technology, SE-100 44 Stockholm, Sweden

*International Journal of Heat and Fluid Flow* (2017), vol. **66**, 95–107

This work is concerned with a detailed investigation of the steady (laminar), incompressible flow inside bent pipes. In particular, a toroidal pipe is considered in an effort to isolate the effect of the curvature,  $\delta$ , on the flow features, and to compare the present results to available correlations in the literature. More than 110 000 numerical solutions are computed, without any approximation, spanning the entire curvature range,  $0 \leq \delta \leq 1$ , and for bulk Reynolds numbers  $Re$  up to 7 000, where the flow is known to be unsteady. Results show that the Dean number  $De$  provides a meaningful non-dimensional group only below very strict limits on the curvature and the Dean number itself. For  $\delta > 10^{-6}$  and  $De > 10$ , in fact, not a single flow feature is found to scale well with the Dean number. These considerations are also valid for quantities, such as the Fanning friction factor, that were previously considered Dean-number dependent only. The flow is therefore studied as a function of two equally important, independent parameters: the curvature of the pipe and the Reynolds number. The analysis shows that by increasing the curvature the flow is fundamentally changed. Moderate to high curvatures are not only quantitatively, but also qualitatively different from low  $\delta$  cases. A complete description of some of the most relevant flow quantities is provided. Most notably the friction factor  $f$  for laminar flow in curved pipes by Ito [J. Basic Eng. **81**:123–134 (1959)] is reproduced, the influence of the curvature on  $f$  is quantified and the scaling is discussed. A complete database including all the computed solutions is available at [www.flow.kth.se](http://www.flow.kth.se).

**Key words:** bent pipes, Dean number, friction factor

---

## 1. Introduction

Although the investigation of flow through curved conduits dates back to more than a century ago (Boussinesq 1868), the fundamental analysis of the steady (laminar) solution has not been completely carried out, yet. The problem has

been tackled analytically, numerically and experimentally in the past. In each case approximations had to be made or constraints had to be respected, be it for computational or practical reasons. For an in-depth review with an historical perspective, see Kalpakli *et al.* (2016). It appears, though, that in several publications the results obtained in the past were assumed to be valid beyond their limits, as it will be detailed in the following.

Curved pipes are ubiquitous: they are of practical importance in a multitude of engineering applications and are found in nearly all biological systems. Examples of industrial processes concerned with curved tubes include power production, air conditioning, chemical and food industries, space applications and others. For a recent and comprehensive review of the applications of curved pipes in industry, see Vashisth *et al.* (2008). A second fundamental area of research where bent pipes are studied is the medical field. Curved pipes are, in fact, an integral part of our vascular, lymphatic and respiratory systems. Understanding the behaviour of the flow in such bends can aid the prevention of several cardiovascular problems (Berger *et al.* 1983; Bulusu *et al.* 2014).

Amongst the pioneering studies on flow in curved pipes, Thomson (1876, 1877) studied the origin of the windings of rivers and connected their formation and the soil erosion pattern to the topology of the flow in bent pipes. Later, Eustice (1910, 1911) carried out a series of experiments where he measured a reduction of fluid flux and associated it with the curvature of the pipes. He was also the first to directly observe the presence of secondary motion by injecting coloured dye filaments into the water flowing inside transparent pipes. The experiments by Eustice were followed by those of White (1929), focused on the measurement of frictional resistance through the bends.

Following the first experimental investigations, Dean (1927, 1928b) tackled the problem analytically. In both of his papers the curvature of the pipe, defined as the ratio between pipe radius and the radius of the circle in which the pipe is coiled ( $\delta = R_p/R_t$ , see Fig. 1), was assumed to be very small. By means of this and successive approximations Dean was able to derive a solution to the incompressible Navier–Stokes equations for this flow case, and realised that the solution depends on a single, non-dimensional number, later named Dean number in his honour. He was also the first to demonstrate the presence of secondary motion, and found it to be in the form of two counter-rotating vortices that were later given his name. Owing to the influence of his approximations the author himself was forced to admit in the first paper that “a quantitative comparison [with the experiments of Eustice], however, requires a closer approximation than that of this paper”. By dimensional analysis he determined his solution to be valid for  $Re^2 R_p / (1440 R_t) \ll 1$ , corresponding to a bound on the Dean number  $De = Re\sqrt{\delta} \ll 38$ . Even the improved solution presented in his second paper, still affected by approximations, was valid only for  $De < 34$ .

Later, Adler (1934), Keulegan & Beij (1937) and others proceeded to measure the frictional resistance offered by the fluid when flowing through

curved pipes. The most notable of these works were included in a seminal paper by Ito (1959). One of the findings presented in this paper is that the Fanning friction factor for the laminar flow empirically scales with the Dean number up to  $De = 2 \times 10^3$ . As it will be shown in the present work this apparent collapse of the data might be useful in practice, but the flow features are very different.

Van Dyke (1978) extended Dean's approximation and obtained results that agreed well with the available numerical and experimental results up to  $De \approx 100$ . Despite the aforementioned limitations for the applicability of the Dean-number similarity, the common view remained well-represented by the statement by Ito (1987) which states "It is a well-known fact that dynamical similarity for steady laminar flow in a curved circular pipe depends only on the Dean number". A note of caution was, however, given by Berger *et al.* (1983) who pointed out that this dynamical similarity is not valid "for curved-pipe flows in general, but only when  $\delta \ll 1$ " and that the curvature "can play a major role in curved-pipe flows".

Despite this, the Dean number and Dean similarity are still nowadays used to characterise the flow regime. This is the case not only for numerical studies at low Reynolds numbers (Shortis & Hall 1999; Fan *et al.* 2001; Siggers & Waters 2008; Masud *et al.* 2010; Cieślicki & Piechna 2012) but also for some of the literature on turbulent flow (Anwer & So 1993; Rütten *et al.* 2001; Hellström *et al.* 2013; Ghobadi & Muzychka 2016) and the literature focused on the medical field (Bulusu *et al.* 2014; Verkaik *et al.* 2009; van Wyk *et al.* 2015; Najjari & Plesniak 2016) (this list of publications is not exhaustive and includes only some examples). However, as shown in the following, the Dean number is solely appropriate for infinitesimally small curvatures, and the so-called Dean flow is substantially modified by curvature as well.

To address the apparent gap in the literature, we here perform a complete parameter study on the steady, laminar incompressible flow in a toroidal pipe. In particular, the entire Reynolds-number and curvature range is explored via numerical computations, with small steps in  $Re$  and  $\delta$  in order to analyse both integral and spatially-dependent quantities. Beside having theoretical value, unitary curvatures, and curvatures close to unity, can be realised in toroidal pipes by means of innovative ways to force the flow, e.g. using MHD force such as in tokamaks; instead in spatially developing pipes, such as junctions between straight sections, unitary curvatures are actually relatively common. The present paper starts with a description of the methods employed, presented in section 2; section 3 is dedicated to an analysis of the properties of the flow, including considerations on the driving mechanism, the secondary flow and the definition of the friction factor and friction Reynolds number. Section 4 describes the results of the present study, with particular attention to the friction factor, and presents an analysis of the flow as a function of curvature and Reynolds number as separate parameters. The paper concludes with a summary and an outlook in section 5.

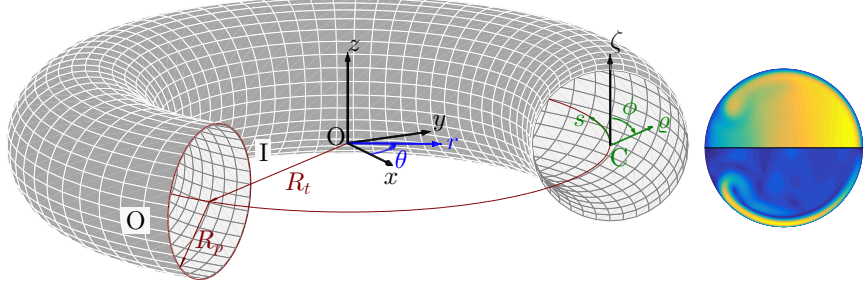


Figure 1: *Left:* Sketch of the toroidal pipe showing the two geometrical quantities,  $R_t$  and  $R_p$ , defining the curvature  $\delta = R_p/R_t$ , equal to  $\delta = 0.3$  for this sketch. The three reference systems employed are also indicated: the Cartesian coordinate system  $(x, y, z)$  in black, the cylindrical coordinate system  $(r, \theta, z)$  in blue, and the toroidal coordinate system  $(\varrho, \phi, s)$  in green. The axis  $\zeta$  corresponds to  $z$  translated in C. The “central plane” or “equatorial plane” of the torus corresponds to the  $x - y$  plane. The “I” and “O” labels indicate the inner, resp. outer portions of the pipe. *Right:* Corresponding base flow for  $Re = 3379$ , coloured by streamwise (top) and in-plane (bottom) velocity magnitude.

## 2. Investigation method

The geometry of the problem consists in a toroidal pipe, sketched in Fig. 1. The pipe has a uniform, circular section of radius  $R_p$ , while the radius of the torus is  $R_t$ . These two radii constitute the non-dimensional parameter of the setup, the curvature, defined as  $\delta = R_p/R_t$ . The centre of the torus is located in O, while C is the centre of the section of the pipe, located in a plane at an angle  $\theta$  from the  $x$ -axis. The  $x - y$  plane, called “central plane” by Dean (1927) or “equatorial plane” by other researchers, is a plane of mirror symmetry for the torus. A pipe section at an angle  $\theta$  can be described in cylindrical coordinates with  $(R_t - r)^2 + z^2 \leq R_p^2$ , this range encloses the area where the equations are discretised in space, as described in the following. At times, see sections 3.2 and 3.3, the toroidal coordinate system is more suitable for the description of the flow. This system is constituted by a polar coordinate pair on the section of the pipe,  $\varrho$  and  $\phi$ , and the curvilinear coordinate  $s = R_t\theta$ .

The fluid is considered as viscous and incompressible, it therefore satisfies the incompressible Navier–Stokes equations

$$\frac{\partial \mathbf{u}}{\partial t} + (\mathbf{u} \cdot \nabla) \mathbf{u} - \frac{1}{Re} \nabla^2 \mathbf{u} + \nabla p = \mathbf{f}, \quad (1a)$$

$$\nabla \cdot \mathbf{u} = 0, \quad (1b)$$

where  $\mathbf{u}(r, t)$  is the velocity vector, with components  $\mathbf{u} = (u_r, u_\theta, u_z)$  in cylindrical coordinates or  $\mathbf{u} = (u_\varrho, u_\phi, u_s)$  when using the toroidal coordinate system.

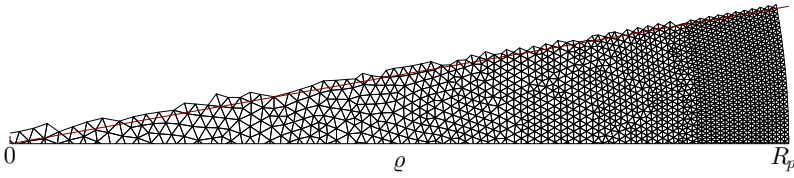


Figure 2: Portion of the mesh showing a circular sector of  $\approx 10^\circ$  in  $\phi$  (highlighted by the red line). The grid size is  $\Delta\ell = 0.02R_p$  in the centre of the pipe and  $\Delta\ell = 0.006R_p$  in the uniform annulus located at  $0.9R_p \leq \varrho \leq R_p$ .

The (dimensionless) pressure  $p$  has been rescaled by dividing by the Reynolds number  $Re$ , and  $\mathbf{f}$  represents a volume force, described in section 3.1. The Reynolds number is based on the diameter of the pipe and the bulk velocity,  $U_b = \int_0^{2\pi} \int_0^{R_p} u_s \varrho d\varrho d\phi$ , i.e.  $Re = 2R_p U_b / \nu$ . Several definitions of the Dean number can be found in the literature: Van Dyke (1978) and Berger *et al.* (1983) provide a valuable comparison between the different versions. The definition used in this work is the one brought forth by Berger *et al.* as the most versatile, i.e.  $De = Re\sqrt{\delta}$ , and it is also the definition generally used in recent publications. As will be discussed later though (see section 4), the Dean number is not, in any of its versions, a suitable non-dimensional parameter to describe the flow.

The steady solutions have been computed with **PaStA**, an in-house developed software package. **PaStA** is a Fortran90 code, written in primitive variables and based on the finite element method (FEM) employing triangular  $\mathbb{P}_2 - \mathbb{P}_1$  elements. The equations are discretised on an unstructured, two-dimensional mesh corresponding to an azimuthal plane of the domain, are written in cylindrical coordinates and are solved by using the **MUMPS** library (Amestoy *et al.* 2000) for the solution of linear systems. For details on the code and its validation, see Canton (2013) and Canton *et al.* (2016). The invariance of the flow with respect to  $s$  allows the solution to be computed on a two-dimensional pipe section (retaining all three velocity components), sensibly reducing the computational cost. The mesh used in the present work, depicted in Fig. 2, is the same employed in Canton *et al.* (2016); i.e. it is formed by 98 870 elements which correspond to 646 327 degrees of freedom for  $(\mathbf{u}, p)$ . It is an unstructured mesh characterised by a grid size  $\Delta\ell = 0.02R_p$  in the centre of the pipe and it features an annulus with smaller, uniform elements with  $\Delta\ell = 0.006R_p$  for  $0.9R_p \leq \varrho \leq R_p$ . The grid size decreases linearly from the centre to the annulus.

The steady solutions to equation (1) are computed via Newton's method written in its *non-incremental formulation* (Canton 2013). Introducing  $\mathcal{N}(\mathbf{x})$  as a shorthand for the steady terms in equation (1), with  $\mathbf{x} = (\mathbf{u}, p)$ , and separating the linear and quadratic parts, the steady solution to equation (1)

can be written as:

$$\mathcal{N}(\mathbf{x}) = \mathcal{Q}(\mathbf{x}, \mathbf{x}) + \mathcal{L}(\mathbf{x}) - \mathbf{f} = 0, \quad (2)$$

where

$$\mathcal{Q}(\mathbf{x}, \mathbf{y}) = \begin{pmatrix} (\mathbf{u} \cdot \nabla) \mathbf{v} \\ 0 \end{pmatrix}, \quad \mathcal{L}(\mathbf{x}) = \begin{pmatrix} -\frac{1}{Re} \nabla^2 \mathbf{u} + \nabla p \\ \nabla \cdot \mathbf{u} \end{pmatrix}, \quad (3)$$

and  $\mathbf{y} = (\mathbf{v}, q)$ . To obtain Newton's method,  $\mathcal{N}(\mathbf{x})$  is expanded in a Taylor series, truncated at first order, in the neighbourhood of an approximate solution  $\mathbf{x}_n$ , i.e.  $\mathcal{N}(\mathbf{x}) \approx \mathcal{N}(\mathbf{x}_n) + \mathcal{J}|_{\mathbf{x}_n}(\mathbf{x} - \mathbf{x}_n) = 0$ . Here  $\mathcal{J}|_{\mathbf{x}_n}$  is the Fréchet derivative of  $\mathcal{N}(\mathbf{x})$  corresponding, after spatial discretisation, to the Jacobian matrix:  $\mathcal{J}|_{\mathbf{y}} = \nabla_{\mathbf{x}} \mathcal{N}|_{\mathbf{y}} = \mathcal{Q}(\mathbf{y}, \dots) + \mathcal{Q}(\dots, \mathbf{y}) + \mathcal{L}$ . The non-incremental formulation of Newton's method then reads:

$$\mathcal{J}|_{\mathbf{x}_n}(\mathbf{x}_{n+1}) = \mathcal{Q}(\mathbf{x}_n, \mathbf{x}_n) + \mathbf{f}. \quad (4)$$

Newton's algorithm is started either from the solution of the Stokes problem ( $\mathcal{L}(\mathbf{x}) = 0$ ) or from a previously computed solution for a different set of  $(\delta, Re)$ . The convergence criterion is based on the infinity norm of the residual, i.e.  $\|\mathcal{N}(\mathbf{x}_n)\|_{L^\infty}$ , and, for all cases presented here, the tolerance is set to  $10^{-15}$ .

The solutions are computed for a unitary bulk velocity; to do so,  $\mathbf{f}$  has to be determined such that  $U_b = \int_0^{2\pi} \int_0^{R_p} u_s(\varrho, \phi) \varrho d\varrho d\phi = 1$ . Since the relationship between  $\mathbf{f}$  and  $U_b$  is nonlinear (Ito 1959) and unknown, as  $u_s$  is a-priori unknown and as further explained in section 3.1, the computation of  $\mathbf{f}$  is done via the secant method. To reduce the number of iterations, which would now amount to those of Newton's method times those of the secant method,  $N_{N \times S}$ , the secant method is “coupled” to Newton's method. At each  $n^{\text{th}}$  iteration  $\mathbf{f}$  is computed via the secant method using the values of  $\mathbf{f}$  and  $U_b$  at the two preceding iterations of Newton's method. This operation increases the number of iterations that would be required by Newton's method keeping  $\mathbf{f}$  fixed, but allows the algorithm to converge to a solution that satisfies (2) and, at the same time, has  $U_b = 1$ . Numerical trials show that coupling the two methods results in a number of iterations sensibly smaller than  $N_{N \times S}$ . The tolerance on  $U_b - 1 = 0$  is set to  $10^{-6}$ , but the final solution is always characterised by a smaller error, typically one or two orders of magnitude lower, as Newton's method still requires a couple more iterations after the secant method has satisfied the tolerance criterion.

### 3. Analysis of the flow

As aforementioned, the flow is invariant with respect to  $s$  and it is symmetric with respect to the equatorial plane of the torus; this is not for construction, but stems from the geometry of the problem (see also Canton *et al.* 2016). As first analytically determined by Dean (1927, 1928*b*), the flow features a pair of symmetric, counter-rotating vortices, called Dean vortices in his honour. These vortices, which develop as a result of the curved geometry, are present for any non-zero curvature and every Reynolds number; see section 3.3 for more

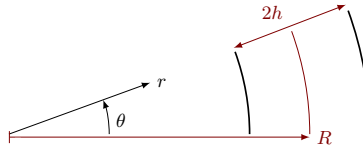


Figure 3: Sketch of a two-dimensional bent channel:  $r$  and  $\theta$  identify the polar coordinate system used in the derivation of the analytical solution. The radius of the centreline of the channel is indicated with  $R$ , while  $h$  is its half-height. The curvature, as with for the torus, is defined as  $\delta = h/R$ , whereas  $a = R - h$  and  $b = R + h$  are the inner (resp. outer) radii of the channel.

details. This section presents an analysis of the driving mechanism that moves the fluid inside of the pipe (§ 3.1), a discussion on the force balance and the definition of friction coefficients (§ 3.2) and concludes with the demonstration of the existence of the secondary motion for any  $(\delta, Re)$  pair (§ 3.3).

Numerous authors (Nandakumar & Masliyah 1982; Yang & Keller 1986; Daskopoulos & Lenhoff 1989; Kao 1992; Yanase *et al.* 1994), with different analytical and/or numerical approximations, have discovered solutions with up to three pairs of vortices. These steady states, however, are mostly unstable and were not observed in our computations; all of the steady states found in the present work show a “classic” two-vortex configuration. We do not exclude the possibility of multiple vortex solutions to be valid solutions to the 2D flow, we however argue that these are not observed in practice.

### 3.1. The driving force

The fluid flows inside of the torus at a constant mass (volume) rate. To understand how to drive the fluid in the torus, the flow inside a two-dimensional bent channel is hereby presented (see Fig. 3). This flow case is selected because of its similarity with the torus, and because its analytical solution can be determined in closed form. This is an ideal case since, in analogy with the torus, a bent channel has period  $2\pi$  in  $\theta$ , hence it cannot allow a pressure gradient in the streamwise direction. This aspect is neglected in the present derivation, as it was in Dean’s original works on the low-curvature toroidal pipe (Dean 1927, 1928*b*) and bent channel (Dean 1928*a*). The flow inside of a bent channel was initially studied by Dean (1928*a*) who, as he had done for the torus, computed an approximate solution valid in the limit of low curvature. A solution valid for all curvatures can be found in Walowit *et al.* (1964) and is also reported in Drazin & Reid (2004); both references, though, do not include considerations on the pressure.

The analytical solution is computed by writing the equations in cylindrical coordinates (Quartapelle & Auteri 2013). Similarly to the flow inside of a straight channel, the assumptions are that the flow is steady, two-dimensional, *i.e.*  $u_z = 0$ , and that the velocity is invariant with respect to the streamwise

direction. The incompressibility constraint, equation (1b), is then reduced to:

$$\nabla \cdot \mathbf{u} = \frac{1}{r} \frac{\partial}{\partial r} (ru_r) + \frac{1}{r} \frac{\partial u_\theta}{\partial \theta} = \frac{1}{r} \frac{d}{dr} (ru_r) = 0, \quad (5)$$

which implies that  $u_r(r) = A/r$ . Since the walls of the channel are impermeable, *i.e.*  $\mathbf{u}(a) = \mathbf{u}(b) = 0$ , then  $A = 0$ . This means that  $u_r(r) = 0 \quad \forall r$ . In other words, the motion of the fluid is purely circular and the velocity field has only one component:  $\mathbf{u} = (0, u_\theta(r), 0)$ . Taking into account the assumptions for this problem and the result obtained from the incompressibility constraint, the momentum equation, (1a), is:

$$-\frac{u_\theta^2}{r} + \frac{\partial p}{\partial r} = 0, \quad (6a)$$

$$-\frac{1}{Re} \left[ \frac{1}{r} \frac{d}{dr} \left( r \frac{du_\theta}{dr} \right) - \frac{u_\theta}{r^2} \right] + \frac{1}{r} \frac{\partial p}{\partial \theta} = 0, \quad (6b)$$

where the two unknowns are  $u_\theta(r)$  and  $p(r, \theta)$ . Differentiating equation (6a) with respect to  $\theta$  results in

$$\frac{\partial^2 p}{\partial r \partial \theta} = 0, \quad (7)$$

since  $u_\theta$  depends only on  $r$ . This implies that the pressure is described by the linear superposition of two independent contributions (and one additive constant),

$$p(r, \theta) = p_r(r) + p_\theta(\theta) + p_0. \quad (8)$$

This result allows the solution of the angular component of the momentum, equation (6b). The equation can, in fact, be rewritten as (Quartapelle & Auteri 2013):

$$\frac{r}{Re} \frac{d}{dr} \left( \frac{1}{r} \frac{d}{dr} (ru_\theta) \right) = \frac{dp_\theta}{d\theta}, \quad (9)$$

where the left hand side is a function dependent on  $r$  only while the right hand side depends only on  $\theta$ . Integrating the equation for  $p_\theta$ ,  $dp_\theta/d\theta = P_G$ , and omitting the integration constant (which is simply added to  $p_0$  by redefining it) yields:

$$p_\theta(\theta) = P_G \theta, \quad (10)$$

which is a linear relationship between one of the contributions to the pressure and  $\theta$ . The azimuthal velocity  $u_\theta$  can now be computed from equation (9) and, successively,  $p_r$  can be derived by integrating equation (6a). For the sake of

brevity, the derivation is not reported here. The complete solution is:

$$u_\theta(r) = \frac{P_G Re}{2} \left[ r \ln r + k_1 r + \frac{k_2}{r} \right], \quad (11a)$$

$$\begin{aligned} p(r, \theta) &= p_r(r) + p_\theta(\theta) + p_0 \\ &= \frac{P_G^2 Re^2}{32} \left[ \frac{4k_2^2}{r^2} + (5 - 8k_1 + 4k_1^2)r^2 + 8(2k_1 - 1)k_2 \ln r \right. \\ &\quad \left. + 8(k_1 - 1)r^2 \ln r + 4(2k_2 + r^2) \ln(r)^2 \right] + P_G \theta + p_0, \end{aligned} \quad (11b)$$

$$k_1 = -\frac{b^2 \ln b - a^2 \ln a}{b^2 - a^2}, \quad (11c)$$

$$k_2 = \frac{a^2 b^2}{b^2 - a^2} \ln \left( \frac{b}{a} \right). \quad (11d)$$

It can be observed, from (8) or (11b), that the difference in pressure between two points at the same radial position depends on  $P_G$  and  $\Delta\theta$  only, but not on  $r$ :

$$\begin{aligned} \Delta p &= p(r, \theta_2) - p(r, \theta_1) = p_r(r) + p_\theta(\theta_2) + p_0 - p_r(r) - p_\theta(\theta_1) - p_0 \\ &= P_G(\theta_2 - \theta_1) = P_G \Delta\theta. \end{aligned} \quad (12)$$

This result is consistent with the limit for  $\delta \rightarrow \infty$  of this geometry, which corresponds to a straight channel. In a straight channel the pressure is uniform on all channel sections and varies linearly along the streamwise direction. This is also the case for the solution derived in equation (11): when  $\delta \rightarrow \infty$  the difference between  $a$  and  $b$  tends to zero and  $p_r(r)$  assumes a uniform value in  $r$ .

Returning to the case of a torus, since it is a closed system, periodic in  $\theta$  with period  $2\pi$ , a pressure gradient along  $s$  cannot be used to drive the flow, as it would result in a discontinuity in pressure every  $2\pi$ . In the present work, a volume force aligned with  $s$  is used instead. To reproduce the two properties just derived for the case of a bent channel, the volume force is defined as  $\mathbf{f} = e_\theta f_v = e_\theta F/r$  in cylindrical coordinates or, equivalently,  $\mathbf{f} = e_s f_v = e_s F/r$  in toroidal coordinates. Here  $F$  is a scalar constant and  $r$  is the distance from the  $z$ -axis (cf. Fig. 1). In the toroidal pipe,  $f_v$  reproduces the effect that the pressure has in the bent channel: the integral of  $f_v$  between two points in the torus yields:

$$\Delta f_v = \int_{s_1}^{s_2} f_v ds = \int_{s_1}^{s_2} \frac{F}{r} ds = \int_{\theta_1}^{\theta_2} \frac{F}{r} r d\theta = F(\theta_2 - \theta_1) = F\Delta\theta. \quad (13)$$

It is immediate to see the correspondence with equation (12): the scalar constant  $F$  has the same role that the pressure gradient has in the channel, and the difference in volume force between two points does not depend on the distance from the axis of the torus. Moreover, consistency with a straight pipe is also

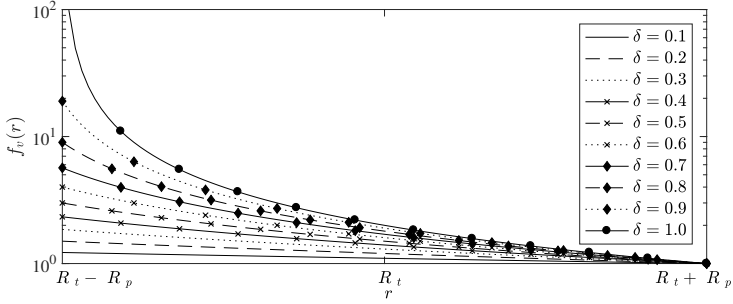


Figure 4: Volume forcing  $f_v$  on a pipe section as a function of curvature. The lines are normalised, for illustrative purposes, such as to have  $f_v(r = R_t + R_p) = 1$ .

ensured: when the curvature tends to zero, *i.e.* the torus approaches a straight pipe,  $f_v$  assumes a uniform value on the section of the pipe. Clearly, since  $f_v$  depends on  $r$ , as does the pressure when imposing a uniform pressure gradient, different curvatures correspond to a different distribution of  $f_v$  on the section of the pipe, as illustrated in Fig. 4.

### 3.2. The force balance and the definition of the friction factor and Reynolds number

For straight pipes it is customary to define a friction coefficient as (Pope 2000):

$$C_f \equiv f \equiv \frac{\tau_w}{\frac{1}{2}\rho U_b^2} = \frac{1}{\frac{1}{2}\rho U_b^2} \frac{R_p}{2L} \Delta p = \frac{1}{\frac{1}{2}\rho U_b^2} \frac{R_p}{2} \frac{dp}{dx}, \quad (14)$$

where  $C_f$  is the so-called *skin-friction coefficient*, also abbreviated with  $f_c$  or  $f$  and then called *Fanning friction factor*,  $\tau_w$  is the *wall shear stress*,  $U_b$  is the bulk velocity,  $R_p$  the pipe radius and  $\Delta p$  is the pressure drop over an axial distance  $L$ , *i.e.*  $dp/dx = \Delta p/L$ . The equality between the definitions in (14) is a straightforward consequence of the force balance in the axial direction of the pipe:

$$\Delta p \pi R_p^2 - \tau_w 2\pi R_p L = 0 \quad \Rightarrow \quad \tau_w = \frac{R_p}{2L} \Delta p = \frac{R_p}{2} \frac{dp}{dx}. \quad (15)$$

Equations (14) and (15) clearly hold for a straight pipe only, where the wall shear stress has only one component aligned with the axis of the pipe.

Such a relationship for the flow inside of a toroidal pipe is now derived. The volume force defined in the previous section is used for the derivation; the same result would be obtained by using the pressure, thanks to the analogy between  $F$  and  $P_G = dp/d\theta$  obtained in 3.1. A convenient way is to start from the torque balance about the  $z$ -axis. In fact, only  $f_v$  and the streamwise component of the wall shear stress,  $\tau_{w,s}$ , contribute to this balance, while the other components of  $\tau_w$  lie in the pipe section plane which also contains their

distance vectors. The torque balance reads:

$$\int_{s_1}^{s_2} \int_0^{2\pi} \int_0^{R_p} f_v r \varrho d\varrho d\phi ds - \int_{s_1}^{s_2} \int_0^{2\pi} \tau_{w,s} r R_p d\phi ds = 0, \quad (16)$$

where  $r$  is the distance from the  $z$ -axis and the integrals are defined in toroidal coordinates for a generic pipe segment with extrema  $s_1 < s < s_2$ . With reference to Fig. 1,  $ds = rd\theta$  is the infinitesimal distance along the torus, while  $\varrho$  and  $\phi$  are the radius and angle measured on the pipe section. Substituting the integration in  $s$  with that in  $\theta$ , using the definition of the volume force  $f_v = F/r$ , considering that the balance must hold for any pipe segment, *i.e.* for any  $s_i = r\theta_i$ , and expressing the distance from the  $z$ -axis as  $r = R_t + \varrho \sin \phi$  (cf. Fig. 1), equation (16) can be rewritten as:

$$\int_0^{2\pi} \int_0^{R_p} F(R_t + \varrho \sin \phi) \varrho d\varrho d\phi = \int_0^{2\pi} \tau_{w,s} (R_t + R_p \sin \phi)^2 R_p d\phi. \quad (17)$$

The term on the left can be integrated analytically, yielding (after rearranging a few terms):

$$\pi R_t R_p F = \int_0^{2\pi} \tau_{w,s} (R_t + R_p \sin \phi)^2 d\phi. \quad (18)$$

By defining the average streamwise wall-shear stress acting on a pipe section,

$$\langle \tau_{w,s} \rangle_\phi = \frac{1}{2\pi} \int_0^{2\pi} \tau_{w,s} d\phi, \quad (19)$$

expanding the right-hand-side of (18) and integrating by parts results in:

$$\begin{aligned} \pi R_t R_p F &= 2\pi R_t^2 \langle \tau_{w,s} \rangle_\phi \\ &+ 2R_t R_p \left( 2\pi \langle \tau_{w,s} \rangle_\phi \sin \phi \Big|_0^{2\pi} - \int_0^{2\pi} 2\pi \langle \tau_{w,s} \rangle_\phi \cos \phi d\phi \right) \\ &+ R_p^2 \left( 2\pi \langle \tau_{w,s} \rangle_\phi \sin^2 \phi \Big|_0^{2\pi} - \int_0^{2\pi} 2\pi \langle \tau_{w,s} \rangle_\phi 2 \sin \phi \cos \phi d\phi \right). \end{aligned} \quad (20)$$

It is immediate to verify that the right-hand-side of this expression is zero, except for the first term. The analytical expression for  $\langle \tau_{w,s} \rangle_\phi$  is then:

$$\langle \tau_{w,s} \rangle_\phi = \frac{R_p}{2R_t} F = \frac{\delta}{2} F = \frac{\delta}{2} \frac{dp}{d\theta} = \frac{R_p}{2} \frac{dp}{ds} \Big|_{r=R_t} \quad (21)$$

considering, as shown in section 3.1, that  $F$  has the same role as a pressure gradient. The derivation presented in this section shows that only the streamwise component of the wall shear stress counterbalances the driving force (pressure). This finding is important since, as the curvature increases, the magnitude of the in-plane component of the wall shear stress greatly increases (see section 4) but the power required to drive the flow is unaffected.

The Fanning friction factor for a bent pipe can then be defined as

$$f \equiv \frac{\langle \tau_{w,s} \rangle_\phi}{\frac{1}{2} \rho U_b^2} = \frac{1}{\frac{1}{2} \rho U_b^2} \frac{\delta}{2} F = \frac{1}{\frac{1}{2} \rho U_b^2} \frac{\delta}{2} \frac{dp}{d\theta} = \frac{1}{\frac{1}{2} \rho U_b^2} \frac{R_p}{2} \frac{dp}{ds} \Big|_{r=R_t} \quad (22)$$

and, consistently, the definition of the friction Reynolds number is

$$Re_\tau \equiv \frac{R_p}{\nu} \sqrt{\frac{\langle \tau_{w,s} \rangle_\phi}{\rho}} = \frac{R_p}{\nu} \sqrt{\frac{\delta}{2\rho} F} = \frac{R_p}{\nu} \sqrt{\frac{\delta}{2\rho} \frac{dp}{d\theta}} = \frac{R_p}{\nu} \sqrt{\frac{R_p}{2\rho} \frac{dp}{ds} \Big|_{r=R_t}}. \quad (23)$$

### 3.3. The secondary flow

The flow inside a bent channel (see section 3.1 and Walowitz *et al.* (1964)) and that between two rotating cylinders (see Taylor 1923) are characterised by a critical condition below which no secondary motion occurs. The flow inside a curved pipe, instead, does not exhibit such a condition, despite what can be found in some textbooks (Isachenko *et al.* 1974). In a toroidal pipe there is no Reynolds number, curvature, nor any combination between the two below which the secondary motion is absent. This can be shown analytically by writing the equations of motion (1), in the absence of a volume force, in cylindrical coordinates (Quartapelle & Auteri 2013), taking into account that the velocity field is  $\theta$ -invariant. As it will be seen, employing a volume force aligned with  $\theta$  (see section 3.1) and considering  $\partial p/\partial\theta = 0$  does not change the result. The equations read:

$$u_r \frac{\partial u_r}{\partial r} - \frac{u_\theta^2}{r} + u_z \frac{\partial u_r}{\partial z} - \frac{1}{Re} \left[ \frac{1}{r} \frac{\partial}{\partial r} \left( r \frac{\partial u_r}{\partial r} \right) + \frac{\partial^2 u_r}{\partial z^2} - \frac{u_r}{r^2} \right] + \frac{\partial p}{\partial r} = 0, \quad (24a)$$

$$u_r \frac{\partial u_\theta}{\partial r} + \frac{u_\theta u_r}{r} + u_z \frac{\partial u_\theta}{\partial z} - \frac{1}{Re} \left[ \frac{1}{r} \frac{\partial}{\partial r} \left( r \frac{\partial u_\theta}{\partial r} \right) + \frac{\partial^2 u_\theta}{\partial z^2} - \frac{u_\theta}{r^2} \right] + \frac{1}{r} \frac{\partial p}{\partial \theta} = 0, \quad (24b)$$

$$u_r \frac{\partial u_z}{\partial r} + u_z \frac{\partial u_z}{\partial z} - \frac{1}{Re} \left[ \frac{1}{r} \frac{\partial}{\partial r} \left( r \frac{\partial u_z}{\partial r} \right) + \frac{\partial^2 u_z}{\partial z^2} \right] + \frac{\partial p}{\partial z} = 0, \quad (24c)$$

$$\frac{1}{r} \frac{\partial}{\partial r} (r u_r) + \frac{\partial u_z}{\partial z} = 0. \quad (24d)$$

The absence of secondary (in-plane) motion requires  $u_r \equiv u_z \equiv 0$ ; this simplifies the equations to:

$$-\frac{u_\theta^2}{r} + \frac{\partial p}{\partial r} = 0, \quad (25a)$$

$$-\frac{1}{Re} \left[ \frac{1}{r} \frac{\partial}{\partial r} \left( r \frac{\partial u_\theta}{\partial r} \right) + \frac{\partial^2 u_\theta}{\partial z^2} - \frac{u_\theta}{r^2} \right] + \frac{1}{r} \frac{\partial p}{\partial \theta} = 0, \quad (25b)$$

$$\frac{\partial p}{\partial z} = 0, \quad (25c)$$

where the continuity equation (24d) is not reported since it is reduced to an identity. Deriving equation (25a) with respect to  $z$  yields:

$$\frac{\partial^2 p}{\partial z \partial r} = \frac{2}{r} u_\theta \frac{\partial u_\theta}{\partial z} = 0 \quad (26)$$

which is zero because of equation (25c). This implies that either  $u_\theta \equiv 0$  or  $\partial u_\theta / \partial z \equiv 0$ . The first condition reduces the flow to a trivial, non-moving motion, while to fulfill the second condition the velocity field must be uniform

in  $z$ . This is clearly possible, and observed for low Reynolds numbers, for the flow inside of a bent channel (Walowitz *et al.* 1964; Gibson & Cook 1974) or that between two rotating cylinders (Taylor 1923), both invariant with respect to  $z$ . It is, instead, an unfulfillable condition for the flow inside of a bent pipe, where the geometry imposes no-slip boundary conditions at the sides of the pipe which only allow  $u_\theta \equiv 0$ . Therefore, assuming  $u_r = u_z = 0$  is not a possible condition for a bent pipe, at any  $Re$  or curvature.

As a further numerical proof, Fig. 7(a) further down presents the flow for  $\delta = 10^{-10}$ ,  $Re = 1$ , corresponding to  $De = 10^{-5}$ . Despite its low magnitude, the secondary flow is still clearly present. Dean numbers as low as  $\delta = 10^{-7}$  have also been investigated, and display the same features. We can therefore conclude that any bent pipe features secondary flow in the form of two symmetrical Dean vortices, as long as  $Re$  and  $\delta$  are larger than zero.

#### 4. Properties of the flow

Having provided a clear definition of the mechanics of the flow, this section is devoted to the analysis of its characteristics as a function of curvature and Reynolds number. As it will be shown in detail the Dean number alone is in general inadequate for a correct description of any of the quantities of interest, both from a scientific as well as engineering point of view. As shown in Canton *et al.* (2016), the flow becomes linearly unstable via a Hopf bifurcation for a Reynolds number of about 4000 for all curvatures greater than zero. This means that any infinitesimal perturbation to the steady state will trigger an instability, which will result in the appearance of periodic oscillations in the flow. The neutral curve associated to the instability, *i.e.* the set of curvature and Reynolds number values where the instability takes place, is therefore reported in the figures where it is relevant. It should be noted that the data for the neutral curve is missing for  $\delta < 0.002$  but the flow is likely linearly unstable for all curvatures greater than zero (Canton *et al.* 2016). Furthermore, subcritical transition, *i.e.* transition to turbulence in the presence of finite-amplitude perturbations, is observed for  $\delta < 0.028$  (Kühnen *et al.* 2015). To analyse the flow in detail, more than 110 000 steady states were computed with PaStA. All curvatures were investigated for  $0 < Re \leq 7\,000$  with a fixed step in Reynolds number  $\Delta Re = 10$ . Steady states were computed even above the instability in order to compare with results in the literature, and to provide a reference for possible future studies concerned with the control of this instability. The curvature was varied in the range  $2.5 \times 10^{-13} \leq \delta \leq 1$ ; for the higher curvature range,  $0.01 \leq \delta \leq 1$ , a step of  $\Delta\delta = 0.01$  was used, while the lower curvatures were investigated with a step in curvature equispaced in logarithmic scale, *i.e.*  $-12.6 \leq \log_{10}(\delta) < -2$ , with  $\Delta \log_{10}(\delta) = 0.2$ .

##### 4.1. The friction factor

One of the most important quantities that concerns both the researcher and, in particular, the engineer is the friction that the fluid encounters when going

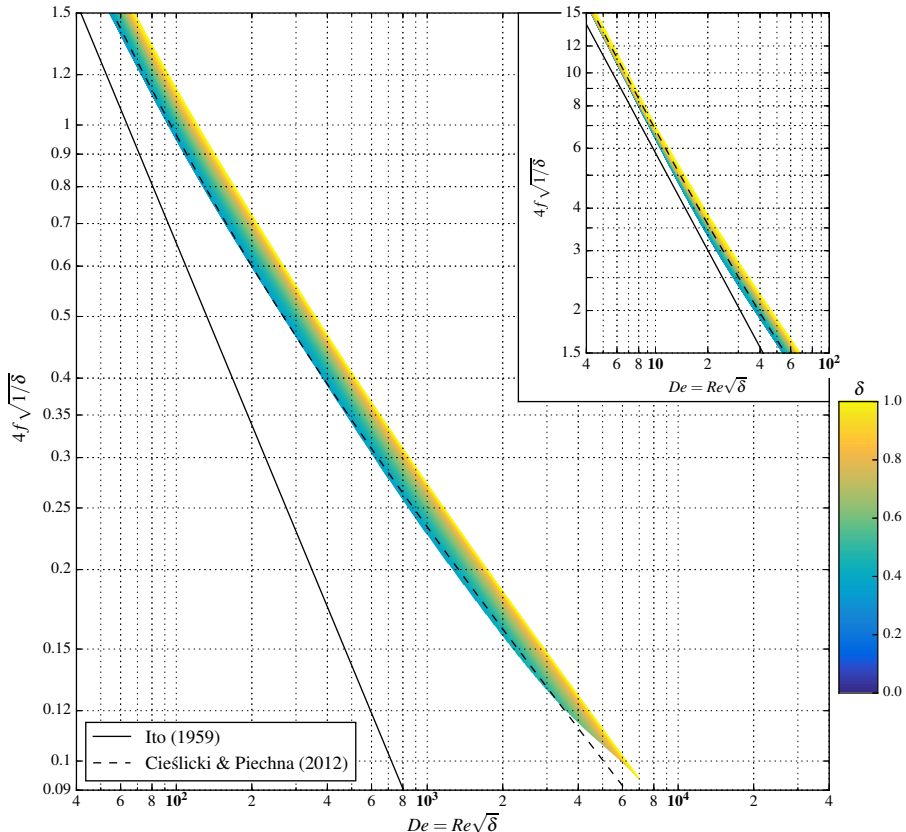


Figure 5: Fanning friction factor as defined in equation (22) multiplied by four and scaled with the curvature, plotted in logarithmic scale as a function of Dean number, as reported by Ito (1959) in figure 6 of his paper (the same axis limits and grid-lines have been used). Individual lines are coloured by the corresponding curvature. The “band” of lines becomes thinner for higher  $De$  not because it collapses, but because the maximum  $Re$  was limited to 7 000 for all values of  $\delta$ , resulting in a different maximum  $De$  dependent on the curvature.

through a bend. More precisely, the interest lies in quantifying  $f$  and its dependence on the Reynolds number and the curvature.

Ito (1959) reported the friction factors measured in his experiments and in the works by White (1929), Adler (1934) and Keulegan & Beij (1937) along with theoretical and empirical regression lines. In that paper,  $f$  was scaled with the square root of the inverse of the curvature (see figure 6 in Ito's paper and Fig. 5 in the present work) and plotted against the Dean number. Looking at Ito's paper all of the data collapse onto one single line (within

experimental uncertainties), confirming Dean's hypothesis on the existence of a single non-dimensional number governing the flow in bent pipes. More recently, Cieślicki & Piechna (2012) conducted an experimental and numerical study concluding that "for many applications the knowledge of  $De$  is sufficient to estimate the flow resistance of wavy tubes, with reasonable accuracy, according to the approximation (1) proposed in this work".

The actual picture, obtained from our data, looks somewhat different: as can be seen in Fig. 5, which reproduces Ito's plot with the present results, the lines do indeed show a common trend, but do not collapse onto a single one. The figure also reports Ito's regression line  $f = 344\sqrt{\delta}/(1.56 + \log_{10} De)^{5.73}$  and Cieślicki & Piechna's resistance formula  $f = 16/Re(0.080 + \sqrt{(1 - 0.080)^2 + 0.109^2 De})$ . The data represent a wide band where the value of  $f$  changes with curvature. Selecting, for example,  $De = 1\,000$  the Fanning friction factor varies between  $f \approx 0.0128$  for  $\delta = 0.05$  and  $f \approx 0.068$  for  $\delta = 1$ ; the relative difference between these two values and Ito's regression line is -78% and 18% respectively (Ito's formula predicts  $f \approx 0.0576$ ). Even at  $De = 10$  the friction range is still quite wide, with  $0.004 \leq f \leq 1.74$  and a relative difference with respect to Ito's formula ( $f \approx 1.575$ ) of -100% and 10% respectively. Cieślicki & Piechna's regression line does not do a better job. Considering the absolute values the scaling looks even worse: there is a factor of 5.3 between minimum and maximum  $f$  for  $De = 1\,000$ , which increases to 75 for  $De = 100$  and 435 for  $De = 10$ . Hence, while the relations might be qualitatively representative, they are by no means "reasonably accurate" for practical applications.

The conclusions from this first analysis on the friction factor is that the Dean number does not work as a unique scaling parameter for  $f$ , not even for comparatively low values of  $De$ : the curves do not collapse and the uncertainty in the friction would prevent any engineer from designing a piping system based on this plot. This could already be deduced from Dean's papers (Dean 1927, 1928b) where he immediately assumes the curvature to be negligible and estimates his results to be valid only if, in the first paper,  $Re^2 R_p / (1\,440 R_t) \ll 1$  which translates to an upper bound on the Dean number of  $De = Re\sqrt{\delta} \ll 37.94$ , and in the second paper if  $2Re^2 R_p / R_t \ll 400$ , which moves the upper bound on the Dean number to  $De \ll 14.14$ .

The latter bound, and more information, can be deduced from an analysis on the friction Reynolds number, presented in Fig. 6. This figure shows the friction Reynolds number in a bent pipe as a function of curvature and bulk Reynolds number. The plot is split in two parts, highlighting the very low curvature range in panel (a) and the low to high curvature range in panel (b). The labelled (white) isocontours of  $Re_\tau$  indicate the friction Reynolds number that characterises a straight pipe flow for bulk Reynolds numbers of 1 000, 2 000, ..., 7 000. The isocontours for the bent pipe are straight lines, independent of  $\delta$  or  $Re$ , up until  $De \approx 10$  and for  $\delta < 10^{-6}$ . This indicates that below these values the streamwise wall shear stress in a bent pipe behaves exactly like that in a straight pipe, a useful information for hydraulic engineers.

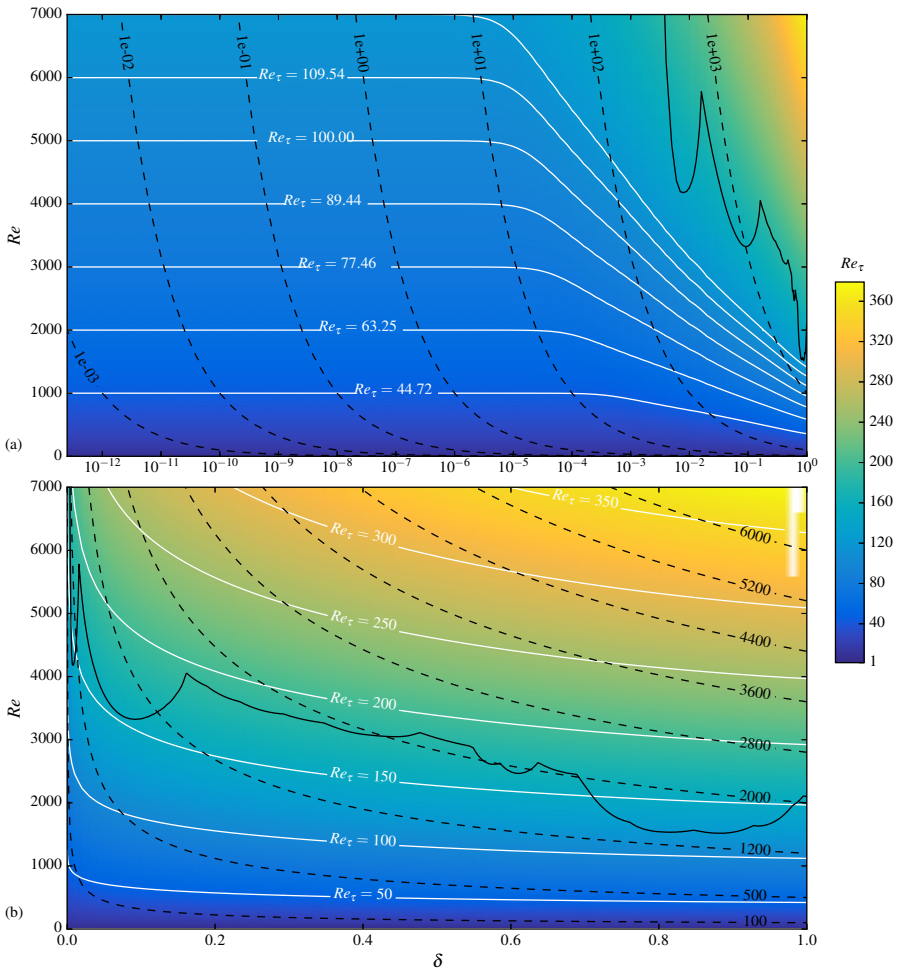


Figure 6: Friction Reynolds number as a function of curvature and bulk Reynolds number. Panel (a) highlights the very low curvature range in semi-logarithmic scale, while (b) shows the low to high curvature range in linear scale. The dashed (black) lines show isocontours of Dean number. The continuous (black) line is the neutral curve computed by Canton *et al.* (2016). The continuous (white) lines represent isocontours of  $Re_\tau$ . In (a) these isocontours correspond to the friction Reynolds number of a straight pipe with fluid flowing at the bulk Reynolds numbers indicated by the  $y$ -labels, *i.e.* 1 000, 2 000, . . . , 7 000.

This observation confirms Dean's second lower bound for the validity of his approximation, *i.e.*  $De \ll 14.14$ , and finally quantifies the “negligible curvature” limit, which holds for  $\delta < 10^{-6}$ .

A second important aspect can be observed in Fig. 6: the friction of the steady flow in a curved pipe is always either equal (below the aforementioned limits) or higher than that in a straight pipe for the same Reynolds number. For a given  $Re$ , the friction Reynolds number  $Re_\tau$  increases faster than exponentially with curvature, while the flow remains laminar. As an example, the curvature range  $0.15 \leq \delta \leq 0.55$  reaches  $Re_\tau = 180$  displaying a steady and laminar flow (Canton *et al.* 2016), while the flow in a straight pipe for the same  $Re_\tau$  would already be turbulent. Additional considerations on the wall shear stress for low curvatures can be found, *e.g.* in Noorani & Schlatter (2015). Identical considerations can be drawn by plotting the ratio between the wall shear stress in bent pipes and that of a straight pipe (not reported in this article).

Dean's approximation and self similarity are thus clearly only valid when the curvature is so low that the flow is barely different from that in a straight pipe at the same bulk Reynolds number. Above these limits the curvature's influence becomes more and more important for the flow and (nonlinearly) modifies its characteristics (see also section 4.2), so that one single scaling parameter is not sufficient anymore. Future research should bear this in mind and limit the usage of the Dean number and similarity outside of their validity limits. This is perhaps even more important in spatially evolving flows, such as 90 degree bends, where transient effects are clearly dependent on the curvature and Reynolds number independently.

#### 4.2. Description of the flow as a function of curvature and Reynolds number

As mentioned above, the curvature of the pipe influences the characteristics of this flow to a point where it must be considered as a parameter with the same importance as the Reynolds number. Fig. 7 presents six solutions for different curvatures at constant Reynolds number. It is immediate to see the impact of the curvature on the structure of the flow. An effect of similar magnitude can be observed even for constant Dean number, as can be seen, for example, in Masud *et al.* (2010). What follows is an analysis of some of the most relevant quantities for this flow.

Quasi-straight pipe behaviour. As discussed in the previous section, below  $\delta = 10^{-6}$  the flow in a bent pipe behaves very closely to the flow in a straight pipe. Looking at Fig. 7(a), which depicts the laminar flow for  $\delta = 10^{-10}$ ,  $Re = 1$ , it is possible to observe that the streamwise velocity field has a quasi-parabolic profile, with the maximum located nearly exactly in the centre of the pipe. What differentiates this flow from that of a straight pipe is the presence of (weak) secondary motion, highlighted both by the isocontours of in-plane streamfunction  $\psi$  (computed here by solving the Poisson equation  $\nabla^2\psi = -\omega_s$ ) and by a non-zero in-plane velocity field. The magnitude of the in-plane velocity, though, is

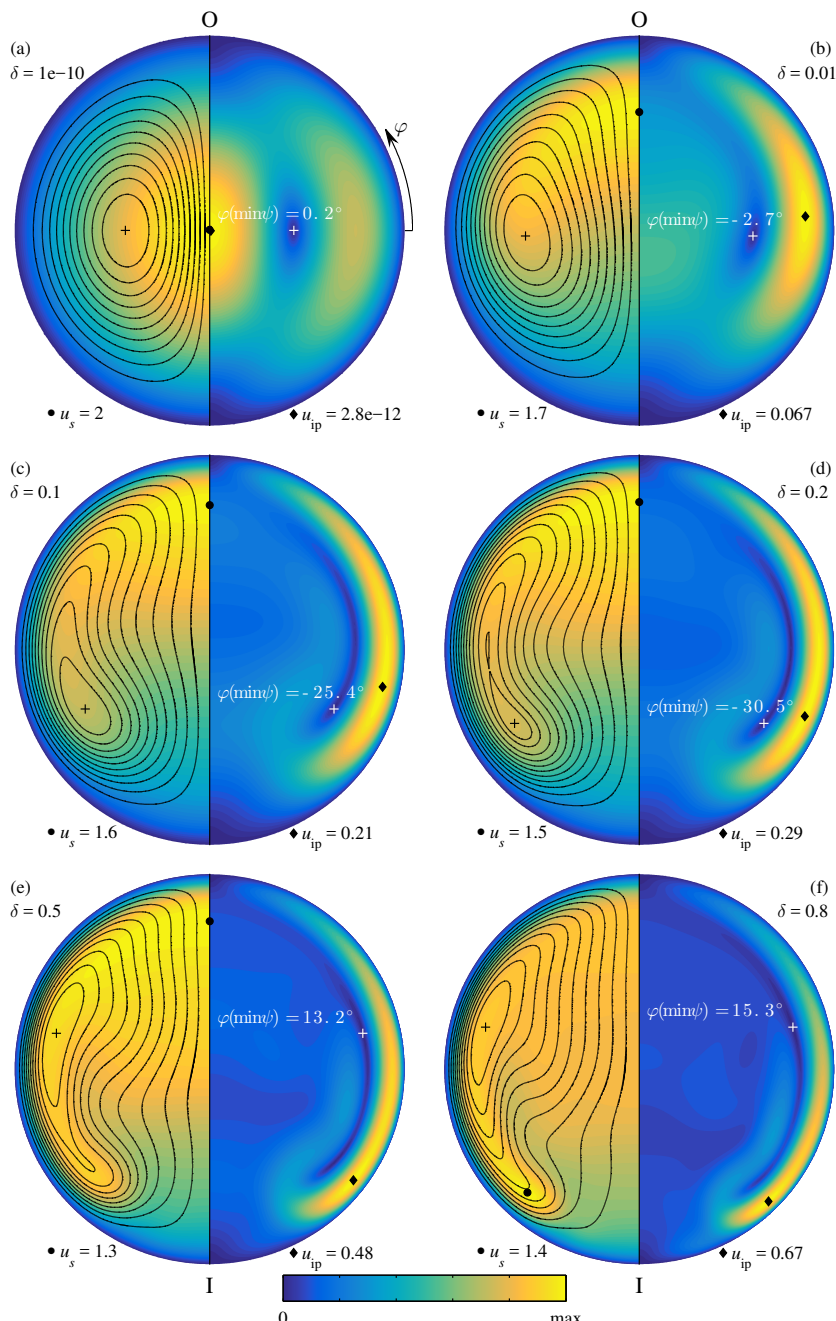


Figure 7: (Caption on the following page.)

Figure 7: (On the previous page.) Steady, laminar, stable solutions for different curvature and Reynolds number. The curvature of the pipe is indicated next to the panel label. All solutions are for  $Re = 1000$  except for (a) for which  $Re = 1$ . All panels depict the streamwise velocity component,  $u_s$  and isocontours of the streamfunction,  $\psi$  (on the left-half) along with the magnitude of the in-plane velocity components, *i.e.*  $u_{ip} = \sqrt{(u_\varrho^2 + u_\phi^2)}$  (on the right-half). The colour-scale is the same for all scalar fields; the colourbar is reported on the bottom of the figure and the values of the maxima are reported in each panel. The positions of the maxima are also marked with symbols: a bullet for  $\max u_s$ , a diamond for  $\max u_{ip}$ , and plus symbols for the extrema of  $\psi$ , identifying the core of the vortices. The angular position of the cores is also reported (in degrees) with a redefined angle  $\varphi = \pi - \phi$  (cf. Fig. 1).

twelve orders of magnitude lower than that of the streamwise velocity, and the contours of  $\psi$  are nearly symmetric with respect to the  $(\zeta, s)$  plane (see Fig. 1).

These and most other characteristics of the flow (one obvious exception being the shear stress presented in Fig. 6) do not depend on curvature nor Reynolds number up to  $\delta = 10^{-6}$ . This is clearly visible in Figs. 8, 9 and 10 which depict the maximum streamwise velocity, the position of the vortex cores, and a measure of the intensity of the vortices, respectively.

Between  $\delta = 10^{-6}$  and  $\delta = 10^{-2}$  the flow is gradually modified: the maximum  $u_s$  moves towards the outside of the bend, while the maximum in-plane velocity jumps from the equatorial plane to the outer side of the pipe. A boundary layer begins to form towards the lateral sides of the pipe, although it is still quite thick at such low curvatures, and the magnitude of the in-plane velocity quickly gains 10 orders of magnitude (so does the circulation, see Fig. 10). The Dean vortices deform and their centres move towards the outer portion of the bend, as can be seen in Figs. 7(b) and 9(a), the peak of streamwise velocity is gradually reduced (Fig. 8(a)) and the region of high  $u_s$  becomes larger.

These general features of the flow at very low curvatures are well known and documented in the literature. A few important characteristics are, though, usually overlooked: while some quantities, such as  $\max u_s$  and  $\phi(\min \psi)$ , do reasonably scale with the Dean number up to  $De = 100$  (see Figs. 8(a) and 9(a) respectively), other quantities do not display a relationship with  $De$  (see, for example, the intensity of the vortices in Fig. 10). Moreover, the deformation and intensity of the vortices are not accurately captured in papers that present solutions computed with the “low- $\delta$ ” approximation. For curvatures higher than 0.01 all features of the flow need to be described as a function of  $\delta$  and  $Re$  separately. Certain quantities display a “smooth” trend with curvature and  $Re$  as, for example, the friction on the pipe walls (Fig. 6(b)) and the intensity of the vortices (Fig. 10(b)). Other features, on the other hand, present discontinuities as the curvature is increased.

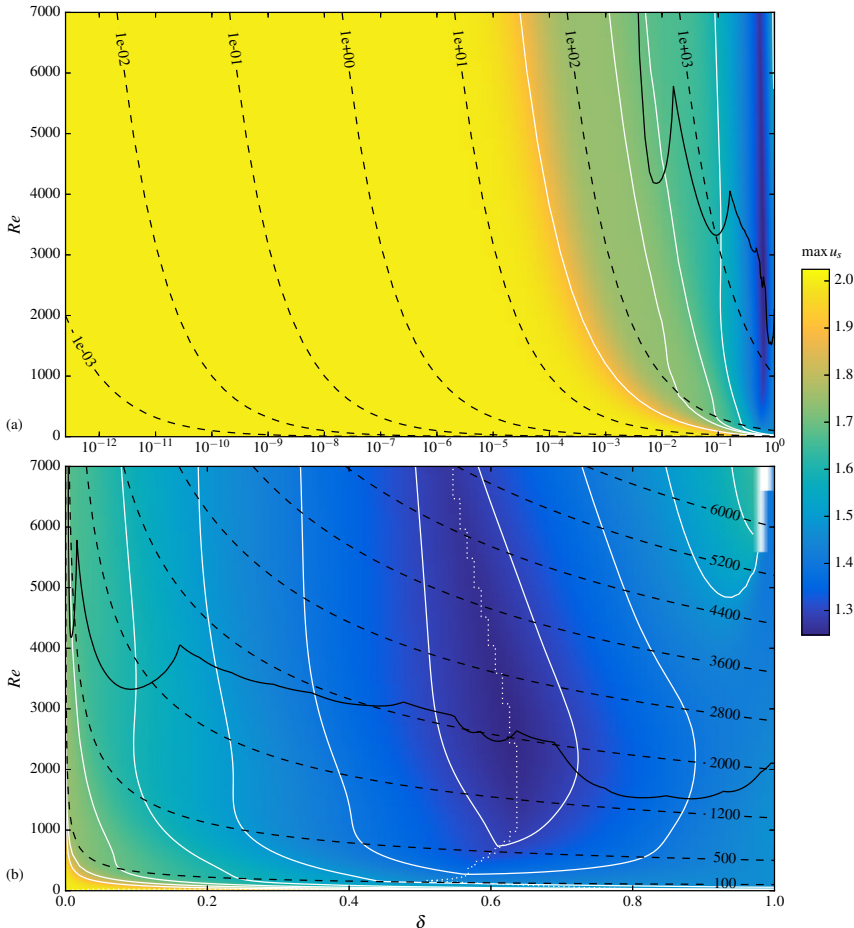


Figure 8: Maximum streamwise velocity in the pipe as a function of curvature and bulk Reynolds number. The continuous (white) lines show isocontours of  $\max u_s$  to improve the readability of the figure. Panel (a) highlights the very low curvature range in semi-logarithmic scale, while (b) shows the low to high curvature range in linear scale. The dashed (black) lines show isocontours of Dean number. The continuous (black) line is the neutral curve computed by Canton *et al.* (2016). It can be observed that up to  $De \approx 20$  there is little difference with respect to a straight pipe (which features  $\max u_s = 2$ , panel (a)). Panel (b), on the other hand, shows two important features:  $u_s$  reaches a minimum value of approximately  $1.25U_b$  for  $\delta \approx 0.63$ ; this minimum coincides with a discontinuity in the flow structure: the position of  $\max u_s$  jumps from the outer portion of the pipe to the inner bend (see also Fig. 7). The discontinuity is indicated by the dotted (white) line.

Streamwise flow. The maximum streamwise velocity is not always located towards the outer portion of the bend (as typically reported in the literature): there are actually two maxima in  $u_s$  (clearly one absolute and the other relative). For curvatures below 0.5 the absolute maximum is situated towards the outer section of the pipe, as can be observed by the markers in Figs. 7(a–e). As the curvature increases, though, the value of this maximum decreases and, consequently, the area of high streamwise velocity expands (note that the bulk velocity is fixed), as can be observed in Figs. 7(c–e). During this “transition” the relative maxima, located towards the inner bend, increase in magnitude (Fig. 7(e)). For  $0.51 < \delta < 0.64$  (see Fig. 8(b)) the two maxima reach the same value of about  $1.25U_b$ , which coincides with the absolute minimum of  $u_s$ , and exchange the absolute/relative property. This modification in the topology of the flow was also observed by Masud *et al.* (2010), although only a qualitative analysis of this phenomenon was presented.

For curvatures above this discontinuity the flow features two (symmetric) absolute maxima of  $u_s$ , located in close proximity to the maxima of in-plane velocity (see Fig. 7(f) for an example). As far as the authors are aware, this observation cannot be found in the literature. In this region of the  $(\delta, Re)$  plane the maximum of streamwise velocity has a nearly constant value of about  $1.4U_b$ , only marginally influenced by curvature and Reynolds number. Another notable feature of such high curvatures is that, while the absolute max  $u_s$  is located towards the inner bend, the outer portion of the curved pipe still features a wide region of relatively high streamwise velocity. This configuration is markedly different from the low-curvature regime, where the flow in the outer portion of the bend is nearly twice as fast as the flow in the inner part. The cause behind the modification of the streamwise velocity profile is not completely clear. A possible explanation is given by the distribution of the driving force (or pressure gradient) on the pipe section (see Fig. 4): as the curvature increases the ratio between inner and outer  $f_v$  grows faster than exponentially, with  $f_v(R_t - R_p)/f_v(R_t + R_p) = (1 + \delta)/(1 - \delta)$ . This is a direct consequence of a bend geometry: as the curvature increases the ratio between the length of two paths, one on the inside of the bend and the other on the outside, grows exactly as  $(1 + \delta)/(1 - \delta)$ . Two mechanisms are therefore acting on the flow at the same time: the centrifugal force pushes the central, fast flowing, fluid towards the outside of the bend (Fig. 7(b–e)), and a higher pressure gradient accelerates the fluid located towards the inner side of the bend (Figs. 4 and 7(f)).

In-plane flow and Dean vortices. The behaviour of the two vortices is even more complicated than that of  $\max u_s$ . While for  $\delta < 0.01$  and  $De < 100$  the cores are located towards the outer bend, their position scales well with Dean number, and their intensity increases with curvature, the remainder of the  $(\delta, Re)$  plane is harder to analyse. Note that, while by looking at Fig. 9(b) it may seem that the position of the cores scales with Dean number up to  $De = 100$  for any curvature, there actually are “jumps” in  $\varphi(\min \psi)$  for  $Re < 50$ , although they are admittedly not visible in the figure.

Similarly to the streamwise velocity, the in-plane streamfunction  $\psi$  (computed here by solving the Poisson equation  $\nabla^2\psi = -\omega_s$ ) presents more than a single maximum as well. This is visible in Figs. 7(d,e) where it can be observed that the vortex core is highly stretched and pushed towards the side of the pipe. While the in-plane streamfunction in Fig. 7(e) does not yet present a local maximum, the innermost isocontour of  $\psi$  in Fig. 7(d) highlights this peculiar feature of the vortices. For the values of  $(\delta, Re)$  where such a local maximum is present, the core of the vortices is split into two co-rotating cells linked by a saddle node. This condition is highlighted by the discontinuity in Fig. 9(b): by increasing the curvature the absolute minimum (and its symmetric maximum) of  $\psi$  “jumps” from the inner side of the bend to the outer side. This jump can also qualitatively be observed in the results by Masud *et al.* (2010), although the authors did not present a quantitative analysis. The Reynolds number corresponding to this discontinuity is strongly affected by the curvature, and does not exhibit a monotonic relationship to  $\delta$ . The position of such a discontinuity is another example of a feature that cannot be predicted by an analysis based on the Dean number alone. This abrupt change in the position of the vortex cores does not affect the flow globally, as quantities like the shear stress,  $\max u_s$  and even the magnitude of the vortices itself do not present any particular modification corresponding to this jump. It can, though, present an unwanted condition for mixing and thermal-exchange applications, as the portion of flow captured by one cell would never be in contact with that in the other cell.

Beside the above considerations on the maximum, the streamfunction, along with the magnitude of in-plane velocity, also highlights great qualitative changes taking place in the flow as the curvature changes. As mentioned above, an increase in curvature causes an increase of the intensity of the secondary motion. By looking at the flow fields in Fig. 7 it can be noticed that as  $\delta$  increases the boundary layers on the lateral sides of the pipe become thinner. This is a direct consequence of the increase in curvature: higher  $\delta$  implies higher  $u_{ip}$  and, consequently, a higher friction Reynolds number on the pipe sides.

Even the intensity of the vortices cannot be described by the Dean number alone. This can be observed both in Fig. 10 which reports the value of the circulation of one vortex, defined as the integral of the streamwise component of the vorticity over one half of the pipe section:  $\Gamma_v = \int_{\Omega/2} \omega_s$ . As already mentioned, for very low curvatures  $\Gamma_v$  depends nearly only on the curvature of the pipe. For low to high curvatures, on the other hand, the vortex intensity exhibits a complex behaviour:  $\Gamma_v$  increases very rapidly with Reynolds number for  $Re < 50$ , while it then presents a constant value or even a decreasing trend up to  $Re \approx 1000$  (depending on  $\delta$ ) and then exhibits a slowly increasing trend. With respect to curvature,  $\Gamma_v$  grows approximately proportionally to  $\sqrt{\delta}$ , but only up to  $\delta \approx 0.6$ , for higher curvatures it actually displays a trend proportional to  $\delta^2$ .

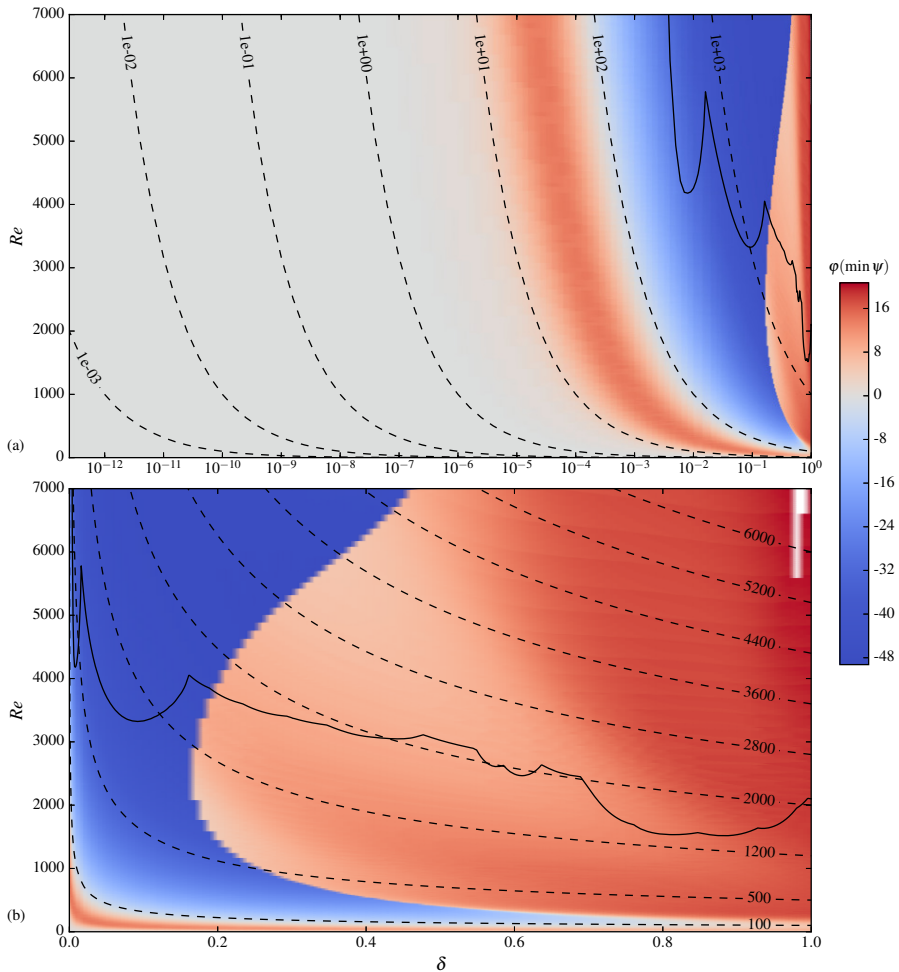


Figure 9: Angular position (in degrees) of the core of the vortices as a function of curvature and bulk Reynolds number. The angle has been redefined for convenience as  $\varphi = \pi - \phi$  (cf. Fig. 1): positive values of  $\varphi$  indicate the outer portion of the pipe, while negative values correspond to the inner part (see also Fig. 7). Panel (a) highlights the very low curvature range in semi-logarithmic scale, while (b) shows the low to high curvature range in linear scale. The dashed (black) lines show isocontours of Dean number. The continuous (black) line is the neutral curve computed by Canton *et al.* (2016).

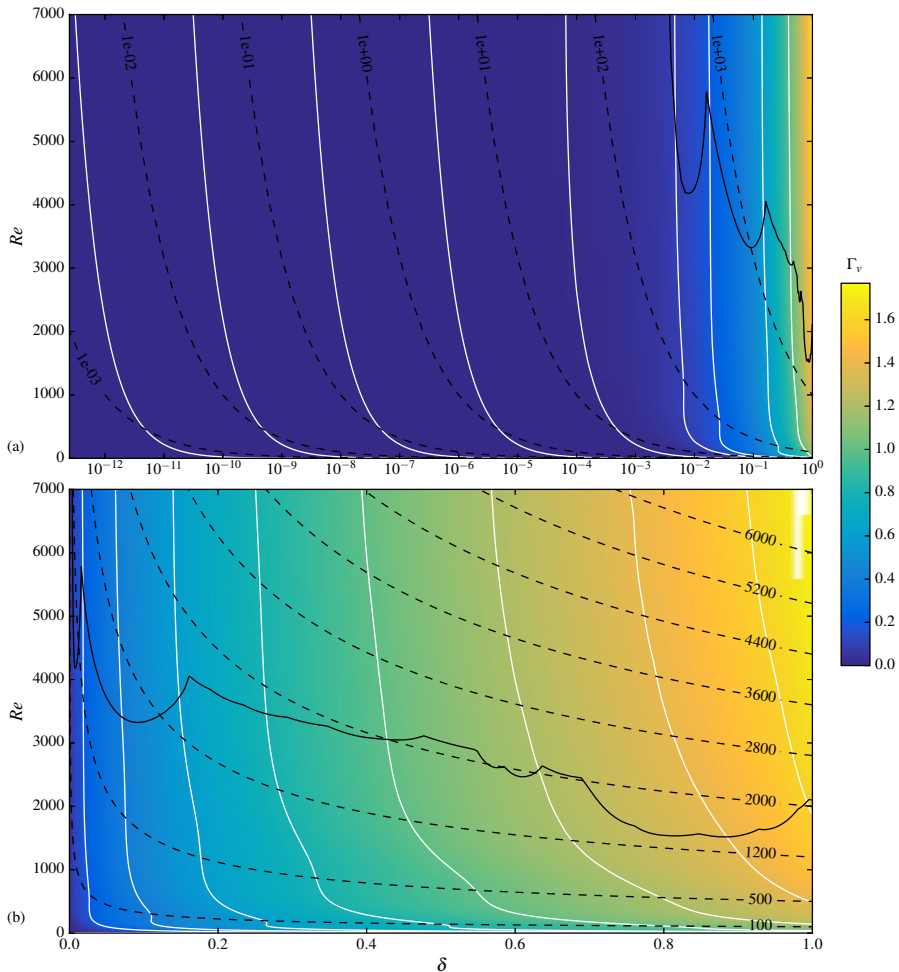


Figure 10: Circulation of the vortices  $\Gamma_v$  as a function of curvature and bulk Reynolds number. The continuous (white) lines show isocontours of  $\Gamma_v$  to improve the readability of the figure. Panel (a) highlights the very low curvature range in semi-logarithmic scale, while (b) shows the low to high curvature range in linear scale. The dashed (black) lines show isocontours of Dean number. The continuous (black) line is the neutral curve computed by Canton *et al.* (2016). For  $10^{-2} < \delta < 0.1$  the circulation nearly only depends on curvature, while lower and higher curvatures are characterised by an increase of  $\Gamma_v$  with  $Re$ .

## 5. Conclusions

The present work re-analyses and extends the knowledge on the steady, laminar flow inside curved pipes. More than 110 000 numerical solutions are computed to a high degree of accuracy in the entire curvature range ( $0 < \delta \leq 1$ ). The upper limit on the Reynolds number is set to  $Re = 7\,000$ , where the flow is, in any practical situation, unsteady following a Hopf bifurcation (Canton *et al.* 2016) or subcritical transition (Kühnen *et al.* 2015) depending on the curvature.

It is shown that a Dean number-based analysis is valid only below very low bounds on curvature and Dean number:  $\delta < 10^{-6}$  and  $De < 10$ . These bounds are shown to be strict even for quantities that were believed to scale with Dean number up to much higher values of  $\delta$  and  $De$ , e.g. the friction factor  $f$ . It was quantified that, despite what it may be found in the literature (Ito 1959; Cieślicki & Piechna 2012), computing  $f$  based on the knowledge of the Dean number alone results in an uncertainty comprised between 17% and 340%.

The present analysis clearly shows that it is not possible to quantify any flow feature as a function of a single scaling parameter: the curvature and the Reynolds number are equally important for the description of this flow. The proof of this statement for a toroidal pipe in the low- $Re$ , laminar regime should serve as an even greater warning for researchers dealing with spatially developing, turbulent or pulsating flows, where even more non-dimensional numbers become relevant. These considerations should be taken into account in any future research concerned with bent pipes.

The present paper also presents an analysis of some of the most relevant flow characteristics as a function of the two governing parameters. A number of previously unknown phenomena are documented and discussed such as, most prominently, the shift in position of the maximum streamwise velocity, and the splitting of the vortex cores. A discontinuity for a curvature of about 0.6 is found to provide a remarkable boundary for the characteristics of the flow: while for  $\delta \lesssim 0.6$  the flow is qualitatively similar to what can be found in the literature, higher curvatures feature a significantly different structure of the solution.

Amongst other quantities, the location of maximum streamwise velocity is of fundamental importance. As an example, the genesis and evolution of the meandering of rivers is dictated by the position of  $\max u_s$ : a higher flow velocity towards the outer bank of a river curve results in higher soil erosion at the outer bank and, consequently, higher deposition of soil at the inner bank (Thomson 1876, 1877; Yalin 1992). Since the windings of rivers can be well approximated by a sine-generated curve (Leopold & Langbein 1966; Langbein & Leopold 1966; Ferreira Da Silva 2006), the maximum curvature of a river meander can never exceed  $\delta = 0.24$ ; for a higher curvature, in fact, two consecutive bends enter in contact with one another and an oxbow lake forms. If rivers could form tighter bends, or if the jump in position of  $\max u_s$  were to take place for lower  $\delta$ , the topography of rivers could be very different.

The complete database including all the computed solutions is available online at [www.flow.kth.se](http://www.flow.kth.se)

## Acknowledgments

Financial support by the Swedish Research Council (VR) is gratefully acknowledged. Computer time was provided by the Swedish National Infrastructure for Computing (SNIC). P. S. acknowledges support by the Knut and Alice Wallenberg Foundation.

## REFERENCES

- ADLER, M. 1934 Strömung in gekrümmten Rohren. *ZAMM-Z. Angew. Math. Mech.* **14**, 257–275.
- AMESTOY, R., DUFF, I. & L'EXCELLENT, J.-Y. 2000 Multifrontal parallel distributed symmetric and unsymmetric solvers. *Comput. Methods Appl. Math.* **184**, 501–520.
- ANWER, M. & SO, R. M. C. 1993 Swirling turbulent flow through a curved pipe. part 1: Effect of swirl and bend curvature. *Exp. Fluids* **14**, 85–96.
- BERGER, S. A., TALBOT, L. & YAO, L. S. 1983 Flow in curved pipes. *Annu. Rev. Fluid Mech.* **15**, 461–512.
- BOUSSINESQ, M. J. 1868 Mémoire sur l'influence des frottements dans les mouvements réguliers des fluides. *J. Math. Pure Appl.* **13**, 377–424.
- BULUSU, K. V., HUSSAIN, S. & PLESNIAK, M. W. 2014 Determination of secondary flow morphologies by wavelet analysis in a curved artery model with physiological inflow. *Exp. Fluids* **55**, 1832.
- CANTON, J. 2013 Global linear stability of axisymmetric coaxial jets. Master's thesis, Politecnico di Milano, Italy, <https://www.politesi.polimi.it/handle/10589/87827>.
- CANTON, J., SCHLATTER, P. & ÖRLÜ, R. 2016 Modal instability of the flow in a toroidal pipe. *J. Fluid Mech.* **792**, 894–909.
- CIEŚLICKI, K. & PIECHNA, A. 2012 Can the Dean number alone characterize flow similarity in differently bent tubes? *J. Fluids Eng.* **134**, 051205.
- DASKOPOULOS, P. & LENHOFF, A. M. 1989 Flow in curved ducts: bifurcation structure for stationary ducts. *J. Fluid Mech.* **203**, 125–148.
- DEAN, W. R. 1927 XVI. Note on the motion of fluid in a curved pipe. *London, Edinburgh, Dublin Philos. Mag. J. Sci.* **4**, 208–223.
- DEAN, W. R. 1928a Fluid Motion in a Curved Channel. *Proc. R. Soc. A Math. Phys. Eng. Sci.* **121**, 402–420.
- DEAN, W. R. 1928b The streamline motion of fluid in a curved pipe. *Phil. Mag.* **5**, 673–693.
- DRAZIN, P. G. & REID, W. H. 2004 *Hydrodynamic Stability*. Cambridge University Press.
- EUSTICE, J. 1910 Flow of water in curved pipes. *Proc. R. Soc. London, Ser. A* **84**, 107–118.
- EUSTICE, J. 1911 Experiments on stream-line motion in curved pipes. *Proc. R. Soc. A Math. Phys. Eng. Sci.* **85**, 119–131.
- FAN, Y., TANNER, R. I. & PHAN-THIEN, N. 2001 Fully developed viscous and viscoelastic flows in curved pipes. *J. Fluid Mech.* **440**, 327–357.

- FERREIRA DA SILVA, A. M. 2006 On why and how do rivers meander. *J. Hydraul. Res.* **44**, 579–590.
- GHOBADI, M. & MUZYCHKA, Y. S. 2016 A review of heat transfer and pressure drop correlations for laminar flow in curved circular ducts. *Heat Transf. Eng.* **37**, 815–839.
- GIBSON, R. D. & COOK, A. E. 1974 The stability of curved channel flow. *Q. J. Mech. Appl. Math.* **27**, 149–160.
- HELLSTRÖM, L. H. O., ZLATINOV, M. B., CAO, G. & SMITS, A. J. 2013 Turbulent pipe flow downstream of a 90° bend. *J. Fluid Mech.* **735**, R7.
- ISACHENKO, V., OSIROVA, V. & SUKOMEL, A. 1974 *Heat Transfer*, 2nd edn. Mir Publishers.
- ITO, H. 1959 Friction factors for turbulent flow in curved pipes. *J. Basic Eng.* **81**, 123–134.
- ITO, H. 1987 Flow in Curved Pipes. *JSME Int. J.* **30** (262), 543–552.
- KALPAKLI, A., ÖRLÜ, R. & ALFREDSSON, P. H. 2016 Turbulent flows in curved pipes: recent advances in experiments and simulations. *Appl. Mech. Rev.* **68**, 050802.
- KAO, H. C. 1992 Some aspects of bifurcation structure of laminar flow in curved ducts. *J. Fluid Mech.* **243**, 519–539.
- KEULEGAN, G. H. & BEIJ, K. H. 1937 Pressure losses for fluid flow in curved pipes. *J. Res. Nat. Bur. Stand.* **18**, 89–114.
- KÜHNEN, J., BRAUNSHIER, P., SCHWEGEL, M., KUHLMANN, H. C. & HOF, B. 2015 Subcritical versus supercritical transition to turbulence in curved pipes. *J. Fluid Mech.* **770**, R3.
- LANGBEIN, W. B. & LEOPOLD, L. B. 1966 River meanders – Theory of minimum variance. *U.S. Geol. Surv. Prof. Pap.* 422-H pp. 1–15.
- LEOPOLD, L. B. & LANGBEIN, W. B. 1966 River meanders. *Sci. Am.* **214**, 60–70.
- MASUD, M. A., ISLAM, M. R., SHEIKH, M. R. & ALAM, M. M. 2010 Stable solution zone for fluid flow through curved pipe with circular cross-section. *J. Nav. Archit. Mar. Eng.* **7**, 19–26.
- NAJJARI, M. R. & PLESNIAK, M. W. 2016 Evolution of vortical structures in a curved artery model with non-newtonian blood-analog fluid under pulsatile inflow conditions. *Exp. Fluids* **57**, 100.
- NANDAKUMAR, K. & MASLIYAH, J. H. 1982 Bifurcation in steady laminar flow through curved tubes. *J. Fluid Mech.* **119**, 475–490.
- NOORANI, A. & SCHLATTER, P. 2015 Evidence of sublaminar drag naturally occurring in a curved pipe. *Phys. Fluids* **27**, 035105.
- POPE, S. B. 2000 *Turbulent Flows*. Cambridge University Press.
- QUARTAPELLE, L. & AUTERI, F. 2013 *Fluidodinamica incomprimibile*. CEA.
- RÜTTEN, F., MEINKE, M. & SCHRÖDER, W. 2001 Large-eddy simulations of 90° pipe bend flows. *J. Turbulence* **2**, 1–15.
- SHORTIS, T. A. & HALL, P. 1999 On the nonlinear stability of the oscillatory viscous flow of an incompressible fluid in a curved pipe. *J. Fluid Mech.* **379**, 145–163.
- SIGGERS, J. H. & WATERS, S. L. 2008 Unsteady flows in pipes with finite curvature. *J. Fluid Mech.* **600**, 133–165.
- TAYLOR, G. I. 1923 Stability of a viscous liquid contained between two rotating cylinders. *P. R. Soc. Lond. A-Conta.* **223**, 289–343.

- THOMSON, J. 1876 On the origin of winding rivers in alluvial plains, with remarks on the flow of water round bends in pipes. *Proc. R. Soc. London* **25**, 5–8.
- THOMSON, J. 1877 Experimental demonstration in respect to the origin of windings of rivers in alluvial plains, and to the mode of flow of water round bends of pipes. *Proc. R. Soc. London* **26**, 356–357.
- VAN DYKE, M. 1978 Extended Stokes series: laminar flow through a loosely coiled pipe. *J. Fluid Mech.* **86**, 129–145.
- VASHISTH, S., KUMAR, V. & NIGAM, K. D. P. 2008 A review on the potential applications of curved geometries in process industry. *Ind. Eng. Chem. Res.* **47**, 3291–3337.
- VERKAIK, A. C., BEULEN, B. W. A. M. M., BOGAERDS, A. C. B., RUTTEN, M. C. M. & VAN DE VOSSE, F. N. 2009 Estimation of volume flow in curved tubes based on analytical and computational analysis of axial velocity profiles. *Phys. Fluids* **21**, 023602.
- WALOWIT, J., TSAO, S. & DiPRIMA, R. C. 1964 Stability of flow between arbitrarily spaced concentric cylindrical surfaces including the effect of a radial temperature gradient. *J. Appl. Mech.* **31**, 585–593.
- WHITE, C. M. 1929 Streamline flow through curved pipes. *Proc. R. Soc. London Ser. A* **123**, 645–663.
- VAN WYK, S., WITTBERG, L. P., BULUSU, K. V., FUCHS, L. & PLESNIAK, M. W. 2015 Non-Newtonian perspectives on pulsatile blood-analog flows in a 180° curved artery model. *Phys. Fluids* **27**, 071901.
- YALIN, M. S. 1992 *River Mechanics*. Pergamon Press.
- YANASE, S., YAMAMOTO, K. & YOSHIDA, T. 1994 Effect of curvature on dual solutions of flow through a curved circular tube. *Fluid Dyn. Res.* **13**, 217.
- YANG, Z. & KELLER, H. B. 1986 Multiple laminar flows through curved pipes. *Appl. Numer. Math.* **2**, 257–271.

**2**

**Paper 2**



# Modal instability of the flow in a toroidal pipe

Jacopo Canton<sup>1,2</sup>, Philipp Schlatter<sup>1,2</sup> and Ramis Örlü<sup>1</sup>

<sup>1</sup>Linné FLOW Centre, KTH Mechanics, Royal Institute of Technology, SE-100 44  
Stockholm, Sweden

<sup>2</sup>Swedish e-Science Research Centre (SeRC), Royal Institute of Technology, SE-100  
44 Stockholm, Sweden

*Journal of Fluid Mechanics* (2016), vol. **792**, 894–909

The modal instability encountered by the incompressible flow inside a toroidal pipe is studied, for the first time, by means of linear stability analysis and direct numerical simulation (DNS). In addition to the unquestionable aesthetic appeal, the torus represents the smallest departure from the canonical straight pipe flow, at least for low curvatures. The flow is governed by only two parameters: the Reynolds number  $Re$  and the curvature of the torus  $\delta$ , *i.e.* the ratio between pipe radius and torus radius. The absence of additional features, such as torsion in the case of a helical pipe, allows us to isolate the effect that the curvature has on the onset of the instability. Results show that the flow is linearly unstable for all curvatures investigated between 0.002 and unity, and undergoes a Hopf bifurcation at  $Re$  of about 4000. The bifurcation is followed by the onset of a periodic regime, characterised by travelling waves with wavelength  $O(1)$  pipe diameters. The neutral curve associated with the instability is traced in parameter space by means of a novel continuation algorithm. Tracking the bifurcation provides a complete description of the modal onset of instability as a function of the two governing parameters, and allows a precise calculation of the critical values of  $Re$  and  $\delta$ . Several different modes are found, with differing properties and eigenfunction shapes. Some eigenmodes are observed to belong to groups with a set of common characteristics, deemed ‘families’, while others appear as ‘isolated’. Comparison to nonlinear DNS shows excellent agreement, confirming every aspect of the linear analysis, its accuracy, and proving its significance for the nonlinear flow. Experimental data from the literature are also shown to be in considerable agreement with the present results.

**Key words:** bifurcation, instability, nonlinear dynamical systems

---

## 1. Introduction

Bent pipes are ubiquitous in both man-made devices and biological systems. Their application in industry ranges from junctions between sections of straight pipes, to exhaust tubes, and heat exchangers, just to name a few examples. The reasons for their vast employment are, amongst others, their enhanced

cross-sectional mixing and improved mass and heat transfer coefficients, which make them an attractive alternative to traditional mechanical systems (for a comprehensive review see Vashisth *et al.* 2008). Even biological organisms contain curved “pipes” which constitute, for instance, respiratory and vascular systems. In these cases the interest lies in understanding the influence that the vortical structures, formed due to the secondary flow, have on the circulation of fluid (Bulusu *et al.* 2014). In addition, the flow inside bent pipes is important for the research on hydrodynamic stability and transition to turbulence. In fact, the geometry of bent pipes exhibits only a few differences with respect to that of the most canonical and studied wall-bounded flow case of the past century, *i.e.* the straight pipe, but little is known about the onset of turbulence in curved pipes.

The earliest studies on bent pipes date as far back as to the nineteenth century (Boussinesq 1868). At the beginning of the past century, Eustice (1910) measured a reduction of fluid flux and was able to correlate it directly with the curvature of the pipe. He later demonstrated, in a series of experiments, the existence of secondary flow by injecting coloured filaments of dye into water flowing through coiled pipes. Dean (1927) analysed the structure of the secondary motion by solving an approximate form of the Navier–Stokes equations valid in the limit of vanishing curvature. By considering a toroidal pipe he deduced that the flow could be described by a single dimensionless parameter which accounted for both Reynolds number and curvature. Employing this approximation he qualitatively confirmed the results of Eustice and showed that the secondary flow is composed of two counter-rotating vortices located mirror-symmetrically with respect to the equatorial plane of the torus. The non-dimensional number and the two vortices were later given Dean’s name in his honour. It is worth noting that, since Dean’s original work, the Dean number has been given several different definitions (see Berger *et al.* 1983, p. 471). In the present work, for the short part where it is needed, the following definition is employed:  $De = Re\sqrt{\delta}$ , as strongly suggested by Berger *et al.* (1983), and employed in the vast majority of follow-up studies. Here, and in the following,  $Re$  is the Reynolds number, based on the diameter of the pipe, bulk velocity and fluid kinematic viscosity, *i.e.*  $Re = 2R_p U_b / \nu$ , while the curvature of the torus is the ratio between pipe and torus radii, *i.e.*  $\delta = R_p / R_t$ , cf figure 1. Following Dean, other authors analysed the behaviour of the flow in a toroidal pipe (see e.g. McConalogue & Srivastava 1968; Van Dyke 1978; Dennis 1980), further characterising the steady state solution in the low curvature limit (comprehensive reviews can be found in Berger *et al.* 1983; Ito 1987).

Experimental works were initially aimed at characterising the consequences of the secondary flow in mildly bent pipes. In particular, measurements of frictional resistance for turbulent flow in curved tubes were presented by a number of authors (see, most prominently, Ito 1959, and more recently Cioncolini & Santini 2006). The first studies that touch the topic of transition are those by White (1929); Taylor (1929), conducted in helical pipes and devoted to frictional

resistance measurements. Later, Sreenivasan & Strykowski (1983) conducted similar experiments with a helical pipe at low curvatures. The authors employed both dye streaks and hot-wire anemometry to obtain insight into the transitional flow. Although, as stated in the paper, their investigation was at a preliminary stage, these authors were, to the best of our knowledge, the first ones to observe the subcritical transition boundary for low curvatures. A more detailed analysis is provided by Webster & Humphrey (1993, 1997) who examined the flow inside a helical pipe with curvature  $\delta = 0.055$ . They observed a transition from steady to periodic flow occurring for a Reynolds number  $Re = 5060$ . The periodic regime revealed the presence of a travelling wave on top of the Dean vortices.

Without the small curvature approximation, Hüttl & Friedrich (2001) presented direct numerical simulations (DNS) of the flow inside portions of toroidal and helical pipes with curvatures of 0.01 and 0.1. The computations were performed with a finite volume code and periodic boundary conditions were applied at the end sections. Their paper focuses mainly on the reduction of turbulence intensity due to the curvature, and does not present quantitative comparisons with the experiments by Sreenivasan & Strykowski (1983); Webster & Humphrey (1997), which are in a similar range of Reynolds numbers. Noorani *et al.* (2013) reproduced the results for low curvature, confirming their validity, and provided the first turbulence budgets for bent pipes.

Di Piazza & Ciofalo (2011) simulated the flow in the entirety of a torus, with another finite volume code. This is, to the best of our knowledge, the first work aimed at understanding the cause of instability of this flow. Two values of curvature were investigated (0.1 and 0.3) and both showed a transition from stationary to periodic, quasi-periodic and then chaotic flow. However, as indicated by Kühnen *et al.* (2015) and as will be shown herein, these results should be considered inaccurate, with the exception of the symmetry characteristics observed in the flow. The only experiments employing toroidal pipes are those by Kühnen *et al.* (2014, 2015). These authors sacrificed the  $2\pi$  (streamwise) periodicity and the mirror symmetry of the system by introducing a steel sphere in the tube to drive the fluid. This resulted, as mentioned in their first paper, in a non symmetric mean flow and the absence of any considerations on the symmetry characteristics of the periodic flow. Their results for  $0.028 < \delta < 0.1$  confirmed the findings of Webster & Humphrey (1993), *i.e.* that the first instability leads the flow to a periodic regime, while for  $\delta < 0.028$  subcritical transition was observed, as in Sreenivasan & Strykowski (1983). With the exception of these papers focusing on the low curvature limit, no complete stability analysis for this flow is available in the literature.

The present analysis is conducted in a toroidal pipe in order to isolate the effect of the curvature from that of the torsion of a helix as well as that of inflow and outflow sections. A straight pipe is characterised by a central symmetry through its axis. Bending the pipe breaks this symmetry and leaves the system with a discrete reflectional symmetry about the equatorial plane of the torus. Bending the pipe further into an helical one breaks this symmetry as

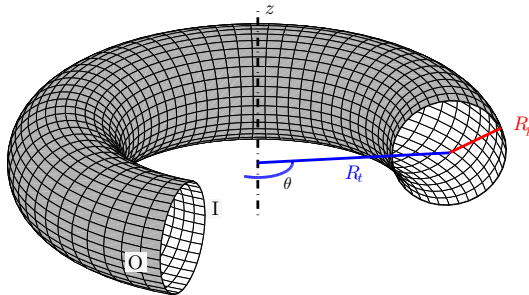


Figure 1: Sketch of the torus showing the definition of the curvature  $\delta = R_p/R_t$ . The “I” and “O” labels indicate the inner, resp. outer, portions of the pipe;  $z$  is the axis of the torus. The pipe is cut for illustrative purposes only.

well. Thus, although moderate curvature or torsion may not significantly affect global quantities, such as the pressure drop between inlet and outlet, these deformations structurally modify the geometry of the flow. The paper continues with a description of the approach employed, presented in §2, while the base flow and its characteristics are described in §3. Section 4 presents the results of the linear analysis which are then compared to the nonlinear behaviour in §5 and finally discussed and compared to the literature in §6.

## 2. Numerical setup

The fluid inside the torus is considered viscous and incompressible and therefore satisfies the incompressible Navier–Stokes equations

$$\frac{\partial \mathbf{u}}{\partial t} + (\mathbf{u} \cdot \nabla) \mathbf{u} - \frac{1}{Re} \nabla^2 \mathbf{u} + \nabla p = \mathbf{f}, \quad (1a)$$

$$\nabla \cdot \mathbf{u} = 0, \quad (1b)$$

where  $\mathbf{u}(\mathbf{r}, t)$  is the velocity vector, with components  $\mathbf{u} = (u_r, u_\theta, u_z)$  in cylindrical coordinates,  $p$  is the (dimensionless) pressure which has been rescaled by dividing by the Reynolds number  $Re$ , and  $\mathbf{f}$  represents a volume force. The Reynolds number is based on the diameter of the pipe and the bulk velocity, i.e.  $Re = 2R_p U_b / \nu$ .

The steady solutions and the stability results presented in this paper have been computed with **PaStA**, an in-house developed software package. **PaStA** is a Fortran90 code, written in primitive variables and based on the finite element method (FEM) employing triangular  $\mathbb{P}_2 - \mathbb{P}_1$  elements; it relies on the **MUMPS** library (Amestoy *et al.* 2000) for the solution of linear systems (for details, see Canton 2013). The time-dependent simulations, on the other hand, have been performed by means of the spectral element code **nek5000** (Fischer *et al.* 2008). Convergence and accuracy tests have been performed to a more than satisfactory degree by comparing results to reference ones, whenever possible,

or by comparing the two codes when results were new. These tests are omitted from this article for conciseness; some can be found in Canton (2013); Nooran *et al.* (2013). However, we demonstrate excellent agreement between the linear analysis and the nonlinear direct numerical simulations performed with two different codes, employing two different methods, in §5.

The stability of the flow is studied in a classical framework: as a first step, a fixed point for the system, *i.e.* a steady solution to (1), is computed with the nonlinear solver, which employs Newton's method. Subsequently, its stability properties are investigated by linearising the system about this steady state, and computing the leading eigenvalues of the linearised Navier–Stokes operator,  $\mathcal{L}$ . By employing an expansion in normal modes, the perturbation fields are defined as

$$\mathbf{u}'(r, \theta, z, t) = \hat{\mathbf{u}}(r, z) \exp i(k\theta - \omega t), \quad p'(r, \theta, z, t) = \hat{p}(r, z) \exp i(k\theta - \omega t), \quad (2)$$

where  $k \in \mathbb{R}$  is the streamwise wave number,  $\omega = \omega_r + i\omega_i \in \mathbb{C}$  is the eigenvalue and  $\hat{\mathbf{u}} \in [\mathbb{C}]_2^3$  and  $\hat{p} \in [\mathbb{C}]_2$  form the eigenfunction  $\hat{\mathbf{x}} = (\hat{\mathbf{u}}, \hat{p})$ . Note that here, and in the following, the symbols  $[\mathbb{A}]_d^c$  are used to denote a  $c$ -dimensional vector space  $\mathbb{A}$  in a  $d$ -dimensional physical space; it is clear that when  $c$  is omitted  $\mathbb{A}$  represents a scalar space. Although  $k$  is in principle a real number, the  $2\pi$ -periodicity of the torus restricts it to  $\mathbb{Z}$ .

The linearised Navier–Stokes equations, discretised via the finite element method, are thus reduced to a generalised eigenvalue problem of the form

$$i\omega M \hat{\mathbf{x}} = L_k \hat{\mathbf{x}}, \quad (3)$$

where  $\hat{\mathbf{x}}$  is the discretised eigenvector,  $M \in \mathbb{R}^{\text{dof} \times \text{dof}}$  is the (singular) generalised mass matrix,  $L_k \in \mathbb{C}^{\text{dof} \times \text{dof}}$  represents the discretisation of the linearised Navier–Stokes operator  $\mathcal{L}$ , parametrised by the streamwise wave number  $k$ . Finally, ‘dof’ is a shorthand for the total number of degrees of freedom, the number of unknowns of the problem, which accounts for both velocity and pressure, *i.e.*  $\text{dof} = c(\mathbb{P}_2 \text{ nodes}) + (\mathbb{P}_1 \text{ nodes})$ . The eigensolutions are computed to machine precision through an interface to the ARPACK library (Lehoucq *et al.* 1998), where the shift-invert spectral transformation is used to accelerate convergence to the desired portion of the spectrum. The eigenmodes determine whether the fixed point is stable or not, to locate the non-hyperbolic points of the system and, in the event of a bifurcation point, to determine the type of the bifurcation.

Once a bifurcation is identified and its type determined, its neutral curve can be traced in parameter space, separating the stable and unstable regions. In order to track a bifurcation, an augmented set of equations describing the system at the bifurcation point, *i.e.* where the critical eigenvalue has zero growth rate, needs to be solved. Equation (4) presents this system in the case of a Hopf bifurcation, which is the type of bifurcation encountered by this flow,

$$N\mathbf{x} = 0, \quad (4a)$$

$$i\omega_r M \hat{\mathbf{x}} = L_k \hat{\mathbf{x}}, \quad (4b)$$

$$\phi \cdot \hat{\mathbf{x}} = 1, \quad (4c)$$

where  $N = N(Re, \delta, x) \in \mathbb{R}^{\text{dof} \times \text{dof}}$ ,  $M = M(\delta) \in \mathbb{R}^{\text{dof} \times \text{dof}}$ , and  $L_k = L_k(Re, \delta, x) \in \mathbb{C}^{\text{dof} \times \text{dof}}$ . The unknowns for this system are: the base flow, *i.e.* the steady solution to (1), comprising both velocity and pressure,  $x = (u, p) \in \mathbb{R}^{\text{dof}}$ ; the frequency of the critical eigenmode,  $\omega_r \in \mathbb{R}$ , and the corresponding eigenvector,  $\hat{x} = (\hat{u}, \hat{p}) \in \mathbb{C}^{\text{dof}}$ . The pair  $Re, \delta \in \mathbb{R}$  can act as unknown/parameter or, vice versa, as parameter/unknown, where one is fixed while the other is obtained as part of the solution. Equation (4a) is a real equation which determines the base flow:  $N$  constitutes the discretised steady state Navier–Stokes equations, *i.e.* it is shorthand for a steady solution to (1). This is the nonlinear equation that is solved when computing a steady state, regardless of whether it is on the neutral curve or not. Equation (4b) is a complex equation which represents the eigenvalue problem (3) in the particular case where a pair of complex conjugate eigenvalues has zero growth rate. This equation forces the solution of the system to be on the neutral curve. Equation (4c) is a complex equation as well, it fixes the phase and amplitude of the eigenvector. The constant vector  $\phi$  is chosen as the real part of the initial guess for  $\hat{x}$ , so that this linear equation mimics an  $L^2$  norm.

Newton's method is employed for this large nonlinear system as well. In contrast with the standard procedure, though, the full Jacobian matrix for (4) is not assembled, as its size would be  $3\text{dof} + 2 \times 3\text{dof} + 2$ , and its sparsity pattern would need to be created. Instead, a block Gauss factorisation and linear algebra are used to split the resulting system into five  $\text{dof} \times \text{dof}$  linear systems, two real and three complex. Beside reducing memory requirements, these systems have matrices with the same sparsity pattern as those already used for the solution of the steady state and the eigenvalue problem. The method is similar to those presented in Salinger *et al.* (2002), but here the Jacobian matrix for the steady state is not equivalent to the linearised Navier–Stokes operator  $L_k$ . The tolerance for the iterative solution of (4) was chosen as to have an uncertainty of  $Re$  on the neutral curve of  $\pm 10^{-4}\%$  on a mesh with 98870 elements, corresponding to  $\text{dof} = 646327$ .

### 3. Base flow

The fluid, flowing inside the pipe at constant mass rate, is maintained in motion by a volume force aligned with the centreline of the torus and defined as  $\mathbf{f} = e_\theta F/r$ . Here  $F$  is a scalar constant and  $r$  represents the distance from the axis of the torus. The inverse proportionality to  $r$  is required so that the integral of  $\mathbf{f}$  along the curvilinear coordinate  $s = r\theta$  is independent of  $r$ , *i.e.*  $\int \mathbf{f} \cdot d\mathbf{s} = \int \frac{F}{r} r e_\theta \cdot d\theta = F(\theta - \theta_0) \forall r$ . This property confers on  $\mathbf{f}$  a role similar to that of the pressure in straight pipes (or channels) and it ensures continuity with a straight pipe for a torus in the limit of vanishing curvature. In fact, when  $\delta \rightarrow 0$ ,  $r \rightarrow \infty$  on the section of the toroidal pipe, then  $\mathbf{f}$  tends to a value which is uniform on the section of the pipe, as the pressure in a straight pipe. The value of  $F$  is determined via the secant method such as to have unitary bulk velocity. This cannot be done analytically since the relationship between  $\mathbf{f}$  and  $U_b$  is nonlinear and *a priori* unknown (see Ito 1959).

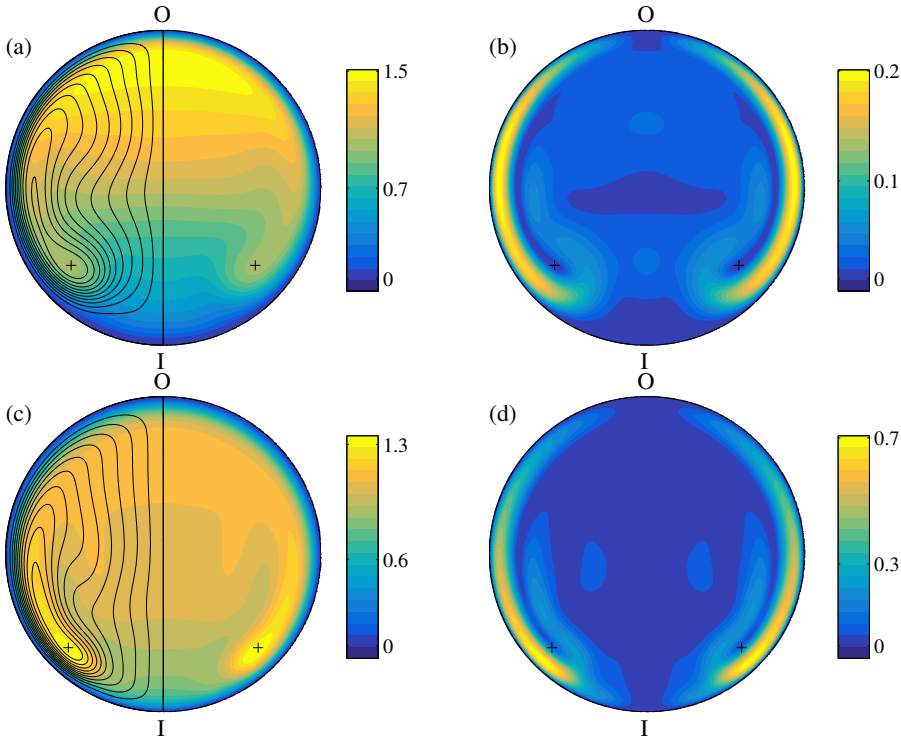


Figure 2: Steady state solutions for  $De = 759$  at different curvatures and Reynolds number:  $\delta = 0.1$ ,  $Re = 2400$  (a,b),  $\delta = 0.9$ ,  $Re = 800$  (c,d). Panels (a) and (c) depict the magnitude of the streamwise velocity component  $u_\theta$ , and contours of the in-plane streamfunction  $\psi$  for positive values; the plus symbols are located at the position of the maximum and minimum of  $\psi$ . Panels (b) and (d) show the magnitude of the in-plane velocity. Quantities are normalised with the bulk velocity. The “I/O” labels indicate the inner and outer portions of the pipe (see figure 1).

The steady state solution inherits both the rotational invariance and the mirror symmetry of the toroidal geometry and it is thus independent of  $\theta$  and symmetric with respect to the equatorial plane of the torus. Beside being evident from geometrical considerations, this has been confirmed by three-dimensional DNSs performed for values of  $\delta$  and  $Re$  below criticality. The invariance with respect to  $\theta$  allows the solutions to be computed on a two-dimensional section (retaining three velocity components), sensibly reducing the computational cost.

The base flow is characterized by the presence of two symmetric, counter-rotating Dean vortices. The side with the counterclockwise rotating vortex is visible in the contours of the streamfunction in figure 2a,c, and the centres of the

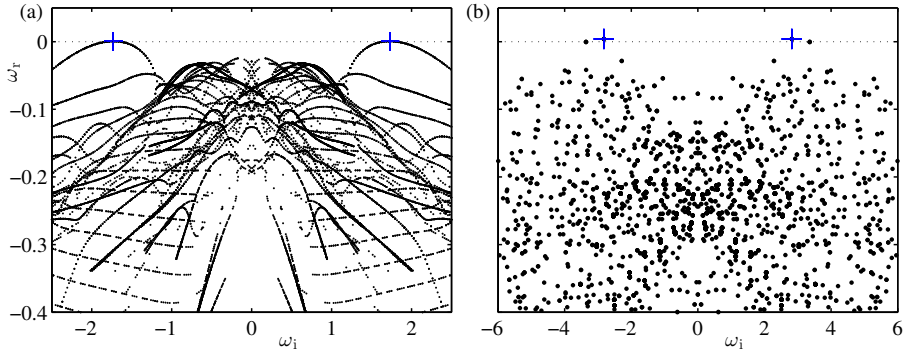


Figure 3: Eigenvalue spectra for the flow in a toroidal pipe. Panel (a) presents the spectrum for  $\delta = 0.01$ ,  $Re = 4300$ , corresponding to  $De = 430$ , while (b) is for  $\delta = 0.3$ ,  $Re = 3400$ , corresponding to  $De \approx 1862$ . Both cases are moderately above criticality: the flow for  $\delta = 0.01$  becomes unstable for  $Re > 4257$ , while for  $\delta = 0.3$   $Re_c = 3379$ . The least stable eigenvalues are highlighted with plus symbols. The wavenumber of the critical mode for  $\delta = 0.01$  is 74, while for  $\delta = 0.3$   $k = 7$ . The corresponding eigenvectors are depicted in figure 4. Notice the striking difference in the structure of the spectra.

vortices are indicated with plus symbols. These vortices develop as a result of the centrifugal force arising from breaking the central symmetry characterising a straight pipe and are thus present at *every* Reynolds number and for *any* non-zero curvature. The question of a critical Dean number below which no recirculation occurs has been discussed in textbooks (see, for instance Isachenko *et al.* 1974, p. 218). However, even for  $\delta = 10^{-11}$ ,  $Re = 1$ , corresponding to  $De = Re\sqrt{\delta} \approx 3 \times 10^{-6}$ , the vortices are present, albeit exhibiting low intensity; their presence for any non-zero curvature can also be shown analytically, cf. Dean (1927).

As can be observed in figure 2, which depicts two steady states for the same Dean number,  $De = 759$ , the curvature of the torus plays a primary role in determining the behaviour of the base flow, starting at least from  $\delta = 0.1$ . It greatly influences, among other features, the shape of the vortices, the position of the maximum velocity and the magnitude of the in-plane flow. An example can be observed in figure 2: the maximum of  $u_\theta$  moves from the outer portion of the pipe for low curvature, figure 2a, to the centre of the vortices, 2c, for high curvature. Moreover, as discussed in the next section, the curvature is of primary importance for the characteristics of the first instability. We thus observe that the curvature of the pipe should be considered as a separate parameter with as much importance as the Reynolds number and that the Dean number alone is insufficient to describe the flow fully.

#### 4. Stability analysis

The first step of the stability analysis was the computation of eigenvalue spectra on a coarse grid of points in parameter space,  $(\delta, Re) \in ([0.005, 1], [500, 10^4])$ . All curvatures in the grid revealed spectra with unstable eigenvalues for  $Re < 6 \times 10^3$ . This result confirms the numerical observations by Di Piazza & Ciofalo (2011) as well as the experiments by Kühnen *et al.* (2014, 2015) and extends these studies, which are limited to the low curvature range. Most importantly, it proves that this flow is linearly unstable, in obvious contrast to the flow inside a straight pipe (see Schmid & Henningson 1994, and citations therein). Each spectrum in the grid exhibits a pair of complex conjugate eigenvalues as most unstable mode, indicating that the cause of the modal instability is a supercritical Hopf bifurcation. In fact, DNSs confirm that the flow transitions from a steady state to a periodic state, characteristic of the stable limit cycle identified by this bifurcation. For a thorough discussion, see §5.

Figure 3 presents, as examples, two supercritical eigenvalue spectra. These are for very low and moderate curvature,  $\delta = 0.01$  and  $0.3$  respectively, and each has a complex conjugate eigenpair with positive growth rate. Although the instability is caused by a Hopf bifurcation for every curvature, the associated critical mode changes with the curvature of the pipe. This can be seen in figure 4, which shows the different spatial structure of the two critical modes presented in figure 3. The eigenmodes differ in their wave numbers, temporal frequencies, spatial structure, and symmetry properties. Figure 3 demonstrates a striking difference in the structure of the two spectra and the variation of the frequency of the critical mode. The set of spectra computed on the grid revealed a non-monotonic relationship between critical Reynolds number and curvature; even the variation of eigenmode characteristics, e.g. wavenumber, as a function of  $(\delta, Re)$  does not have a continuous trend. It is clear that a detailed analysis of the whole parameter space cannot be performed employing a coarse grid of points and interpolation between them.

Employing the method described in §2, the neutral curve of every critical mode has thus been traced in the parameter space as a function of curvature and Reynolds number. The result is a complex picture, depicted in figure 5. It presents five “families” and three “isolated” modes; their envelope constitutes the global neutral curve for the flow. All eigenmodes on this curve share the characteristic of representing a travelling wave, while all the other properties are modified along the neutral curve. As anticipated in §3, the curvature of the pipe plays a key role in determining the identity of the critical mode and its characteristics. The neutral curves cannot, in fact, be collapsed onto one another as a function of a single non-dimensional parameter, thereby confirming the need for two parameters ( $\delta$  and  $Re$ ) to describe this flow.

A “family” comprises eigenmodes that share common characteristics, while the eigenvalues designated as “isolated” are those which contribute to the global neutral curve while being dissimilar to the modes belonging to the neighbouring neutral curves. In more detail, all modes belonging to a given family display the

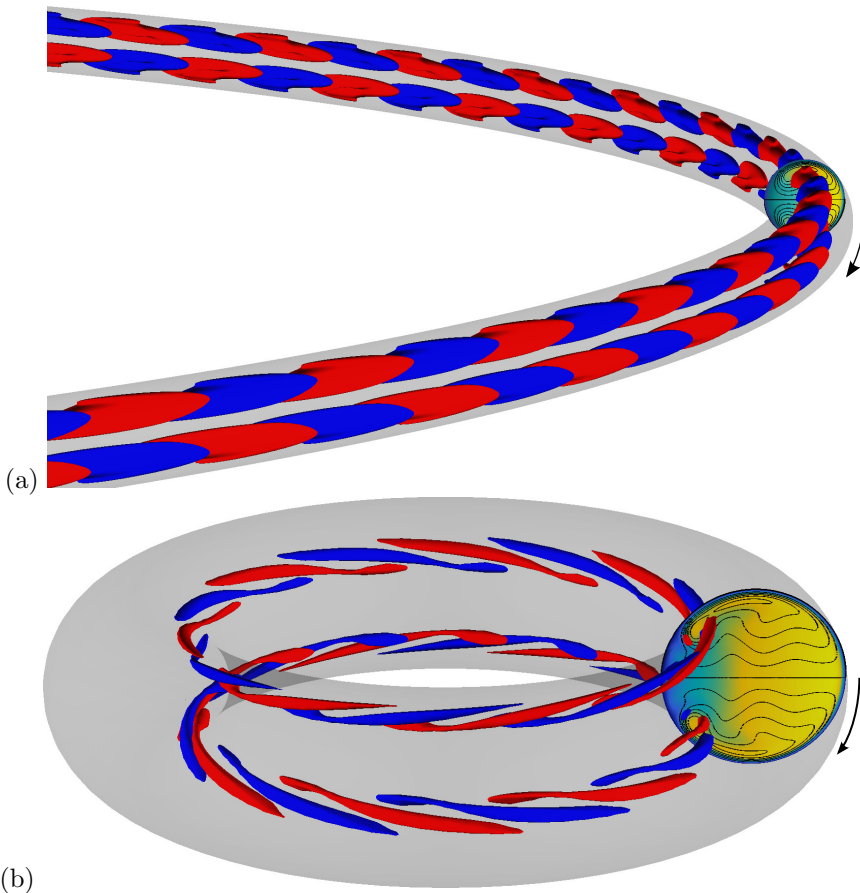


Figure 4: Critical modes for  $\delta = 0.01$ ,  $Re = 4257$  (a) and  $\delta = 0.3$ ,  $Re = 3379$  (b). Both modes are antisymmetric with respect to the equatorial plane of the torus. The wavenumbers are  $k = 74$  and  $k = 7$  respectively. Isocontours of opposite values of the streamwise velocity component are depicted in blue and red,  $u_\theta = \pm 0.15$  in (a) and  $u_\theta = \pm 2.2$  in (b). The vertical cuts depict the streamwise velocity and in-plane streamlines of the corresponding base flow. The fluid is flowing clockwise, as indicated by the arrows.

same spatial structure and symmetry properties, they have approximately equal phase speed and comparable wavelength. In addition, while the wavenumber does not vary monotonically along the envelope of neutral curves, it does so inside families. Furthermore, eigenvalues in the same family lie on the same branch. This is very clear for low curvatures: in figure 3a the two uppermost branches comprise eigenvalues belonging to the same family, the same holds for the two, nearly straight-line, branches just below them, and so on. Possibly

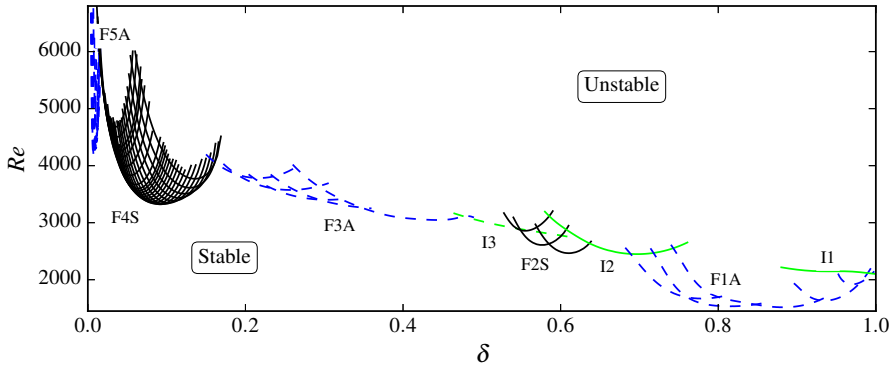


Figure 5: Neutral curve in the  $\delta - Re$  plane.  $\delta \in [0.002, 1]$ . Each line corresponds to the neutral curve of one mode. The neutral curve for the flow is formed by the envelope of the lines. Five families (black and blue) and three isolated modes (green) are marked by labels. Symmetric modes are indicated with continuous lines while antisymmetric modes are represented with dashed lines. Note that the curves are not interpolated, *i.e.* they are segments connecting computed solutions with  $\Delta\delta = \mathcal{O}(10^{-3})$ . The uncertainty on the Reynolds number is  $\pm 10^{-4}\%$ .

even more characteristic is the fact that the eigenmodes forming a family have neutral curves with a very similar trend  $(\delta, Re(\delta))$ . This can readily be observed in figure 5 where each neutral curve is purposely plotted beyond the envelope line to illustrate this feature.

#### 4.1. Description of the neutral curve

As previously mentioned, all neutral curves in figure 5 are traced beyond the point(s) where they leave the envelope for the sole purpose of illustrating their shape. For example, I1 is traced up to  $\delta = 0.9$ , but it stops being relevant for the instability boundary for  $\delta < 0.99$ , where the rightmost curve of F1A has lower  $Re$  for the same curvatures.

Starting at unit curvature, the first contribution to the envelope of neutral curves is given by an isolated mode: the rightmost continuous line in figure 5, labelled I1. I1 represents a singular case for  $0.99 < \delta \leq 1$ : this is the only range of curvature values that has a critical mode with zero spatial wavenumber. This is, in fact, the only eigenmode with a stationary, symmetric structure pulsating at non-zero temporal frequency. This peculiar property is the effect of the singular geometrical condition approached by the pipe when  $\delta$  nears unity, namely that of a ring torus with no “hole”: a *horn* torus. For  $\delta \leq 0.99$  all critical modes are characterised by non-zero wave number. More specifically,  $k$  increases monotonically as the curvature is lowered, but only between modes

belonging to the same family; it has, however, discontinuities across different families.

A first family of eigenmodes (F1A in figure 5) appears at high curvature and relatively low Reynolds number. These modes are antisymmetric with respect to the equatorial plane of the torus and are characterised by  $4 \leq k \leq 8$  and particularly high phase speed (cf. figure 6). To the left of this family, for  $0.64 \leq \delta < 0.69$ , a second isolated mode appears. This eigensolution has  $k = 6$  and has a symmetric spatial structure dissimilar to that of the two neighbouring families. In spite of these differences, this mode is also characterised by moderately high phase speed, somewhat similar to F1A.

The reason for the high phase speed of the modes at high curvature is probably due to a modification in the base flow. In fact, for  $\delta > \delta_s \approx 0.6$  (the exact value depends on the Reynolds number) the maximum of streamwise velocity moves from the outer portion of the torus to the inner portion. The steady solutions depicted in figure 2 provide a clear example of this phenomenon. This shift causes a qualitative as well as quantitative change in the structure of the base flow which has, for  $\delta > \delta_s$ , two symmetric maxima in the velocity field, located close to the cores of the Dean vortices. Both F1A and I2 comprise eigenvectors with a structure located very close to the Dean vortices. The oscillations that these modes produce in the flow are thus rapidly transported inside the pipe, giving rise to high frequency fluctuations. At medium curvature, for  $0.54 \leq \delta < 0.64$ , the instability is caused by a second family of symmetric modes, F2S. These modes, with  $4 \leq k \leq 6$ , are still located close to the Dean vortices but have moderate phase speed. The third isolated mode, on the other hand, is antisymmetric, has  $k = 4$  and high phase speed, and is critical for  $0.48 \leq \delta < 0.54$ .

The third family, F3A, is responsible for the onset of the instability for  $0.16 < \delta < 0.48$ . Even at this moderately low curvature the wave number associated with the eigenmodes grows slowly, ranging from six to ten in this family of antisymmetric modes. Both frequency and phase speed decrease as the curvature is lowered, with the phase speed reaching its lowest value of 0.57 for  $\delta = 0.16$ . The Reynolds number, on the other hand, varies non-monotonically from 3112 to 4059. As an example, the critical mode for  $\delta = 0.3$  is depicted in figure 4b, and the corresponding spectrum is in figure 3b. Di Piazza & Ciofalo (2011) performed numerical simulations for  $\delta = 0.3$  that confirm the transition of the flow to a periodic regime exhibiting an anti-symmetric, varicose travelling wave. However, their result indicates the stability of the steady state up to  $Re \approx 4575$ , a value 35% higher than ours, and the appearance of a travelling wave with  $k = 8$ , in contrast to the present  $k = 7$ .

Low curvatures are characterised by more organised eigenvalue spectra with isolated and ordered branches of modes (cf. figure 3). This feature is visible in figure 5 as well: the two leftmost families, F4S and F4A, are in fact more populated and continuous than the other ones. A further difference between low and high  $\delta$  is that low-curvature eigenmodes show a spatial structure located

towards the centre of the pipe, not close to the Dean vortices as observed for higher curvatures. This change in the structure of the modes, and the corresponding eigenspectra, is not surprising. In fact,  $\delta$  is nearing its lower limit, and the torus is tending towards a straight pipe.

Family F4S has symmetric modes with  $11 \leq k \leq 60$  and is responsible for the instability for  $0.016 \leq \delta \leq 0.16$ . The eigenvalues belonging to this family can be observed in figure 3a, where they form the branches just below the critical ones. This family was the one found by Kühnen *et al.* (2015), in the range  $0.026 \leq \delta \leq 0.1$ . It appears, from this experimental investigation, that F4S constitutes the instability boundary not only for toroidal pipes, but for low pitch helical pipes as well. Di Piazza & Ciofalo (2011) presented a second set of data for  $\delta = 0.1$ . For this curvature, though, they found steady states up to  $Re = 5139$ , a value 54% higher than the present  $Re_c = 3331$ . Moreover they observed an hysteresis in the value of the Reynolds number separating the steady and periodic regimes. This observation is inconsistent with both the experimental results of Kühnen *et al.* (2015), and the numerical data presented here.

Our data presents one last family of modes below  $\delta = 0.016$ : F5A, constituted by antisymmetric eigenmodes. One of these eigenmodes is depicted in figure 4a and the eigenvalues belonging to F5A constitute the most unstable branches in figure 3a. The wave number associated with these modes grows rapidly from  $k = 55$  to  $k = 95$ , where our neutral curves stop, but the computed eigenvalue spectra indicate that eigenvalues with  $k > 200$  belong to this family. As it will be shown in §6, however, this range of curvatures has subcritical transition at lower Reynolds numbers.

Figure 6 shows the envelopes of wavelength,  $\lambda = 2\pi R_t/k$ , and phase speed,  $v_p = \omega_r R_t/k$ , along the neutral curve, two characteristic quantities associated to the modes. Both quantities show the separation between families and isolated modes and illustrate the complexity of the neutral curve for this flow. The wavelength displays a steep increase for very low curvatures. The modes belonging to F5A, in fact, are characterised by a wavelength tending towards infinity for  $\delta \rightarrow 0$  (the upper limit is cut out from the figure). This feature can be related to the characteristics of a straight pipe, which has structures with no streamwise dependence as the most amplified linear transient disturbances (Schmid & Henningson 1994). The phase speed shows that for low curvatures the travelling waves are advected with, approximately, the average velocity of the flow in the pipe. When  $\delta$  is increased, on the other hand, the speed of the eigenmodes increases as well, reaching up to four times the value of the average velocity of the base flow. It is worth noting that the discontinuities located inside the families are inherent to the geometry. The wavenumber is, in fact, restricted to assume integer values by the  $2\pi$ -periodicity of the torus. The curves would otherwise be continuous, except at the boundaries between families.

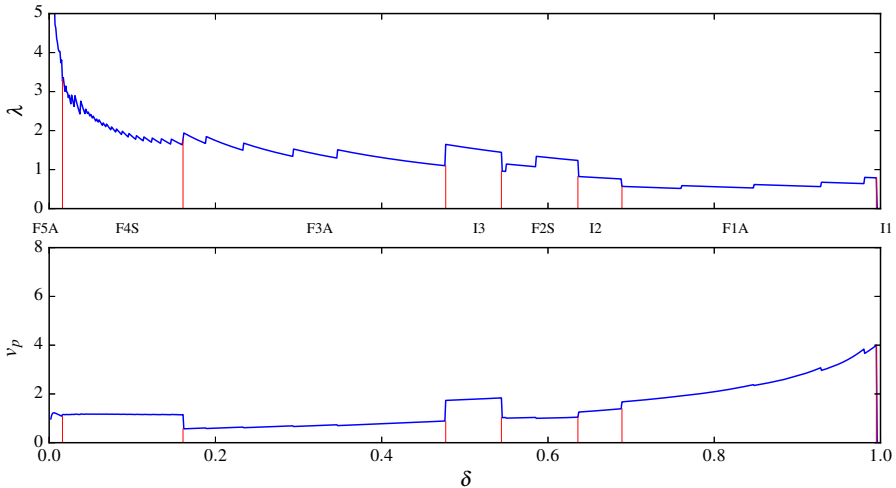


Figure 6: Envelopes of wavelength  $\lambda$ , and phase speed  $v_p$ , of the critical modes along the neutral curve. The boundaries between families and isolated modes are highlighted by thin vertical (red) lines. Both quantities are scaled with pipe diameter and bulk velocity.

## 5. Comparison with the nonlinear behaviour

Nonlinear direct numerical simulations (DNS) have been performed to confirm the results of the linear stability analysis. The values of  $\delta$  and  $Re$  of these simulations are reported in table 1. A randomly perturbed Poiseuille profile was used as the initial condition for all simulations. Each value of curvature investigated has a transition from a steady to a periodic regime, confirming the presence of an Hopf bifurcation. Figure 7 confirms it by depicting the amplitude of saturated flow oscillations as a function of  $Re$ ; the result is  $A \propto \sqrt{Re - Re_c}$ , characteristic of a Hopf bifurcation (Guckenheimer & Holmes 1983). Amongst others, the most relevant quantities used for the comparison are: the critical Reynolds number, the wavenumber of the travelling wave, its symmetry properties, growth rate and temporal frequency. The simulations show excellent agreement with the results of the linear analysis, confirming all properties related to the critical modes. While quantities like the wavenumber, symmetry, growth rate and temporal frequency could be measured directly, the critical Reynolds number needed to be derived from the other quantities. To do so, the amplitude of the oscillating flow has been measured in simulations across the neutral curve. The envelopes of these oscillations have then been extracted from the time intervals where the signals exhibited exponentially growing, resp. decaying behaviour (depending on  $Re$ , of course). The time-averaged growth rate and the Reynolds numbers of the two simulations have

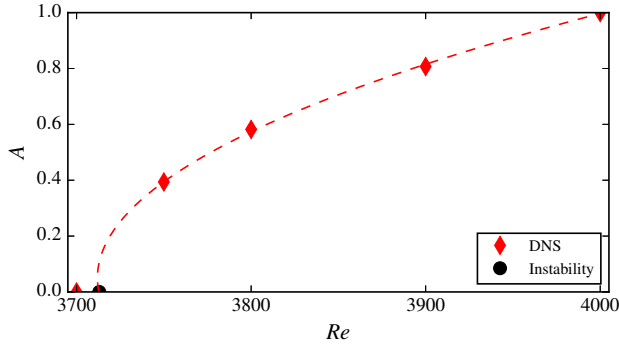


Figure 7: Saturation amplitude,  $A$ , measured as a function of Reynolds number for curvature  $\delta = 0.05$ . The critical Reynolds number is  $Re_c = 3713$ . The round (black) marker corresponds to the critical  $Re$  computed through the linear stability analysis. The dashed line represents a second-order polynomial fit to the DNS data; its intercept with the horizontal axis was computed by linearly interpolating the growth rate, resp. decay, of the oscillations measured in the simulations for  $Re = 3750$ , resp.  $Re = 3700$ .

$\delta$	$Re$	$\delta$	$Re$
0.05	3700, 3750, 3800, 3900, 4000	0.6	2520, 3000
0.1	3202, 3350	0.7	2860, 3000
0.3	3000, 3480, 4500, 4899	0.9	2000
0.5	3500		

Table 1: Values of curvature and Reynolds number at which direct numerical simulations were performed. All DNSs were performed in a full, three-dimensional torus.

then been employed in a two-point, linear interpolation to estimate the Reynolds number corresponding to zero growth rate for the nonlinear flow. An example of this procedure is shown in figure 7 for  $\delta = 0.05$ . For this curvature the interpolation between the DNSs for  $Re = 3700$  and  $3750$  gives  $Re_c \approx 3713.2$ , the linear analysis predicts a critical Reynolds number  $Re_c = 3713.36$ . All other quantities compared between nonlinear DNS and the linear analysis are affected by differences of the same order of magnitude.

## 6. Discussion and conclusions

The present results are compared to the literature in figure 8 (in the range where previous data are available). It can be noted that, in spite of the different methods employed, all previous works indicate subcritical transition for

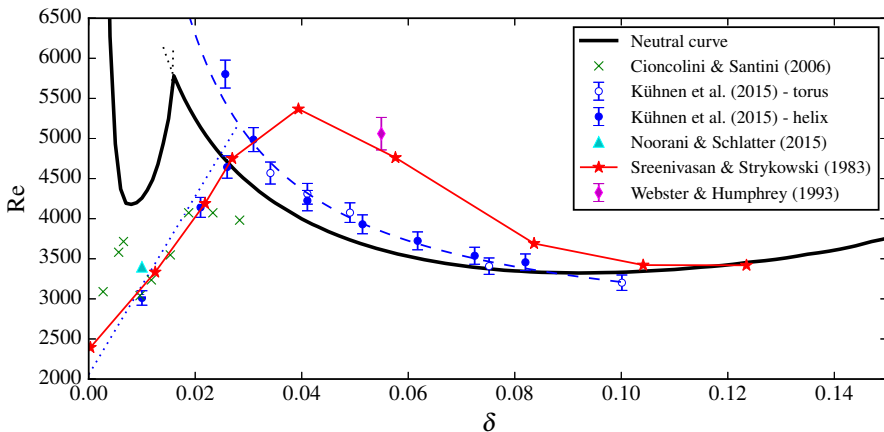


Figure 8: Comparison of the neutral curve with experimental and numerical data from the literature. The continuous (black) line represent the envelope of families F4S and F5A (the intersection is at  $\delta = 0.016$ , where the two dotted lines highlight the continuation of the two families). The data by Cioncolini & Santini (2006) refers to the first discontinuity in their friction measurements, while the reported data by Sreenivasan & Strykowski (1983) is the curve they refer to as the “conservative lower critical limit”, and that by Noorani & Schlatter (2015) is for sublaminar friction drag. The interpolants provided by Kühnen *et al.* (2015) are also depicted: with a dashed (blue) line the fit for the supercritical transition and with a dotted (blue) line the fit for subcritical transition. All results agree on subcritical transition for very low curvature, with the data by Kühnen *et al.* (2015) falling on top of that by Sreenivasan & Strykowski (1983).

curvatures below 0.02–0.04. This phenomenon was expected since  $\delta$  is nearing its lower limit and the effect that the centrifugal force has on the flow becomes less relevant. Moreover, the diameter of the torus is so large in comparison to that of the pipe that the feedback-like mechanism caused by the  $2\pi$ -periodicity in the streamwise direction becomes almost irrelevant to the flow.

Higher curvatures, on the other hand, present a different picture. Both Sreenivasan & Strykowski (1983) and Kühnen *et al.* (2015) appear to have identified family F4S. The former selected the appearance of the first ‘bursts’ near the outer wall as a definition for the critical Reynolds number. This explains the higher estimate of  $Re$  where supercritical transition occurs, but also answers their question on the cause behind the non-monotonic behaviour of their data: the switch from subcritical to supercritical transition. Kühnen and co-workers, on the other hand, aware of the supercritical transition identified by Webster & Humphrey (1993); Di Piazza & Ciofalo (2011), report the Reynolds number corresponding to the onset of the periodic state. These measurements are in

fair agreement with F4S. They confirm the relevance of the linear instability and that the first instability is caused by a Hopf bifurcation. The discrepancy in Reynolds number, and the trend of their interpolant may well be due to an optimistic estimate of the accuracy of their measurements, as well as the absence of data at higher curvatures. In fact, the DNS performed at the rightmost point of their dataset,  $\delta = 0.1$ ,  $Re = 3202$ , confirms the absence of oscillations.

In conclusion, the toroidal geometry allows the isolation of the effect that  $\delta$  has on the first instability. It will now be possible to separate these effects from others when investigating differently curved pipes. Results show that a very little curvature is sufficient to make this flow linearly unstable via a Hopf bifurcation that leads the flow to a periodic regime. The neutral curve associated with this bifurcation has been traced in parameter space exploring, for the first time, the whole range of possible curvatures. The Reynolds number and the wavelength of the critical modes diverge when approaching  $\delta = 0$ , suggesting a continuous transition to the straight pipe, which has modes with high  $\lambda$ , *i.e.* quasi-streamwise independent, as the least stable ones.

Financial support by the Swedish Research Council (VR) is gratefully acknowledged. Computer time was provided by the Swedish National Infrastructure for Computing (SNIC).

## REFERENCES

- AMESTOY, R., DUFF, I. & L'EXCELLENT, J.-Y. 2000 Multifrontal parallel distributed symmetric and unsymmetric solvers. *Comput. Methods Appl. Math.* **184**, 501–520.
- BERGER, S. A., TALBOT, L. & YAO, L. S. 1983 Flow in curved pipes. *Annu. Rev. Fluid Mech.* **15**, 461–512.
- BOUSSINESQ, M. J. 1868 Mémoire sur l'influence des frottements dans les mouvements réguliers des fluides. *J. Math. Pure Appl.* **13**, 377–424.
- BULUSU, K. V., HUSSAIN, S. & PLESNIAK, M. W. 2014 Determination of secondary flow morphologies by wavelet analysis in a curved artery model with physiological inflow. *Exp. Fluids* **55**, 1832.
- CANTON, J. 2013 Global linear stability of axisymmetric coaxial jets. Master's thesis, Politecnico di Milano, Italy, <https://www.politesi.polimi.it/handle/10589/87827>.
- CIONCOLINI, A. & SANTINI, L. 2006 An experimental investigation regarding the laminar to turbulent flow transition in helically coiled pipes. *Exp. Therm. Fluid Sci.* **30**, 367–380.
- DEAN, W. R. 1927 XVI. Note on the motion of fluid in a curved pipe. *London, Edinburgh, Dublin Philos. Mag. J. Sci.* **4**, 208–223.
- DENNIS, S. C. R. 1980 Calculation of the steady flow through a curved tube using a new finite-difference method. *J. Fluid Mech.* **99**, 449–467.
- EUSTICE, J. 1910 Flow of water in curved pipes. *Proc. R. Soc. London, Ser. A* **84**, 107–118.
- FISCHER, P. F., LOTTES, J. W. & KERKEMEIR, S. G. 2008 Nek5000 Web page.
- GUCKENHEIMER, J. & HOLMES, P. 1983 *Nonlinear Oscillations, Dynamical Systems, and Bifurcations of Vector Fields*. Springer.

- HÜTTL, T. J. & FRIEDRICH, R. 2001 Direct numerical simulation of turbulent flows in curved and helically coiled pipes. *Computers & fluids* **30**, 591–605.
- ISACHENKO, V., OSIPOVA, V. & SUKOMEL, A. 1974 *Heat Transfer*, 2nd edn. Mir Publishers.
- ITO, H. 1959 Friction factors for turbulent flow in curved pipes. *J. Basic Eng.* **81**, 123–134.
- ITO, H. 1987 Flow in Curved Pipes. *JSME Int. J.* **30** (262), 543–552.
- KÜHNEN, J., BRAUNSHIER, P., SCHWEGEL, M., KUHLMANN, H. C. & HOF, B. 2015 Subcritical versus supercritical transition to turbulence in curved pipes. *J. Fluid Mech.* **770**, R3.
- KÜHNEN, J., HOLZNER, M., HOF, B. & KUHLMANN, H. C. 2014 Experimental investigation of transitional flow in a toroidal pipe. *J. Fluid Mech.* **738**, 463–491.
- LEHOUCQ, R. B., SORENSEN, D. C. & YANG, C. 1998 ARPACK users guide: solution of large-scale eigenvalue problems with implicitly restarted Arnoldi methods.
- MCCONALOGUE, D. J. & SRIVASTAVA, R. S. 1968 Motion of a fluid in a curved tube. *Proc. R. Soc. London Ser. A* **307**, 37–53.
- NOORANI, A., EL KHOURY, G. K. & SCHLATTER, P. 2013 Evolution of turbulence characteristics from straight to curved pipes. *Int. J. Heat Fluid Flow* **41**, 16–26.
- NOORANI, A. & SCHLATTER, P. 2015 Evidence of sublaminar drag naturally occurring in a curved pipe. *Phys. Fluids* **27**, 035105.
- DI PIAZZA, I. & CIOFALO, M. 2011 Transition to turbulence in toroidal pipes. *J. Fluid Mech.* **687**, 72–117.
- SALINGER, A. G., BOU RABEE, N. M., PAWLowski, R. P., WILKES, E. D., BORROUGHS, E. A., LEHOUCQ R. B. & ROMERO, L. A. 2002 LOCA, Library Of Continuation Algorithms: Theory and Implementation Manual.
- SCHMID, P. J. & HENNINSON, D. S. 1994 Optimal energy density growth in Hagen–Poiseuille flow. *J. Fluid Mech.* **277**, 197–225.
- SREENIVASAN, K. R. & STRYKOWSKI, P. J. 1983 Stabilization effects in flow through helically coiled pipes. *Exp. Fluids* **1**, 31–36.
- TAYLOR, G. I. 1929 The criterion for turbulence in curved pipes. *Proc. R. Soc. London Ser. A* **124**, 243–249.
- VAN DYKE, M. 1978 Extended Stokes series: laminar flow through a loosely coiled pipe. *J. Fluid Mech.* **86**, 129–145.
- VASHISTH, S., KUMAR, V. & NIGAM, K. D. P. 2008 A review on the potential applications of curved geometries in process industry. *Ind. Eng. Chem. Res.* **47**, 3291–3337.
- WEBSTER, D. R. & HUMPHREY, J. A. C. 1993 Experimental observations of flow instability in a helical coil (Data bank contribution). *J. Fluid Eng.-T. ASME* **115**, 436–443.
- WEBSTER, D. R. & HUMPHREY, J. A. C. 1997 Travelling wave instability in helical coil flow. *Phys. Fluids* **9**, 407–418.
- WHITE, C. M. 1929 Streamline flow through curved pipes. *Proc. R. Soc. London Ser. A* **123**, 645–663.

# Paper 3

3



# Approaching zero curvature: modal instability in a bent pipe

Jacopo Canton, Enrico Rinaldi, and Philipp Schlatter

Linné FLOW Centre and Swedish e-Science Research Centre (SeRC), KTH Mechanics, Royal Institute of Technology, SE-100 44 Stockholm, Sweden

*Technical report* (2018)

Canton *et al.* [J. Fluid Mech. **792**:894–909 (2016)] showed that the flow in a toroidal pipe is linearly unstable for any pipe curvature  $\delta$  greater than 0.002. The same authors later provided a detailed characterisation of the laminar steady flow, reporting lower limits for the influence of the pipe curvature [Canton *et al.* Int. J. Heat Fluid Fl. **66**:95–107 (2017)]. The objective of the present work is to investigate the behaviour of the linear instability as the curvature of the pipe tends to zero. Results indicate that the toroidal pipe remains linearly unstable for curvatures as low as  $10^{-7}$ . While the critical Reynolds number  $Re$  necessary for the instability grows with an approximately algebraic trend below  $\delta = 0.002$ , the neutral curve also closes in onto the limit of negligible curvature. It therefore appears that there could be values of  $\delta$  and  $Re$  where a linearly unstable toroidal flow could be connected to the linearly stable straight pipe flow.

**Key words:** eigenmodes, low curvature, spectral methods

---

## 1. Introduction

It is well known that straight pipe (Hagen–Poiseuille) flow is linearly stable, for Reynolds numbers at least up to  $Re = 10^7$ , where the highly accurate spectral computations by Meseguer & Trefethen (2003) stop. This flow could in principle be linearly unstable for higher Reynolds numbers: there are analytical proofs demonstrating its linear stability to axisymmetric disturbances (Romanov 1973; Herron 1991), but only numerical proofs exist for non-axisymmetric perturbations. Hagen–Poiseuille flow does anyway undergo subcritical transition for  $Re \gtrsim 1700$ , so a linear instability for  $Re > 10^7$  would not have much relevance for practical applications.

Similarly to straight pipe flow, the flow inside of a toroidal pipe undergoes subcritical transition at low pipe curvatures (defined as the ratio between pipe and torus radii  $\delta = R_p/R_t$ ), as was shown both experimentally (Sreenivasan & Strykowski 1983; Kühnen *et al.* 2015) and numerically (Rinaldi *et al.* 2018). Differently from Hagen–Poiseuille, though, this flow is linearly unstable for

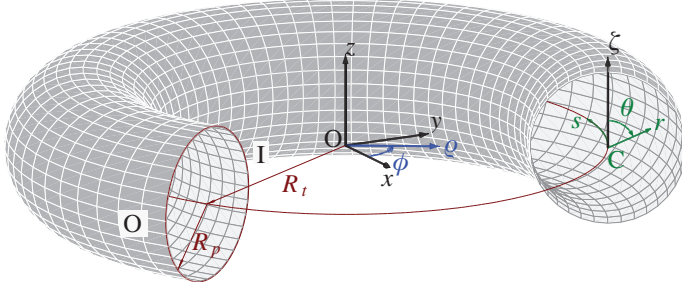


Figure 1: Sketch of the toroidal pipe showing the two geometrical quantities,  $R_t$  and  $R_p$ , defining the curvature  $\delta = R_p/R_t$ , equal to  $\delta = 0.3$  for this sketch. The three reference systems employed are also indicated: the Cartesian coordinate system ( $x, y, z$ ) in black, the cylindrical coordinate system ( $\rho, \phi, z$ ) in blue, and the toroidal coordinate system ( $s, r, \theta$ ) in green. The axis  $\zeta$  corresponds to  $z$  translated in C. The “central plane” or “equatorial plane” of the torus corresponds to the  $x - y$  plane. The “I” and “O” labels indicate the inner, resp. outer portions of the pipe.

Reynolds numbers of about 4000, at least for any  $\delta > 0.002$  (Canton *et al.* 2016). It is also apparent that since the curvature is the only parameter that differentiates toroidal pipe flow from Hagen–Poiseuille flow, as  $\delta$  tends to zero the flow in a torus must “reconnect” to the flow in a straight pipe. The infinitesimally small curvature limit was investigated by Canton *et al.* (2017) for  $\delta$  as low as  $10^{-13}$ . However, this study only presented an analysis on steady-state solutions, while no considerations on stability or any kind of perturbation to these steady states were made.

The present study focuses entirely on the stability characteristics of the flow in a torus in the very low curvature limit. A description of the numerical methods employed is presented in section 2, while the results are presented and discussed in § 3.

## 2. Numerical methods

The flow is considered as viscous and incompressible, and it therefore satisfies the incompressible Navier–Stokes equations, written here in nondimensional form:

$$\frac{\partial \mathbf{u}}{\partial t} + (\mathbf{u} \cdot \nabla) \mathbf{u} - \frac{1}{Re} \nabla^2 \mathbf{u} + \nabla p = \mathbf{f}, \quad (1a)$$

$$\nabla \cdot \mathbf{u} = 0, \quad (1b)$$

where  $\mathbf{u}(r, t)$  is the velocity vector, with components  $\mathbf{u} = (u_\rho, u_\phi, u_z)$  in cylindrical coordinates or  $\mathbf{u} = (u_s, u_r, u_\theta)$  when using the toroidal coordinate system. The (dimensionless) pressure  $p$  has been rescaled by dividing by the Reynolds number  $Re$ , and  $\mathbf{f}$  represents a volume force, described in detail in Canton *et al.*

(2017). The Reynolds number is based on the diameter of the pipe and the bulk velocity,  $U_b = \int_0^{2\pi} \int_0^{R_p} u_s r dr d\theta$ , i.e.  $Re = 2R_p U_b / \nu$ . When the curvature tends to zero, i.e. the radius of the torus tends to infinity, the toroidal coordinate system tends to a cylindrical coordinate system, and  $s$  from a curvilinear to a rectilinear axis.

When steady, the flow inside of a torus is invariant with respect to the streamwise direction  $s$ . This allows the computation of steady states on a two-dimensional pipe cross-section, while retaining all three velocity components. Eigensolutions can also be computed on a two-dimensional mesh after the introduction of a normal modes ansatz, as will be described shortly.

All steady states and the first eigenmodes were computed with PASTA, an in-house developed finite-element code written in primitive variables and using triangular  $\mathbb{P}_2 - \mathbb{P}_1$  elements. The code was already used in Canton *et al.* (2016, 2017) and had been previously validated extensively (for details see Canton 2013; Canton *et al.* 2017a). PASTA is written in cylindrical coordinates, with  $(u_\varrho, u_\phi, u_z)$  as unknowns. A circular mesh of triangles is generated on the  $\varrho - z$  plane, and the curvature is changed by moving the centre of this pipe cross-section at  $\varrho = R_t$ . If the mesh is moved too far away from the  $z$  axis, i.e. the curvature is lowered below a certain limit, numerical issues may arise. Computers have finite precision, therefore the distance between grid-points and the discrete quadrature schemes are subject to cancellation errors when the  $z$  coordinate is increased.

This problem can be solved by using a code solving the equations in toroidal coordinates, where the mesh is not affected by the aforementioned problems. In order to do so, one needs to start from the incompressible Navier–Stokes equations (1) written in toroidal coordinates (Germano 1982; Hüttl *et al.* 2004), which read as follows:

*continuity equation:*

$$\partial_s(ru_s) + \partial_r(h_sru_r) + \partial_\theta(h_su_\theta) = 0; \quad (2)$$

*s-momentum:*

$$\begin{aligned} \frac{\partial u_s}{\partial t} + \frac{1}{h_s} \partial_s(u_s u_s) + \frac{1}{h_s r} \partial_r(h_s r u_s u_r) + \frac{1}{h_s r} \partial_\theta(h_s u_s u_\theta) + \frac{\delta \sin \theta}{h_s} u_s u_r \\ + \frac{\delta \cos \theta}{h_s} u_s u_\theta = -\frac{1}{h_s} \partial_s p + \frac{1}{Re} \left[ \frac{2}{h_s} \partial_s \left( \frac{1}{h_s} (\partial_s(u_s) + \delta \sin \theta u_r + \delta \cos \theta u_\theta) \right) \right. \\ + \frac{1}{h_s r} \partial_r \left( h_s h_s r \partial_r \left( \frac{u_s}{h_s} \right) + r \partial_s(u_r) \right) + \frac{1}{h_s r} \partial_\theta \left( \frac{h_s h_s}{r} \partial_\theta \left( \frac{u_s}{h_s} \right) + \partial_s(u_\theta) \right) \\ \left. + \delta \sin \theta \left( \partial_r \left( \frac{u_s}{h_s} \right) + \frac{1}{h_s h_s} \partial_s(u_r) \right) + \delta \cos \theta \left( \frac{1}{r} \partial_\theta \left( \frac{u_s}{h_s} \right) + \frac{1}{h_s h_s} \partial_s(u_\theta) \right) \right]; \end{aligned} \quad (3)$$

*r-momentum:*

$$\begin{aligned} \frac{\partial u_r}{\partial t} + \frac{1}{h_s} \partial_s(u_s u_r) + \frac{1}{h_s r} \partial_r(h_s r u_r u_r) + \frac{1}{h_s r} \partial_\theta(h_s u_r u_\theta) - \frac{\delta \sin \theta}{h_s} u_s u_s - \frac{1}{r} u_\theta u_\theta \\ = -\partial_r p + \frac{1}{Re} \left[ \frac{1}{h_s} \partial_s \left( h_s \partial_r \left( \frac{u_s}{h_s} \right) + \frac{1}{h_s} \partial_s(u_r) \right) + \frac{2}{h_s r} \partial_r(h_s r \partial_r(u_r)) \right. \\ + \frac{1}{h_s} \partial_\theta \left( h_s \left( \frac{1}{rr} \partial_\theta(u_r) + \partial_r \left( \frac{u_\theta}{r} \right) \right) \right) - \frac{2\delta \sin \theta}{h_s h_s} (\partial_s(u_s) + \delta \sin \theta u_r + \delta \cos \theta u_\theta) \\ \left. - \frac{2}{rr} (\partial_\theta(u_\theta) + u_r) \right]; \end{aligned} \quad (4)$$

*$\theta$ -momentum:*

$$\begin{aligned} \frac{\partial u_\theta}{\partial t} + \frac{1}{h_s} \partial_s(u_s u_\theta) + \frac{1}{h_s r} \partial_r(h_s r u_r u_\theta) + \frac{1}{h_s r} \partial_\theta(h_s u_\theta u_\theta) - \frac{\delta \cos \theta}{h_s} u_s u_s + \frac{1}{r} u_r u_\theta \\ = -\frac{1}{r} \partial_\theta p + \frac{1}{Re} \left[ \frac{1}{h_s} \partial_s \left( \frac{h_s}{r} \partial_\theta \left( \frac{u_s}{h_s} \right) + \frac{1}{h_s} \partial_s(u_\theta) \right) \right. \\ + \frac{1}{h_s r} \partial_r \left( h_s \left( \partial_\theta(u_r) + rr \partial_r \left( \frac{u_\theta}{r} \right) \right) \right) + \frac{2}{h_s rr} \partial_\theta(h_s (\partial_\theta(u_\theta) + u_r)) \\ \left. - \frac{2\delta \cos \theta}{h_s h_s} (\partial_s(u_s) + \delta \sin \theta u_r + \delta \cos \theta u_\theta) + \left( \frac{1}{rr} \partial_\theta(u_r) + \partial_r \left( \frac{u_\theta}{r} \right) \right) \right], \end{aligned} \quad (5)$$

where  $h_s = 1 + \delta r \sin \theta$ .

The stability of the flow is then studied with a classical approach: computing the least stable eigenvalues of the system linearised around a steady state (base flow). The corresponding linearised equations are presented in Appendix A. The perturbation fields are then expanded in normal modes along streamwise direction, and their temporal and spatial behaviours are separated as follows (primes are dropped):

$$\mathbf{u}(s, r, \theta, t) = \hat{\mathbf{u}}(r, \theta) \exp(i(\alpha s / \delta - \omega t)), \quad (6a)$$

$$p(s, r, \theta, t) = \hat{p}(r, \theta) \exp(i(\alpha s / \delta - \omega t)), \quad (6b)$$

where  $\alpha \in \mathbb{R}$  is the streamwise wavenumber,  $\omega = \omega_r + i\omega_i \in \mathbb{C}$  is the eigenvalue and  $\hat{\mathbf{u}} \in [\mathbb{C}]_2^3$  and  $\hat{p} \in [\mathbb{C}]_2$  form the eigenfunction  $\hat{\mathbf{x}} = (\hat{\mathbf{u}}, \hat{p})$ . As in Canton *et al.* (2016), the symbols  $[\mathbb{A}]_d^c$  are used to denote a  $c$ -dimensional vector space  $\mathbb{A}$  in a  $d$ -dimensional physical space; when  $c$  is omitted  $\mathbb{A}$  represents a scalar space. Although  $\alpha$  is in principle a real number, the  $2\pi$ -periodicity of the torus restricts it to  $\mathbb{Z}$ . The non-dimensionalisation of  $\alpha$  by  $\delta$  provides it with the same value it has in Canton *et al.* (2016), *i.e.* it indicates the number of wavelengths a mode has in a  $2\pi$  torus.

The equations are solved with a fully spectral Fourier–Chebyshev discretisation; the routines for the one-dimensional derivatives are taken from Weideman

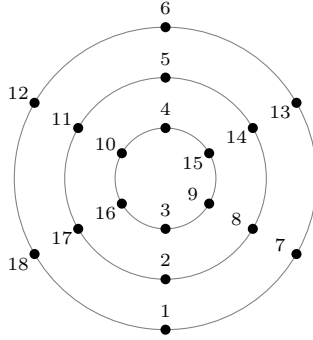


Figure 2: Sketch of the polar mesh for the Fourier–Chebyshev discretisation. In this example  $N_D = N_\theta = 6$ . The node ordering is also indicated.

& Reddy (2000). The Fourier expansion is used for the harmonic  $\theta$  direction, while Chebyshev polynomials are used for  $r$ . Fourier modes are naturally periodic for  $\theta \in [0, 2\pi)$ , while Chebyshev polynomials are defined for  $r \in [-1, 1]$ . In order to avoid any singularity in  $r = 0$  when solving the equations, it is convenient to set  $R_p = 1$  and to use an even number of Chebyshev polynomials; by doing so the grid refinement is at the wall, and there are no grid points in the centre of the pipe. However, this introduces an issue when combining the two discretisations: the Fourier modes, with co-located unknowns and grid points, intersect the diameter twice: in  $\theta = 0$  and  $\pi$ . The solution is to cleverly arrange the two-dimensional derivative matrices with respect to  $r$ , and to take into account the sign change across  $r = 0$  which depends on the evenness of the derivative and on the symmetry of the unknown field.

The grid nodes are ordered as illustrated in figure 2. By defining shorthands for the matrices for the one-dimensional derivatives in  $r$  and  $\theta$  as

$$D_r^{1D} = [d_r^{i,j}], \quad D_\theta^{1D} = [d_\theta^{i,j}], \quad (7)$$

and ordering the  $N = N_D/2 \times N_\theta$  unknowns by radius and angle as  $u = (u_1, u_7, u_{13}, \dots, u_{16})$ , the two-dimensional differentiation matrices for the derivatives in  $\theta$  are  $N \times N$  block matrices in the form

$$D_\theta = \begin{bmatrix} D_\theta^{1D} & & \\ & D_\theta^{1D} & \\ & & D_\theta^{1D} \end{bmatrix}, \quad (8)$$

while the two-dimensional differentiation matrices for the derivatives in  $r$  need a different ordering. Defining a shorthand for the following submatrix

$$D_r^{i,j} = d_r^{i,j} I^{n_\theta/2 \times n_\theta/2}, \quad (9)$$

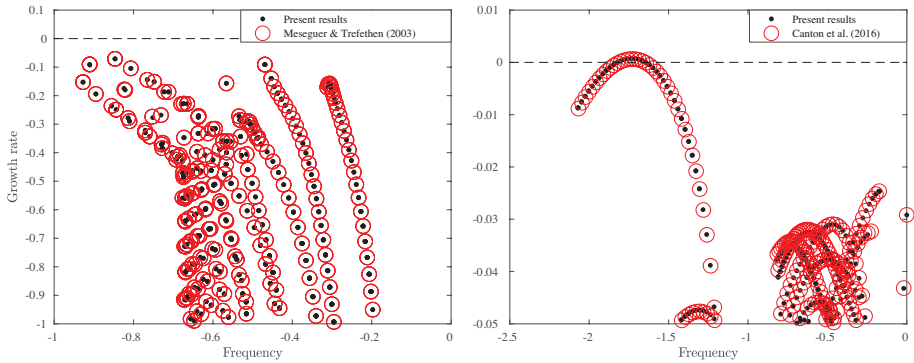


Figure 3: Validation of the present eigenvalue code. *Left:* eigenvalue spectrum of the flow in a straight pipe for  $Re = 1000$ , streamwise wavenumber 1, azimuthal wavenumbers are below 150; comparison with Meseguer & Trefethen (2003), figure 1. *Right:* eigenvalue spectrum of the flow in a toroidal pipe for  $\delta = 0.01$  and  $Re = 4300$ , streamwise wavenumbers  $0 \leq \alpha \leq 90$ ; comparison with Canton *et al.* (2016), figure 3(a).

where  $N_\theta$  is the number of Fourier modes in theta, the matrix  $D_r$  corresponding to the example grid of figure 2 is defined as:

$$D_r = \begin{bmatrix} D_r^{1,1} & D_r^{1,6} & D_r^{1,2} & D_r^{1,5} & D_r^{1,3} & D_r^{1,4} \\ D_r^{6,1} & D_r^{6,6} & D_r^{6,2} & D_r^{6,5} & D_r^{6,3} & D_r^{6,4} \\ D_r^{2,1} & D_r^{2,6} & D_r^{2,2} & D_r^{2,5} & D_r^{2,3} & D_r^{2,4} \\ D_r^{5,1} & D_r^{5,6} & D_r^{5,2} & D_r^{5,5} & D_r^{5,3} & D_r^{5,4} \\ D_r^{2,1} & D_r^{3,6} & D_r^{3,2} & D_r^{3,5} & D_r^{3,3} & D_r^{3,4} \\ D_r^{4,1} & D_r^{4,6} & D_r^{4,2} & D_r^{4,5} & D_r^{4,3} & D_r^{4,4} \end{bmatrix}. \quad (10)$$

The matrices for the second derivatives are assembled with the same sparsity patterns.

In order to validate the new code, the spectra of both straight and bent pipes were computed and compared with reference data. Figure 3 presents two of these spectra: for a straight pipe on the left and for a toroidal pipe with  $\delta = 0.01$  on the right. In both cases the section of the pipe was discretised with 100 Chebyshev modes on the diameter and 50 Fourier modes in  $\theta$ .

The eigenvalues for a straight pipe were computed at  $Re = 1000$  and a streamwise wavenumber  $\alpha = 1$ . Note that in a straight pipe  $\alpha$  is not non-dimensionalised by  $\delta$ , and has the usual linear relationship to the wavelength of the modes  $\lambda = 2\pi/\alpha$ . The reference eigenvalues were computed with the code provided by Meseguer & Trefethen (2003), which employs a similar spatial

discretisation but also has the azimuthal ( $\theta$ ) wavenumber  $n$  as parameter. Typically straight pipe spectra are visualised for individual values of  $\alpha$  and  $n$ , as in Meseguer & Trefethen (2003) figure 1, while the spectrum in figure 3 includes azimuthal wavenumbers between 0 and 150. The spectrum for the torus at  $\delta = 0.01$  was computed for  $Re = 4300$ , which is just above criticality for this curvature (Canton *et al.* 2016). In this case streamwise wavenumbers between 0 and 90 were computed. In both cases the eigensolutions are computed to machine precision via the shift-invert Arnoldi algorithm implemented in the ARPACK library (Lehoucq *et al.* 1998), and there is very good agreement between the results of the different codes.

### 3. Linear stability analysis

In a paper characterising the laminar, steady flow, Canton *et al.* (2017) documented how the base flow tends to that of a straight pipe as the curvature is lowered, and reported lower limits for the influence of  $\delta$  on the flow. Figure 5(a) reports one such limit, below which the viscous wall friction of the flow in a toroidal pipe is less than 1% different from that of the flow in a straight pipe.

The steady state is not the only feature of this flow that tends towards a straight pipe when the curvature is lowered. To begin the analysis, linear optimal initial conditions are computed as a function of curvature, with the aim of assessing whether the similarity of the base flow below the 1% demarcation line also results in a similarity of the linearised behaviour. These computations were done for  $Re = 1750$ , which is a subcritical value for transition in a straight pipe. For this Reynolds number the highest peak of kinetic energy amplification is reached for a time  $T = 21.35$ , which is also used for the present computations (see, *e.g.*, Meseguer & Trefethen 2003; Pringle & Kerswell 2010). Figure 4 presents the results for some of the curvatures investigated. As it can be visually noticed by comparing panels (b)–(f), and as is summarised in panel (a), lowering the curvature below the 1% threshold does indeed result in a similarity of the linearised behaviour. It is clear that relatively high curvatures are qualitatively different: The spatial structure of the optimal is different and maximum energy amplification is achieved at earlier times. Below  $\delta = 10^{-4}$ , instead, the optimal tends towards that of a straight pipe, with the same energy growth and spatial structure (see, *e.g.*, figure 2 in Pringle & Kerswell 2010, for a visual comparison). Despite the presence of (weak) secondary motion in the shape of Dean vortices, the optimal initial condition is formed by two counter-rotating cells disposed across the plane of symmetry of the torus and two anti-symmetric streamwise rolls.

Continuing the neutral curve of Canton *et al.* (2016) is a more computationally expensive analysis. While for the linear optimals all parameters were fixed except for the curvature, each point on the neutral curve is characterised by three scalar unknowns (the critical Reynolds number  $Re_c$ , the wavenumber and temporal frequency of the most unstable mode) and the corresponding steady state. The bifurcation tracking algorithm presented in Canton *et al.* (2016)

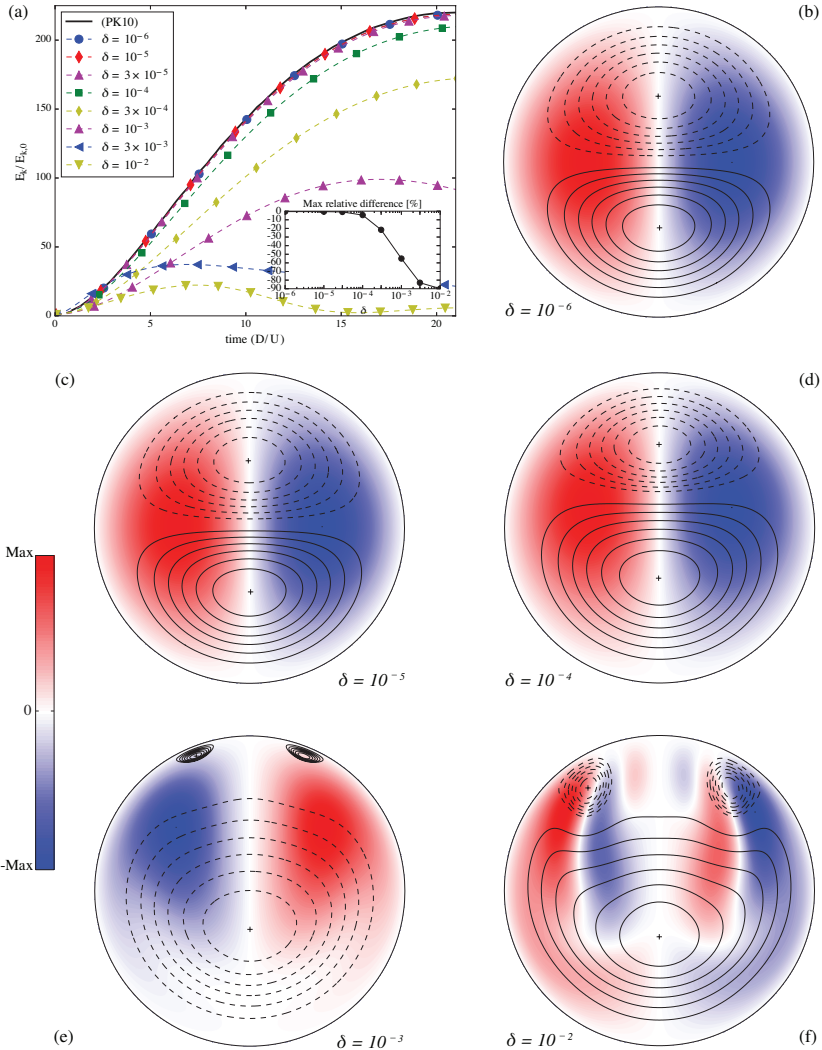


Figure 4: Linear optimal initial conditions for the flow in a toroidal pipe at  $Re = 1750$  and different curvatures (see also figure 5). The values of curvature are indicated in each panel. In (b)–(f) colours represent the streamwise velocity component  $u_s$ , while dashed and continuous lines are isocontours of the streamfunction. Panel (a) reports the energy growth, as a function of time, for these initial conditions, three intermediate curvatures (not shown) and a comparison to the straight pipe (PK10 is a shorthand for Pringle & Kerswell 2010). Panel (b) can be directly compared with the optimal initial condition in a straight pipe (see e.g., Meseguer & Trefethen 2003; Pringle & Kerswell 2010).

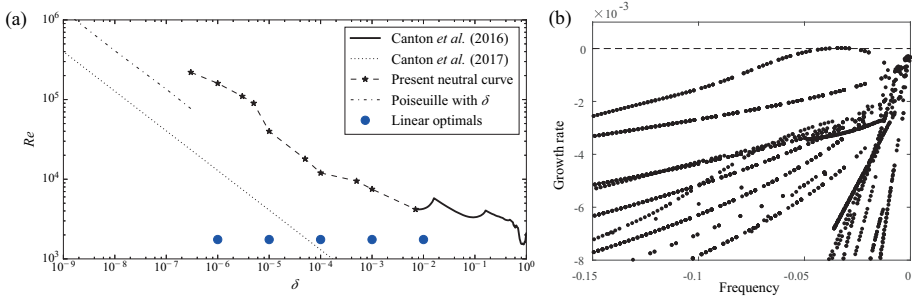


Figure 5: Panel(a): neutral curve of the flow in a toroidal pipe. The black thick line is the neutral curve computed by Canton *et al.* (2016) for  $\delta > 0.007$ , while the dotted line marks the 1% departure from the flow in a straight pipe (Canton *et al.* 2017). The dashed-starred line indicates the present continuation of the neutral curve, while the dashed-dotted line is the neutral curve for Poiseuille flow with  $\delta \neq 0$ . Round (blue) markers indicate the locations of the linear optimals depicted in figure 4. Panel (b): eigenvalue spectrum for the lowest value of curvature in panel (a), *i.e.*  $\delta = 3 \times 10^{-7}$ , and corresponding Reynolds number  $Re_c \approx 220\,000$ . The most unstable mode has a wavelength of about 200 pipe diameters.

is also less and less helpful as the curvature is lowered. While for  $\delta > 10^{-3}$  all unstable modes have wavenumber  $\alpha < 100$ , as the curvature drops the wavenumber drastically increases, at least for the range of curvatures investigated, since the wavelength of the unstable mode remains limited between 0.1 and 100. Moreover, at low curvatures the number of eigenvalue branches close to criticality increases, and the wavenumbers (and associated wavelengths) of the modes on these branches varies from branch to branch by up to two orders of magnitude. A last observation is that it is prohibitively expensive to verify these spectra with direct numerical simulations (DNS): in order to include all allowed wavenumbers to make sure not to have missed any, a full torus would need to be simulated, which is a pipe with length inversely proportional to the curvature  $L_t = 2\pi R_p/\delta$ . It therefore appears necessary, for each pair of  $(\delta, Re)$ , to compute an eigenvalue spectrum for large ranges of wavenumber and temporal frequency, to be considerably sure not to have missed possibly unstable eigenvalues.

Figure 5(a) presents preliminary results. The thick (black) line is the neutral curve computed by Canton *et al.* (2016) for curvatures  $\delta > 0.007$ , while the dotted line marks the 1% departure from the base flow of a straight pipe (Canton *et al.* 2017). The dashed line corresponds to the present continuation of the neutral curve, with markers indicating the values of curvature and respective critical Reynolds number. Figure 5(b) shows the eigenvalue spectrum for the lowest curvature computed up to now:  $\delta = 3 \times 10^{-7}$ , with corresponding critical

Reynolds number  $Re_c \approx 220\,000$ . Additionally, the dashed-dotted line is the neutral curve for a Poiseuille base flow when the perturbation fields are allowed to have  $\delta \neq 0$ . This line continues, with the same slope, at least to  $\delta = 10^{-13}$  and  $Re = 1.2 \times 10^8$ , and is currently under investigation.

It can be noticed that, at least for the curvatures investigated up to now, the neutral curve does not appear to have a clear trend. This is partly due to the small number of curvature values, below  $\delta = 0.007$ , where spectra are computed. More importantly, though, the irregularity is caused by an alternance of the least stable eigenvalue branch which, as for higher curvatures, appears to be uncorrelated to  $\delta$  or other flow parameters. Nevertheless, the distance between the neutral curve and the 1% demarkation line is reducing and, if the trend remains unchanged, the two could meet for  $\delta \approx 10^{-10}$  and  $Re \approx 10^6$ .

At this point it seems worth making a connection to the “real world”: a pipe with a cross-section of 1m in diameter (the diameter of the pipe facility at CICLoPE is 0.9m; Örlü *et al.* 2017) going around the Earth, would form a torus with curvature  $\delta = 1.57 \times 10^{-7}$  (on Mars it would be  $\delta = 2.95 \times 10^{-7}$ ). It is therefore apparent that realising an experimental facility or performing a DNS with the full domain are two highly improbable tasks.

#### **4. Summary and outlook**

The present work is a natural continuation of the neutral curve by Canton *et al.* (2016) towards zero curvature. In order to overcome the numerical issues presented by the original numerical code, a new, fully spectral stability code was written, solving the Navier–Stokes equations in toroidal coordinates. The present code was validated, with excellent results, by comparing it with data from the literature. It was therefore possible to continue the neutral curve of the flow inside a toroidal pipe for curvatures as low as, at the moment of writing,  $\delta = 3 \times 10^{-7}$

Preliminary computations show that the flow remains modally unstable and undergoes a Hopf bifurcation, as for all the other values of curvature previously investigated. However, the critical Reynolds number increases algebraically with decreasing curvature, while for  $0.007 \leq \delta \leq 1$  it was about 4 000. Despite the rapid increase in  $Re_c$ , the neutral curve approaches the line that marks a 1% difference of the base flow from the Hagen–Poiseuille flow, indicating that the two lines could cross for a curvature  $\delta \approx 10^{-10}$ . Further computations for lower curvatures are necessary in order to verify whether or not the two lines do actually intersect. A further outcome of the present work is the numerical code itself which, by re-introducing the torsion term, can readily be used to analyse the stability of the flow in helically coiled pipes.

Financial support by the Swedish Research Council (VR) is gratefully acknowledged. Computer time was provided by the Swedish National Infrastructure for Computing (SNIC).

## Appendix A. Linearised equations in toroidal coordinates

This section presents the Navier–Stokes equations linearised around a steady state  $(\mathbf{U}, P)$  and expressed in toroidal coordinates. The perturbation fields are indicated by  $(\mathbf{u}, p)$ .

Continuity equation:

$$\begin{aligned} \left[ r \frac{\partial}{\partial s} \right] u_s + \left[ (2\delta r \sin(\theta) + 1) + r(\delta r \sin(\theta) + 1) \frac{\partial}{\partial r} \right] u_r \\ + \left[ \delta r \cos(\theta) + (\delta r \sin(\theta) + 1) \frac{\partial}{\partial \theta} \right] u_\theta = 0. \end{aligned} \quad (11)$$

Momentum equation along  $s$ :

$$\begin{aligned} \frac{\partial u_s}{\partial t} + \left[ -\frac{1}{r^2 Re} \frac{\partial^2}{\partial \theta^2} + \frac{2\delta \cos(\theta) U_\theta}{\delta r \sin(\theta) + 1} + \frac{\partial U_r}{\partial r} + \frac{3}{r} U_r + \frac{1}{r} \frac{\partial U_\theta}{\partial \theta} - \frac{2U_r}{r(\delta r \sin(\theta) + 1)} \right. \\ \left. + \frac{\delta^2}{Re(\delta r \sin(\theta) + 1)^2} + \left( U_r + \frac{1}{r Re(\delta r \sin(\theta) + 1)} - \frac{2}{r Re} \right) \frac{\partial}{\partial r} \right. \\ \left. + \left( \frac{U_\theta}{r} - \frac{\delta \cos(\theta)}{r Re(\delta r \sin(\theta) + 1)} \right) \frac{\partial}{\partial \theta} - \frac{2}{Re(\delta r \sin(\theta) + 1)^2} \frac{\partial^2}{\partial s^2} - \frac{1}{Re} \frac{\partial^2}{\partial r^2} \right. \\ \left. + \frac{2U_s}{\delta r \sin(\theta) + 1} \frac{\partial}{\partial s} \right] u_s \\ + \left[ \frac{1}{r Re} \left( \frac{3}{(\delta r \sin(\theta) + 1)^2} - \frac{4}{\delta r \sin(\theta) + 1} \right) \frac{\partial}{\partial s} + \frac{\partial U_s}{\partial r} - \frac{2U_s}{r(\delta r \sin(\theta) + 1)} \right. \\ \left. + \frac{3}{r} U_s - \frac{1}{Re(\delta r \sin(\theta) + 1)} \frac{\partial^2}{\partial s \partial r} + U_s \frac{\partial}{\partial r} \right] u_r \\ + \left[ \frac{2\delta \cos(\theta) U_s}{\delta r \sin(\theta) + 1} + \frac{1}{r} \frac{\partial U_s}{\partial \theta} - \frac{1}{r Re(\delta r \sin(\theta) + 1)} \frac{\partial^2}{\partial s \partial \theta} \right. \\ \left. - \frac{3\delta \cos(\theta)}{Re(\delta r \sin(\theta) + 1)^2} \frac{\partial}{\partial s} + \frac{U_s}{r} \frac{\partial}{\partial \theta} \right] u_\theta \\ + \left[ \frac{1}{\delta r \sin(\theta) + 1} \frac{\partial}{\partial s} \right] p = 0. \end{aligned} \quad (12)$$

Momentum equation along  $r$ :

$$\begin{aligned}
& \frac{\partial u_r}{\partial t} + \left[ \left( \frac{U_r}{\delta r \sin(\theta) + 1} + \frac{3}{r Re (\delta r \sin(\theta) + 1)} - \frac{3}{r Re (\delta r \sin(\theta) + 1)^2} \right) \frac{\partial}{\partial s} \right. \\
& + \frac{2U_s}{r (\delta r \sin(\theta) + 1)} - \frac{2}{r} U_s - \frac{1}{Re (\delta r \sin(\theta) + 1)} \frac{\partial^2}{\partial s \partial r} \Big] u_s \\
& + \left[ \frac{1}{r^2 Re (\delta r \sin(\theta) + 1)^2} \left( r Re (\delta r \sin(\theta) + 1) \left( (\delta r \sin(\theta) + 1) \left( 2r \frac{\partial U_r}{\partial r} + \frac{\partial U_\theta}{\partial \theta} \right) \right. \right. \right. \\
& \left. \left. \left. + (4\delta r \sin(\theta) + 2) U_r + \delta r \cos(\theta) U_\theta \right) + 4\delta r \sin(\theta) (\delta r \sin(\theta) + 1) + 2 \right) \right. \\
& - \frac{1}{r^2 Re} \frac{\partial^2}{\partial \theta^2} + \left( 2U_r + \frac{2}{r Re (\delta r \sin(\theta) + 1)} - \frac{4}{r Re} \right) \frac{\partial}{\partial r} \\
& + \left( \frac{U_\theta}{r} - \frac{\delta \cos(\theta)}{r Re (\delta r \sin(\theta) + 1)} \right) \frac{\partial}{\partial \theta} - \frac{1}{Re (\delta r \sin(\theta) + 1)^2} \frac{\partial^2}{\partial s^2} \\
& \left. - \frac{2}{Re} \frac{\partial^2}{\partial r^2} + \frac{U_s}{\delta r \sin(\theta) + 1} \frac{\partial}{\partial s} \right] u_r \\
& + \left[ \left( \frac{1}{r} \frac{\partial U_r}{\partial \theta} + \frac{\delta \cos(\theta) (r Re U_r + 3)}{r Re (\delta r \sin(\theta) + 1)} - \frac{2}{r} U_\theta - \frac{2\delta \cos(\theta)}{r Re (\delta r \sin(\theta) + 1)^2} \right) \right. \\
& \left. + \left( \frac{U_r}{r} + \frac{3}{r^2 Re} \right) \frac{\partial}{\partial \theta} - \frac{\delta \cos(\theta)}{Re (\delta r \sin(\theta) + 1)} \frac{\partial}{\partial r} - \frac{1}{r Re} \frac{\partial^2}{\partial r \partial \theta} \right] u_\theta \\
& + \left[ \frac{\partial}{\partial r} \right] p = 0. \tag{13}
\end{aligned}$$

Momentum equation along  $\theta$ :

$$\begin{aligned}
& \frac{\partial u_\theta}{\partial t} + \left[ \left( \frac{U_\theta}{\delta r \sin(\theta) + 1} + \frac{3\delta \cos(\theta)}{Re (\delta r \sin(\theta) + 1)^2} \right) \frac{\partial}{\partial s} \right. \\
& - \frac{1}{r Re (\delta r \sin(\theta) + 1)} \frac{\partial^2}{\partial s \partial \theta} - \frac{2\delta \cos(\theta) U_s}{\delta r \sin(\theta) + 1} \Big] u_s \\
& + \left[ \frac{1}{r^2 Re} \left( \frac{1}{\delta r \sin(\theta) + 1} - 4 \right) \frac{\partial}{\partial \theta} + \frac{\partial U_\theta}{\partial r} - \frac{U_\theta}{r (\delta r \sin(\theta) + 1)} + \frac{3}{r} U_\theta \right. \\
& \left. - \frac{2\delta \cos(\theta)}{r Re (\delta r \sin(\theta) + 1)^2} - \frac{1}{r Re} \frac{\partial^2}{\partial r \partial \theta} + U_\theta \frac{\partial}{\partial r} \right] u_r \\
& + \left[ \frac{2\delta \cos(\theta) U_\theta}{\delta r \sin(\theta) + 1} + \frac{1}{r} \left( r \frac{\partial U_r}{\partial r} + 3U_r + 2 \frac{\partial U_\theta}{\partial \theta} \right) - \frac{U_r}{r (\delta r \sin(\theta) + 1)} \right. \\
& \left. + \frac{2\delta^2}{Re (\delta r \sin(\theta) + 1)^2} + \frac{1}{r^2 Re} \left( \frac{3}{\delta r \sin(\theta) + 1} - \frac{2}{(\delta r \sin(\theta) + 1)^2} \right) - \frac{2}{r^2 Re} \frac{\partial^2}{\partial \theta^2} \right. \\
& \left. + \left( U_r + \frac{1}{r Re (\delta r \sin(\theta) + 1)} - \frac{2}{r Re} \right) \frac{\partial}{\partial r} + \left( \frac{2}{r} U_\theta - \frac{2\delta \cos(\theta)}{r Re (\delta r \sin(\theta) + 1)} \right) \frac{\partial}{\partial \theta} \right. \\
& \left. - \frac{1}{Re (\delta r \sin(\theta) + 1)^2} \frac{\partial^2}{\partial s^2} - \frac{1}{Re} \frac{\partial^2}{\partial r^2} + \frac{U_s}{\delta r \sin(\theta) + 1} \frac{\partial}{\partial s} \right] u_\theta \\
& + \left[ \frac{1}{r} \frac{\partial}{\partial \theta} \right] p = 0. \tag{14}
\end{aligned}$$

## REFERENCES

- CANTON, J. 2013 Global linear stability of axisymmetric coaxial jets. Master's thesis, Politecnico di Milano, Italy, <https://www.politesi.polimi.it/handle/10589/87827>.
- CANTON, J., AUTERI, F. & CARINI, M. 2017a Linear global stability of two incompressible coaxial jets. *J. Fluid Mech.* **824**, 886–911.
- CANTON, J., ÖRLÜ, R. & SCHLATTER, P. 2017b Characterisation of the steady, laminar incompressible flow in toroidal pipes covering the entire curvature range. *Int. J. Heat Fluid Flow* **66**, 95–107.
- CANTON, J., SCHLATTER, P. & ÖRLÜ, R. 2016 Modal instability of the flow in a toroidal pipe. *J. Fluid Mech.* **792**, 894–909.
- GERMANO, M. 1982 On the effect of torsion on a helical pipe flow. *J. Fluid Mech.* **125**, 1–8.
- HERRON, I. 1991 Observations on the role of vorticity in the stability theory of wall bounded flows. *Stud. Appl. Maths* **85** (3), 269–286.
- HÜTTL, T. J., CHAUDHURI, M., WAGNER, C. & FRIEDRICH, R. 2004 Reynolds-stress balance equations in orthogonal helical coordinates and application. *ZAMM-Z. Angew. Math. Me.* **84** (6), 403–416.
- KÜHNEN, J., BRAUNSHIER, P., SCHWEGEL, M., KUHLMANN, H. C. & HOF, B. 2015 Subcritical versus supercritical transition to turbulence in curved pipes. *J. Fluid Mech.* **770**, R3.
- LEHOUCQ, R. B., SORENSEN, D. C. & YANG, C. 1998 ARPACK users guide: solution of large-scale eigenvalue problems with implicitly restarted Arnoldi methods.
- MESEGUER, Á. & TREFETHEN, L. N. 2003 Linearized pipe flow to Reynolds number 107. *J. Comput. Phys.* **186** (1), 178–197.
- ÖRLÜ, R., FIORINI, T., SEGALINI, A., BELLANI, G., TALAMELLI, A. & ALFREDSSON, P. H. 2017 Reynolds stress scaling in pipe flow turbulence – first results from CICLoPE. *Philos. Trans. R. Soc. A* **375** (2089), 20160187.
- PRINGLE, C. C. T. & KERSWELL, R. R. 2010 Using nonlinear transient growth to construct the minimal seed for shear flow turbulence. *Phys. Rev. Lett.* **105**, 154502.
- RINALDI, E., CANTON, J. & SCHLATTER, P. 2018 The collapse of strong turbulent fronts in bent pipes. *Submitted*.
- ROMANOV, V. A. 1973 Stability of plane-parallel Couette flow. *Functional Anal. & Appl.* **7** (2), 137–146.
- SREENIVASAN, K. R. & STRYKOWSKI, P. J. 1983 Stabilization effects in flow through helically coiled pipes. *Exp. Fluids* **1**, 31–36.
- WEIDEMAN, J. A. C. & REDDY, S. C. 2000 A MATLAB differentiation matrix suite. *ACM T. Math. Software* **26** (4), 465–519.



# Paper 4

4



# The collapse of strong turbulent fronts in bent pipes

Enrico Rinaldi, Jacopo Canton, and Philipp Schlatter

Linné FLOW Centre and Swedish e-Science Research Centre (SeRC), KTH  
Mechanics, Royal Institute of Technology, SE-100 44 Stockholm, Sweden

*Submitted (2018)*

Isolated patches of turbulence in transitional straight pipes are sustained by a strong instability at their upstream front, where the production of turbulent kinetic energy (TKE) is up to five times higher than in the core. Direct numerical simulations presented in this paper show no evidence of such strong fronts if the pipe is bent. We examine the temporal and spatial evolution of puffs and slugs in a toroidal pipe with pipe-to-torus diameter ratio  $\delta = D/d = 0.01$  at several subcritical Reynolds numbers. Results show that the upstream overshoot of TKE production is at most one-and-a-half times the value in the core and that the average cross-flow fluctuations at the front are up to three times lower if compared to a straight pipe, while attaining similar values in the core. Localised turbulence can be sustained at smaller energies through a redistribution of turbulent fluctuations and vortical structures by the in-plane Dean motion of the mean flow. This asymmetry determines a strong localisation of TKE production near the outer bend, where linear and nonlinear mechanisms optimally amplify perturbations. We further observe a substantial reduction of the range of Reynolds numbers for long-lived intermittent turbulence, in agreement with experimental data from the literature. Moreover, no occurrence of nucleation of spots through splitting could be detected in the range of parameters considered. Based on the present results, we argue that this mechanism gradually becomes marginal as the curvature of the pipe increases and the transition scenario approaches a dynamical switch from subcritical to supercritical.

**Key words:** subcritical transition, isolated turbulence

---

## 1. Introduction

Over a century ago Osborne Reynolds observed that transition to turbulence in pipe flow is initiated by the appearance of localised travelling patches of chaotic motion (Reynolds 1883). He identified as the key parameter for the onset of turbulence the non-dimensional flow rate  $Re = \bar{U}D/\nu$ , later named the Reynolds number, where  $\bar{U}$  is the mean flow speed,  $D$  is the pipe diameter, and  $\nu$  is the kinematic viscosity of the fluid. Successive experiments detailed this

scenario and drew the distinction between turbulent spots that do not grow in size, *puffs*, and spots that expand in the surrounding laminar flow, *slugs* (see, e.g. Lindgren 1969; Wygnanski & Champagne 1973; Wygnanski *et al.* 1975; and the review by Mullin 2011).

Pipe flow presents the peculiarity of having a linearly stable laminar velocity profile (Meseguer & Trefethen 2003), *i.e.* all small perturbations decay and no critical Reynolds number can be defined using linear theory. However, experiments and simulations show that subcritical transition to turbulence can occur for  $Re \gtrsim 1700$  if perturbations are sufficiently large. Only recently a statistical description of the intermittent flow in pipes has provided an accurate estimate of a critical Reynolds number,  $Re \approx 2040$  (Avila *et al.* 2011). Below this threshold, the probability of a puff decaying outweighs the probability of a new puff being generated through a splitting mechanism. On the other hand, if the Reynolds number is higher than the threshold, the probability of splitting rapidly increases and puffs proliferate. Theoretical models have been proposed and quantitatively capture this subcritical transition scenario, which falls into the directed percolation universality class (Barkley 2011; Barkley *et al.* 2015; Shih *et al.* 2015). For  $Re \gtrsim 2300$  puffs turn into slugs, which rapidly fill the pipe thereby marking the onset of sustained space-filling turbulence. The reader is referred to the review by Barkley (2016) for further details.

The spatial structure of puffs and slugs has been the subject of several studies initiated by Wygnanski & Champagne (1973); Wygnanski *et al.* (1975) and followed by both experimental and numerical investigations (see e.g. Darbyshire & Mullin 1995; Nishi *et al.* 2008; and Duguet *et al.* 2010; Song *et al.* 2017, respectively). Results show a high concentration of turbulent fluctuations at the *strong* upstream front and a gradual decrease at the *weak* downstream front. In fact, an instability is responsible for extracting energy from the upstream laminar flow and transferring it to the fluctuating field, while the downstream front corresponds to decaying turbulence. At sufficiently high Reynolds numbers, the weak downstream front turns into a strong front that feeds on the downstream laminar flow (Song *et al.* 2017). The core of the slugs was shown to have the same characteristics of a fully turbulent flow (see the previously referenced studies and also Cerbus *et al.* 2018).

Transition to turbulence in bent pipes has received less attention compared to straight pipes. For this flow case an additional governing parameter comes into play, namely the non-dimensional curvature  $\delta = D/d$ , with  $d$  indicating the coiling diameter. White (1929) was the first to observe that the flow in a bent pipe can be maintained in a laminar state for higher Reynolds numbers than in a straight pipe. More recent experiments by Sreenivasan & Strykowski (1983) reported relaminarisation of a turbulent flow entering a coiled pipe and provided Reynolds number ranges for subcritical transition to turbulence for low curvatures. However, this is not the only transition mechanism in bent pipes. Webster & Humphrey (1993, 1997); Kühnen *et al.* (2014) have reported supercritical transition from a steady to a periodic flow presenting a travelling

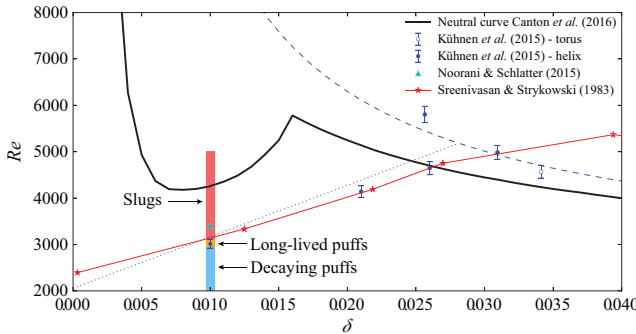


Figure 1: Stability map of the flow in a bent pipe. The continuous black line is the neutral curve calculated using linear theory (Canton *et al.* 2016). Red stars indicate the critical limit for transition as measured by Sreenivasan & Strykowski (1983). The triangle is a DNS of a fully turbulent flow by Noorani & Schlatter (2015). Circles are experiments by Kühnen *et al.* (2015) indicating 50% intermittency (for  $\delta \lesssim 0.028$ ) or the appearance of a periodic travelling wave. The blue lines are the interpolants by Kühnen *et al.* (2015) showing the onset of the subcritical transition (dotted) and of a supercritical bifurcation cascade (dashed). The coloured boxes indicate the flow regimes characterised in this paper: slugs ( $Re > 3100$ ), long-lived puffs ( $2950 < Re < 3100$ ), and decaying puffs ( $Re < 2950$ ).

wave for medium-high curvatures. Supercritical transition indicates a qualitative difference between straight and bent pipes, which are characterised by a modal instability for all curvatures different from zero (Canton *et al.* 2016). A unifying picture for transition in bent pipes was provided by Kühnen *et al.* (2015) who reported that subcritical transition dominates for  $\delta \lesssim 0.028$ , while above this value transition to turbulence occurs through a supercritical bifurcation cascade. Figure 1 reports the neutral curve for the flow in a torus (Canton *et al.* 2016) in the  $\delta - Re$  plane, and experimental data indicating the onset of turbulence taken from the literature. Subcritical transition in bent pipes was described as being “very similar as in straight pipes, where laminar and turbulent flows can coexist” (Kühnen *et al.* 2015). However, to the best of our knowledge, an in-depth analysis of this regime is still missing.

In order to ensure that the nature of transition investigated here is subcritical, we choose  $\delta = 0.01$ . This curvature is sufficiently lower than the threshold for the onset of a supercritical bifurcation cascade ( $\delta \approx 0.028$  according to Kühnen *et al.* 2015), while introducing a significant deviation of the laminar flow from the one of a straight pipe (Canton *et al.* 2017). At  $\delta = 0.01$ , the laminar flow is linearly unstable for  $Re > 4257$  (Canton *et al.* 2016). On the other hand, Kühnen *et al.* (2015) measured 50% intermittency for  $Re \approx 3000$  and numerical simulations show that the flow is in a sustained fully turbulent

state above  $Re = 3400$  (see Noorani *et al.* 2013; Noorani & Schlatter 2015). Figure 1 presents a sketch of the range of Reynolds numbers considered in the present study,  $2900 \leq Re \leq 5000$ , and gives an overview of our results in terms of turbulent structures. We present a fully numerical study where direct numerical simulations (DNS) are performed using the spectral element solver NEK5000 (Fischer *et al.* 2008), which was previously validated on turbulent straight and bent pipes (El Khoury *et al.* 2013; Noorani *et al.* 2013). In order to observe the large-scale evolution of puffs and slugs, our domains are of length  $L_s = 100D$  and  $L_s = \pi d/3 \simeq 105D$  for straight and bent pipes respectively, where the subscript  $s$  indicates the streamwise direction. Our spatial resolution satisfies typical DNS requirements for fully turbulent flows at Reynolds numbers slightly higher than the ones considered here.

The paper continues in §2 with an analysis of the space-time dynamics of localised turbulent structures. Section 3 presents considerations on the budget of turbulent kinetic energy, and §4 analyses the vortical structures embedded in puffs and slugs. Section 5 is dedicated to a discussion of the results.

## 2. Space-time dynamics of localised turbulence

We begin by examining how the space–time dynamics of localised turbulence is affected by the curvature. Figure 2 illustrates the main message of the paper by displaying the evolution of the cross-flow velocity fluctuations,  $q$ , for puffs (figure 2(a)) and slugs (figure 2(b)) in both straight and bent pipes. We use the scalar quantity  $q$  as an indicator of the level of turbulence in accordance with the literature regarding transitional flows in straight pipes (see, e.g. Barkley 2011) and adapt its definition to the case of bent pipes as

$$q(s, t) = \sqrt{\int_0^{2\pi} \int_0^R \left( (u_r - U_r)^2 + (u_\theta - U_\theta)^2 \right) r dr d\theta}. \quad (1)$$

Here,  $s$ ,  $r$  and  $\theta$  indicate the streamwise, radial and azimuthal directions in toroidal co-ordinates. The instantaneous velocity components are  $u_s = u_s(s, r, \theta, t)$ ,  $u_r = u_r(s, r, \theta, t)$  and  $u_\theta = u_\theta(s, r, \theta, t)$ ; capital letters denote the laminar flow at a given curvature and Reynolds number.  $U_r = U_r(r, \theta; \delta, Re)$  and  $U_\theta = U_\theta(r, \theta; \delta, Re)$  are zero in a straight pipe but not in a curved one, where the Dean vortices (Dean 1927) constitute a secondary motion that can exhibit intensities comparable to that of the streamwise flow (Canton *et al.* 2017). We plot  $q = q(s - u_f t, t)$ , calculated in a frame of reference that moves with a constant streamwise velocity  $u_f$ , and use the same range of colour levels for straight and bent pipes to allow for a direct visual comparison. The reason for the different Reynolds numbers is that similar flow structures with similar characteristics, *i.e.* isolated puffs moving at approximately constant speed (figure 2(a)) and slugs expanding at a similar rate (figure 2(b)), are found at different  $Re$  in the two pipes.

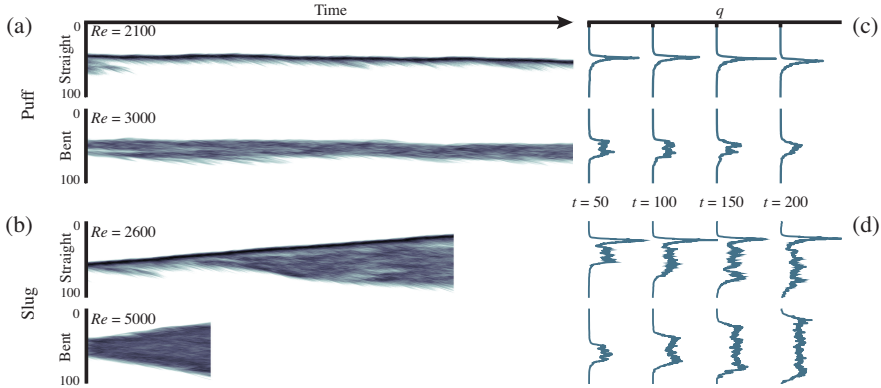


Figure 2: Space-time evolution of the cross-flow velocity fluctuations  $q$ , defined by equation (1), for exemplary puffs (a) and slugs (b) in straight and curved pipes. Colours represent  $\log_{10} q$ , white corresponds to laminar flow, dark colours to high fluctuations. Panels (c,d) report the spatial distribution of  $q$  sampled at four time instants. The (horizontal) scale used to indicate the magnitude of  $q$  is the same for the straight and curved pipes.

A clear and distinctive feature differentiates puffs and slugs between the two pipes: the absence of a strong upstream front if the pipe is bent. Space-time diagrams show the well-known concentration of turbulent fluctuations, indicated by the dark tone of the colour, at the upstream front in straight pipes (Barkley 2011, 2016; Song *et al.* 2017). Conversely, the flow in bent pipes shows no evidence of this strong front and is characterised by a somewhat uniform distribution of  $q$ . A further peculiarity is that puffs extend over a streamwise length that is approximately twice the one reported in the absence of curvature. One-dimensional profiles of  $q$ , sampled at several subsequent times, are reported in figures 2(c) and (d), and facilitate the comparison between the straight and bent pipe flow cases. The overshoot of turbulent fluctuations is prominent if the pipe is straight and can reach values significantly higher than the ones downstream of the front, while in the curved pipe the upstream front has intensity comparable to that of the core of the structure.

The structure of puffs and slugs is quantitatively characterised by means of a projection of the flow trajectory on the  $u_s - q$  phase space (Song *et al.* 2017), with  $u_s$  now being the maximum streamwise velocity on the cross-section on which  $q$  is calculated. Figure 3 presents the data for a single realisation of a slug in a straight pipe at  $Re = 2600$  and three slugs in a bent pipe at  $Re = 3100$ ,  $3300$  and  $5000$ . The loops for each flow case are obtained by time averaging  $u_s - q$  pairs over a length of 20 diameters across the upstream and the downstream fronts. Large filled symbols are space-time averages of the trajectory in the core. All values of  $q$  are normalised by the average turbulent

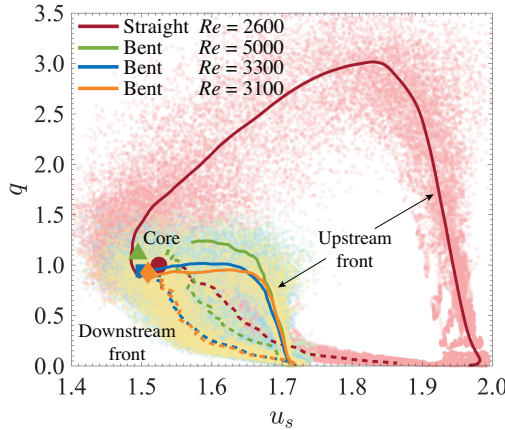


Figure 3: Trajectories of turbulent slugs in the  $u_s - q$  phase space for straight and curved pipes. The clouds indicate a subset of the instantaneous values while the continuous lines are the average over time.

fluctuations in the core of the slug in the straight pipe at  $Re = 2600$ . Moving in the direction of the flow, which corresponds to following loops in anti-clockwise direction, the laminar velocity profile flattens, which is indicated by a decrease of  $u_s$ , and the turbulent fluctuations rapidly increase. The overshoot of  $q$  is clearly visible in the case of straight pipe, where maximum values can be over three times larger than in the core. On the other hand, if the pipe is bent,  $q$  settles to approximately the same value attained in the core in a nearly monotonic fashion.

The steep increase of  $q$  is a common feature of the upstream fronts in straight and bent pipes, and indicates that a similar mechanism of instability sustains the slug by extracting energy from the surrounding laminar flow. This is a key similarity that suggests that the analogy between transitional pipe flow and an excitable medium (Barkley 2012), such as a nerve axon, still holds in its essence if the pipe is bent. However, our results indicate a significant reduction of super-threshold perturbations at the upstream front as the curvature increases. This goes hand in hand with the emergence of strong Dean vortices that enhance the mixing and redistribution of turbulent fluctuations (the supplementary video 1 gives a graphical representation of the action of Dean vortices). As opposed to the upstream front, the downstream front corresponds to decaying turbulence, as in straight pipes, although a clear identification of a refractory region is not as obvious due to the absence of a definite upstream overshoot, see 2(c).

The features of puffs and slugs discussed above are not affected by the choice of the parameter indicating the level of turbulence. The definition of  $q$  reduces the velocity field to a single value by integrating over the cross-section of the

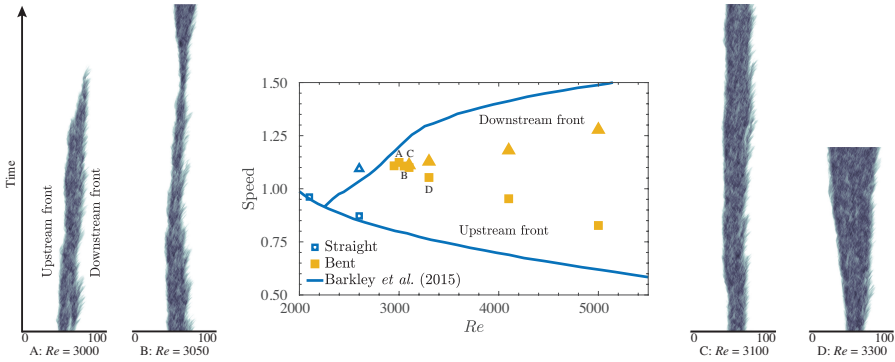


Figure 4: Front speed in straight (empty symbols) and bent pipes (filled symbols) as a function of the Reynolds number. Squares and triangles indicate the upstream and downstream fronts, respectively. At a given  $Re$ , a single entry in speed identifies a puff. The continuous line is the model from Barkley *et al.* (2015) for straight pipe. The lateral panels show the space–time diagrams corresponding to four selected cases. The time scale (vertical axis) is the same for all panels; the puff at  $Re = 3000$  decays after  $\tau \approx 700 D/U$ .

pipe. This is a reasonable approximation in the case of a straight pipe, where the azimuthal direction is homogeneous. Nevertheless,  $q$  can still underestimate the level of turbulence in the presence of strong localisation in the radial direction. In the case of a bent pipe the azimuthal direction is not homogeneous, due to the curvature, and the flow is asymmetric between the inner and outer bend; this can lead to further underestimation of the turbulence intensity when quantifying it by means of  $q$ . We have verified that replacing (the average)  $q$  with its local maxima results in the same monotonic increase towards the core with no trace of overshoot.

Figure 4 presents a parametric study of the effect of the Reynolds number over the evolution of localised turbulence in the  $\delta = 0.01$  bent pipe. The aim is to define an approximate lower bound on  $Re$  for long-lived ( $\tau > 1000 D/U$ ) localised turbulence in the form of puffs, and to pinpoint the onset of expanding turbulence. The image includes space–time diagrams of  $q$  and an estimate of the velocity of the upstream and downstream fronts.

Our results indicate that for  $\delta = 0.01$  turbulence decays for Reynolds numbers below 2950. Isolated puffs seeded into a steady flow relaminarise, as do initially fully turbulent flows computed for higher Reynolds numbers, following a protocol analogous to Moxey & Barkley (2010). At  $Re = 3000$  a single realisation of an isolated puff decays in approximately 700 advection time units (see point A in figure 4). On the other hand, a flow initialised with a fully turbulent field appears to persist as such. At  $Re = 3050$  two simulations initialised with localised turbulence show no return to a laminar state. The first

separation between the upstream and downstream fronts speed (approximately 1%) occurs at  $Re = 3100$  and marks the onset of the slug regime.

The limited number of realisations presented in this paper does not allow a precise computation of front speeds and decay times. Nonetheless, figure 4 provides an overview of the subcritical transition scenario in bent pipes and how it differs from straight ones. We document an overall increase of the Reynolds numbers at which subcritical transition is triggered. The range of values at which long-lived localised turbulence persists is also significantly narrowed, reducing from  $1900 < Re < 2300$  for a straight pipe to  $3000 < Re < 3100$ , above which puffs turn into slugs. The same behaviour was observed by Sreenivasan & Strykowski (1983) with experiments on helical pipes, and our numerical results are in good agreement with their data and with the  $Re$  value indicated by Kühnen *et al.* (2015) for 50% intermittency. The Reynolds number is not the only quantity to increase for bent pipes as compared to straight ones: the mean advection velocity of puffs and slugs is also larger. Puffs are faster than the bulk flow, while in a straight pipe they are slower, and the upstream front of slugs is slower than the mean flow only for  $Re \gtrsim 3600$ . Conversely, the expansion rate of slugs is reduced when compared to a straight pipe, indicating that these structures travel downstream more quickly but perturb a stationary point for a shorter time.

### 3. Turbulent kinetic energy budget

In order to get further insight into the structure of localised turbulence in bent pipes, figure 5 presents the budget of turbulent kinetic energy calculated in the frame of reference co-moving with a slug and centered on the upstream front. Figure 5(a) presents the budget for a straight pipe at  $Re = 2600$  and a comparison with data by Song *et al.* (2017). Figure 5(b)-(d) shows the present results in bent pipes for  $Re = 3100, 3300$  and  $5000$ . In the relative frame of reference the budget reads

$$\frac{\partial k}{\partial t} = P_k - \varepsilon_k - (\bar{u} - u_f) \hat{s} \cdot \nabla k - \nabla \cdot \mathbf{T}_k = 0, \quad (2)$$

$$P_k = -\overline{u'_i u'_j} \frac{\partial \bar{u}_i}{\partial x_j}, \quad \varepsilon_k = \frac{2}{Re} \overline{s_{ij} s_{ij}}, \quad T_{k,i} = \frac{1}{2} \overline{u'_i u'_j u'_j} + \overline{u'_i p'} - \frac{2}{Re} \overline{u'_j s_{ij}}, \quad (3)$$

where overlines indicates time-averaged quantities, primes indicate fluctuation fields and  $s_{ij} = 1/2 (\partial u'_i / \partial x_j + \partial u'_j / \partial x_i)$  is the shear rate. The terms in equation (2) are averaged over the pipe cross-section and normalised by the production rate in the core of each slug. As for  $q$  in the previous section, we have verified that using mean or local values does not affect the results.

The most striking difference between straight and bent pipes is the value of  $P_k$  and  $\varepsilon_k$  at the upstream front. While in a straight pipe the average production at the front is approximately five times higher than in the core, in a bent pipe it is only one-and-a-half times the value of the core. The second relevant difference is that in a straight pipe the peak of production preceeds the peak of dissipation by about one pipe diameter, as can be seen in figure 5(a), while in a bent pipe

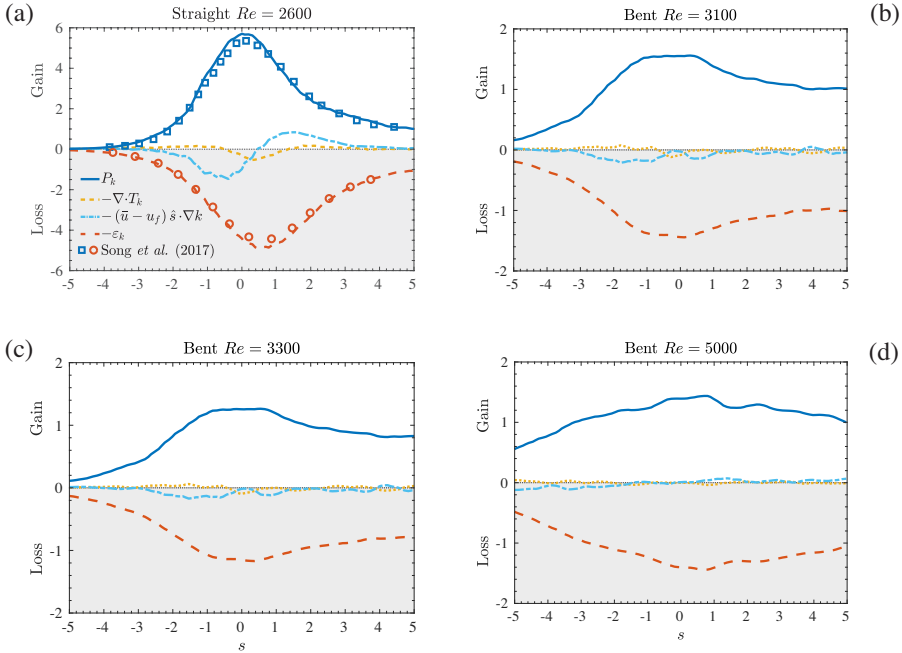


Figure 5: Turbulent kinetic energy budget integrated over the pipe cross-section in a straight pipe (a) and in a bent pipe for different Reynolds numbers (b)–(d). Panel (a) also reports the data by Song *et al.* (2017). The budget is calculated in a moving frame of reference centered at the upstream front of the slug. The terms of the budget are normalised by the value that  $P_k$  assumes in the core of the slug, note the different scaling of the vertical axes.

they are almost at the same location (see panels (b)–(d)). Since for slugs in a bent pipe  $P_k$  and  $\varepsilon_k$  are in near equilibrium at each streamwise location, the rates of energy flux and convection provide a minor contribution to the budget.

Since bent pipes are not invariant to rotations on the section, one-dimensional budgets provide only partial information. As reported by Sreenivasan & Strykowski (1983) turbulent fluctuations in bent pipes appear first in the outer portion of the bend, while they pervade the whole cross-section only for higher Reynolds numbers. To complement figure 5, figure 6 presents the time averaged distributions of production and dissipation over a cross-section of the pipe.

The panels in the top row of figure 6 are computed at the upstream front of slugs, which corresponds to  $s = 0$  in figure 5. In a straight pipe  $P_k$  and  $\varepsilon_k$  are mainly concentrated in the near-wall region and in a ring around the centre of the pipe. Conversely, the budget in a bent pipe shows a high localisation towards the outside of the bend and lower peak values. This confirms that the

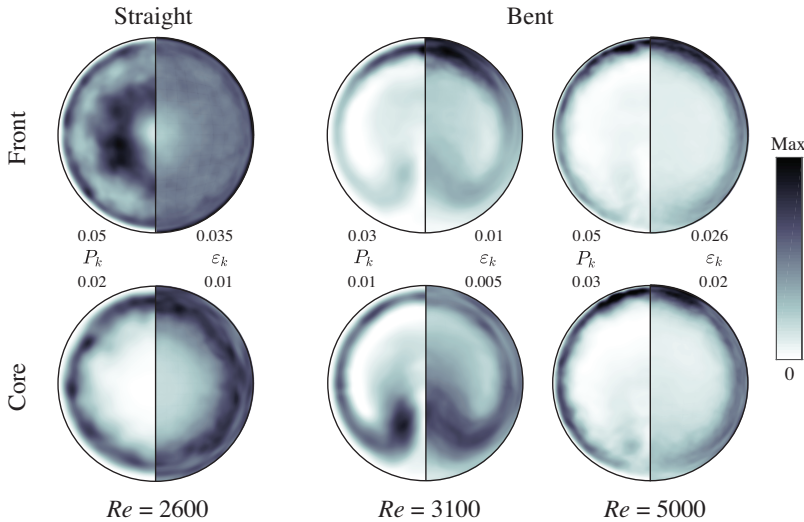


Figure 6: Turbulent kinetic energy production (left halves) and dissipation (right halves) at the front and core of slugs in straight and bent pipes. All quantities are averaged over time by tracking the slug, and over the cross-section taking into account the mirror symmetry of the torus, the axial invariance of the pipe has not been used in order not to alter the comparison. The text labels in the centre report the maxima of  $P_k$  and  $\varepsilon_k$  on each section (see also figure 5).

collapse of the strong upstream front is not an artifact of spatial averaging, but a specific feature pertaining to bent pipes. The spatial localisation and lower local values of  $P_k$  and  $\varepsilon_k$  also suggest that an additional mechanism must come into play in sustaining turbulent patches. We argue that the secondary motion created by the Dean vortices is at the root of both these phenomena. As the curvature is increased from a straight to a bent pipe, the linear and nonlinear optimal perturbations become increasingly localised in the same region where the peaks of  $P_k$  and  $\varepsilon_k$  are located. This is illustrated in figure 7, which depicts the optimal initial velocity distribution for the linearised flow (panel (a)) and for the full set of nonlinear equations (panel (b)). Linear optimals are calculated using the finite element code PASTA (Canton 2013; Canton *et al.* 2016). Nonlinear optimal perturbations are computed using a standard gradient-based optimisation algorithm (see, e.g. Pringle & Kerswell 2010), which was implemented in the code NEK5000 (Schanen *et al.* 2016). It therefore appears that the region near the outer bent, where the recirculating flow impinges on the wall of the pipe, is highly receptive to flow perturbations and is responsible for their amplification. The generated fluctuations are then transported along the walls of the pipe and lifted up towards the inner section.



Figure 7: Optimal perturbations in a bent pipe. Linear optimal initial condition (a): the left and right half of the pipe section depict  $E_{sw} = \frac{1}{2}u_s^2$  and  $E_{cf} = \frac{1}{2}(u_r^2 + u_\theta^2)$ , respectively. Values are normalised by  $\max(E_{sw})$ . The optimal initial condition is calculated at  $Re = 2870$ . The energy grows by as much as a factor 106 by  $t = 7.5$ . Nonlinear optimal initial condition (b): contours of the streamwise velocity ( $-3.5 \times 10^{-3}U$  and  $2.5 \times 10^{-3}U$ ). The optimisation is performed at  $Re = 3000$ , imposing a constraint on the initial perturbation energy  $E_0 = 4 \times 10^{-5}U^2$  (integrated over the volume) and over the maximum integration time  $T = 60D/U$ . The length of the domain is  $L_s = 2\pi D$ . The growth of energy at the final time is a factor of 1074.

The bottom row of figure 6 presents the distribution of production and dissipation at the core of the slugs. In a straight pipe the ring of high  $P_k$ , which was observed at the front, disappears. Production and dissipation are localised in the near-wall region and are the same as in a fully turbulent pipe flow. For high Reynolds numbers, when slugs expand rapidly, the spatial distribution of  $P_k$  and  $\varepsilon_k$  in bent pipes is qualitatively unchanged between the front and the core, as can be seen in the rightmost column of figure 6. At intermediate Reynolds numbers, instead, the cores are qualitatively different. The peaks of  $P_k$  and  $\varepsilon_k$  are localised in two lobes in the bottom half of the pipe, near the symmetry axis, as can be seen in the central column of figure 6 for  $Re = 3100$ . The same behaviour is observed for  $Re = 3300$  (not shown in the figure). These lobes are likely connected with a low frequency, highly energetic mode responsible for the so-called sublaminar drag in the range  $2900 \lesssim Re \lesssim 4000$  (Noorani & Schlatter 2015).

#### 4. Vortical structures at the front

We conclude our analysis by discussing the dynamics of vortical structures at the upstream front of slugs. Figure 8 reports instantaneous fields of vortices visualised using the  $\lambda_2$  criterion (Jeong & Hussain 1995) for both straight and bent pipes.

The flow in a straight pipe shows a high concentration of vortices at the upstream front, distributed in the typical conical shape going from the near-wall

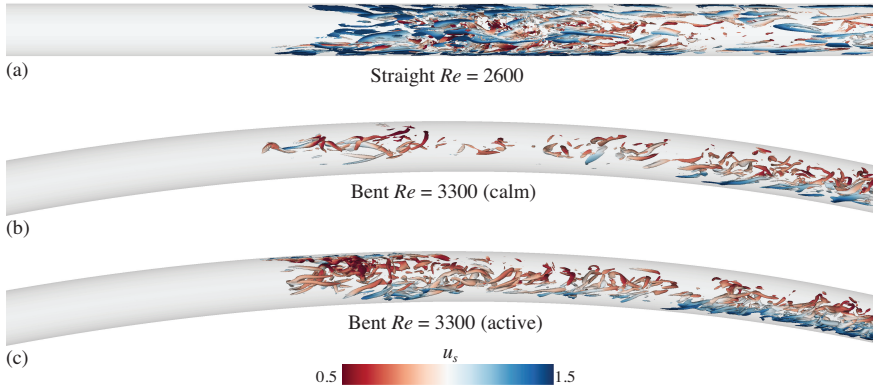


Figure 8: Snapshots of the flow at the upstream front of a slug. The figure depicts iso-contours of negative  $\lambda_2$  coloured by streamwise velocity magnitude. The slug in the bent pipe is represented in both its “calm” and “active” phases. See also the supplemental videos 1–4.

region towards the centre (figure 8(a)). These vortices form a relatively sharp boundary with the laminar flow upstream of the front and are generated at an approximately constant rate, as can be seen in the supplementary video 2. Their concentration in the centre of the pipe reduces downstream of the front and is limited to the near wall region, consistently with the distribution of  $P_k$  discussed in §3.

If the pipe is bent, the upstream front gradually emerges from the laminar flow and is considerably less densely populated by vortical structures. The generation of new vortices is modulated in time and is organised over the succession of “active” and “calm” phases, see figures 8 (b)–(c) and supplementary videos 3–5. This is particularly evident for moderately expanding slugs. During the active phase new vortices are generated at the outer bend, where  $P_k$  is maximum and perturbations are amplified, as discussed in §3. During the calm phase vortical structures are generated at a lower rate near the centre of the pipe. The alternation of calm and active phases is illustrated in figure 9, which reports the time history of the friction Reynolds number and of the total perturbation kinetic energy. The former is defined as  $Re_\tau = (Re/\nu) \sqrt{(R/2\rho)(dp/ds)}$ , and is computed using the mean pressure gradient calculated over the entire domain. The latter reads  $E_{tot} = (1/2) \int_{Vol} \sum \Delta u_i^2 dV$ , with  $\Delta u_i = u_i - U_i$ , and is calculated on a 20-diameter long moving frame of reference centred on the upstream front of the slug. The signal of  $Re_\tau$  shows a decreasing trend that is consistent with the fact that a fully turbulent flow at  $Re = 3300$  is characterised by sub-laminar drag (see Cioncolini & Santini 2006; Noorani & Schlatter 2015). Active and calm phases appear as local oscillations on top of this trend. In particular, active phases correspond to a local plateau and subsequent decrease

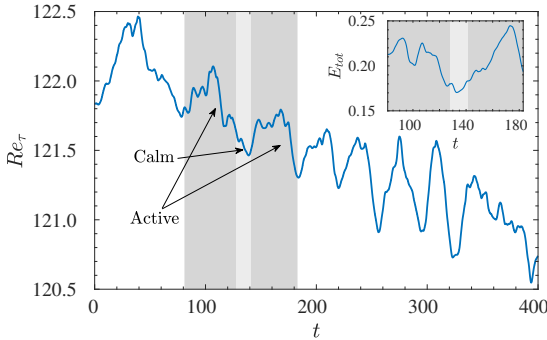


Figure 9: Time history of the friction Reynolds number ( $Re_\tau$ ) calculated over the whole computational domain, and of the perturbation kinetic energy ( $E_{tot}$ ) calculated on a sub-domain co-moving with the upstream front of the slug at  $Re = 3300$ . Dark and light shaded areas highlight examples of active and calm phases at the front.

in the profile of  $Re_\tau$ , and are connected by calm phases where  $Re_\tau$  reaches a local minimum before starting to rise again. Active phases typically last for a time  $t = \mathcal{O}(40 D/U)$ , while calm phases are shorter,  $t = \mathcal{O}(20 D/U)$ . Since  $Re_\tau$  is based on an integral quantity calculated over the whole computational domain, which is filled by the turbulent slug as time advances, the effect of the dynamics at the front is gradually less visible. The perturbation kinetic energy calculated across the slug front shows that active phases consistently correspond to high values of  $E_{tot}$ .

In addition to the spatial localisation and lower values of  $P_k$  discussed in §3, the temporal modulation also contributes to weaker upstream fronts if compared to straight pipes. To the best of our knowledge, this is the first time this phenomenon is documented on the fronts of expanding turbulence in pipe flows.

The curvature also influences the transport of vortices inside the slug. This can be clearly seen in the supplementary video 1, which presents a comparison between a straight and a bent pipe. The video shows vortical structures in a one-diameter long section as seen from inside the pipe while following the upstream front. While in the straight pipe the vortices move chaotically, in the bent pipe they are clearly transported in a coherent circulatory motion dictated by the Dean vortices. This visually shows how a localised production of vortices is sufficient to sustain the extended structure of a slug.

## 5. Summary and conclusions

We have studied the dynamics of localised turbulent structures in a bent pipe with curvature 0.01. The analysis was performed by means of direct numerical

simulations for Reynolds numbers between 2900 and 5000. Our results show that subcritical transition to turbulence occurs over  $3000 \lesssim Re \lesssim 3100$ , where laminar and turbulent flow coexist in an intermittent fashion. The indicated range is significantly narrower than the one documented for a straight pipe, which is in good agreement with the literature on the subject (see, e.g. Sreenivasan & Strykowski 1983; Kühnen *et al.* 2015).

Localised turbulent structures in bent pipes bear qualitative similarities to those in straight pipes in that they appear in the form of puffs and slugs that are sustained by an instability at their upstream front. However, the most striking difference is a substantial weakening of the front if the pipe is bent. We report velocity fluctuations that are three times smaller than the ones observed in straight pipes. Furthermore, the turbulent kinetic energy budget shows that production at the front is at most one-and-a-half times the one in the core of the slug, while in straight pipes it is up to five times larger than in the core. Production and dissipation are strongly localised towards the outer bend, in a region that is highly receptive to flow perturbations. We argue that the emergence of a strong secondary flow (Dean 1927) is responsible for the localisation and is crucial for the effective mixing of vortical structures. A further peculiarity encountered in bent pipes is that the generation of vortices at the front occurs through a succession of active (longer) and calm (shorter) phases, which contribute to the overall small values of production and dissipation. This is to the best of our knowledge the first time that such temporal modulation of the upstream front is reported in pipe flows.

The final difference between bent and straight pipes is the apparent absence of puff splitting when the pipe is bent, at least for the choice of parameters investigated here. Since the genesis of a child puff from a mother puff is a statistical (non-deterministic) phenomenon, we cannot completely exclude it based on our limited number of simulations. A thorough, possibly experimental, investigation focused on this phenomenon should be performed to verify our claim. We conjecture that the absence of puff splitting is connected to the weak and localised upstream fronts. Turbulent structures that leave a mother puff have a low probability of entering the small region of high amplification located near the outer wall, which would trigger the instability that sustains a puff. Moreover, due to the secondary motion, the few vortical structures that visit this region do not linger for long enough to generate a new puff.

Simulations and post-processing were performed on resources provided by the Swedish National Infrastructure for Computing (SNIC) at PDC (Beskow and Tegner). The authors would like to acknowledge M. Schanen and O. Marin their support in developing the nonlinear optimisation routines. Financial support by the Swedish Science Foundation (VR) and the Knut and Alice Wallenberg Foundation via the Wallenberg Academy Fellow programme is gratefully acknowledged.

## REFERENCES

- AVILA, K., MOXEY, D., DE LOZAR, A., AVILA, M., BARKLEY, D. & HOF, B. 2011 The onset of turbulence in pipe flow. *Science* **333** (6039), 192–196.
- BARKLEY, D. 2011 Simplifying the complexity of pipe flow. *Phys. Rev. E* **84** (1), 016309.
- BARKLEY, D. 2012 Pipe flow as an excitable medium. *Rev. Cub. Fis.* **29** (1E), 27–30.
- BARKLEY, D. 2016 Theoretical perspective on the route to turbulence in a pipe. *J. Fluid Mech.* **803**, P1.
- BARKLEY, D., SONG, B., MUKUND, V., LEMOULT, G., AVILA, M. & HOF, B. 2015 The rise of fully turbulent flow. *Nature* **526** (7574), 550–553.
- CANTON, J. 2013 Global linear stability of axisymmetric coaxial jets. Master's thesis, Politecnico di Milano, Italy, <https://www.politesi.polimi.it/handle/10589/87827>.
- CANTON, J., ÖRLÜ, R. & SCHLATTER, P. 2017 Characterisation of the steady, laminar incompressible flow in toroidal pipes covering the entire curvature range. *Int. J. Heat Fluid Flow* **66**, 95–107.
- CANTON, J., SCHLATTER, P. & ÖRLÜ, R. 2016 Modal instability of the flow in a toroidal pipe. *J. Fluid Mech.* **792**, 894–909.
- CERBUS, R. T., LIU, C.-C., GIOIA, G. & CHAKRABORTY, P. 2018 Laws of resistance in transitional pipe flows. *Phys. Rev. Lett.* **120**, 054502.
- CIONCOLINI, A. & SANTINI, L. 2006 An experimental investigation regarding the laminar to turbulent flow transition in helically coiled pipes. *Exp. Therm. Fluid Sci.* **30**, 367–380.
- DARBYSHIRE, A. G. & MULLIN, T. 1995 Transition to turbulence in constant-mass-flux pipe flow. *J. Fluid Mech.* **289**, 83–114.
- DEAN, W. R. 1927 XVI. Note on the motion of fluid in a curved pipe. *London, Edinburgh, Dublin Philos. Mag. J. Sci.* **4**, 208–223.
- DUGUET, Y., WILLIS, A. P. & KERSWELL, R. R. 2010 Slug genesis in cylindrical pipe flow. *J. Fluid Mech.* **663**, 180–208.
- EL KHOURY, G. K., SCHLATTER, P., NOORANI, A., FISCHER, P. F., BRETHOUWER, G. & JOHANSSON, A. V. 2013 Direct numerical simulation of turbulent pipe flow at moderately high reynolds numbers. *Flow Turbul. Combust.* **91** (3), 475–495.
- FISCHER, P. F., LOTTES, J. W. & KERKEMEIR, S. G. 2008 Nek5000 Web page.
- JEONG, J. & HUSSAIN, F. 1995 On the identification of a vortex. *J. Fluid Mech.* **285**, 69–94.
- KÜHNEN, J., BRAUNSHIER, P., SCHWEGEL, M., KUHLMANN, H. C. & HOF, B. 2015 Subcritical versus supercritical transition to turbulence in curved pipes. *J. Fluid Mech.* **770**, R3.
- KÜHNEN, J., HOLZNER, M., HOF, B. & KUHLMANN, H. C. 2014 Experimental investigation of transitional flow in a toroidal pipe. *J. Fluid Mech.* **738**, 463–491.
- LINDGREN, E. R. 1969 Propagation velocity of turbulent slugs and streaks in transition pipe flow. *Phys. Fluids* **12** (2), 418–425.
- MESGUER, Á. & TREFETHEN, L. N. 2003 Linearized pipe flow to Reynolds number 107. *J. Comput. Phys.* **186** (1), 178–197.
- MOXEY, D. & BARKLEY, D. 2010 Distinct large-scale turbulent-laminar states in transitional pipe flow. *Proc. Natl. Acad. Sci. U.S.A.* **107** (18), 8091–8096.

- MULLIN, T. 2011 Experimental studies on transition to turbulence in a pipe. *Annu. Rev. Fluid Mech.* **43**, 1–24.
- NISHI, M., ÜNSAL, B., DURST, F. & BISWAS, G. 2008 Laminar-to-turbulent transition of pipe flows through puffs and slugs. *J. Fluid Mech.* **614**, 425–446.
- NOORANI, A., EL KHOURY, G. K. & SCHLATTER, P. 2013 Evolution of turbulence characteristics from straight to curved pipes. *Int. J. Heat Fluid Flow* **41**, 16–26.
- NOORANI, A. & SCHLATTER, P. 2015 Evidence of sublaminar drag naturally occurring in a curved pipe. *Phys. Fluids* **27**, 035105.
- PRINGLE, C. C. T. & KERSWELL, R. R. 2010 Using nonlinear transient growth to construct the minimal seed for shear flow turbulence. *Phys. Rev. Lett.* **105**, 154502.
- REYNOLDS, O. 1883 An experimental investigation of the circumstances which determine whether the motion of water shall be direct or sinuous, and of the law of resistance in parallel channels. *Phil. Trans. R. Soc. Lond.* **174**, 935–982.
- SCHANEN, M., MARIN, O., ZHANG, H. & ANITESCU, M. 2016 Asynchronous two-level checkpointing scheme for large-scale adjoints in the spectral-element solver Nek5000. *Procedia Comput. Sci.* **80**, 1147–1158.
- SHIH, H.-Y., HSIEH, T.-L. & GOLDENFELD, N. 2015 Ecological collapse and the emergence of travelling waves at the onset of shear turbulence. *Nature Physics* **12**, 245–248.
- SONG, B., BARKLEY, D., HOF, B. & AVILA, M. 2017 Speed and structure of turbulent fronts in pipe flow. *J. Fluid Mech.* **813**, 1045–1059.
- SREENIVASAN, K. R. & STRYKOWSKI, P. J. 1983 Stabilization effects in flow through helically coiled pipes. *Exp. Fluids* **1**, 31–36.
- WEBSTER, D. R. & HUMPHREY, J. A. C. 1993 Experimental observations of flow instability in a helical coil (Data bank contribution). *J. Fluid Eng.-T. ASME* **115**, 436–443.
- WEBSTER, D. R. & HUMPHREY, J. A. C. 1997 Travelling wave instability in helical coil flow. *Phys. Fluids* **9**, 407–418.
- WHITE, C. M. 1929 Streamline flow through curved pipes. *Proc. R. Soc. London Ser. A* **123**, 645–663.
- WYGNANSKI, I. J. & CHAMPAGNE, F. H. 1973 On transition in a pipe. Part 1. The origin of puffs and slugs and the flow in a turbulent slug. *J. Fluid Mech.* **59** (2), 281–335.
- WYGNANSKI, I. J., SOKOLOV, M. & FRIEDMAN, D. 1975 On transition in a pipe. Part 2. The equilibrium puff. *J. Fluid Mech.* **69** (2), 283–304.

# Paper 5

5



# A critical point for bifurcation cascades and intermittency

Jacopo Canton, Enrico Rinaldi, Ramis Örlü,  
and Philipp Schlatter

Linné FLOW Centre and Swedish e-Science Research Centre (SeRC), KTH  
Mechanics, Royal Institute of Technology, SE-100 44 Stockholm, Sweden

*To be submitted (2018)*

Transition to turbulence in straight pipe flow is a subcritical process, dominated by the proliferation of isolated patches of turbulence. However, experiments and computations suggest that when the pipe is bent above a pipe-to-coiling diameter ratio  $\delta \gtrsim 0.028$  a supercritical Hopf bifurcation initiates a cascade, leading through increasing flow complexity and, ultimately, to a fully turbulent state. In this Letter we prove this speculation correct by reconstructing, from nonlinear simulations at  $\delta = 0.05$ , a stable two-periodic attractor and measuring incommensurable frequencies in the flow. We also report evidence, in a limited region of the  $\delta - Re$  parameter space, of the coexistence of fully turbulent flow and of a stable supercritical limit cycle; both being attracting states with finite and complementary basins. This is the first time that a fluid flow is shown to be stable in both turbulent and laminar states (other than the steady solution) for a fixed combination of flow parameters.

**Key words:** transition to turbulence, dynamical systems, intermittency

---

Transition to turbulence in shear flows has been of primary interest to fluid dynamicists and engineers at least since the seminal experiments by Reynolds in 1883 (Reynolds 1883). The motivation driving research through the past 130 years, besides the intrinsic appeal of the subject, is the possibility of delaying, or even suppressing, turbulence hence reducing drag and costs.

Early studies on transition focused on finding linear instabilities of the laminar state. This approach proved to be successful for several flow cases: Rayleigh–Bénard thermally driven convection, Taylor–Couette (when only the inner cylinder rotates) and the flow around a circular cylinder are but a few examples. However, linear theory fails in other flow cases, such as plane Poiseuille (channel) flow, Couette and Hagen–Poiseuille (straight pipe) flow, where experiments detect turbulence at Reynolds numbers  $Re$  (non-dimensional flow rate) where no linear instability is predicted. For these flow cases transition to turbulence is initiated by finite amplitude perturbations, and is characterised

by large-scale spatio-temporal intermittency and the proliferation of isolated patches of chaotic motion (puffs in pipes, stripes in channels and Couette).

In the past two decades, a successful approach to subcritical transition has borrowed tools from nonlinear dynamical systems theory. The accepted picture is that of a phase space populated by exact unstable solutions of the Navier–Stokes equations, e.g. travelling waves or periodic orbits. These states are transiently visited by trajectories which leave the laminar attractor, when sufficiently perturbed, and eventually enter the stable manifold of turbulence (Hof *et al.* 2004; Schneider *et al.* 2007; Duguet *et al.* 2008; Budanur *et al.* 2017). An alternative take on the subject is the analogy between the onset of subcritical transition and non-equilibrium phase transition, in particular directed percolation (DP). Pomeau (1986) suggested this connection more than 30 years ago, yet the theory was only recently corroborated by experiments and numerical simulations in channel and Couette flows, where the universal exponents of DP were calculated (Lemoult *et al.* 2016; Sano & Tamai 2016; Chantry *et al.* 2017). Transition to turbulence in a straight pipe bears similarities to other shear flows, e.g. Couette flow, in particular regarding the superexponential dependence of puff decay and splitting time scales on  $Re$  (Avila *et al.* 2011), which is well captured by analytical models (Barkley *et al.* 2015; Shih *et al.* 2015). Notably, the second referenced model is asymptotically equivalent to DP at the critical  $Re$  for transition. However, an experimental proof of this link in straight pipe flow is still missing, due to the prohibitively long observation times (three orders of magnitude longer than for Couette flow).

There exists few flow cases where both of the transition scenarios described above can be observed. Whether transition is subcritical, triggered by finite amplitude perturbations, or supercritical, caused by a linear instability, depends on some specific choices of the flow parameters. Examples are Taylor–Couette and rotating Couette flow, for which a change in the direction of rotation clearly separates the two transition scenarios (Andereck *et al.* 1986; Tsukahara *et al.* 2010). The flow in a bent pipe is a unique example of this class of fluid flows: here the thresholds for subcritical and supercritical transition intersect as one of the two flow parameters—the pipe-to-coiling diameter ratio  $\delta$ —is gradually changed (Kühnen *et al.* 2015). Experiments and numerical simulations have shown that transition is subcritical below  $\delta \approx 0.028$  and that the phenomenology is similar to the flow in a straight pipe (Sreenivasan & Strykowski 1983; Kühnen *et al.* 2015; Rinaldi *et al.* 2018). On the other hand, for larger curvatures transition is initiated by the appearance of a supercritical Hopf bifurcation (Kühnen *et al.* 2014, 2015; Canton *et al.* 2016). In this case, the spatio-temporal complexity of the flow increases with  $Re$  in what experiments suggest to be a cascade of Hopf bifurcations, eventually leading to the fully turbulent state. To date there are, however, no precise measurements of incommensurable frequencies that would confirm this scenario. Another intriguing question from the dynamical systems perspective is what happens in the region of the parameter space where subcritical and supercritical transition coexist and possibly overlap.

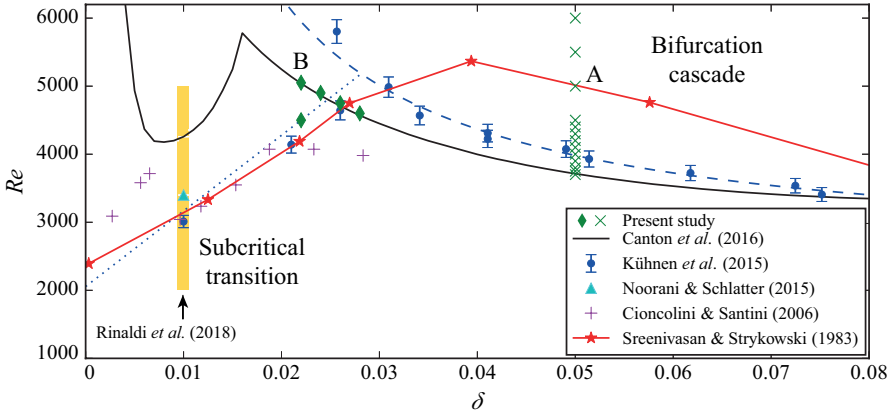


Figure 1: Portion of the  $\delta - Re$  parameter space of the flow in a toroidal pipe. Experimental and numerical data from the literature are reported as well as the location of the present computations. The data by Cioncolini & Santini (2006) refers to the first discontinuity in their friction measurements, while the data by Sreenivasan & Strykowski (1983) is the curve they refer to as the “conservative lower critical limit”. Point A is supercritical, and illustrated in figure 2(b), while point B is critical and is detailed in figure 3.

In this Letter we address these issues by performing direct numerical simulations (DNS) of the flow in a toroidal pipe<sup>1</sup>, where the Reynolds number is based on pipe diameter  $D$ , bulk velocity  $U$  and kinematic viscosity  $\nu$ , *i.e.*  $Re = UD/\nu$ . Our aim is i) to provide the first accurate measurements of the supercritical bifurcation cascade at moderate–high curvatures and ii) to map the flow behaviour in the region of parameter space where the line for the onset of subcritical transition intersects the neutral curve of the Hopf bifurcation (referred to as *critical point* in the following). The second point is of particular relevance, as there are no known fluid flows where these two diametrically opposed scenarios coexist.

As a first step we focus on curvature  $\delta = 0.05$ , which is far enough from the critical point to guarantee the absence of subcritical transition. Canton *et al.* (2016) previously verified with nonlinear simulations that the flow does indeed undergo a Hopf bifurcation, as predicted by their modal analysis, but stopped this investigation at  $Re = 4000$ . Figure 2(a) depicts the state of the system at this Reynolds number: the flow is constituted by the nonlinear travelling wave caused by a supercritical Hopf bifurcation, and all trajectories in the phase space eventually converge to the corresponding limit cycle. The power spectral density (PSD) of the velocity signal shows the presence of a single frequency,  $f_1 \approx 0.48$ , and its harmonics (made dimensionless with bulk velocity

<sup>1</sup>The incompressible Navier–Stokes equations are solved using the open-source code NEK5000 (Fischer *et al.* 2008). The numerical setup was previously validated for straight and bent pipes (El Khoury *et al.* 2013; Noorani *et al.* 2013).

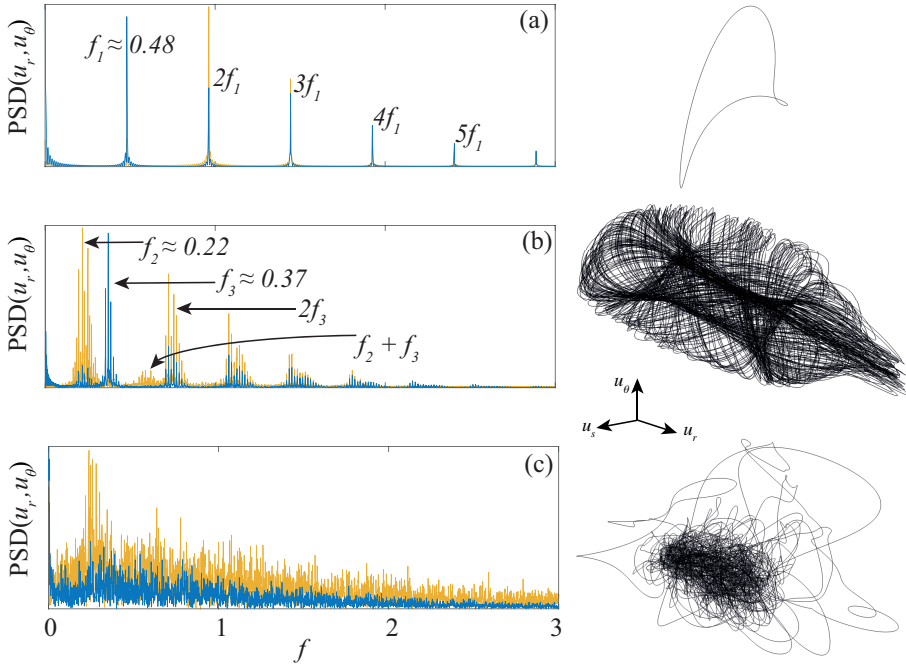


Figure 2: Power spectral densities (PSD) and corresponding phase spaces for point velocity measurements at  $\delta = 0.05$  and  $Re = 4000$  (a),  $Re = 4500$  (b), and  $Re = 6000$  (c). Yellow lines represent the PSD of  $u_r$ , while blue lines are the PSD of  $u_\theta$ .

and pipe diameter, *i.e.*  $f = f^* D/U$ ). When the Reynolds number is increased the system undergoes a second Hopf bifurcation to a quasi-periodic orbit. The attractor is now a torus  $T^2$ , depicted in figure 2(b), and the PSD highlights two incommensurable frequencies,  $f_2$  and  $f_3$ , with their linear combinations and higher harmonics. As the Reynolds number is increased further the flow eventually becomes turbulent, as can be seen in figure 2(c). Here the power spectrum is characterised through its broadband nature, although two or three peaks can still be isolated with the knowledge gained at lower  $Re$ , and the trajectory in the corresponding phase space is chaotic. A quasi-periodic 3-torus could not, at the moment of writing, be detected; however, Newhouse *et al.* (1978) showed that for  $T^m$  tori with  $m \geq 3$  any arbitrarily small disturbance can lead the system to chaos. We can conclude—given that the neutral curve of the first Hopf bifurcation extends to  $\delta = 1$  (Canton *et al.* 2016)—that for curvatures sufficiently higher than  $\delta \approx 0.025$  the flow undergoes a Ruelle–Takens–Newhouse route to chaos (Ruelle & Takens 1971; Newhouse *et al.* 1978). This scenario was previously hypothesised by Kühnen *et al.* (2014) who, however, could not make measurements with sufficient accuracy.

We now turn our attention to the region of parameter space where the neutral curve meets the lines indicating subcritical transition, *i.e.*  $\delta \approx 0.025$  and

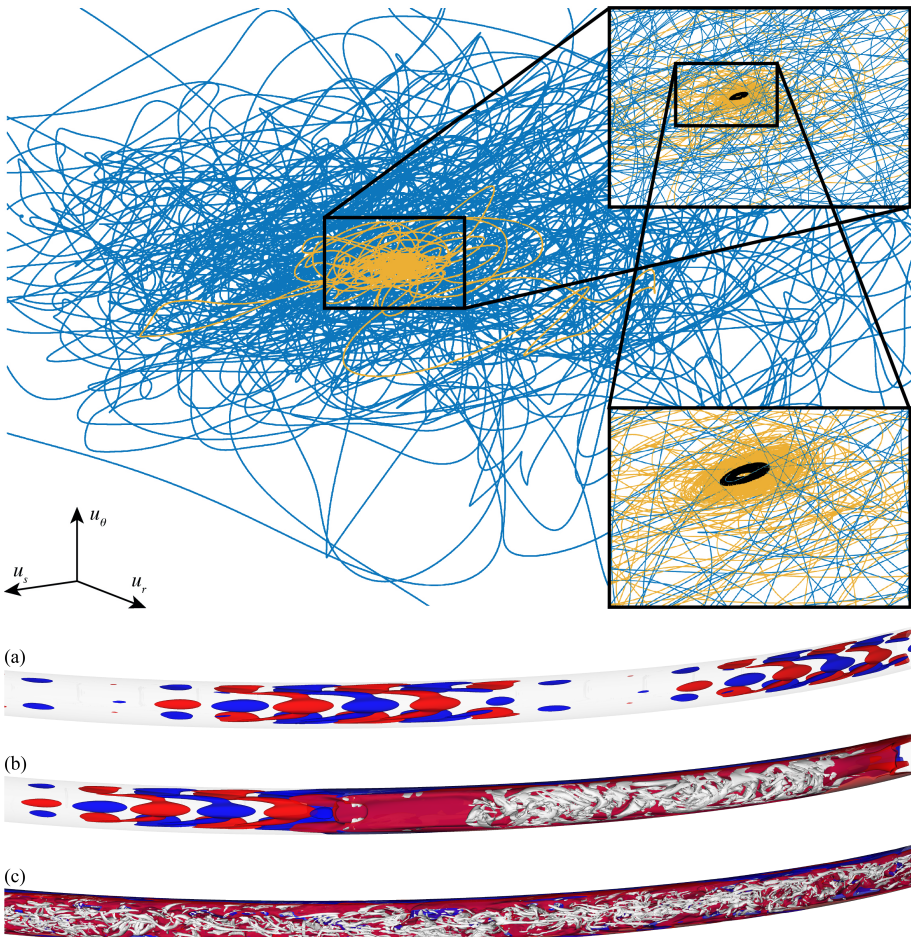


Figure 3: Top: phase space for  $\delta = 0.022$  and  $Re = 5050$  (point B in figure 1). All trajectories start in the neighbourhood of the travelling wave, the closest being the black line (a snapshot is depicted in panel (a)). The yellow trajectory is turbulent for  $t \approx 100D/U$  and then slowly returns to the stable limit cycle (snapshot in panel (b)), while the blue trajectory remains turbulent for  $t > 1000D/U$  (snapshot in panel (c)). Bottom: snapshots of the flow field along the three phase space trajectories. Red and blue colours are isocontours of streamwise velocity for two opposite values, *i.e.*  $u_s = \pm 0.005U$ ; white isocontours are of negative  $\lambda_2$ .

$4000 < Re < 5000$ . As a first step it is necessary to verify that both sub- and supercritical behaviours can still be isolated. We therefore perform nonlinear simulations for  $\delta = 0.022$  and  $Re = 4500$ , with two domains of different length, about  $10D$  and  $20D$ , respectively. The simulations are initialised with puffs

computed by Rinaldi *et al.* (2018) which, for both domains, grow in length in the form of slugs and turn the whole domain to turbulent flow, confirming once more the subcritical transition lines by Sreenivasan & Strykowski (1983); Kühnen *et al.* (2015) and the findings by Rinaldi *et al.* (2018). The second verification is at  $\delta = 0.028$  and  $Re = 4600$ , just above the neutral curve, which for this curvature marks the linear instability at  $Re = 4570$ , and below the subcritical transition thresholds. Here the flow is initialised with a paraboloidal profile perturbed with random noise, and converges to the nonlinear travelling wave created by the Hopf bifurcation, as previously explained for  $\delta = 0.05$ .

We proceed by lowering the curvature, while remaining above the neutral curve, and investigate three more pairs of  $(\delta, Re)$ , *i.e.*  $(0.026, 4750)$ ,  $(0.024, 4900)$ , and  $(0.022, 5050)$ . The last pair of values corresponds to point B in figure 1, and is illustrated in figure 3. In this region of parameter space the two transition scenarios coexist. The beginning of the Ruelle–Takens–Newhouse route to chaos can be observed in the form of stable, nonlinear travelling waves, while subcritical transition is found in the form of expanding slugs. In point B, for example, a simulation initialised with a randomly perturbed parabolic velocity profile slowly converges to a nonlinear travelling wave, as predicted by the modal analysis. This process is illustrated by the black trajectory in the phase space of figure 3 and with a snapshot of the flow field in figure 3(a). On the other hand, if the simulation is initialised with a localised disturbance, the disturbance grows and invades the whole pipe, turning the flow into a fully turbulent state; in agreement with the location of the lines indicating subcritical transition.

The intermediate cases are what makes this flow unique. When the travelling wave is perturbed with a *highly* energetic puff the subcritical transition scenario dominates: the puff expands and creates a fully turbulent flow. For this particular combination of  $\delta$  and  $Re$ , *highly* energetic means that the kinetic energy of the puff,  $E_{k,\text{puff}}$ , has to be more than approximately 6.3 times that of the travelling wave,  $E_{k,\text{wave}}$ . This is the case represented by the blue trajectory in figure 3 and the corresponding flow field in panel (c), where the white  $\lambda_2$  isocontours (Jeong & Hussain 1995) illustrate the spatially chaotic nature of turbulence, while the temporal disorder is visualised by the trajectory. Conversely, if the puff has lower energy, *i.e.*  $E_{k,\text{puff}} < 6.3E_{k,\text{wave}}$ , it will grow in size but only transiently, before diffusing and disappearing completely. The yellow trajectory in figure 3 illustrates this process: it starts from an initial condition close to that represented in panel (b), then travels through the turbulent region of phase space (main panel and upper insert), and finally returns to the attracting limit cycle of the travelling wave (lower insert). We can conclude that both transition mechanisms, sub- and supercritical, are present in this critical region of parameter space. The structures corresponding to these processes are all stable, and their basins of attraction are complementary and finite. This is the first time that these two transition scenarios are shown to coexist.

Financial support by the Swedish Research Council (VR) and the Knut and Alice Wallenberg Foundation via the Wallenberg Academy Fellow programme is gratefully acknowledged. Computer time was provided by the Swedish National Infrastructure for Computing (SNIC).

#### REFERENCES

- ANDERECK, C. D., LIU, S. S. & SWINNEY, H. L. 1986 Flow regimes in a circular Couette system with independently rotating cylinders. *J. Fluid Mech.* **164**, 155–183.
- AVILA, K., MOXEY, D., DE LOZAR, A., AVILA, M., BARKLEY, D. & HOF, B. 2011 The onset of turbulence in pipe flow. *Science* **333** (6039), 192–196.
- BARKLEY, D., SONG, B., MUKUND, V., LEMOULT, G., AVILA, M. & HOF, B. 2015 The rise of fully turbulent flow. *Nature* **526** (7574), 550–553.
- BUDANUR, N. B., SHORT, K. Y., FARAZMAND, M., WILLIS, A. P. & CVITANOVIĆ, P. 2017 Relative periodic orbits form the backbone of turbulent pipe flow. *J. Fluid Mech.* **833**, 274–301.
- CANTON, J., SCHLATTER, P. & ÖRLÜ, R. 2016 Modal instability of the flow in a toroidal pipe. *J. Fluid Mech.* **792**, 894–909.
- CHANTRY, M., TUCKERMAN, L. S. & BARKLEY, D. 2017 Universal continuous transition to turbulence in a planar shear flow. *J. Fluid Mech.* **824**, R1.
- CIONCOLINI, A. & SANTINI, L. 2006 An experimental investigation regarding the laminar to turbulent flow transition in helically coiled pipes. *Exp. Therm. Fluid Sci.* **30**, 367–380.
- DUGUET, Y., WILLIS, A. & KERSWELL, R. R. 2008 Transition in pipe flow: The saddle structure on the boundary of turbulence. *J. Fluid Mech.* **613**, 255–274.
- EL KHOURY, G. K., SCHLATTER, P., NOORANI, A., FISCHER, P. F., BRETHOUWER, G. & JOHANSSON, A. V. 2013 Direct numerical simulation of turbulent pipe flow at moderately high reynolds numbers. *Flow Turbul. Combust.* **91** (3), 475–495.
- FISCHER, P. F., LOTTES, J. W. & KERKEMEIR, S. G. 2008 Nek5000 Web page.
- HOF, B., VAN DOORNE, C. W. H., WESTERWEEL, J., NIEUWSTADT, F. T. M., FAISST, H., ECKHARDT, B., WEDIN, H., KERSWELL, R. R. & WALEFFE, F. 2004 Experimental observation of nonlinear traveling waves in turbulent pipe flow. *Science* **305**, 1594–1598.
- JEONG, J. & HUSSAIN, F. 1995 On the identification of a vortex. *J. Fluid Mech.* **285**, 69–94.
- KÜHNEN, J., BRAUNSHIER, P., SCHWEGEL, M., KUHLMANN, H. C. & HOF, B. 2015 Subcritical versus supercritical transition to turbulence in curved pipes. *J. Fluid Mech.* **770**, R3.
- KÜHNEN, J., HOLZNER, M., HOF, B. & KUHLMANN, H. C. 2014 Experimental investigation of transitional flow in a toroidal pipe. *J. Fluid Mech.* **738**, 463–491.
- LEMOULT, G., SHI, L., AVILA, K., JALIKOP, S. V., AVILA, M. & HOF, B. 2016 Directed percolation phase transition to sustained turbulence in Couette flow. *Nature Phys.* **12**, 254–258.
- NEWHOUSE, S., RUELLE, D. & TAKENS, F. 1978 Occurrence of strange axiom A attractors near quasi periodic flows on  $T^m$ ,  $m \geq 3$ . *Commun. Math. Phys.* **64**, 35–40.

- NOORANI, A., EL KHOURY, G. K. & SCHLATTER, P. 2013 Evolution of turbulence characteristics from straight to curved pipes. *Int. J. Heat Fluid Flow* **41**, 16–26.
- POMEAU, D. 1986 Front motion, metastability and subcritical bifurcations in hydrodynamics. *Physica D* **23**, 3–11.
- REYNOLDS, O. 1883 An experimental investigation of the circumstances which determine whether the motion of water shall be direct or sinuous, and of the law of resistance in parallel channels. *Phil. Trans. R. Soc. Lond.* **174**, 935–982.
- RINALDI, E., CANTON, J. & SCHLATTER, P. 2018 The collapse of strong turbulent fronts in bent pipes. *Submitted*.
- RUELLE, D. & TAKENS, F. 1971 On the nature of turbulence. *Commun. Math. Phys.* **20** (3), 167–192.
- SANO, M. & TAMAI, K. 2016 A universal transition to turbulence in channel flow. *Nature Phys.* **12**, 249–253.
- SCHNEIDER, T. M., ECKHARDT, B. & YORKE, J. A. 2007 Turbulence transition and the edge of chaos in pipe flow. *Phys. Rev. Lett.* **99** (3), 034502.
- SHIH, H.-Y., HSIEH, T.-L. & GOLDENFELD, N. 2015 Ecological collapse and the emergence of travelling waves at the onset of shear turbulence. *Nature Physics* **12** (3), 245.
- SREENIVASAN, K. R. & STRYKOWSKI, P. J. 1983 Stabilization effects in flow through helically coiled pipes. *Exp. Fluids* **1**, 31–36.
- TSUKAHARA, T., TILLMARK, N. & ALFREDSSON, P. H. 2010 Flow regimes in a plane Couette flow with system rotation. *J. Fluid Mech.* **648**, 5–33.

# Paper 6

6



# The three-dimensional structure of swirl-switching in bent pipe flow

Lorenz Hufnagel<sup>1</sup>, Jacopo Canton<sup>1</sup>, Ramis Örlü<sup>1</sup>, Oana Marin<sup>2</sup>, Elia Merzari<sup>2</sup> and Philipp Schlatter<sup>1</sup>

<sup>1</sup>Linné FLOW Centre and Swedish e-Science Research Centre (SeRC), KTH Mechanics, Royal Institute of Technology, SE-100 44 Stockholm, Sweden

<sup>2</sup>Mathematics and Computer Science Division, Argonne National Laboratory, Argonne, IL, USA

*Journal of Fluid Mechanics* (2018), vol. **835**, 86–101

Swirl-switching is a low-frequency oscillatory phenomenon which affects the Dean vortices in bent pipes and may cause fatigue in piping systems. Despite thirty years worth of research, the mechanism that causes these oscillations and the frequencies that characterise them remain unclear. Here we show that a three-dimensional wave-like structure is responsible for the low-frequency switching of the dominant Dean vortex. The present study, performed via direct numerical simulation, focuses on the turbulent flow through a 90° pipe bend preceded and followed by straight pipe segments. A pipe with curvature 0.3 (defined as ratio between pipe radius and bend radius) is studied for a bulk Reynolds number  $Re = 11\,700$ , corresponding to a friction Reynolds number  $Re_\tau \approx 360$ . Synthetic turbulence is generated at the inflow section and used instead of the classical recycling method in order to avoid the interference between recycling and swirl-switching frequencies. The flow field is analysed by three-dimensional proper orthogonal decomposition (POD) which for the first time allows the identification of the source of swirl-switching: a wave-like structure that originates in the pipe bend. Contrary to some previous studies, the flow in the upstream pipe does not show any direct influence on the swirl-switching modes. Our analysis further shows that a three-dimensional characterisation of the modes is crucial to understand the mechanism, and that reconstructions based on 2D POD modes are incomplete.

**Key words:** pipe flow boundary layer, turbulence simulation

---

## 1. Introduction

Bent pipes are an essential component of a large number of industrial machines and processes. They are ideal for increasing mass and momentum transfer, passively mixing different fluids, which makes them effective as heat exchangers, inverters, and other appliances. For a review of the applications of bent pipes in

industry see Vashisth *et al.* (2008); the most recent advances in experiments and simulations can be found in the review by Kalpakli Vester *et al.* (2016). The high mass and momentum transfer is generated by the secondary motion caused by the centrifugal force acting on the fluid in the curved sections. This secondary motion, which is of Prandtl's first kind, takes the shape of two counter-rotating vortices, illustrated in figure 1, which move the fluid towards the outside of the bend, along the centreline, and back towards the inside along the wall, therefore increasing the mass and momentum transfer across the pipe section.

These vortices were first observed by Boussinesq (1868) and Eustice (1910), and later described analytically by Dean (1928) from whom they received the name of Dean vortices. The intensity of these vortices increases with Reynolds number, here based on pipe diameter and bulk velocity (*i.e.*  $Re = DU_b/\nu$ , where  $\nu$  is the kinematic viscosity of the fluid), as well as with pipe curvature, defined as the ratio between pipe radius and bend radius,  $\delta = R/R_c$  (see Canton *et al.* 2017 for laminar flow; Noorani *et al.* 2013, the review by Kalpakli Vester *et al.* 2016, and references therein, for turbulent flows).

For laminar, steady flow the Dean vortices are symmetric with respect to the bend symmetry plane (the *I-O* plane in figure 1); but when the flow becomes unstable the vortices start oscillating periodically (Kühnen *et al.* 2014, 2015; Canton *et al.* 2016). These large-scale oscillations are caused by the appearance of periodic travelling waves which, as also observed in other flows (see, *e.g.* Hof *et al.* 2004), are at the base of transition to turbulence for toroidal and helical pipes.

A different kind of large-scale oscillations is observed for high Reynolds numbers: here the turbulent flow is modulated by a low-frequency alternation of the dominant Dean vortex. This vortex alternation excites the pipe structure and is presumed to be the cause of structural, low-frequency oscillations observed in heat exchangers (*e.g.* in microgravity conditions such as in a test for the international space station; Brücker 1998), as well as the origin of secondary motion in the bends of the cooling system of nuclear reactors (Kalpakli Vester *et al.* 2016). The Dean vortex alternation was initially, and unexpectedly, observed by Tunstall & Harvey (1968), who experimentally studied the turbulent flow through a sharp, L-shaped bend ( $\delta = 1$ ). These authors measured "low random-frequency" switches between two distinct states and, by means of flow visualisations, were able to identify an either clockwise or anti-clockwise predominance of the swirling flow following the bent section. The switching was found to have a Strouhal number  $St = fD/U_b$  highly dependent on  $Re$  and comprised between  $2 \times 10^{-4}$  and  $4.5 \times 10^{-3}$ . Tunstall & Harvey attributed the origin of the switching to the presence of a separation bubble in the bend and to the "occasional existence of turbulent circulation entering the bend".

To the best of our knowledge, the first author to continue the work by Tunstall & Harvey (1968) was Brücker (1998), who analysed the phenomenon via particle image velocimetry (PIV) and coined the term "swirl-switching". Brücker studied a smoothly curved pipe with  $\delta = 0.5$  and identified the oscillations as a

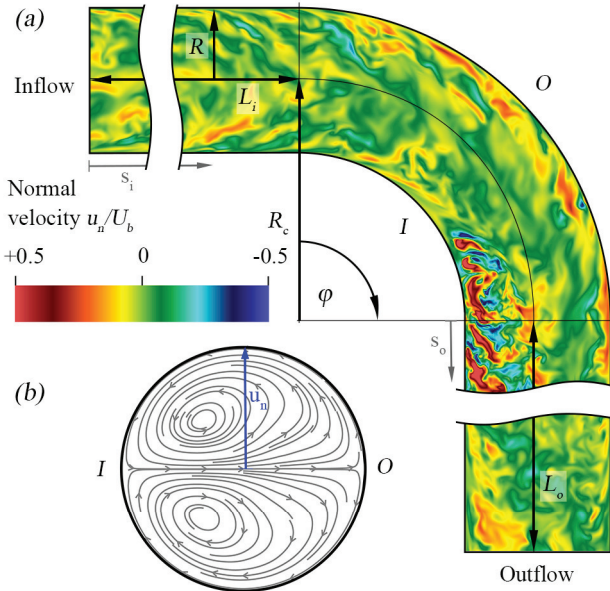


Figure 1: Schematic of the computational domain. (a) A section of the pipe with curvature  $\delta = R/R_c = 0.3$ , including the definition of the geometrical parameters and an instantaneous flow field coloured by normal velocity, *i.e.* normal to the bend symmetry plane. (b) Streamlines of the mean cross-flow showing the Dean vortices on a cross-section extracted at  $s_o = 0$ . An animated view of the setup is provided in the supplementary online material, `movie1.m4v`.

continuous transition between two mirror-symmetric states with one Dean cell larger than the other. He confirmed that the switching takes place only when the flow is turbulent, and he reported two distinct peaks,  $St = 0.03$  and  $0.12$ , at frequencies considerably higher than those measured by Tunstall and Harvey, despite the lower Reynolds numbers considered.

Rütten *et al.* (2001, 2005) were the first to numerically study swirl-switching by performing large-eddy simulations (LES) for  $\delta = 0.167$  and  $0.5$ . The main result of this analysis is that the switching takes place even without flow separation; moreover, Rütten and co-workers found that the structure of the switching is more complex than just the alternation between two distinct symmetric states, since the outer stagnation point “can be found at any angular position within  $\pm 40^\circ$ ”. Rütten *et al.* found a high-frequency peak at  $St \approx 0.2$ , attributed to a shear-layer instability, and, only for their high Reynolds number case, one low-frequency peak for  $St \approx 5.5 \times 10^{-3}$ , which was connected to the swirl-switching. However, the simulations for Rütten *et al.*’s work were performed by using a “recycling” method, where the results from a straight pipe simulation were used as inflow condition for the bent pipe. These periodic

straight pipes were of length  $L = 3.5D$  and  $5D$  and likely influenced the frequencies measured in the bent pipes since the periodicity of the straight pipes introduced a forcing for  $St = U_b/L = 1/3.5$  and  $1/5$ , respectively.

Sakakibara *et al.* (2010) were the first to analyse the flow by means of two-dimensional proper orthogonal decomposition (2D POD) performed on snapshots extracted from stereo PIV. Their results for  $\delta = 0.75$  reveal anti-symmetric structures that span the entire pipe cross-section and contain most of the energy of the flow. A spectral analysis of the corresponding time coefficients shows peaks between  $St \approx 0.07$  at  $s_o = 2D$  and  $St \approx 0.02$  for  $s_o = 25D$ , in the range found by Brücker (1998). In a subsequent work Sakakibara & Machida (2012) conjectured that the swirl-switching is caused by very large-scale motions (VLSM) formed in the straight pipe preceding the bend.

Hellström *et al.* (2013) and Kalpakli & Örlü (2013) also presented results based on 2D POD. The former performed experiments for  $\delta = 0.5$  and found non-symmetric modes resembling a tilted variant of the Dean vortices with  $St = 0.16$  and  $0.33$ , corresponding to the shear-layer instabilities found by Rütten *et al.* (2005). Kalpakli & Örlü (2013), on the other hand, studied a pipe with  $\delta = 0.31$ ; differently from previous works, the section of straight pipe following the bend was only 0.67 diameters long. Their results at the exit of this short segment show clearly antisymmetric modes as most dominant structures. The swirl-switching frequency obtained from the POD time coefficients was  $St = 0.04$ ; peaks of  $St = 0.12$  and  $0.18$  were also measured but were found not to be related to swirl-switching. In a later work Kalpakli Vester *et al.* (2015) repeated the experiments for  $\delta = 0.39$  and found again a dominant frequency corresponding to  $St = 0.04$ .

Carlsson *et al.* (2015) performed LES in a geometry similar to that of Kalpakli & Örlü (2013), namely, with a short straight section following the bend, for four different curvatures. The inflow boundary condition was generated by means of a recycling method, as in Rütten *et al.* (2001, 2005), with a straight pipe of length  $7D$ , exciting the flow in the bent pipe at  $St = 1/7$ . The three lower curvatures were therefore dominated by the spurious frequencies artificially created in the straight pipe by the recycling method, while the frequencies measured for  $\delta = 1$ , corresponding to  $0.5 < St < 0.6$ , were in the same range identified by Hellström *et al.* (2013) but were found to be mesh dependent.

Noorani & Schlatter (2016) were the first to investigate the swirl-switching by means of direct numerical simulations (DNS). By using a toroidal pipe they showed that swirl-switching is not caused by structures coming from the straight pipe preceding the bend, but is a phenomenon inherent to the curved section. Two curvatures were investigated,  $\delta = 0.1$  and  $0.3$ , and both presented a pair of antisymmetric Dean vortices as the most energetic POD mode with  $St = 0.01$  and  $0.087$ .

Table 1 summarises the main results of the aforementioned studies. It is clear from this literature review that there is a strong disagreement among previous works not only on what is the mechanism that leads to swirl-switching,

Reference	$\delta$	$Re$	$St$
Tunstall & Harvey (1968)	1	50 000 – 230 000	$2 \times 10^{-4} – 4.5 \times 10^{-3}$
Brücker (1998)	0.5	5 000	0.03, 0.12
Rütten <i>et al.</i> (2001, 2005)	0.167, 0.5	27 000	$5.5 \times 10^{-3}$
Sakakibara <i>et al.</i> (2010)	0.75	120 000	0.02 – 0.07
Hellström <i>et al.</i> (2013)	0.5	25 000	0.16, 0.33
Kalpakli & Örlü (2013)	0.31	34 000	0.04
Kalpakli Vester <i>et al.</i> (2015)	0.39	24 000	0.04
Carlsson <i>et al.</i> (2015)	0.32, 0.5, 0.7, 1	34 000	0.003 – 0.01, 0.13, 0.5 – 0.6
Noorani & Schlatter (2016)	0.1, 0.3	11 700	0.01, 0.087

Table 1: Reference Strouhal numbers measured in previous studies and attributed to swirl-switching. The analysis in the present work is performed at  $Re = 11\,700$  in a bent pipe with curvature  $\delta = 0.3$ .

but also on what is the frequency that characterises this phenomenon. In the present work an answer to both questions will be given, which will also explain the discrepancies between previous studies.

The paper continues with a description of the numerical methods employed for the analysis, presented in §2, devoting special attention to the inflow boundary conditions. The results of the simulations and POD analysis are presented in §3 and are discussed and compared with the literature in §4.

## 2. Analysis methods

### 2.1. Numerical discretisation

The present analysis is performed via DNS of the incompressible Navier–Stokes equations. The equations are discretised with the spectral-element code `Nek5000` (Fischer *et al.* 2008) using a  $\mathbb{P}_N - \mathbb{P}_{N-2}$  formulation. After an initial mesh-dependency study, the polynomial order was set to  $N = 8$  for the velocity and, consequently,  $N = 6$  for the pressure. We consider a  $90^\circ$  bent pipe with curvature  $\delta = 0.3$  for a Reynolds number  $Re = 11\,700$ , corresponding to a friction Reynolds number  $Re_\tau \approx 360$  (referred to the straight pipe sections). A straight pipe of length  $L_i = 7D$  precedes the bent section (see §3.1), and a second straight segment of length  $L_o = 15D$  follows it. Further details about the mesh, including element number and size, are reported in table 2. The supplementary video `movie1.m4v` shows the setup and a visualization of the flow.

### 2.2. Inflow boundary and divergence-free synthetic eddy method

Since the aim of the present work is to reproduce and study swirl-switching, a periodic or quasi-periodic phenomenon, the treatment of the inflow boundary is of utmost importance. The flow field prescribed at the inflow boundary should not introduce any artificial frequency, in order to avoid the excitation of unphysical phenomena or a modification of the frequencies inherent to the swirl-switching. A recycling method, as the one used by Rütten *et al.* (2001,

$n_{\text{el}}$	$n_{\text{dof}}$	$\Delta r^+$	$\Delta(R\theta)^+$	$\Delta z^+$
$\delta = 0.3$	480 000	595 258 500	(0.56, 4.89)	(2.26, 4.40)

Table 2: Details of the mesh employed in the present work.  $n_{\text{el}}$  corresponds to the number of hexahedral elements, while  $n_{\text{dof}}$  is the total number of degrees of freedom (velocity and pressure). Quantities indicated as  $(\cdot)^+$  are reported in viscous scaling, and the numbers between parenthesis correspond to minimum and maximum values.

2005) and Carlsson *et al.* (2015), should therefore be avoided, as highlighted in §1.

In the present work the velocity field at the inlet boundary of the straight pipe preceding the bend is prescribed via a divergence-free synthetic eddy method (DFSEM). This method, introduced by Poletto *et al.* (2011) and based on the original work by Jarrin *et al.* (2006), works by prescribing a mean flow modulated in time by fluctuations in the vorticity field. The superposition of the two reproduces up to second order the mean turbulent fluctuations of a reference flow and requires a short streamwise adjustment length to fully reproduce all quantities. The fluctuations are provided by a large number of randomly distributed “vorticity spheres” (or “eddies”) which are generated and advected with the bulk velocity in a fictitious cylindrical container located around the inflow section. When a sphere exits the container, a new, randomly located sphere is created to substitute it. The cylindrical container is dimensioned such that newly created eddies do not touch the inlet plane upon their creation and they have stopped affecting it before exiting the container, *i.e.* the cylinder extends from  $-\max(D_{\text{eddies}})$  to  $\max(D_{\text{eddies}})$  (see figure 5 in Poletto *et al.* 2013, for an illustration of the container).

The random numbers required to create the fluctuations are generated on a single processor with a pseudo random number generator (Chandler & Northrop 2003) featuring an algorithmic period of  $2^{1376}$  iterations, large enough to exclude any periodicity in the simulations, which feature approximately 10 000 synthetic eddies. The size of the spheres is selected to match the local integral turbulence length scale, and their intensity is scaled to recover the reference turbulent kinetic energy, producing isotropic but heterogeneous second-order moments. The method prescribes isotropic turbulence, instead of the correct anisotropic variant, because it was shown that the former leads to a shorter adjustment length in wall-bounded flows (see figure 11 in Jarrin *et al.* 2006). In order to satisfy the continuity equation, no synthetic turbulence is created below  $(R - r)^+ < 10$ ; however, this does not significantly affect the adjustment length since the dynamics of the viscous sublayer are faster than the mean and converge to a fully developed state in a shorter distance. The turbulence statistics necessary for the method, specifically the mean flow  $U(r)$ , the turbulent kinetic energy  $k(r)$ , and the dissipation rate  $\epsilon(r)$ , were extracted

from the straight pipe DNS performed by El Khoury *et al.* (2013). Section 3.1 presents the validation of our implementation of the DFSEM; more details can be found in Hufnagel (2016).

### 2.3. Proper orthogonal decomposition

Besides point measures, we use POD (Lumley 1967) to extract coherent structures from the DNS flow fields and identify the mechanism responsible for swirl-switching. More specifically, we use snapshot POD (Sirovich 1987) where  $n$  three-dimensional, full-domain flow fields of dimension  $d$  (corresponding to the number of velocity unknowns) are stored as snapshots. POD decomposes the flow in a set of orthogonal spatial modes  $\Phi_i(\mathbf{x})$  and corresponding time coefficients  $a_i(t)$  ranked by kinetic energy content, in decreasing order. The most energetic structure extracted by POD corresponds to the mean flow and will be herein named ‘‘zeroth mode’’, while the term ‘‘first mode’’ will be reserved for the first time-dependent structure.

A series of instantaneous flow fields (snapshots) is ordered column-wise in a matrix  $\mathbf{S} \in \mathbb{R}^{d \times n}$  and decomposed as:

$$\mathbf{S} = \mathbf{U}\Sigma\mathbf{V}^\top = \sum_{i=1}^d \Phi_i a_i, \quad (1)$$

where  $\mathbf{U} \in \mathbb{R}^{d \times d}$ ,  $\Sigma = \text{diag}(\sigma_1, \sigma_2, \dots, \sigma_m, 0)$ , with  $m = \min(d, n)$ , and  $\mathbf{V} \in \mathbb{R}^{n \times n}$ . The decomposition in (1) is obtained by computing the singular value decomposition (SVD) of  $\mathbf{M}^{1/2}\mathbf{ST}^{1/2}$ , where  $\mathbf{M}$  is the mass matrix and  $\mathbf{T}$  is the temporal weights matrix, which results in  $\tilde{\mathbf{U}}\Sigma\tilde{\mathbf{V}}^\top$ , where  $\tilde{\mathbf{U}}$  and  $\tilde{\mathbf{V}}$  are unitary matrices ( $\tilde{\mathbf{U}}^\top\tilde{\mathbf{U}} = \mathbf{I}$  and  $\tilde{\mathbf{V}}^\top\tilde{\mathbf{V}} = \mathbf{I}$ ); the POD modes are then obtained as  $\mathbf{U} = \mathbf{M}^{-1/2}\tilde{\mathbf{U}}$  and  $\mathbf{V} = \mathbf{T}^{-1/2}\tilde{\mathbf{V}}$ . To improve the convergence of the decomposition, we exploit the symmetry of the pipe about the  $I - O$  plane, which results into a statistical symmetry for the flow, and store an additional mirror image for each snapshot (Berkooz *et al.* 1993).

## 3. Results and analysis

### 3.1. Inflow validation

An auxiliary simulation for  $Re_\tau = 360$  was set up to test the performance of the DFSEM in a  $25D$  long straight pipe, provided with the same mesh characteristics used for the bent pipes. Classical statistical quantities were used for the validation and compared with the reference values by El Khoury *et al.* (2013). The comparison is presented in figure 2(a) as a function of distance from the inflow boundary, and shows that the DFSEM approaches a fully developed turbulent state (within  $\pm 1\%$  of error) at approximately  $5D$  from the inflow boundary. Figures 2(b-d) present the velocity, stress profiles, and the turbulent kinetic energy budget at the chosen streamwise position of  $s_i = 5D$ , which confirm the recovery of fully developed turbulence by the divergence-free synthetic eddy method.

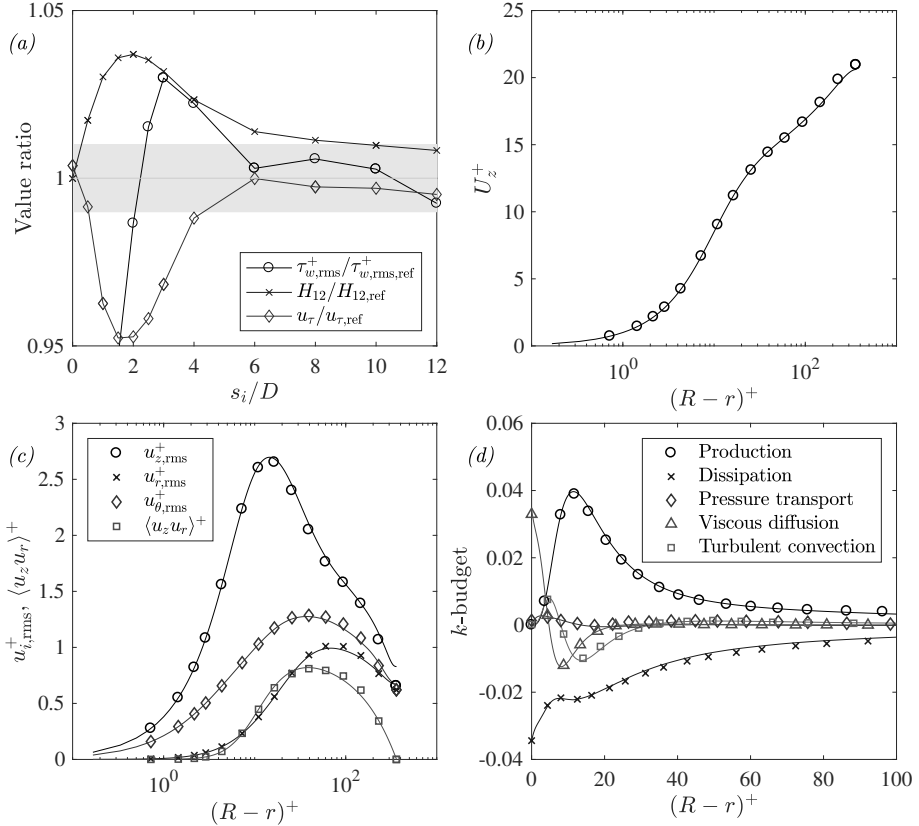


Figure 2: Recovery of fully developed turbulence statistics for the divergence-free synthetic eddy method at  $Re_\tau = 360$ , compared to the reference values by El Khoury *et al.* (2013). Panel (a) shows the ratio between the DFSEM and the reference data as a function of streamwise distance from the inflow plane. The grey shaded area indicates a  $\pm 1\%$  tolerance with respect to the data by El Khoury *et al.* (2013). Panels (b-d) show classical statistical profiles as a function of radial position at  $s_i = 5D$ . Solid lines indicate the reference data, while symbols represent the current results (note that the number of shown points is reduced and does therefore not represent the grid resolution; see table 2).

A length of  $7D$  was therefore chosen for the straight pipe preceding the bent section, in order to allow for some tolerance and to account for the (weak, up to  $1D$ ) upstream influence of the Dean vortices (Anwer *et al.* 1989; Sudo *et al.* 1998). For comparison, the more commonly used approach where random noise is prescribed at the inflow requires a development length between  $50$  and  $110D$  (Doherty *et al.* 2007). POD modes were also computed to further check the correctness of this method. The results, not reported here for conciseness, were

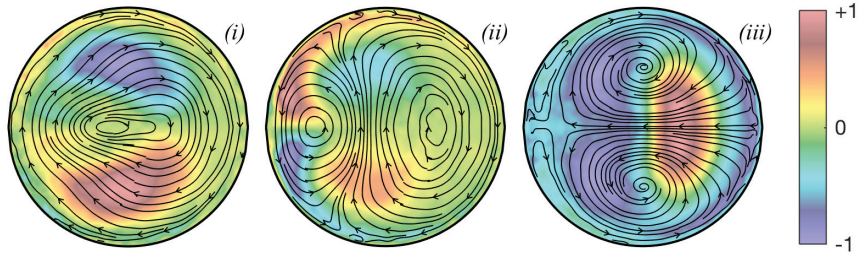


Figure 3: Pseudocolor of the streamwise velocity component and streamlines of the in-plane velocity components for the first three POD modes (*i–iii*). The modes are oriented as in figure 1(b). The snapshots were extracted at  $s_o = 2D$ .

in good agreement with those presented by Carlsson *et al.* (2015) for a periodic straight pipe, that is, streamwise invariant modes with azimuthal wavenumbers between 3 and 7.

### 3.2. Two-dimensional POD

Two-dimensional POD, considering all three velocity components, is employed as a first step in the analysis of swirl-switching. Instantaneous velocity fields are saved at a distance of  $2D$  from the end of the bent section and are used, with their mirror images, to assemble the snapshot matrices (Berkooz *et al.* 1993). 1234 velocity fields were saved at a sampling frequency of  $St = 0.25$ , and the sampling was started only after the solution had reached a statistically steady state. As a consequence of exploiting the mirror symmetry, all modes are either symmetric or antisymmetric, a condition to which they would converge provided that a sufficient number of snapshots had been saved.

The first three modes are shown in figure 3 by means of pseudocolors of their streamwise velocity component and streamlines of the in-plane velocity components. Two out of three modes are antisymmetric: (*i*, *ii*) and are in the form of a single swirl covering the whole pipe section, (*i*), and a double swirl, (*ii*), formed by two counter-rotating vortices disposed along the inner-outer direction on the symmetry plane. The third mode, (*iii*), resembles a harmonic of the Dean vortices.

These findings are in agreement with previous experimental work, such as that of Sakakibara *et al.* (2010) and Kalpakli & Örlü (2013), which attributed the dynamics of swirl-switching to the antisymmetric modes. The frequency content of these modes is presented in figure 4, in terms of Welch's power spectral density estimate for the time coefficients of the first three modes, corresponding to the structures shown in figure 3. It can be observed that the spectra have a low peak-to-noise ratio and that each mode is characterised by a different spectrum and peak frequency, in agreement with previous 2D POD studies: see, *e.g.*, figure 8 in Hellström *et al.* (2013), which presents

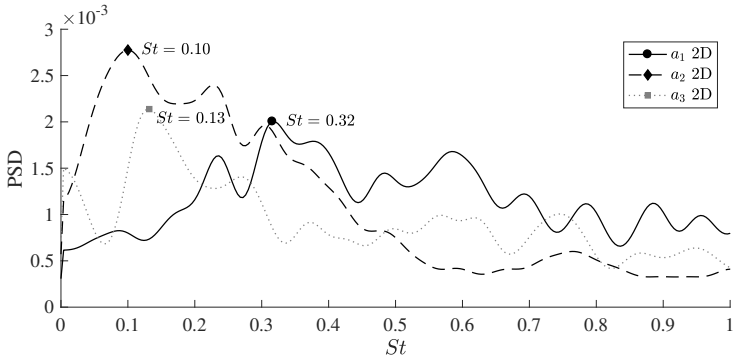


Figure 4: Welch's power spectral density estimate for the time coefficients  $a_i$  of the most energetic 2D POD modes. The frequencies are scaled with pipe diameter and bulk velocity. The 2D modes were extracted at  $s_o = 2D$ . The markers and corresponding labels report the frequency of the highest peak of each spectrum.

peaks with similar values to the present ones, although their study was for a slightly larger curvature of  $\delta = 0.5$ . This fact has caused some confusion in the past, with disagreeing authors attributing different causes to the various peaks, without being able to come to the same conclusion about the frequency, nor the structure, of swirl-switching. The reason is that swirl-switching is caused by a three-dimensional wave-like structure, as will be shown by 3D POD in §3.3, and a two-dimensional cross-flow analysis cannot distinguish between the spatial and temporal amplitude modulations created by the passage of the wave. A simple analytical demonstration of this concept is provided in the Appendix, and shows that conclusions drawn from a flow reconstruction based on 2D POD modes (see, e.g., Hellström *et al.* 2013) are incomplete.

### 3.3. Three-dimensional POD

For the 3D POD, the same snapshots as for 2D POD were used. In order to reduce memory requirements, the snapshots were interpolated on a coarser mesh before computing the POD. This is, however, not a problem because the swirl-switching is related to large-scale fluctuations in the flow.

The four most energetic modes are depicted in figure 5 by means of pseudo-colors of normal and streamwise velocity components, as well as streamlines of the in-plane velocity. It can be observed that the modes come in pairs: 1-2 and 3-4, as is usual for POD modes and their time coefficients in a convective flow. The first coherent structure extracted by the POD is formed by modes 1 and 2 and constitutes a damped wave-like structure that is convected by the mean flow (see figure 5 for the spatial structure and figure 6 for the corresponding time coefficients; the supplementary video `movie2_modes0-2.mov` shows their

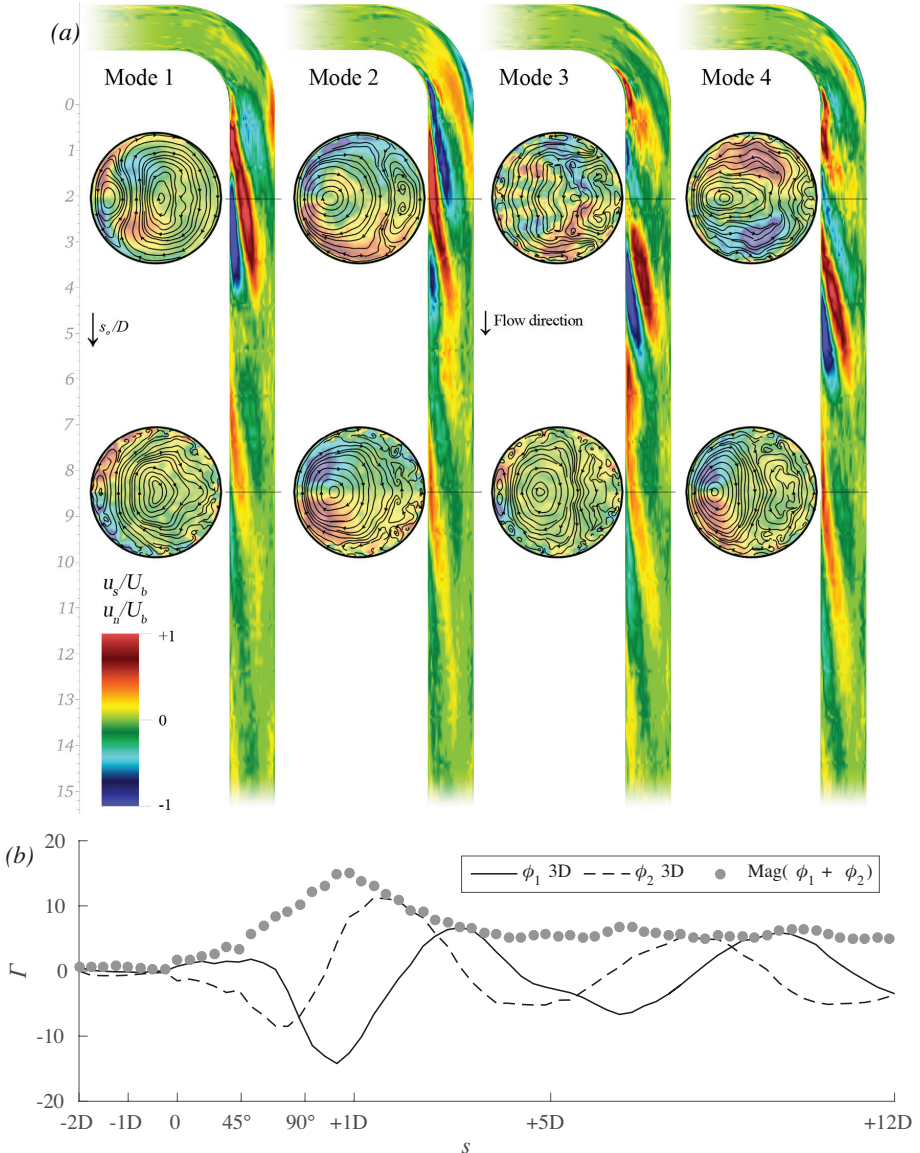


Figure 5: Panel (a) shows the four most energetic three-dimensional POD modes. The four longitudinal cuts show pseudocolours of the normal velocity component  $u_n$ , while the eight cross-sections display the in-plane streamlines and are coloured by streamwise velocity  $u_s$ . The supplementary material includes two videos showing the reconstruction of the flow based on these modes. Panel (b) shows the swirl intensity, measured by circulation  $\Gamma$ , along the streamwise axis of the two most energetic modes,  $\phi_1$  and  $\phi_2$ , and their envelope. The spatially decaying, wave-like behaviour can be appreciated.

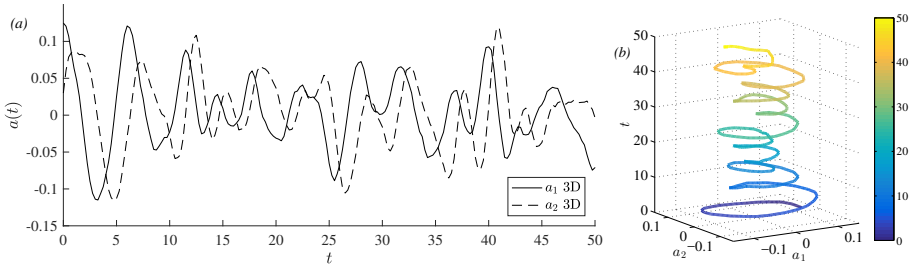


Figure 6: Time coefficients  $a_i(t)$  of the two most energetic three-dimensional POD modes. Panel (a) shows the temporal signal, which allows to observe the qualitative quarter-period phase shift of mode 2 with respect to mode 1; panel (b) shows the (colorcoded) time over coefficients  $a_1$  and  $a_2$ , illustrating the oscillating character. The time axis is (arbitrarily) cut at  $t = 50D/U_b$  for illustration purposes, the total recorded signal is over  $300D/U_b$ .

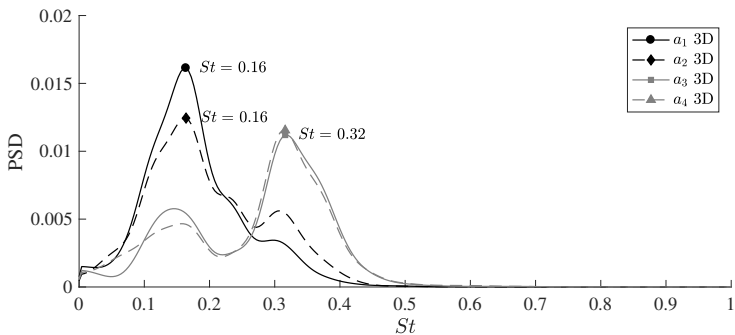


Figure 7: Welch's power spectral density estimate for the time coefficients  $a_i$  of the most energetic 3D POD modes. The frequencies are scaled with pipe diameter and bulk velocity. The markers and corresponding labels report the frequency corresponding to the peak of each spectrum. The range of the Strouhal number is identical to that of figure 4 to ease comparison.

behaviour in time). This is not a travelling wave such as those observed in transitional flows, as the ones of the examples mentioned in the introduction, but a coherent structure extracted by POD from a developed turbulent background that persists in fully developed turbulence, and is just a regular component of the flow on which irregular turbulent fluctuations are superimposed (see, *e.g.*, Manhart & Wengle 1993, for a similar case). Nevertheless, the present wave-like structure could be a surviving remnant of pre-existing, purely time-periodic, flow structures formed in the bent section and arising in the process of transition to turbulence past bends (see, *e.g.*, the case of the flow past a circular cylinder by Sipp & Lebedev 2007). It was found that the first instability of the flow inside of

a toroidal pipe is characterised by the appearance of travelling waves (Kühnen *et al.* 2014; Canton *et al.* 2016). It is therefore possible that similar waves appear in the transition to turbulence of the present flow case, and continue to modulate the large scales of the flow at high Reynolds numbers while being submerged in small-scale turbulence. To support this hypothesis, the frequencies and wavelengths of the present coherent structures are in the same range as those measured in toroidal pipes (Canton *et al.* 2016), and Brücker (1998) observed swirl-switching even for  $Re$  as low as 2 000, although the measured oscillations had very low amplitude.

The present modes are, obviously, not strictly periodic in space nor in time: as can be seen in figure 5(*b*) showing the swirl intensity, the intensity of the modes is essentially zero upstream of the bend ( $s < 0$ ), reaches a maximum at about  $1D$  downstream of the bend end, and then decreases with the distance from the bend. Furthermore, the respective time coefficients are only quasiperiodic, as can be observed from their temporal signal, depicted in figure 6(*a*), and by their frequency spectra, figure 7(*a*). Nevertheless, it can be observed in figure 5 that the spatial structure of these modes is qualitatively sinusoidal along the streamwise direction  $s_o$ , with a wavelength of about 7 pipe diameters. The figures in Brücker (1998) actually already suggest the appearance of a wave-like structure in the presence of swirl-switching.

This wave-like structure is formed by two counter-rotating swirls, visible in the 2D cross-sections in figure 5, which are advected in the streamwise direction while decaying in intensity and, at the same time, move from the inside of the bend towards the outside, as can be seen in the longitudinal cuts in figure 5 and in the supplementary video `movie2_modes0-2.mov`. The temporal amplitude of these modes is also qualitatively cyclic, as illustrated by the projection along the time coefficients in figure 6(*b*). The wave-like behaviour can be appreciated even better in the aforementioned video showing the flow reconstructed with these two modes, `movie2_modes0-2.mov`. Modes 1 and 2 are phase-shifted by a quarter of their quasi-period: figure 5 shows that the structure of mode 2 is located approximately a quarter of a wavelength further downstream of the structure of mode 1; while, figure 6 illustrates the constant delay of the time coefficient of mode 2 with respect to that of mode 1.

The second structure, formed by modes 3 and 4, has a spatial layout that closely resembles that of the first pair, *i.e.* it is also a wave-like structure, and constitutes the first ‘harmonic’ of the wave formed by modes 1 and 2. The spatial structure of modes 3 and 4 has half of the main wavelength of modes 1 and 2, and the highest peak in the spectrum of the third and fourth time coefficients is at exactly twice the frequency of the peaks of  $a_1$  and  $a_2$ , as can be seen in figure 7(*a*). The video `movie3_modes0-4.mov` shows the reconstruction of the flow field by including modes 3 and 4. It can be observed that these modes introduce oscillations with higher frequency and smaller amplitude when compared to the reconstruction employing only modes 1 and 2.

As can be observed from figure 5, the modes do not present any connection to the straight pipe section preceding the bend. This is in direct contrast with the findings of Carlsson *et al.* (2015), whose results were likely altered by the interference of an intrinsic frequency and wavelength on the recycling inflow boundary with the structure of the swirl-switching. Our results are, instead, in agreement with Noorani & Schlatter (2016) who observed swirl-switching in a toroidal pipe (*i.e.* in the absence of a straight upstream section) confirming that these large-scale oscillations are not caused by structures formed in the straight pipe, but by an effect which is intrinsic to the bent section.

The power spectral density analysis of the time coefficients of these modes, computed as a Welch's estimate, is presented in figure 7. One can see that, unlike the PSD of the two-dimensional POD modes (figure 4), the three-dimensional modes present two distinct peaks, one per pair of modes. The peak for the first modal pair is located at  $St \approx 0.16$ , which is in the range of Strouhal numbers found by both Brücker (1998) and Hellström *et al.* (2013). More importantly, this frequency is the lowest for this pair of modes and matches that given by the wavelength and propagation speed of the wave as well as that of the swirl-switching, as observed by reconstructing the flow field with the most energetic POD modes (see the online movies).

The present analyses were also performed on a pipe with curvature  $\delta = 0.1$  for the same Reynolds number. Swirl-switching was observed in this case as well, with dynamics which is qualitatively identical to the one observed for  $\delta = 0.3$ , but is characterised by lower frequencies, peaking at  $St \approx 0.045$ . The lower frequencies and larger scales (wavelength of about  $20D$ ) characterising the wave-like structure at this curvature meant that a quantitative analysis was too expensive with the present setup. We have therefore limited this work to the study of one curvature only, but preliminary, not converged results can be found in Hufnagel (2016).

#### 4. Summary and conclusions

This work presents the first DNS analysis of swirl-switching in a  $90^\circ$  bent pipe. The simulations were performed by using a synthetic eddy method to generate high-quality inflow conditions, in an effort to avoid any interference between the incoming flow and the dynamics of the flow in the bent section, as was observed in previous studies. Three-dimensional POD was used to isolate the dominant structures of the flow. This method allowed the identification of a wave-like structure, originating in the bent section, constituted by the first modal pair. A reconstruction of the flow field using the most energetic modal pair confirmed that the swirl-switching is caused by this structure.

The swirl-switching frequency found in the present study is in the range of those deduced by Brücker (1998) and Hellström *et al.* (2013). The structure of the modes, which presents no connection to the upstream straight pipe, confirms what was conjectured by Noorani & Schlatter (2016), who observed

swirl-switching in a toroidal pipe, namely that swirl-switching is a phenomenon intrinsic to the bent pipe section.

Clearly, the present findings are in contrast with previous conclusions drawn from flow reconstructions based on 2D POD modes and Taylor's frozen turbulence hypothesis (see, *e.g.*, Hellström *et al.* 2013): the 2D analysis mixes convection and true temporal variation, and thus cannot reveal the full three-dimensional structure of travelling modes. This does not only apply to the present flow case, but to any streamwise inhomogeneous flow in which 2D POD is utilised in the cross-flow direction.

The wave-like structure found in the present study is different from those observed in transitional flows (see, *e.g.* Hof *et al.* 2004), in the sense that it is simply a coherent structure extracted by POD from a turbulent background flow, as opposed to an exact coherent state. Nevertheless, we conjecture that this structure may be a surviving remnant of a global instability caused by the bend (Kühnen *et al.* 2014; Canton *et al.* 2016).

Financial support by the Swedish Research Council (VR) is gratefully acknowledged. Computer time was provided by the Swedish National Infrastructure for Computing (SNIC). We acknowledge that part of the results of this research have been achieved using the DECI resource SiSu based in Finland at CSC with support from the PRACE aisbl. This material is also based in part upon work supported by the US Department of Energy, Office of Science, under contract DE-AC02-06CH11357.

## Appendix A. Considerations on the use of 2D POD

This section explains, analytically, the reasons why a two-dimensional cross-flow POD analysis is an ineffective tool for understanding swirl-switching. In order to capture the essence of the phenomenon, the example is without spatial dissipation and noise, but these can be added at will without changing the discussion or the results. A Matlab script performing the operations described in this section is provided as part of the supplementary online material.

Consider a sine wave of period  $2\pi l$ , travelling at speed  $v$ , and with amplitude modulated at a frequency  $\omega/(2\pi)$ :

$$g(x, t) = \sin\left(\frac{x - vt}{l}\right) \cos(\omega t). \quad (2)$$

When measuring its passage at a given spatial position, say  $g(x_m, t)$ , the recorded time signal will contain two frequencies,  $f_1 = (\omega - v/l)/(2\pi)$  and  $f_2 = (\omega + v/l)/(2\pi)$ , that combine the spatial component,  $f_s = v/(2\pi l)$ , and the temporal component,  $f_t = \omega/(2\pi)$ . This combination is a result of the fact that  $g$  can be rewritten, using one prosthaphaeresis formula, separating the time and space dependencies:

$$g(x, t) = \frac{1}{2} \sin\left[\frac{x}{l} + \left(\omega - \frac{v}{l}\right)t\right] + \frac{1}{2} \sin\left[\frac{x}{l} - \left(\omega + \frac{v}{l}\right)t\right]. \quad (3)$$

The two components,  $f_s$  and  $f_t$ , would be measured in isolation if the function  $g$  were a pure travelling wave ( $\omega = 0$ ) or a pure standing wave ( $v = 0$ ). However, when both aspects are present ( $\omega \neq 0$  and  $v \neq 0$ ) a complete knowledge of  $g$  is necessary in order to separate  $f_s$  from  $f_t$ . This, clearly, is possible in the present example, where the analytical expression of  $g(x, t)$  is known. When studying an unknown phenomenon (such as swirl-switching) the knowledge of  $f_1$  and  $f_2$  is insufficient: one does not know what is causing the measured frequencies: it could be two travelling waves advected at different speeds (or provided with different period); two standing waves modulated at different frequencies; or, as in this case, one travelling wave with modulated amplitude.

This problem can be transferred to a POD analysis as well: the 2D POD in the pipe corresponds to a zero-dimensional POD in this example, which employs the measurements  $g(x_m, t_i)$  as snapshots, while the 3D POD of the bent pipe flow corresponds to a one-dimensional POD which uses the function  $g(x, t_i)$  over the whole  $x$  domain as snapshots.

The 0D POD returns a single mode which assumes a value of either +1 or -1 and does not provide any information about the spatial structure of  $g$ . The spectrum of the time coefficient corresponding to this single mode contains both frequencies  $f_1$  and  $f_2$ . When using 0D POD one does not have any information about the spatial nature of  $g$ , and it leads to believe that the oscillations measured in  $x_m$  are caused by two periodic phenomena with frequencies  $f_1$  and  $f_2$ . This likely is what has caused so much disagreement in the literature about the value of the Strouhal number related to the swirl-switching and on the 2D POD mode responsible for this phenomenon. The answer is that none of the 2D POD modes reported in the literature is actually the swirl-switching mode, and the Strouhal numbers extracted from time coefficients do not provide a correct description.

A 1D POD analysis of the function  $g$ , which is the analogue of the 3D POD in the bent pipe, provides the correct answers. It results in two sinusoidal modes which, with the corresponding time coefficients, reproduce the complete travelling and oscillatory behaviour of  $g$ . The spectra of the time coefficients still contain only  $f_1$  and  $f_2$ , but have a much higher peak to noise ratio compared to the 0D POD, as observed in the bent pipe by comparing figures 4 and 7. Moreover, by analysing the reconstruction of  $g$ , they allow the separation of  $f_s$  from  $f_t$ .

It is now clear why in the case of a streamwise-dependent spatial structure, such as the one creating swirl-switching (as shown in §3.3), only a fully three-dimensional analysis can correctly identify the actual spatial and temporal components.

## REFERENCES

- ANWER, M., SO, R. M. C. & LAI, Y. G. 1989 Perturbation by and recovery from bend curvature of a fully developed turbulent pipe flow. *Phys. Fluids* **1**, 1387–1397.

- BERKOOZ, G., HOLMES, P. & LUMLEY, J. L. 1993 The proper orthogonal decomposition in the analysis of turbulent flows. *Annu. Rev. Fluid Mech.* **25**, 539–575.
- BOUSSINESQ, M. J. 1868 Mémoire sur l'influence des frottements dans les mouvements réguliers des fluides. *J. Math. Pure Appl.* **13**, 377–424.
- BRÜCKER, C. 1998 A time-recording DPIV-study of the swirl switching effect in a 90° bend flow. *Proc. 8th Int. Symp. Flow Vis. Sorrento (NA), Italy* pp. 171.1–171.6.
- CANTON, J., ÖRLÜ, R. & SCHLATTER, P. 2017 Characterisation of the steady, laminar incompressible flow in toroidal pipes covering the entire curvature range. *Int. J. Heat Fluid Flow* **66**, 95–107.
- CANTON, J., SCHLATTER, P. & ÖRLÜ, R. 2016 Modal instability of the flow in a toroidal pipe. *J. Fluid Mech.* **792**, 894–909.
- CARLSSON, C., ALENIUS, E. & FUCHS, L. 2015 Swirl switching in turbulent flow through 90° pipe bends. *Phys. Fluids* **27**, 085112.
- CHANDLER, R. & NORTHRUP, P. 2003 Fortran random number generation. <http://www.ucl.ac.uk/~ucakarc/work/randgen.html>.
- DEAN, W. R. 1928 The streamline motion of fluid in a curved pipe. *Phil. Mag.* **5**, 673–693.
- DOHERTY, J., MONTY, J. & CHONG, M. 2007 The development of turbulent pipe flow. In *16th Australas. Fluid Mech. Conf.*, pp. 266–270.
- EL KHOURY, G. K., SCHLATTER, P., NOORANI, A., FISCHER, P. F., BRETHOUWER, G. & JOHANSSON, A. V. 2013 Direct numerical simulation of turbulent pipe flow at moderately high Reynolds numbers. *Flow, Turbul. Combust.* **91**, 475–495.
- EUSTICE, J. 1910 Flow of water in curved pipes. *Proc. R. Soc. London, Ser. A* **84**, 107–118.
- FISCHER, P. F., LOTTES, J. W. & KERKEMEIR, S. G. 2008 Nek5000 Web page.
- HELLSTRÖM, L. H. O., ZLATINOV, M. B., CAO, G. & SMITS, A. J. 2013 Turbulent pipe flow downstream of a 90° bend. *J. Fluid Mech.* **735**, R7.
- HOF, B., VAN DOORNE, C. W. H., WESTERWEEL, J., NIEUWSTADT, F. T. M., FAISST, H., ECKHARDT, B., WEDIN, H., KERSWELL, R. R. & WALEFFE, F. 2004 Experimental observation of nonlinear traveling waves in turbulent pipe flow. *Science* **305**, 1594–1598.
- HUFNAGEL, L. 2016 On the swirl-switching in developing bent pipe flow with direct numerical simulation. Msc thesis, KTH Mechanics, Stockholm, Sweden.
- JARRIN, N., BENHAMADOUCHE, S., LAURENCE, D. & PROSSER, R. 2006 A synthetic-eddy-method for generating inflow conditions for large-eddy simulations. *Int. J. Heat Fluid Flow* **27**, 585–593.
- KALPAKLI, A. & ÖRLÜ, R. 2013 Turbulent pipe flow downstream a 90° pipe bend with and without superimposed swirl. *Int. J. Heat Fluid Flow* **41**, 103–111.
- KALPAKLI VESTER, A., ÖRLÜ, R. & ALFREDSSON, P. H. 2015 POD analysis of the turbulent flow downstream a mild and sharp bend. *Exp. Fluids* **56**, 57.
- KALPAKLI VESTER, A., ÖRLÜ, R. & ALFREDSSON, P. H. 2016 Turbulent flows in curved pipes: recent advances in experiments and simulations. *Appl. Mech. Rev.* **68**, 050802.
- KÜHNEN, J., BRAUNSHIER, P., SCHWEGEL, M., KUHLMANN, H. C. & HOF, B. 2015 Subcritical versus supercritical transition to turbulence in curved pipes. *J. Fluid Mech.* **770**, R3.

- KÜHNEN, J., HOLZNER, M., HOF, B. & KUHLMANN, H. C. 2014 Experimental investigation of transitional flow in a toroidal pipe. *J. Fluid Mech.* **738**, 463–491.
- LUMLEY, J. L. 1967 The structure of inhomogeneous turbulent flows. In *Atmos. Turbul. Radio Wave Propag.* (ed. A. M. Yaglom & V. I. Tatarski), pp. 166–178. Moscow.
- MANHART, M. & WENGLER, H. 1993 A spatiotemporal decomposition of a fully inhomogeneous turbulent flow field. *Theor. Comput. Fluid Dyn.* **5**, 223–242.
- NOORANI, A., EL KHOURY, G. K. & SCHLATTER, P. 2013 Evolution of turbulence characteristics from straight to curved pipes. *Int. J. Heat Fluid Flow* **41**, 16–26.
- NOORANI, A. & SCHLATTER, P. 2016 Swirl-switching phenomenon in turbulent flow through toroidal pipes. *Int. J. Heat Fluid Flow* **61**, 108–116.
- POLETTI, R., CRAFT, T. & REVELL, A. 2013 A new divergence free synthetic eddy method for the reproduction of inlet flow conditions for LES. *Flow, Turbul. Combust.* **91**, 519–539.
- POLETTI, R., REVELL, A., CRAFT, T. J. & JARRIN, N. 2011 Divergence free synthetic eddy method for embedded LES inflow boundary conditions. In *7th Int. Symp. Turbul. Shear Flow Phenom.* Ottawa.
- RÜTTEN, F., MEINKE, M. & SCHRÖDER, W. 2001 Large-eddy simulations of 90° pipe bend flows. *J. Turbul.* **2**, N3.
- RÜTTEN, F., SCHRÖDER, W. & MEINKE, M. 2005 Large-eddy simulation of low frequency oscillations of the Dean vortices in turbulent pipe bend flows. *Phys. Fluids* **17**, 035107.
- SAKAKIBARA, J. & MACHIDA, N. 2012 Measurement of turbulent flow upstream and downstream of a circular pipe bend. *Phys. Fluids* **24**, 041702.
- SAKAKIBARA, J., SONOBE, R., GOTO, H., TEZUKA, H., TADA, H. & TEZUKA, K. 2010 Stereo-PIV study of turbulent flow downstream of a bend in a round pipe. In *14th Int. Symp. Flow Vis.*. EXCO Daegu, Korea.
- SIPP, D. & LEBEDEV, A. 2007 Global stability of base and mean flows: a general approach and its applications to cylinder and open cavity flows. *J. Fluid Mech.* **593**, 333–358.
- SIROVICH, L. 1987 Turbulence and the dynamics of coherent structures. Part I: coherent structures. *Q. Appl. Math.* **45**, 561–571.
- SUDO, K., SUMIDA, M. & HIBARA, H. 1998 Experimental investigation on turbulent flow in a circular-sectioned 90-degree bend. *Exp. Fluids* **25**, 42–49.
- TUNSTALL, M. J. & HARVEY, J. K. 1968 On the effect of a sharp bend in a fully developed turbulent pipe-flow. *J. Fluid Mech.* **34**, 595–608.
- VASHISTH, S., KUMAR, V. & NIGAM, K. D. P. 2008 A review on the potential applications of curved geometries in process industry. *Ind. Eng. Chem. Res.* **47**, 3291–3337.

# Paper 7

7



# On large-scale friction control in turbulent wall flow in low Reynolds number channels

Jacopo Canton<sup>1</sup>, Ramis Örlü<sup>1</sup>, Cheng Chin<sup>2</sup>, Nicholas Hutchins<sup>2</sup>, Jason Monty<sup>2</sup> and Philipp Schlatter<sup>1</sup>

<sup>1</sup>Linné FLOW Centre KTH Mechanics, Royal Institute of Technology, SE-100 44 Stockholm, Sweden

<sup>2</sup>Department of Mechanical Engineering, University of Melbourne, Parkville, Victoria 3010, Australia

*Flow Turbulence and Combustion* (2016), vol. **97**, 811–827

The present study reconsiders the control scheme proposed by Schoppa & Hussain [Phys Fluids **10**:1049–1051 (1998)], using a new set of numerical simulations. The computations are performed in a turbulent channel at friction Reynolds numbers of 104 (the value employed in the original study) and 180. In particular, the aim is to better characterise the physics of the control as well as to investigate the optimal parameters. The former purpose lead to a re-design of the control strategy: moving from a numerical imposition of the mean flow to the application of a volume force. A comparison between the two is presented. Results show that the original method only gave rise to transient drag reduction. The forcing method, on the other hand, leads to sustained drag reduction, and thus shows the superiority of the forcing approach for all wavelengths investigated. A clear maximum efficiency in drag reduction is reached for the case with a viscous-scaled spanwise wavelength of the vortices of 1200, which yields a drag reduction of 18%, as compared to the smaller wavelength of 400 suggested as the most efficient vortex in Schoppa & Hussain. Various turbulence statistics are considered, in an effort to elucidate the causes of the drag-reducing effect. For instance, a region of negative production was found, which is quite unusual for developed turbulent channel flow.

**Key words:** flow control, skin-friction reduction, turbulent channel flow, direct numerical simulation

---

## 1. Introduction

There is a significant cost both for the environment and economy, associated with overcoming the drag exerted on streamlined bodies moving through fluids. At typical speeds and sizes encountered in transportation (as for instance airplanes, cars, pipelines) the Reynolds number is always so high such that the flow needs to be considered fully turbulent. Therefore, classical schemes to delay

transition are not applicable in such circumstances, but rather the drag caused by the turbulent flow needs to be reduced directly. The literature contains a number of successful techniques to achieve this goal, mostly by modifying the immediate near-wall region, *e.g.* by uniform or intermittent blowing (Kametani *et al.* 2015), opposition control via localised blowing and suction (Stroh *et al.* 2015) or volume forces (Choi *et al.* 1994), wall oscillations (Jung *et al.* 1992) or travelling waves (Quadrio *et al.* 2009). As opposed to these active schemes, passive measures have also been used, such as the well-known riblets modifying the wall surface (Garcia-Mayoral & Jiménez 2011). All these methods, at least for low Reynolds numbers, can achieve a drag reduction of 10% or more, both in simulations and in practical implementations (Gad-el Hak 2007).

During recent years, the large-scale structure of turbulent wall-bounded flows has received considerable attention (Jiménez 1998; Marusic & Adrian 2013). Similarly, Schoppa & Hussain (1998) (sometimes indicated with ‘SH’ in the following) have shown that artificially creating and strengthening such large-scale, essentially streamwise oriented vortices, can be an effective method to reduce the frictional drag in channel flows. These authors considered a number of cases, employing both decaying and frozen vortices, and were able to obtain sustained reduction of the drag by approximately 15%. The interesting feature of the latter control scheme is that the modification in the flow is not imposed directly in the near-wall region, but rather further away from the wall, on correspondingly much larger scales. The method of frozen vortices has, in fact, found application in *e.g.* optimisation studies of electrostatic precipitators (Soldati 2001), where such large-scale structures are naturally occurring. Therefore, this scheme appears to be a good candidate of practical relevance, even for higher Reynolds numbers which are characterised by very small near-wall scales of turbulence, for which usually micro-electromechanical systems (MEMS) flow sensors/actuators are required (Kasagi *et al.* 2009).

It is thus the aim of the present work to further study the control scheme proposed by Schoppa & Hussain, using new sets of numerical simulations, to better characterise the physics behind it and the influence of the parameters involved. A thorough study on the influence of the Reynolds number and the potential application in open boundary layer flows is left for future studies.

The paper is organised as follows: section 2 describes the numerical method and setups employed, section 3 presents a validation and an extension of the control technique by SH. Section 4 introduces a variant of said control method and compares it to that by SH; 5 analyses the new technique in detail and provides an insight into the mechanisms behind drag reduction. Section 6 concludes the paper with a discussion on the results and an outlook on possible improvements.

## 2. Numerical setup

In the following, incompressible channel flows at fixed bulk Reynolds number  $Re_b$ , based on half-height  $h$ , and bulk velocity  $U_b$ , are considered. All simulations

are performed using the fully spectral code **SIMSON** (Chevalier *et al.* 2007), where periodicity in the wall-parallel directions  $x$  (streamwise) and  $z$  (spanwise) is imposed, and the no-slip condition is applied on the two channel walls. The wall-parallel directions are discretized using Fourier series, where aliasing errors are removed by using 1.5 times the number of modes prescribed, while a Chebyshev series is employed in the wall-normal direction. The temporal discretisation is carried out by a combination of a third order, four stage Runge–Kutta scheme for the non-linear term, and a second order Crank–Nicolson scheme for the linear terms. The time step is chosen such that the Courant number is always below 0.8.

In the first part of the paper, the frozen control strategy proposed by SH is reproduced. This method considers a simple model of streamwise vortices superimposed onto the flow in the form

$$\begin{aligned} U_{\text{con}} &= 0, \\ V_{\text{con}}(y, z) &= A\beta \cos(\beta z)(1 + \cos(\pi y/h)), \\ W_{\text{con}}(y, z) &= A\pi/h \sin(\beta z) \sin(\pi y/h), \end{aligned} \quad (1)$$

where  $A$  is the control amplitude, proportional to the maximum of the wall-normal velocity, *i.e.*  $\max(V_{\text{con}}) = 2A\beta$ , and  $\beta$  represents the spanwise wavenumber of the vortices. The frame of reference for equation (1) is translated in  $y$  and  $z$  with respect to the one used by SH (Schoppa & Hussain 1998), but the vortices are unchanged. SH fixed the amplitude  $A$  such that  $\max(V_{\text{con}}) = 0.06U_c$ , where  $U_c$  indicates the average streamwise velocity measured in the centre of the channel, and chose  $\beta$  in order to have  $2\pi/\beta^+ = 400$ . With “frozen forcing” the authors indicated a simulation performed with the  $x$ -mean Fourier coefficients fixed in time, excluding  $k_z = 0$ . These coefficients were specified as “the flow-field resulting after one turnover time of viscous, 2D evolution of the initial condition (1). In this way, relaxation of the control flow is permitted before it is frozen...”. Instead of fixing the relaxation time, the present study considers it as an additional parameter for the control strategy,  $T_r$ , to better understand its influence on the controlled flow. To implement this technique two steps are necessary: at first a two-dimensional simulation is performed in the streamwise-perpendicular plane ( $y - z$ ). In this computation the flow field defined in (1) is superimposed to a Poiseuille profile, set as initial condition and let freely evolve in time. The second step, controlling the flow, is initialised from a fully developed channel flow; when the control is activated, the streamwise-mean Fourier coefficients are fixed to be equal to the flow field resulting from the 2D simulation. This technique actually imposes, at every time instant, the shape of the spatial mean of the flow field.

In the second part of the paper, a different implementation of the idea by Schoppa & Hussain is presented. In this case, the large-scale vortices are not imposed by fixing the mean flow but are, instead, set up as a volume force with

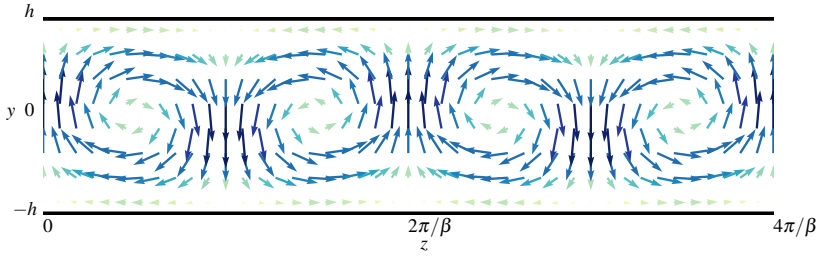


Figure 1: Sketch of the expression governing the vortices (equations (1) and (2)) on a channel plane perpendicular to the streamwise direction. Two complete wavelengths are depicted.

the same form of equation (1), viz.

$$\begin{aligned} F_x &= 0, \\ F_y(y, z) &= A\beta \cos(\beta z)(1 + \cos(\pi y/h)), \\ F_z(y, z) &= A\pi/h \sin(\beta z) \sin(\pi y/h). \end{aligned} \quad (2)$$

In this case both the forcing amplitude  $A$  and the wavenumber  $\beta$  are varied, looking for optimum values. The strength of the vortices in the resulting flow is measured by the maximum amplitude of the wall-normal mean velocity:  $\max |\langle v \rangle_{x,t}|$ , where  $\langle \cdot \rangle_{x,t}$  denotes the average in the streamwise direction and time. Note that this quantity vanishes in the uncontrolled case for both methods.

Three sets of simulations are performed: two for  $Re_\tau = 104$ , reproducing the setup by SH and introducing the new method, and one for  $Re_\tau = 180$ , analysing the effect of the new method for the control on the flow. The first two sets of DNSs consist of channel flows with the bulk Reynolds number fixed at  $Re_b = U_b h / \nu = 1518$ ; when reproducing SH the size of the box is set to  $8h \times 2h \times 3.832h$  and the number of modes used for the discretization is (48,65,48) in  $(x, y, z)$  before dealiasing. The unusual  $z$ -span is needed in order to accommodate a full period of the vortices with the same  $\Lambda^+$  employed by SH. When introducing the vortices via volume force the simulation parameters in  $x$  and  $y$  are unaltered, while the width of the box is changed to  $6.6h$  and  $9.9h$  to accommodate the different wavelengths presented in section 4, and the number of modes is set to 65 and 96 respectively. The second set is performed for  $Re_b = 2800$  in a  $12h \times 2h \times 6.6h/9.9h$  box with (128,97,96/144) modes. Wider boxes have also been employed to ensure that the results were independent of the number of vortex-periods simulated. Figure 1 depicts a sketch of the vortices defined by equations (1) and (2); note that this corresponds to the initial condition used by SH, before relaxation is allowed, not to the actual control (see figure 3).

The most important quantity of this study is the drag reduction DR. This is measured as the relative reduction in the streamwise pressure gradient  $p_x$

necessary to achieve a certain bulk flow. This index can be related to the ratio of the wall-integrated strain rate  $\Omega_w$  between the controlled and uncontrolled cases, employed by SH, with the following expression:

$$\text{DR} = \frac{p_{x_{\text{unc}}} - p_{x_{\text{con}}}}{p_{x_{\text{unc}}}} = 1 - \frac{p_{x_{\text{con}}}}{p_{x_{\text{unc}}}} = 1 - \frac{\Omega_{w_{\text{con}}}}{\Omega_{w_{\text{unc}}}}; \quad (3)$$

$$\Omega_w = \frac{1}{L_x(z_2 - z_1)} \int_0^{L_x} \int_{z_1}^{z_2} \frac{\partial u}{\partial y} \Big|_{y=0} dx dz. \quad (4)$$

All of the statistics presented have been averaged over suitably long integration times, *i.e.* for  $Re_\tau = 104$  a time span of 25500 convective-time units was used for the frozen vortices and 10500 convective-time units for the volume force cases, while for  $Re_\tau = 180$  a time span of 1500 convective-time units was found to be sufficient. The uncertainty in the measured mean value of DR is quantified by its mean square error as follows (Tropea *et al.* 2007):

$$\sigma_{\langle \text{DR} \rangle}^2 = \frac{1}{T} \int_{-T}^T \left(1 - \frac{|\tau|}{T}\right) C_{\text{DR DR}}(\tau) d\tau \quad (5)$$

where  $C_{\text{DR DR}}(\tau)$  is the autocovariance of DR and  $T$  is the length of the integration time employed for the mean. Where not specified, quantities are scaled with the bulk velocity  $U_b$  and the channel half width  $h$ .

### 3. Frozen vortices

To better understand the effect of the control mechanism on the flow, and to verify the correct implementation of the vortices in our code, a new set of numerical simulations has been performed, reproducing the flow case presented by SH. This consists of a fully developed channel flow at  $Re_c = U_c h / \nu = 1800$ ,

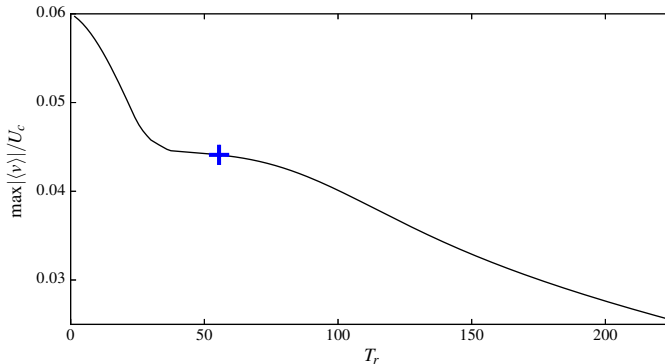


Figure 2: Intensity of the frozen vortices as a function of the relaxation time  $T_r$ . The plus symbol (blue) highlights the point employed for the analysis and corresponds to  $T_r = 55.5$ ,  $\max |\langle v \rangle|/U_c \approx 0.044$ .

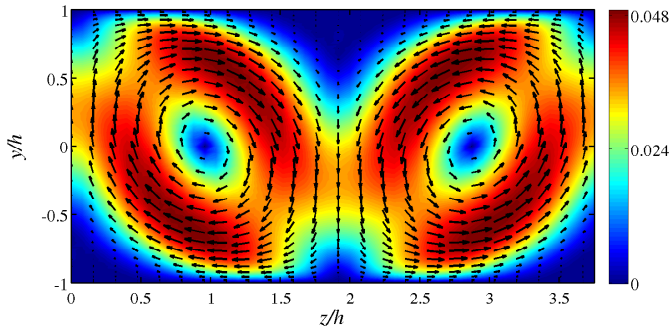


Figure 3: Shape and intensity of the control vortices after a relaxation time  $T_r = 55.5$ , as used in the analysis. Magnitude (colour) and vector plot of the in-plane velocity components  $v$  and  $w$ . The magnitude is scaled by the centreline velocity, *i.e.* colours represent  $\sqrt{v^2 + w^2}/U_c$ .

which corresponds to a bulk Reynolds number  $Re_b \approx 1518$  or, equivalently, a friction Reynolds number  $Re_\tau \approx 104$ .

To demonstrate the effectiveness of their control method, SH presented results for vortices with a wavelength  $\Lambda^+ = 2\pi/\beta^+ = 400$ . They argued that “even much larger-scale control [...] may be possible in practice”, but did not present simulations for higher or lower wavelengths. The present paragraph is thus limited to the investigation of frozen vortices with  $\Lambda^+ = 400$ .

As mentioned in §2, the flow field of equation (1) is allowed to “relax” for a time  $T_r$  by superposing it to an  $x$ -invariant, undisturbed channel flow. This allows for the shape of the vortices to adapt and for their intensity to decay before they are employed for control. The reduction in intensity against relaxation time is depicted in figure 2.

A relaxation time  $T_r = 55.5$  approximately corresponds to the turnover time employed by SH. The vortices, which are then used to control the flow, are depicted in figure 3. It is possible to observe that, in spite of the appreciable time elapsed, the shape of the vortices is still very close to that given by equation (1). The intensity, on the other hand, is reduced to 74% of the original value before the vortices are used for control, and its distribution is not as uniform as it was at the beginning of the relaxation process.

Figure 4 presents the evolution in time of the controlled case. In particular it shows, as presented in SH, the wall-integrated shear stress as a measure of the frictional drag. The upper panel employs the same axis limits as in SH and bears a striking resemblance with figure 2 in their paper, in spite of the approximation of the turnover time and the inherent sensitivity of the turbulent flow. This plot confirms the effect of the control vortices on the flow observed by SH, reducing the instantaneous drag by over 18%, and the mean drag by

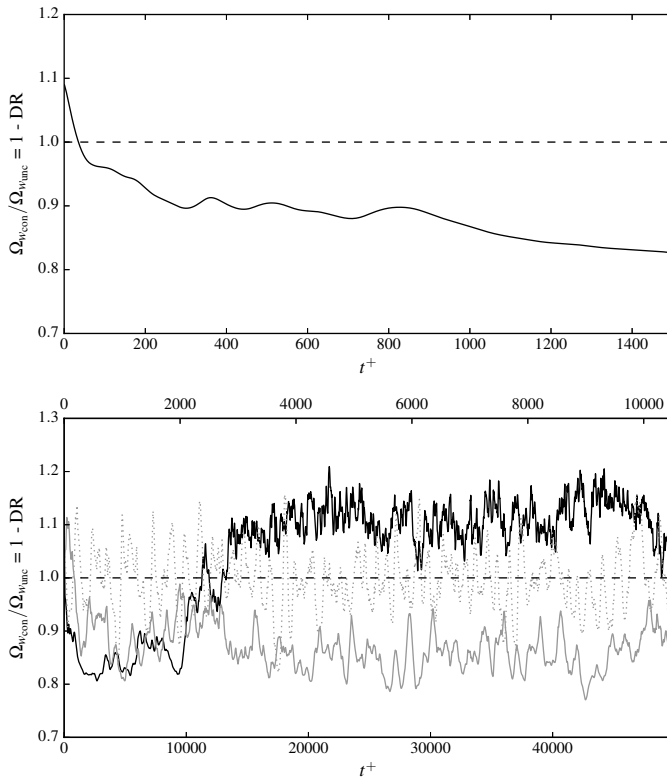


Figure 4: Time evolution of the wall-integrated strain rate normalised by the time average of the uncontrolled case. (*top*): time history for the first 1500 viscous-time units (see figure 2 in SH) illustrating over 18% instantaneous drag reduction (15% when averaged for the second half of the plot). (*bottom*): Same plot for a longer integration time ( $\approx 50000$  viscous-time units, corresponding to 10500 convective-time units, see upper  $x$ -axis), revealing actually an increase in the frictional drag by 10.8% after  $t^+ \approx 13000$ . Only the first half of the total simulation time is shown. Additionally, the *bottom* panel depicts the uncontrolled case (dotted, light gray) and the best performing case obtained via volume forcing (solid, light gray line, cf. §4).

15%. However, the data presented by SH stop at 1500 wall-time units. A very different picture appears when prolonging the time integration to 25500 convective time units, corresponding to approximately 121020 viscous-time units. As can be seen in the lower panel of figure 4, in fact, the drag-reducing effect due to the frozen vortices rapidly decreases after 9000 viscous-time units, and completely disappears for  $t^+ > 13000$ . The long term effect results in a drastic 10.8% increase in the frictional drag.

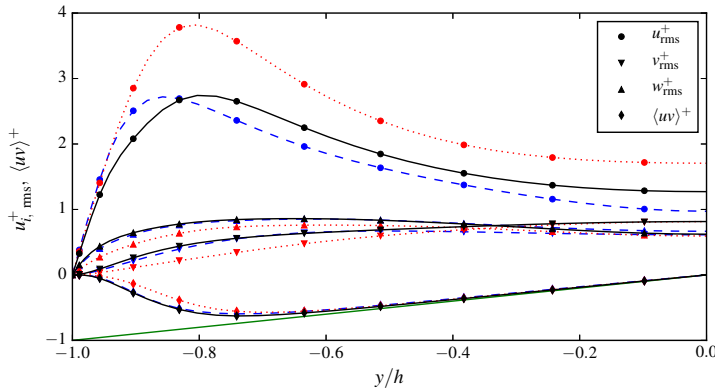


Figure 5: Comparison between short (dotted, red) and long (continuous, black) term effect of the frozen vortices with respect to the uncontrolled flow (dashed, blue).  $Re_\tau = 104$ . The figure depicts the rms of the velocity fluctuations and the Reynolds shear stress computed about the space- and time-averaged mean flow. The green solid line represents the linear shear stress relation. All quantities are scaled in respective plus units.

To better understand the short and long term behaviour of the vortices, figure 5 depicts typical turbulence statistics for both cases. The statistics for the short term behaviour are collected for  $t^+$  between 1200 and 9500, where the drag reducing effect starts to vanish; for the long term behaviour, instead, between  $t^+ = 19000$  and 121020 (see figure 4). When the vortices act as proposed by SH, *i.e.* desirable in terms of DR (dotted lines in figure 5), the inner-scaled streamwise fluctuations are increased, but shifted away from the channel walls. This is not simply an effect of the scaling in plus units:  $u_{rms}/\langle u \rangle_{local}$  is also increased, confirming the drastic growth in in-plane fluctuations magnitude. Conversely, the wall-normal and spanwise fluctuations are reduced to nearly one half of the value they assume in the uncontrolled case (blue, dashed lines). Similarly, the Reynolds shear stress  $\langle uv \rangle$  is significantly reduced close to the wall, although it still approaches the linear relationship towards the centre of the channel. When the vortices stop working and induce an increase in frictional drag (black lines) the statistics show a somewhat different picture. The streamwise velocity fluctuations are reduced and their peak is moved away from the wall, but they are not particularly affected in the viscous sublayer. A small increase in wall-normal and spanwise fluctuations confirms that the vortices are now having an opposite effect on the flow. The Reynolds shear stress is, similarly, uniformly increased, enhancing the production (not depicted) in the whole domain and especially in the viscous wall region.

Figure 6 further helps understanding the difference between short and long term behaviour of the frozen vortices. It depicts the turbulent kinetic energy for

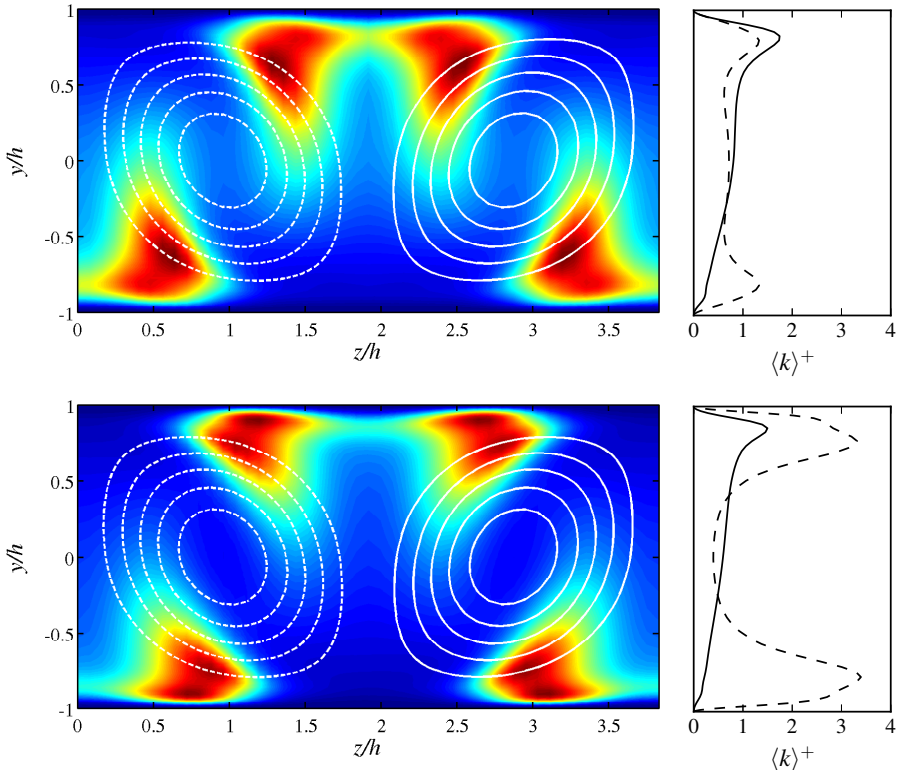


Figure 6: Two-dimensional planes showing the time-averaged turbulent kinetic energy  $\langle k \rangle$  for the short (*top*) and long (*bottom*) term behaviours. The white lines depict isocontours of the in-plane streamfunction, highlighting the position and shape of the vortices. The figures on the right side represent the same quantity in plus units along two vertical cuts: at the centre of the channel,  $z/h \approx 1.92$  (continuous line) and through the centre of the left vortex,  $z/h \approx 0.96$  (dashed line).

the two cases averaged over the same time ranges employed for figure 5. Two characteristics are clearly observable. The initial transient, when the vortices are reducing drag, shows a less intense and more diffused turbulent kinetic energy, especially towards the centre of the channel. In particular, it is possible to observe that the region close to the wall is affected to a greater extent when the vortices are increasing the frictional drag. Moreover, the two fields show a qualitatively different distribution of  $k$ : during the initial transient the control mechanism generates peaks of turbulent kinetic energy in the regions where the vortices are lifting fluid away from the wall (see figure 3). Conversely, in

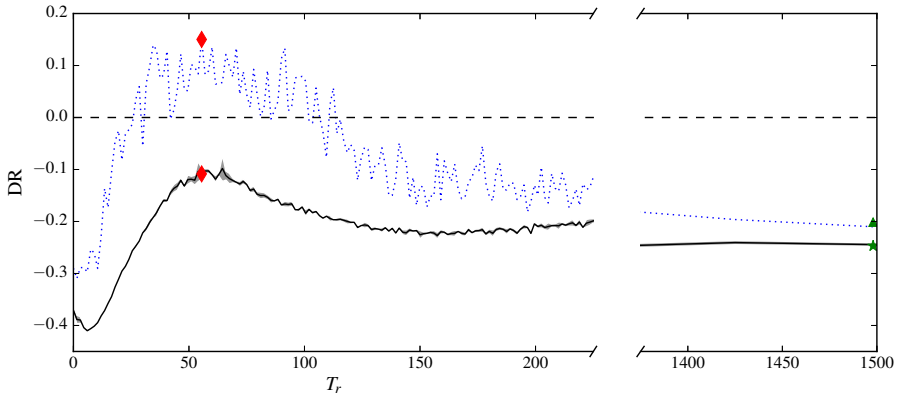


Figure 7: Drag reduction as a function of relaxation time. The dotted (blue) line depicts the short time behaviour of the vortices, displaying an irregular behaviour caused by the short length of the time averaging interval. The continuous (black) line corresponds to the long term behaviour of the control method, showing substantial drag increase for all relaxation times. The shaded area (comparable to the line thickness) shows the uncertainty in the mean value of DR as per equation (5). The (green) symbols on the right show the behaviour for zero amplitude: short term (triangle) and long term (star). The diamonds (red) highlight the flow case analysed in this paragraph.

the long term behaviour the regions of maximum  $k$  are located nearly directly between vortex and walls.

The behaviour described in this paragraph for  $T_r = 55.5$  is observed for other relaxation times, as can be seen in the parametric study depicted in figure 7. Results show the ineffectiveness of the control strategy for any relaxation time. In fact, in spite of a limited range displaying a positive transient effect, all cases induce, in the long term, a substantial increase of frictional drag in the flow. Moreover, setting the vortex amplitude to zero produces a 25% drag increase in the flow. A zero amplitude of the vortices corresponds to an infinitely long  $T_r$ . Consequently, for long relaxation times the two curves in figure 7 converge to the value corresponding to  $A = 0$ . The maximum  $T_r$  investigated is 1500. The drag increasing effect for  $A = 0$  further confirms that the method proposed by SH is unphysical and leads to unexpected, box-size dependent behaviours. In fact, a zero amplitude for the frozen vortices is not equivalent to an uncontrolled flow. On the contrary, setting  $A = 0$  in equation (1) corresponds to enforcing, in Fourier space,  $\hat{v}_{\hat{\alpha},\hat{\beta}}(y) = \hat{w}_{\hat{\alpha},\hat{\beta}}(y) = 0$ , for  $\hat{\alpha} = 0$  and any  $\hat{\beta} \neq 0$ . Here  $\hat{\alpha}$  and  $\hat{\beta}$  are the streamwise and spanwise wavenumbers. Such a restriction on the average wall-normal and spanwise velocity components is not what would result

from an uncontrolled channel simulation. These modes, despite displaying a low amplitude, are non-zero in an uncontrolled flow.

Despite the mentioned issues with the way of imposing the vortices proposed by SH, *i.e.* frozen spanwise varying, but streamwise independent mean flow, their idea of large-scale flow control retains potential as will be shown in the next section.

#### 4. Vortices as a volume force

Beside being ineffective, the approach presented in the previous section also appears to be hardly physically realisable. The idea behind it though, that of employing structures with a spatial scale much larger than the turbulent scales associated with the near-wall region, remains appealing. For this reason the same vortices presented by SH are here re-implemented. This time not by fixing the streamwise mean Fourier coefficients of the simulation, but by introducing the vortices as a force field, defined in equation (2). Applying a volume force is less intrusive than fixing the mean, and allows the fluid to freely adapt to the control mechanism. Moreover, as shown by the results presented in the following, the effect of the force field is not transient. The optimal form of the control depends on the amplitude of the force field,  $A$ , and on the spanwise wavelength of the vortices,  $\Lambda$ ; the influence of both parameters on DR has been investigated. Since  $A$  does not directly reflect the effect that the volume force is having on the controlled flow, the amplitude of the vortices is measured in terms of  $\max |\langle v \rangle_{x,t}|$ . This also allows a direct comparison with the method of frozen vortices.

As a first step, the forcing method is applied to a channel flow for the same Reynolds number employed by Schoppa & Hussain, *i.e.*  $Re_\tau = 104$ , to compare the two methods. The results of this analysis are presented in figure 8 for a number of cases considered. Six different spanwise wavelengths,  $\Lambda = 2\pi/\beta$ , were chosen, including the wavelength identified by SH as the best performing for the frozen vortices, *i.e.*  $\Lambda^+ = 400$ . For each vortex size the amplitude was varied to determine an optimum value. The forcing amplitude  $A$  (normalised with  $\beta$ ) for all cases is shown in the *top* panel of figure 8. It can be observed that the resulting vortex strength (measured in wall-normal velocity amplitude) is directly dependent on the forcing amplitude, a result that is perhaps not surprising.

The wavelength of the vortices, expressed in viscous units, ranges from  $\Lambda^+ = 120$  to  $\Lambda^+ = 1000$ . Figure 8 (*bottom*) clearly shows that the friction on the channel walls is unchanged for very low amplitudes of the imposed vortices (approximately below 0.5%). Negative results are also obtained for strong amplitudes: above 8% of the bulk velocity all cases show significant negative DR, *i.e.* drag increase. Relevant for the present study is the intermediate region of amplitudes, for which all vortex sizes (except  $\Lambda^+ = 120$ ) show at least a 10% reduction of the drag. A clear maximum efficiency is reached for the case with  $\Lambda^+ = 230$ , which peaks at  $DR \approx 16\%$ . It is interesting to note that a larger

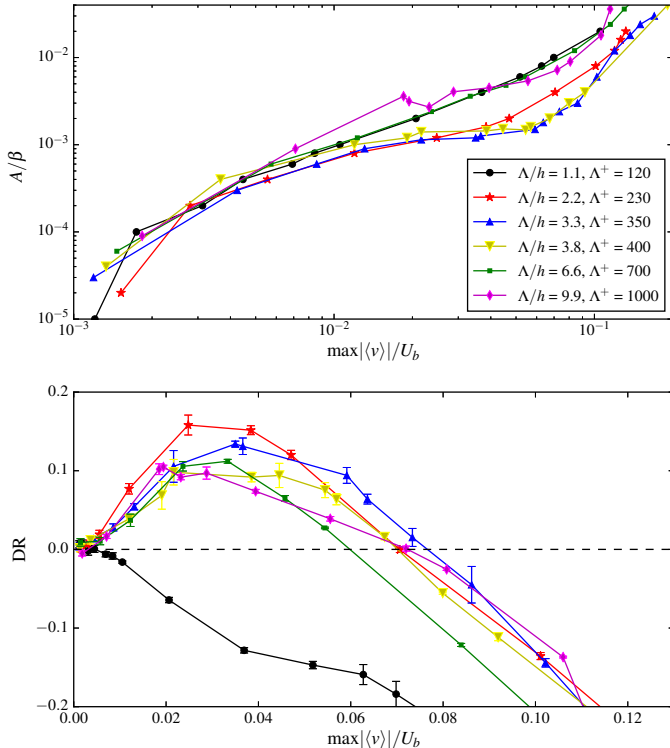


Figure 8:  $Re_\tau = 104$ . *Top:* Forcing amplitude  $A/\beta$  necessary for a vortex of a given strength. *Bottom:* Drag reduction (DR) as a function of vortex strength, measured as the maximum wall-normal velocity, for six different vortex wave lengths  $\Lambda = 2\pi/\beta$ . The error bars on DR show the uncertainty on the mean value as per equation (5).

wavelength of  $\Lambda^+ = 400$  is suggested by SH (using the frozen vortex method) as the most efficient one for this Reynolds number. As can be seen in figure 8, though, vortices with  $\Lambda^+ = 400$  can only provide drag reduction up to 10%.

The results here presented show that flow control via volume forcing is physically sound and practically relevant. Considerable drag reduction is, in fact, achievable with the proposed mechanism, employing small forcing amplitudes. Differently from freezing the mean flow, applying the vortices as a force field allows the flow to freely adapt to the external input instead of constraining it to a fixed shape. Moreover, employing a volume forcing results in sustained drag reduction, as can be observed in the *bottom* panel of figure 4, a feature that the method by SH was failing to provide. We now leave the frozen vortices aside and perform a detailed parameter study and look for the mechanism of

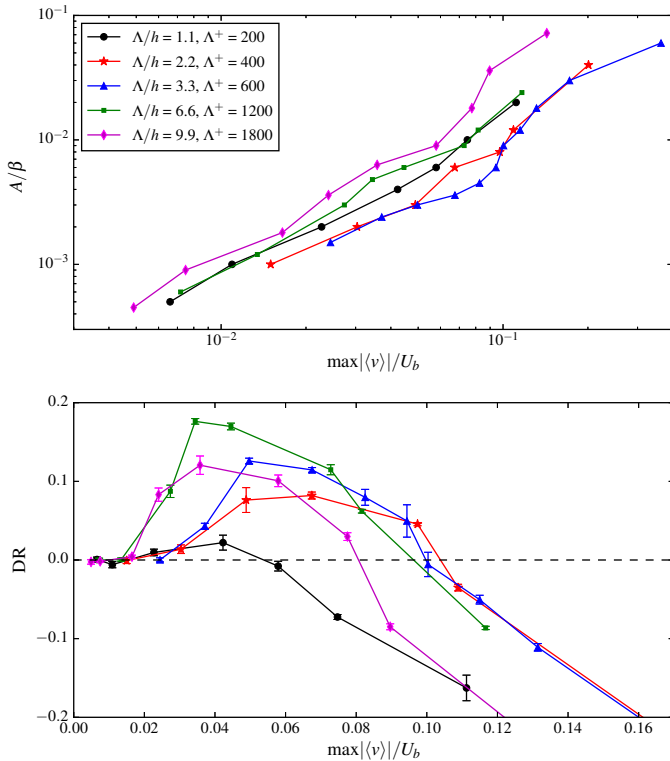


Figure 9:  $Re_\tau = 180$ . *Top:* Forcing amplitude  $A/\beta$  necessary for a vortex of a given strength. *Bottom:* Drag reduction (DR) as a function of vortex strength, measured in  $\max|\langle v \rangle_{x,t}|$ , for five different vortex wave lengths  $\Lambda = 2\pi/\beta$ . The error bars on DR show the uncertainty on the mean value as per equation (5).

drag reduction. This analysis is carried out for a friction Reynolds number  $Re_\tau = 180$ , a value more apt to sustain turbulence.

## 5. Analysis of the volume forcing method for $Re_\tau = 180$

The volume forcing method is now applied to channel flow for  $Re_b = 2800$ , corresponding to  $Re_\tau = 180$ . The same wavelengths employed for  $Re_\tau = 104$ , unmodified in outer units, now range from  $\Lambda^+ = 200$  to  $\Lambda^+ = 1800$  when expressed in viscous units. The relationship between vortex strength and forcing amplitude (*top* panel in figure 9) remains monotonic and approximately according to a power law. Moreover, the forcing amplitude employed for  $Re_\tau = 104$  appears sufficient to obtain the same effect on the flow for as  $Re_\tau = 180$ . Again, low amplitudes of the vortices do not affect the frictional drag, but the ineffective range is extended up to approximately 1.5% for this

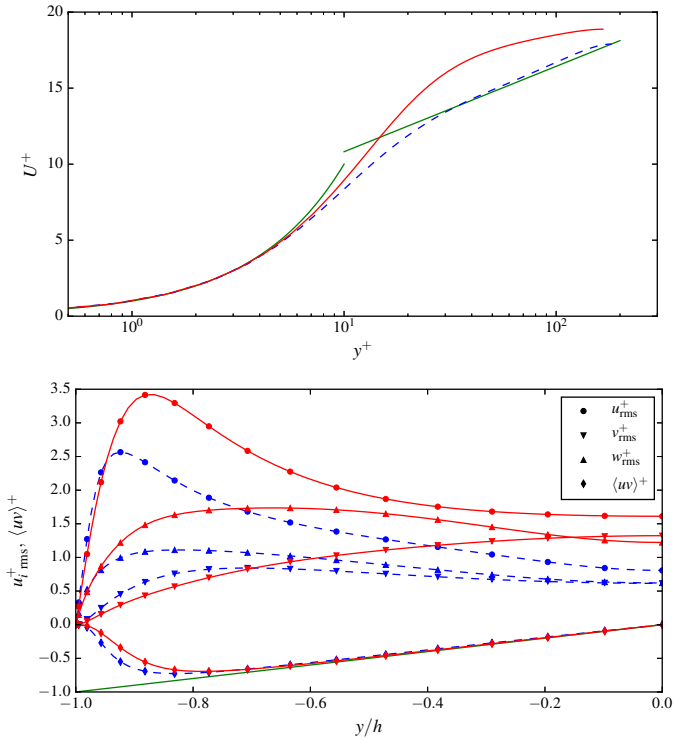


Figure 10: Mean velocity profile (*top*), averaged both in space and in time. The *bottom* panel depicts the rms of the velocity fluctuations and selected stresses computed about the mean. Comparison at  $Re_\tau = 180$  between uncontrolled channel flow (dashed) and highest drag reducing case ( $\Lambda^+ = 1200$ , solid). The green solid line denotes law of the wall, for  $\kappa = 0.41$ ,  $B = 5.2$ , and the linear shear stress relation. Quantities are scaled in respective plus units.

Reynolds number. Consistent results are also obtained for strong amplitudes (above 10%): all wavelengths induce significant drag increase and display a similar slope as their effect becomes undesirable. For this  $Re_\tau$ , though, all vortex wavelengths present a range of forcing amplitudes inducing a decrease of frictional drag. Inspection of the flow fields (shown later) clearly shows that negative DR is caused by the strong shear created by the vortices in the near-wall region, rather than increased turbulence. In fact, for the strongest amplitude of the forcing, turbulence disappears altogether, but the frictional drag is sensibly increased. The drag reduction plot in figure 9 confirms that there is an ideal spacing of the vortices. The optimum performance is provided by vortices with  $\Lambda^+ = 1200$  and a comparably weak intensity of just  $0.04U_b$ . This indicates that the optimum wavelength for the forcing is neither fixed in

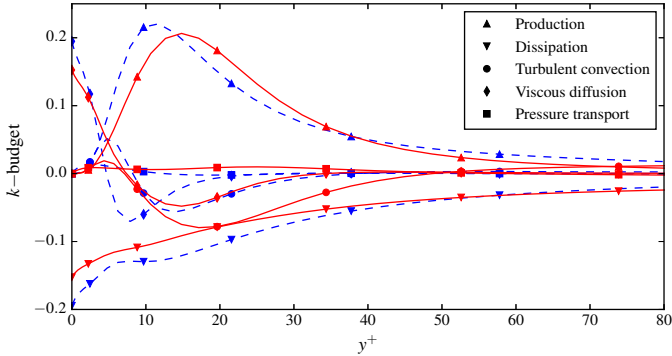


Figure 11: Turbulent kinetic energy budget in the proximity of the wall. Comparison for  $Re_\tau = 180$  between uncontrolled channel flow (dashed) and highest drag reducing case ( $\Lambda^+ = 1200$ , solid). All quantities are scaled in respective plus units.

outer nor in inner units. This form of the control scheme allows a substantial reduction of the frictional drag, peaking at a time-averaged DR  $\approx 18\%$ .

For the remainder of this paper only the most efficient vortices, *i.e.*  $\Lambda^+ = 1200$  with  $\max |\langle v \rangle_{x,t}| / U_b \approx 0.04$ , will be considered. Figure 10 shows typical turbulence statistics for both controlled and uncontrolled flow. The space- and time-averaged velocity profile (*top panel*) becomes more uniform in the channel centre (indicated by a lower slope for large wall distances). This is clearly due to the increased wall-normal momentum exchange induced by the vortices in the channel centre region. At the same time, the inner-scaled streamwise fluctuations are increased by the control and pushed further away from the wall. This phenomenon is similar to what was observed for the short term behaviour of the frozen vortices (see figure 5). A further similarity between the initial transient of the frozen vortices and this flow case is given by the Reynolds shear stress. The magnitude of  $\langle uv \rangle^+$  is, in fact, significantly reduced. The fluctuations of wall-normal and spanwise velocity, instead, behave differently from what is observed in §3:  $w_{rms}^+$  in the controlled case is higher than in the uncontrolled flow throughout the whole height of the channel;  $v_{rms}^+$ , on the other hand, is lower close to the wall, probably caused by the imposed spanwise motion in the proximity of the wall, but increases considerably, becoming greater than  $w_{rms}^+$ , in the centre.

Figure 11 presents the turbulent kinetic energy budget for both the controlled and uncontrolled cases. It may be observed that the production is reduced close to the wall and towards the centre of the channel, confirming the observations on the mean velocity profile. Its peak is also moved further away from the wall, albeit slightly, indicating a shift in the position where the Reynolds shear stress equals the viscous stress. The effect of the vortices at

the wall is also clearly shown by the turbulent convection and the dissipation. Both quantities are, in fact, reduced by 20% at the wall although the viscous transport is more than doubled in the buffer layer. The addition of the vortices as a force field entails the appearance of an additional term in the equation for the turbulent kinetic energy, *i.e.*  $\langle u_i f_i \rangle$ . Its contribution to the budget, though, is three orders of magnitude smaller than that of the smallest term (viscous diffusion), and thus was not included in figure 11.

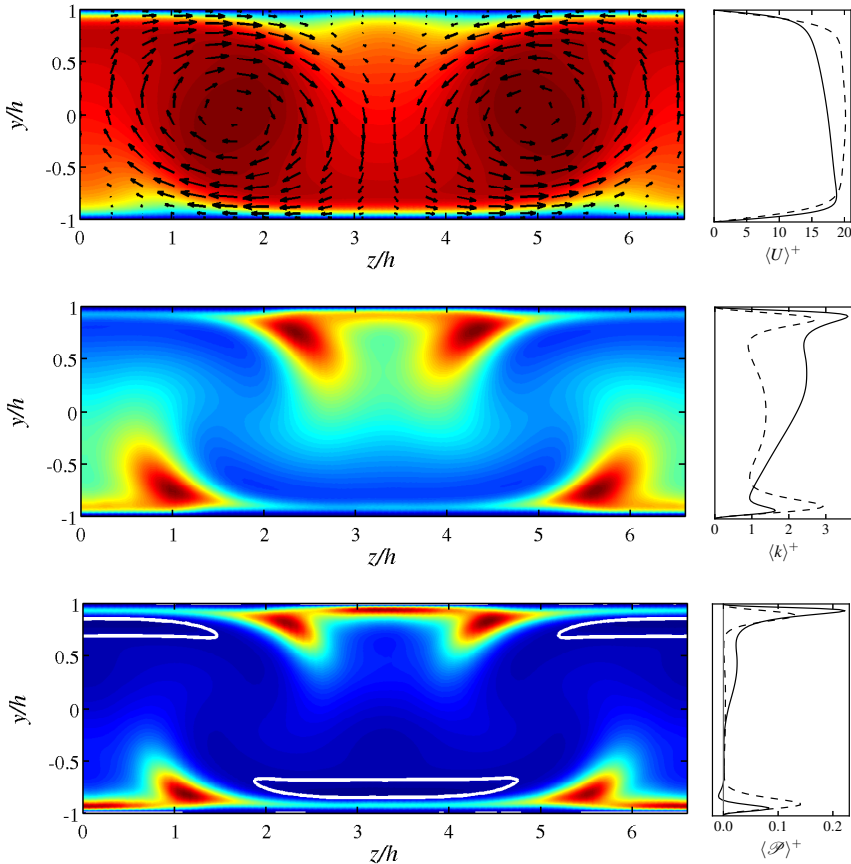


Figure 12: Two-dimensional  $y - z$  planes showing (*top*) streamwise velocity and superimposed in-plane vectors, (*middle*) turbulent kinetic energy  $k$ , (*bottom*) turbulent production  $\mathcal{P}$ ; the white contour encloses negative  $\mathcal{P}$ . The figures on the right side represent the same quantities in plus units along two vertical cuts: at the centre of the channel ( $z/h = 3.3$ , continuous line) and through the centre of the left vortex ( $z/h = 1.65$ , dashed line). The uncontrolled flow exhibits  $\max\langle k \rangle^+ \approx 3.8$  and  $\max\langle \mathcal{P} \rangle^+ \approx 0.2$ ; both quantities reach their minima in the centre of the channel.

Due to the spanwise inhomogeneity of the imposed vortices, better insight can be gained by considering statistics averaged only in the streamwise direction and time. These two-dimensional  $y - z$  planes are shown in figure 12 which features the mean flow (*top* panel), the turbulent kinetic energy  $k$  (*middle*) and the production (*bottom*). The reason for the increased turbulence activity in the near-wall region becomes now clear: the areas where the in-plane mean flow is directed *away* from the wall are characterised by peaks of turbulent kinetic energy. However, the turbulence is lifted from the wall, meaning that these positions feature the lowest local drag. This effect closely resembles the short term behaviour of the frozen vortices: the spatial distribution of  $k$  is comparable to that in figure 6 and the peaks are located on the sides of the vortices. Conversely, the regions exhibiting the highest drag are the essentially relaminarised areas where the vortices are pushing fluid *towards* the wall. As previously mentioned, this increase in drag is not due to higher turbulence intensity but is the result of a reduction in the height of the shear layer, clearly visible in the side panel of the mean flow. It is interesting to note that the production  $\mathcal{P}$  reaches moderately negative values (*i.e.* transport from fluctuations to mean) in exactly those regions.

Further understanding of the modifications induced by the vortices can be gained by measuring the shear stress on the wall. This is depicted in figure 13 which presents both  $\tau_w$  and its fluctuations as measured on the lower wall of the channel ( $y/h = -1$ ). Comparing this figure with the two-dimensional planes in figure 12 confirms what was previously argued: in the centre of the channel, where the vortices are pushing fluid *towards* the wall, the shear stress is increased by more than 20%. This region also features reduced oscillations,  $\tau_{w, \text{rms}}^+$ , characteristic of relaminarised flow (Örlü & Schlatter 2011). The

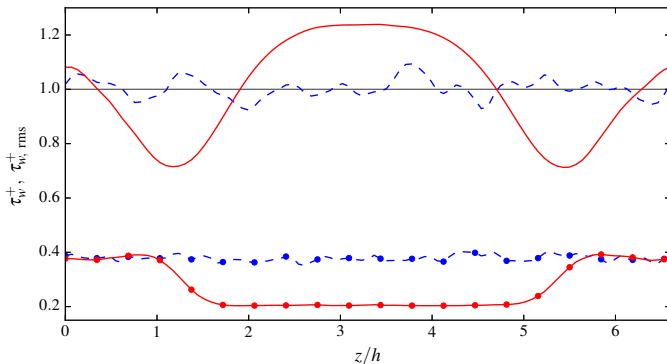


Figure 13: Wall shear stress and its fluctuations (symbols) for  $Re_\tau = 180$  at the lower wall ( $y/h = -1$ ). Comparison between uncontrolled channel flow (dashed) and the best performing controlled case ( $\Lambda^+ = 1200$ , solid). All quantities are normalised by the average  $\tau_w^+$  for the uncontrolled case.

portions of wall exhibiting reduced wall shear stress, instead, correspond to the peaks in turbulent kinetic energy and production displayed in figure 12.

Finally, figure 14 compares three-dimensional instantaneous visualisations of the controlled and uncontrolled flow. Whereas in the uncontrolled case the turbulence activity is homogeneously distributed along the channel walls, the introduction of the vortices leads to spatial inhomogeneity and the formation of the specific regions previously discussed. The turbulence activity (visualised by the presence of the vortical structures) is concentrated in the areas with positive wall-normal flow; the regions with splatting motion are void of turbulent fluctuations, but yet have the highest contribution to the wall friction. As can be seen from the visualisations, the regions presenting large-scale ejection are characterised by fairly “normal” near-wall turbulence. The drag-reducing effect of the vortices mainly consists in moving everything at a higher distance from the walls, not so much in changing the near-wall cycle, similarly to what observed for drag reduction through blowing (Kametani *et al.* 2015).

## 6. Conclusions and outlook

The present study re-analyses and extends the control method presented by Schoppa & Hussain (1998). In particular, it is shown that the original implementation of the scheme, the so-called frozen vortices, achieved by imposing the shape of the instantaneous spatial mean of the wall-normal and spanwise velocity components, does not lead to sustained drag reduction but, conversely, to substantial drag increase for long times. What the authors observed as drag reduction was shown to be a transient feature. Moreover, the frozen vortices have an unphysical behaviour for zero amplitude. We therefore chose to consider a re-implementation of the large-scale vortices in the form of a volume force. This new method was investigated via a thorough analysis of the whole parameter range (amplitude and wavelength). Results prove the validity and good performance of the new approach for a wide range of the governing parameters. In particular, it was shown that for  $Re_\tau = 180$  a clear maximum efficiency is reached employing vortices with  $\Lambda^+ = 1200$ , which yield a sustained drag reduction of 18%. This figure is achieved via a delicate balance between the intensity and extension of two regions: where the vortices lift turbulence away from the wall, reducing the wall shear stress, and where, despite causing relaminarisation, the vortices induce a higher velocity gradient at the wall. Further work is required to determine whether or not the present control scheme is applicable to channel flows at higher Reynolds numbers, and how the optimal parameters change. Additionally, the most important steps towards practical usage of this large-scale control scheme will consist in i) evaluating a practical method to impose the vortices and ii) verifying the effectiveness of the proposed method for high Reynolds numbers and iii) considering the application to spatially developing boundary layers, for the usage in external flows.

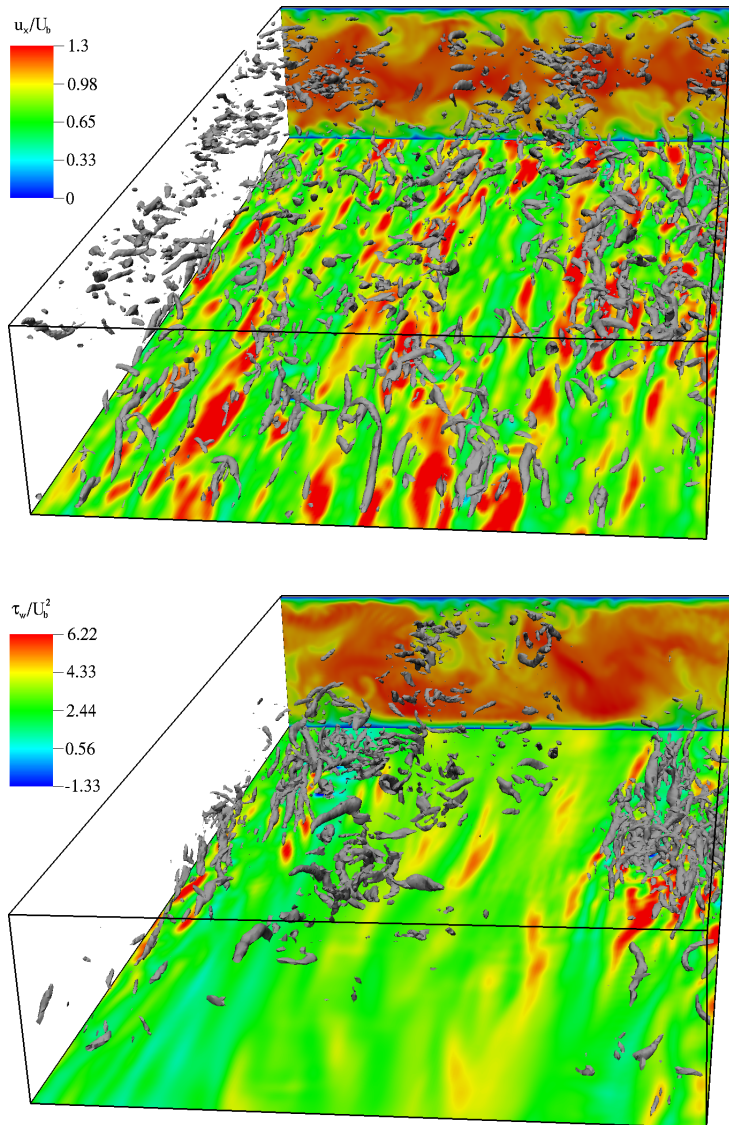


Figure 14: Instantaneous visualisation of the turbulent flow for uncontrolled (*top*) and controlled (*bottom*) cases. The bottom plane of the channel shows the wall-shear stress, while the background plane shows the streamwise velocity. Isocontours of  $\lambda_2 = -2$  are depicted in gray. The legends are the same for the two plots, and quantities are scaled in outer units.

Financial support by the Swedish Research Council (VR) is gratefully acknowledged. Computer time was provided by the Swedish National Infrastructure for Computing (SNIC).

#### REFERENCES

- CHEVALIER, M., SCHLATTER, P., LUNDBLADH, A. & HENNINSON, D. S. 2007 SIMSON - A pseudo-spectral solver for incompressible boundary layer flows. *Tech. Rep. TRITA-MEK 2007:07*. KTH Mechanics, Stockholm, Sweden.
- CHOI, H., MOIN, P. & KIM, J. 1994 Active turbulent control for drag reduction in wall-bounded flows. *J. Fluid Mech.* **262**, 75–110.
- GARCIA-MAYORAL, R. & JIMÉNEZ, J. 2011 Drag reduction by ripples. *Proc. R. Soc. London Ser. A* **369**, 1412–1427.
- GAD-EL HAK, M. 2007 *Flow Control: Passive, Active, and Reactive Flow Management*. Cambridge University Press.
- JIMÉNEZ, J. 1998 The largest scales of turbulent flows. *CTR Annual Research Briefs* pp. 137–154.
- JUNG, W., MANGIAVACCHI, N. & AKHAVAN, R. 1992 Suppression of turbulence in wall-bounded flows by high-frequency spanwise oscillations. *Phys. Fluids* **4**, 1605–1607.
- KAMETANI, Y., FUKAGATA, K., ÖRLÜ, R. & SCHLATTER, P. 2015 Effect of uniform blowing/suction in a turbulent boundary layer at moderate reynolds number. *Int. J. Heat Fluid Flow* **55**, 132–142.
- KASAGI, N., SUZUKI, Y. & FUKAGATA, K. 2009 Microelectromechanical systems-based feedback control of turbulence for skin friction reduction. *Annu. Rev. Fluid Mech.* **41**, 231–251.
- MARUSIC, I. & ADRIAN, R. J. 2013 The Eddies and Scales of Wall Turbulence. *Ten Chapters in Turbulence*, edited by P. Davidson, Y. Kaneda, and KR Sreenivasan, Cambridge University Press, Cambridge, UK. pp. 176–220.
- ÖRLÜ, R. & SCHLATTER, P. 2011 On the fluctuating wall-shear stress in zero pressure-gradient turbulent boundary layer flows. *Phys. Fluids* **23** (2), 021704.
- QUADRIDO, M., RICCO, P. & VIOTTI, C. 2009 Streamwise-traveling waves of spanwise wall velocity for turbulent drag reduction. *J. Fluid Mech.* **627**, 161–178.
- SCHOPPA, W. & HUSSAIN, F. 1998 A large-scale control strategy for drag reduction in turbulent boundary layers. *Phys. Fluids* **10** (5), 1049–1051.
- SOLDATI, A. 2001 Influence of large-scale streamwise vortical ehd flows on wall turbulence. *Int. J. Heat Fluid Flow* **23**, 441–443.
- STROH, A., FROHNAPFEL, B., SCHLATTER, P. & HASEGAWA, Y. 2015 A comparison of opposition control in turbulent boundary layer and turbulent channel flow. *Phys. Fluids* **27**, 075101.
- TROPEA, C., YARIN, A. L. & FOSS, J. F. 2007 *Springer Handbook of Experimental Fluid Mechanics*. Springer Science & Business Media.

# Paper 8

8



# Reynolds number dependence of large-scale friction control in turbulent channel flow

Jacopo Canton<sup>1,2</sup>, Ramis Örlü<sup>1</sup>, Cheng Chin<sup>3</sup>  
and Philipp Schlatter<sup>1,2</sup>

<sup>1</sup>Linné FLOW Centre KTH Mechanics, Royal Institute of Technology,  
SE-100 44 Stockholm, Sweden

<sup>2</sup>Swedish e-Science Research Centre (SeRC), Royal Institute of Technology,  
SE-100 44 Stockholm, Sweden

<sup>3</sup>Department of Mechanical Engineering, University of Melbourne, Parkville,  
3010 Victoria, Australia

*Physical Review Fluids* (2016), vol. 1, 081501

The present work investigates the effectiveness of the control strategy introduced by Schoppa & Hussain [Phys. Fluids **10**:1049–1051 (1998)] as a function of Reynolds number ( $Re$ ). The skin-friction drag reduction method proposed by these authors, consisting of streamwise-invariant, counter-rotating vortices, was analysed by Canton *et al.* [Flow Turbul. Combust. **97**:811–827 (2016)] in turbulent channel flows for friction Reynolds numbers ( $Re_\tau$ ) corresponding to the value of the original study (*i.e.* 104) and 180. For these  $Re$ , a slightly modified version of the method proved to be successful and was capable of providing a drag reduction of up to 18%. The present study analyses the Reynolds-number dependence of this drag-reducing strategy by performing two new sets of direct numerical simulations (DNS) for  $Re_\tau = 360$  and 550. A detailed analysis of the method as a function of the control parameters (amplitude and wavelength) and  $Re$  confirms, on the one hand, the effectiveness of the large-scale vortices at low  $Re$  and, on the other hand, the decreasing and finally vanishing effectiveness of this method for higher  $Re$ . In particular, no drag reduction can be achieved for  $Re_\tau = 550$  for any combination of the parameters controlling the vortices. For low Reynolds numbers the large-scale vortices are able to affect the near-wall cycle and alter the wall-shear-stress distribution to cause an overall drag-reduction effect, in accordance with most control strategies. For higher  $Re$ , instead, the present method fails to penetrate the near-wall region and cannot induce the spanwise velocity variation observed in other more established control strategies, which focus on the near-wall cycle. Despite the negative outcome, the present results demonstrate the shortcomings of the control strategy and show that future focus should be on methods that directly target the near-wall region, or other suitable alternatives.

**Key words:** flow control, skin-friction reduction, Reynolds number effects

The search for an effective mean of reducing turbulent skin-friction drag is one of the most active fields of research in fluid mechanics. The benefits of efficient flow control are numerous: from energy and economical savings, to more efficient and greener machinery, be it aviation or fluid transport and mixing (Gad-el Hak 2007). Several techniques have been investigated, ranging from passive methods such as riblets (García-Mayoral & Jiménez 2011) to active control strategies as, for example, streamwise-travelling waves of blowing and suction (Min *et al.* 2006; Mamori *et al.* 2014), of spanwise wall velocity (Quadrio *et al.* 2009), or of wall deformation (Nakanishi *et al.* 2012), oscillating walls (Mishra & Skote 2015; Skote 2014), uniform blowing and suction (Kametani *et al.* 2015), volume forcing (Moreau 2007), and direct modification of the mean flow (Schoppa & Hussain 1998). Most of these control techniques, though, have been analysed only at low Reynolds numbers ( $Re$ ) and only recently some authors have started investigating the effects that an increasing Reynolds number has on the flow control strategy (see, for instance, Iwamoto *et al.* 2002; Hurst *et al.* 2014; Gatti & Quadrio 2016).

One of the more prominent techniques consists in the large-scale vortices proposed by Schoppa & Hussain (1998) which (in the original study) were embedded in a turbulent channel flow at a friction Reynolds number  $Re_\tau = 104$ , where turbulence is marginally sustainable. This drag reduction strategy was found to be ineffective by Canton *et al.* (2016), since the claimed drag-reduction effect was shown to be of transient nature. Nonetheless, Canton *et al.* (2016) recast the method as a volume forcing control for channel flows that lead to sustainable drag reduction at  $Re_\tau = 180$ . These large-scale vortices had been promoted by their original authors as a promising, feed-forward or passive, control technique capable of reducing the turbulent friction drag from the outside of the viscous layer, and thus independent of the small scales of wall turbulence, which would otherwise limit its applicability at practically relevant Reynolds numbers due to sensor/actuator limitations (Kasagi *et al.* 2009). The vortices would do so by reducing the wall-normal vorticity  $\omega_y$ , therefore preventing streak instability and generation of streamwise vortices (Schoppa & Hussain 1998).

It is well known, though, that near-wall structures scale with viscous units (see, e.g. the seminal paper by Kline *et al.* 1967) and that low Reynolds number effects are present in wall-bounded flows at least up to  $Re_\tau = 395$  (Moser *et al.* 1999). Moreover, it has been found that the performance of different control strategies deteriorates as the Reynolds number is increased; this is the case at least for the active V- and suboptimal control schemes by Iwamoto *et al.* (2002) and the oscillating wall and travelling waves by Hurst *et al.* (2014) and Gatti & Quadrio (2013, 2016). These two observations provide the main motivation for the present analysis, along with the aim of better characterising the large-scale vortex control.

This paper is concerned with direct numerical simulations (DNS) of incompressible channel flows at fixed bulk Reynolds number  $Re_b$ , based on bulk

$Re_\tau$	Integration time $T \cdot [h/U_b]$	Domain size $L_x/h, L_z/h$	Grid points $N_x, N_y, N_z$
104	10500	8, 3.832	48, 65, 48
		8, 6.6	48, 65, 60
		8, 9.9	48, 65, 96
180	1500	12, 6.6	128, 97, 96
		12, 9.9	128, 97, 144
360	1000	12, 6.6	300, 151, 200
		12, 9.9	300, 151, 300
550	400	12, 6.6	432, 193, 300

Table 1: Details of the numerical discretisation employed for the present simulations.  $T$  corresponds to the duration of the controlled simulations;  $N_x$  and  $N_z$  represent the number of Fourier modes employed in the wall-parallel directions (values before dealiasing), while  $N_y$  is the order of the Chebyshev expansion used for the wall-normal direction.

velocity  $U_b$ , channel half-height  $h$  and fluid viscosity  $\nu$ . Four values of bulk Reynolds number are employed:  $Re_b = 1518, 2800, 6240$  and  $10000$ , such as to result in a friction Reynolds number, based on friction velocity  $u_\tau$ ,  $h$  and  $\nu$ , corresponding to  $Re_\tau \approx 104, 180, 360$  and  $550$ , where the lowest Reynolds number corresponds to the value employed in the original study by Schoppa & Hussain (1998). The simulations are performed using the fully spectral code **SIMSON** (Chevalier *et al.* 2007), where periodicity in the wall-parallel directions  $x$  (streamwise) and  $z$  (spanwise) is imposed, and the no-slip and no penetration condition is applied at the two channel walls. The wall-parallel directions are discretised using Fourier series, where aliasing errors are removed by using  $3/2$  times the number of modes prescribed. A Chebyshev expansion is employed in the wall-normal direction  $y$ . Details of the domain sizes and spatial resolutions used for the four sets of simulations are reported in table 1. The temporal discretisation of the nonlinear term is carried out by a four stage Runge–Kutta scheme, while the linear terms are treated with a second order Crank–Nicolson scheme. The time step is automatically set such that the Courant number is always below 0.8.

The simulations are initialised with a randomly perturbed Poiseuille velocity profile. A precursor run is performed with the control turned off until a statistically steady, thus fully turbulent, flow is obtained. All controlled simulations are then initialised with the same snapshot from the uncontrolled case. The controlled simulations are run for a sufficiently long time interval such as to have a reasonably low uncertainty on the statistical quantities presented in this work and, in particular, on the value of drag reduction (see, *e.g.*, figure 2 which presents the error bars on DR). For additional details see Canton *et al.* (2016) and table 1. The large-scale vortices, provided with variable intensity and spanwise wavelength, are imposed via a volume forcing defined as (Schoppa & Hussain 1998):

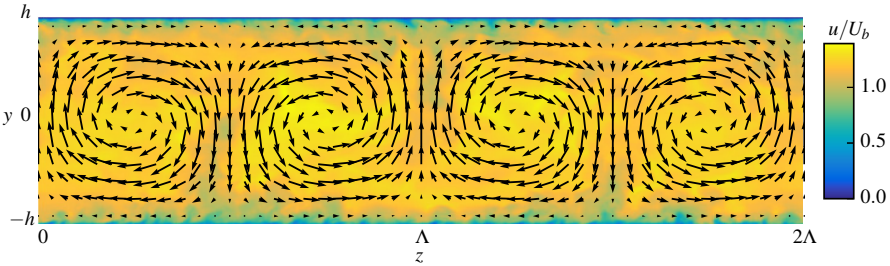


Figure 1: Instantaneous flow field of a controlled simulation for  $Re_\tau = 550$  illustrating the large-scale vortices. The figure depicts two vortex wavelengths, with  $\Lambda = 3.3h$ , on a cross-stream channel plane coloured by streamwise velocity magnitude. The control amplitude is  $\max |\langle v \rangle_{x,t}| \approx 0.07U_b$ .

$$\begin{aligned} f_x &= 0, \\ f_y(y, z) &= A\beta \cos(\beta z)(1 + \cos(\pi y/h)), \\ f_z(y, z) &= A\pi/h \sin(\beta z) \sin(\pi y/h), \end{aligned} \tag{1}$$

where  $A$  is the forcing amplitude and  $\beta$  the wavenumber along  $z$ . The wavenumber was chosen such as to have vortex periods  $\Lambda = 2\pi/\beta$  between  $1.1h$  and  $9.9h$ , corresponding to inner-scaled wavelengths  $\Lambda^+$  between 120 and 3630. Here and in the following, all inner-scaled quantities are referred to the uncontrolled case and are indicated with a plus sign, *i.e.*  $(\cdot)^+$ . A sketch of the control vortices for  $\Lambda = 3.3h$  is depicted in figure 1. Since  $A$  does not correspond to a measurable flow quantity, the maximum wall-normal mean velocity is used to characterise the strength of the vortices, *i.e.*  $\max |\langle v \rangle_{x,t}|/U_b$ , where  $\langle \cdot \rangle_{x,t}$  denotes the average in the streamwise direction and time.

The present vortex control is a good candidate for practical implementation: the required large-scale secondary flow can in fact be generated by using either active or passive control methods that do not require any moving parts. Examples of such methods include, but are not limited to, modifying the surface geometry by introducing vortex generators (Hutchins & Choi 2001), or non-uniform surface roughness (Vanderwel & Ganapathisubramani 2015), exploiting flow instabilities (Matsson & Alfredsson 1990), as well as employing plasma streamwise vortex generators (Choi *et al.* 2011; Wicks *et al.* 2015).

Here, drag reduction is quantified as the relative difference in the time-averaged streamwise pressure gradient  $p_x$ , necessary to fix the mass flux, between controlled  $p_{x,\text{con}}$  and uncontrolled  $p_{x,\text{unc}}$  flow cases:

$$\text{DR} = \frac{p_{x,\text{unc}} - p_{x,\text{con}}}{p_{x,\text{unc}}}. \tag{2}$$

Clearly, positive values correspond to a favourable effect while negative DR indicates drag increase. Note that this definition of DR, in case of a turbulent channel flow, corresponds also to the same ratio between controlled and uncontrolled average wall-shear stress.

The uncertainty on DR is quantified as (Tropea *et al.* 2007):

$$\sigma_{\langle \text{DR} \rangle}^2 = \frac{1}{T} \int_{-T}^T \left( 1 - \frac{|\tau|}{T} \right) C_{\text{DR DR}}(\tau) d\tau \quad (3)$$

where  $C_{\text{DR DR}}(\tau)$  is the autocovariance of DR, and  $T$  is the length of the integration time (see table 1).

A total of 222 controlled simulations have been performed varying the Reynolds number, the control amplitude and the wavelength of the vortices. As shown in Canton *et al.* (2016), the control scheme is effective at both  $Re_\tau = 104$  and 180. For these values of the Reynolds number a drag reduction of up to 16% and 18%, respectively, can be achieved. The performance of the large-scale vortices, though, degrades rapidly: for  $Re_\tau = 360$  the maximum DR is only 8%, and for  $Re_\tau = 550$  no more than  $0.4\% \pm 0.28\%$  can be obtained. It should be noted that, as detailed in the following, the present analysis covers the entire range of control amplitudes and reasonable vortex wavelengths. The drag reduction values presented are, therefore, the highest achievable under optimal conditions. This result is in good agreement with the work by Fukagata *et al.* (2010), who found that selectively damping small-scale velocity fluctuations in a turbulent channel flow for  $Re_\tau = 640$  is more effective than damping their large-scale counterparts, albeit their control targeting the large-scale structures is different from the following approach based on Schoppa & Hussain (1998).

The drag reduction including its uncertainty is illustrated in figure 2 where panel (a) (in semi-log scale) shows the maximum achievable value of DR as a function of the Reynolds number. Panels (b–e) show the details at each Reynolds number by presenting the performance of the control strategy for  $Re_\tau = 104, 180$  and 360 as a function of forcing amplitude and vortex wavelength. It can be observed that the forcing amplitude for optimal drag reduction remains relatively low even as the Reynolds number increases, varying between  $\max |\langle v \rangle_{x,t}| / U_b = 0.025$  and 0.049 for  $Re_\tau$  between 104 and 360.

The optimal wavelength, instead, is affected more significantly, at least for low Reynolds numbers. Analysing its dependence on  $Re$  in outer scaling, the optimal  $\Lambda$  is  $2.2h$  for  $Re_\tau = 104$ . This increases to  $\Lambda = 6.6h$  for  $Re_\tau = 180$ , which appears to be the optimal value for  $Re_\tau = 360$  as well. For  $Re_\tau = 550$ , however, no drag reduction can be achieved for any amplitude of control vortices with  $\Lambda = 6.6h$ . When scaled in inner units, instead, the optimal wavelength  $\Lambda^+$  increases with friction Reynolds number, growing from  $\Lambda^+ = 232$  for  $Re_\tau = 104$  to 1205 and 2415 for  $Re_\tau = 180$  and 360, respectively. Extrapolating this trend in inner units to  $Re_\tau = 550$ , the optimal  $\Lambda^+$  value would be around 3500. Simulations for this Reynolds number, though, controlled with vortices of wavelength equal to  $6.6h$ , corresponding to  $\Lambda^+ = 3600$ , do not exhibit drag

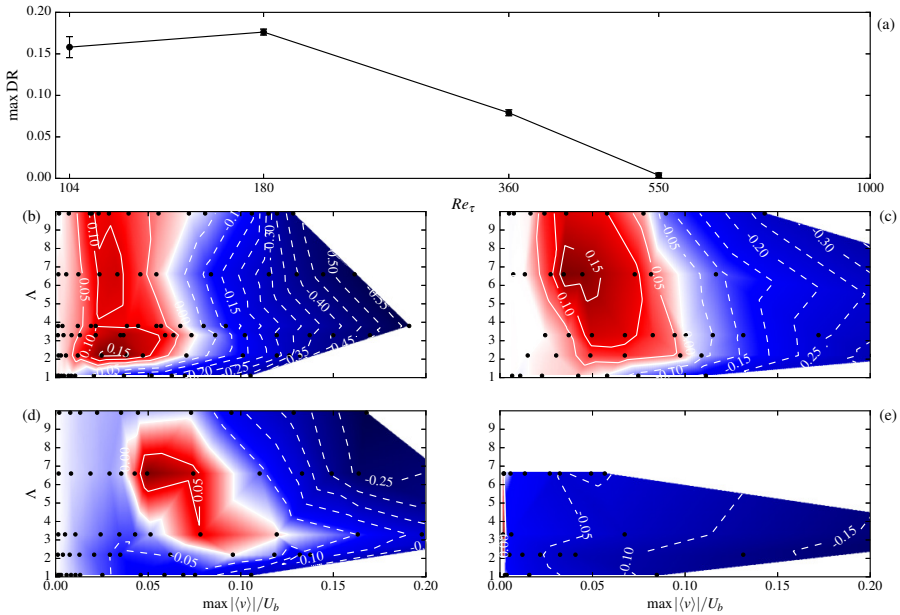


Figure 2: Panel (a): maximum achievable drag reduction as a function of friction Reynolds number (continuous line) and corresponding net power saving (dashed line). The uncertainty of DR is quantified by equation (3); the  $x$ -axis is in logarithmic scale. Panels (b) to (e) depict DR as a function of control strength,  $\max |\langle v \rangle_{x,t}|/U_b$ , and wavelength of the vortices,  $\Lambda$ .  $Re_\tau = 104, 180, 360$  and 550 are reported in (b), (c), (d) and (e), respectively. In (b–e) red and blue colours correspond to interpolated positive, resp. negative, values (reported as labels on the isocontours) of DR, based on the simulations indicated through black points.

reduction for any forcing amplitude. To further verify that the size of the control vortices does not scale in inner units, simulations with two rows of circular vortices were also performed for  $Re_\tau = 180$ . The two rows were placed close to the two channel walls and featured vortices with  $\Lambda = 1.1h$  and different forcing amplitudes. Also this implementation of the control scheme could only provide drag increase.

Since the method under investigation is an active control scheme, the power used to generate and sustain the large-scale vortices needs to be taken into account for a complete assessment of the performance. The net power saving rate is defined as  $S = (P_{\text{unc}} - P_{\text{con}})/P_{\text{con}} = DR - P_{\text{in}}/P_{\text{unc}}$  (see, for instance, Gatti & Quadrio 2016), where  $P_{\text{unc}}$  is the power required to drive the uncontrolled channel flow, while  $P_{\text{in}}$  is the power needed by the control, computed for an ideal actuator as  $P_{\text{in}} = 1/(\Omega T) \int_{\Omega} \int_0^T \mathbf{f} \cdot \mathbf{v} dt d\Omega$ . As it can be

observed in figure 2(a), the Reynolds-number dependence of this figure of merit is qualitatively similar to that of DR, confirming that the large-scale vortices perform well for low Reynolds numbers but fail to provide a positive effect for  $Re_\tau > 550$ . In particular, it was observed that the energy consumed by the ideal actuators does not significantly affect the parameters for the control: both the optimal wavelength and the forcing amplitude exhibit the same values compared to when not considering the power used to generate the large-scale vortices.

Valuable insight on the Reynolds number effect on the large-scale vortices can be obtained by analysing the wall-shear stress as a function of  $Re_\tau$ . Figure 3 presents the profiles of  $\tau_w$ , normalised by the value of the uncontrolled case, measured at the lower channel wall ( $y = -1$ ) for the four investigated  $Re_\tau$  values. The analysis is conducted on vortices with  $\Lambda = 6.6h$  which better highlight the Reynolds-number dependence, but the same trend is observed for all other wavelengths. Two phenomena are clearly observable as the Reynolds number is increased: a reduction in the fluctuation amplitude of  $\tau_w$ , and a modification of the profiles as a function of  $z$ .

The first phenomenon is most probably a direct consequence of the increase in Reynolds number: as  $Re_\tau$  is increased the height of the viscous sublayer, measured in outer units, decreases as  $1/Re_\tau$ . The maximum variation in  $\tau_w$  (for a positive DR) at the centre of two vortices, where the fluid is pushed towards the wall, does also decrease monotonically with  $Re_\tau$ . This may explain why the large-scale vortices cannot penetrate the viscous sublayer as its height decreases, as will become apparent in the comparison in figure 4, and thus cannot affect the near-wall region as  $Re_\tau$  is increased beyond a limit value.

The second phenomenon is well illustrated by comparing figures 3(a,b) with 3(c,d), although it is also apparent in figure 3(c) alone. For controlled flows at low Reynolds numbers the minimum in  $\tau_w$  is achieved close to the vertical vortex axes, at  $z/\Lambda \approx 0.16, 0.84$ ; in this area the vortices are pushing the fluid parallel to the wall, similarly to spanwise travelling waves, which are a proven drag reduction strategy (Du & Karniadakis 2000). As the Reynolds number is increased this minimum is moved to the extrema of the period, where the vortices are lifting the fluid away from the wall (see figure 3(d)). Concurrently, the area where the wall-shear stress is increased becomes wider than  $\Lambda/2$ , extending over the vertical vortex axes. The most relevant modification takes place at  $z/\Lambda = 0$  and 1, where the vortices are lifting fluid from the wall: for low Reynolds numbers this region is characterised by an increase in  $\tau_w$ , while for high  $Re_\tau$  the wall-shear stress is significantly reduced, similarly to what is observed in control via mass injection (*i.e.* blowing, Kametani *et al.* 2015). These modifications are clear at the intermediate  $Re_\tau = 360$  (figure 3(c)) where both low and high Reynolds number profiles of  $\tau_w$  can be observed.

For  $Re_\tau = 550$  both phenomena are observable: the drag is increased even by vortices with very small amplitude, and all forcing amplitudes that have a sensible effect on the flow increase the drag over more than 3/4 of the domain.

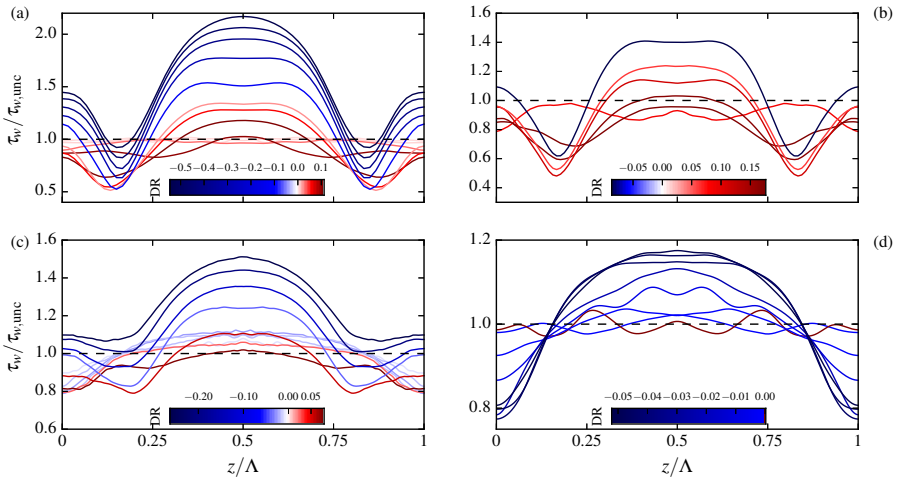


Figure 3: Wall shear stress at the lower channel wall ( $y = -1$ ) normalised by the corresponding value in the uncontrolled case ( $\tau_w = 1$ ). Each line corresponds to a different forcing amplitude. The vortices are pushing fluid towards the wall at  $z/\Lambda = 0.5$  while lifting it at  $z/\Lambda = 0$  and  $1$ , as indicated by the arrows in panel (b) which indicate the spanwise location and direction of the vortices. The four panels (a–d) correspond to increasing Reynolds numbers,  $Re_\tau = 104, 180, 360$  and  $550$ , and show the measurements for control vortices with  $\Lambda = 6.6h$ . A similar picture is observed for the other wavelengths investigated. The curves are colour-coded with their value of DR, reported in the legends. The dark red line in (d) corresponds to a drag reduction of only  $0.02\%$ , the highest achievable value for  $Re_\tau = 550$  for vortices with  $\Lambda = 6.6h$ .

If the first of these phenomena can be easily attributed to an increase of  $Re_\tau$  alone, and only results in a decrease in amplitude, the modification of the  $\tau_w$  profiles is an indication of a more fundamental change in the flow mechanics affected by the large-scale vortices. A third fundamental effect that the Reynolds number has on this drag-reduction strategy concerns relaminarisation. It was observed by Canton *et al.* (2016) that the large-scale vortices induce relaminarisation for  $Re_\tau = 104$  and  $180$  in the region where fluid is pushed towards the wall (see figure 4(c)). The opposite effect is observed for  $Re_\tau = 550$ . For this Reynolds number the RMS of the wall-shear stress is actually increased where the vortices push fluids towards the wall and decreased in the upwelling regions (see figure 4(d)). The reason for this perhaps unexpected behaviour can probably be connected to the reducing effect that the flow control has on the near-wall region when the Reynolds number is increased. For the lower Reynolds numbers the streaks reach the near-wall region and accelerate the flow in the down-draft areas; this, in turn, renders the near-wall region more

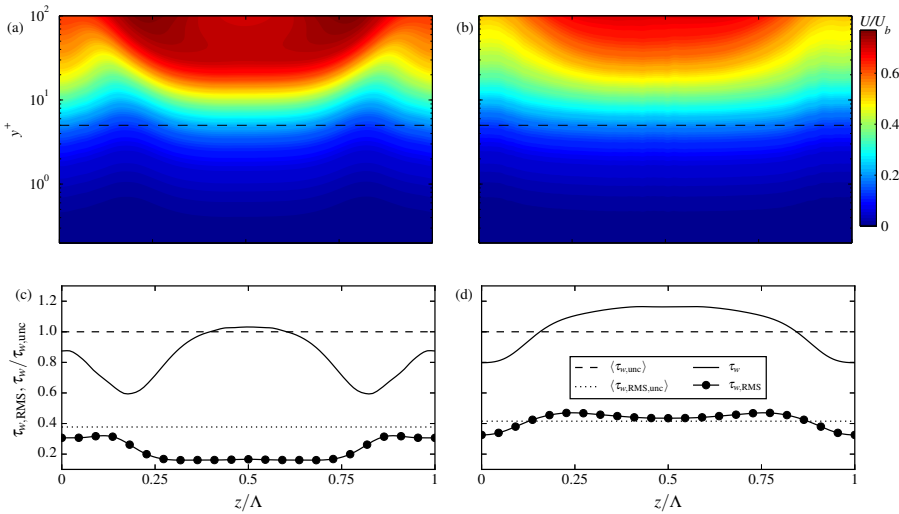


Figure 4: Average streamwise velocity on a cross-stream (*i.e.* spanwise/wall-normal) plane (a,b) and corresponding wall-shear stress and fluctuations on the lower channel wall (c,d), normalised by the average wall-shear stress of the uncontrolled case. Two cases are depicted for friction Reynolds numbers  $Re_\tau = 180$  (a,c) and  $Re_\tau = 550$  (b,d). In both cases the flow is controlled with large-scale vortices with  $\Lambda = 6.6h$  and  $\max |\langle v_x \rangle_t| \approx 0.05U_b$ . It can be observed that the control vortices can only barely penetrate the viscous sublayer (highlighted with a dashed line at  $y^+ = 5$ ) for the higher  $Re_\tau$ . Moreover, while in (a,c) the flow is significantly laminarised in the region where fluid is pushed towards the wall ( $0.25 < z/\Lambda < 0.75$ ), the opposite is observed in (b,d). The arrows in panel (b) indicate the spanwise location and direction of the vortices.

stable and thus leads to laminarisation. On the other hand, when the streaks do not reach down into the near-wall region (at higher  $Re$ ), the main effect is a vertical compression of the near-wall layer, which increases the overall gradient and thus promotes more instabilities, consequently increasing the fluctuations in the wall-shear stress.

To summarise, results show that the large-scale vortices can provide considerable drag reduction for low Reynolds numbers but their performance decreases rapidly and the method becomes completely ineffective by  $Re_\tau = 550$ . Clearly, low Reynolds number effects are still present for  $Re_\tau = 104, 180$  (Moser *et al.* 1999) and the present large-scale control is able to affect the low- $Re$  wall cycle and to reduce the turbulence intensity.  $Re_\tau = 360$  offers a good transitional flow case, close to  $Re_\tau = 395$  which was observed by Moser *et al.* (1999) as being a good lower limit for the absence of low Reynolds number effects. For this Reynolds number, in fact, both the low and high  $Re$  behaviour of the large-scale vortices can be observed. For higher Reynolds numbers the low  $Re$

effects disappear and the present control strategy cannot provide drag reduction anymore. The effect of the vortices on the flow is also changed: while for low  $Re$  the maximum reduction in wall-shear stress is achieved via spanwise variation of the flow, for high  $Re$  it is obtained via a ‘blowing’ mechanism. Despite the negative overall outcome, these results offer ‘food for thought’ upon which to improve the control strategy: the vortices can reduce  $\tau_w$  for high Reynolds numbers in the ‘upwelling’ regions (see figure 3(d)). A control strategy capable of generating such wall jets, without creating a large area of drag increase, would have an overall positive effect on DR. Moreover, a technique capable of generating fluid lift up directly at the wall, differently from the present one based on motion created outside of the viscous layer, would probably be more successful for high Reynolds numbers. A different analysis and further studies should be carried out to investigate the effectiveness of the scheme in spatially developing boundary layers. More positive results could in fact be obtained for open flows since the vortices would not be confined and the fluid pushed towards the wall would come from an undisturbed region void of turbulent small scales.

Comparing the drag reduction mechanism of the current method with two of the more established methods from the literature, *i.e.* the oscillating walls (see e.g. Quadrio *et al.* 2009) and the spanwise travelling waves by volume forcing (Du & Karniadakis 2000) at least qualitative similarities can be pointed out. In all of these cases there is a significant portion of the near-wall region in which the flow experiences a significant spanwise velocity relative to the wall. Even though the amplitudes of this spanwise component are different, and inertial effects do not allow for a direct comparison, the implied modifications of the flow appear to be similar (see Du & Karniadakis), *i.e.* a distortion of the regeneration process. A more quantitative comparison of these methods, and their effect on the near-wall flow, could constitute a further step towards effective flow control.

Financial support by the Swedish Research Council (VR) is gratefully acknowledged. Computer time was provided by the Swedish National Infrastructure for Computing (SNIC). PS acknowledges financial support by the Wallenberg Foundation as part of the Wallenberg Academy Fellow Programme, and RÖ support from the Lundeqvist foundation.

## REFERENCES

- CANTON, J., ÖRLÜ, R., CHIN, C., HUTCHINS, N., MONTY, J. & SCHLATTER, P. 2016 On large-scale friction control in turbulent wall flow in low Reynolds number channels. *Flow, Turbul. Combust.* **97**, 811–827.
- CHEVALIER, M., SCHLATTER, P., LUNDBLADH, A. & HENNINGSON, D. S. 2007 SIMSON - A pseudo-spectral solver for incompressible boundary layer flows. *Tech. Rep.* TRITA-MEK 2007:07. KTH Mechanics, Stockholm, Sweden.

- CHOI, K.-S., JUKES, T. & WHALLEY, R. 2011 Turbulent boundary-layer control with plasma actuators. *Philos. Trans. A. Math. Phys. Eng. Sci.* **369**, 1443–1458.
- DU, Y. & KARNIADAKIS, G. E. 2000 Suppressing wall turbulence by means of a transverse traveling wave. *Science (80-. ).* **288**, 1230–1234.
- FUKAGATA, K., KOBAYASHI, M. & KASAGI, N. 2010 On the friction drag reduction effect by a control of large-scale turbulent structures. *J. Fluid Sci. Technol.* **5**, 574–584.
- GARCÍA-MAYORAL, R. & JIMÉNEZ, J. 2011 Drag reduction by ripples. *Philos. Trans. A. Math. Phys. Eng. Sci.* **369**, 1412–1427.
- GATTI, D. & QUADRI, M. 2013 Performance losses of drag-reducing spanwise forcing at moderate values of the Reynolds number. *Phys. Fluids* **25**, 125109.
- GATTI, D. & QUADRI, M. 2016 Reynolds-dependence of turbulent skin-friction drag reduction induced by spanwise forcing. *J. Fluid Mech.* **802**, 553–582.
- GAD-EL HAK, M. 2007 *Flow Control: Passive, Active, and Reactive Flow Management*. Cambridge University Press.
- HURST, E., YANG, Q. & YONGMANN, M. C. 2014 The effect of Reynolds number on turbulent drag reduction by streamwise travelling waves. *J. Fluid Mech.* **759**, 28–55.
- HUTCHINS, N. & CHOI, K.-S. 2001 Experimental investigation of turbulence suppression by the imposition of a large-scale vortical control flow. In *31st AIAA Fluid Dyn. Conf. Exhib.*, Anaheim, CA.
- IWAMOTO, K., SUZUKI, Y. & KASAGI, N. 2002 Reynolds number effect on wall turbulence: toward effective feedback control. *Int. J. Heat Fluid Flow* **23**, 678–689.
- KAMETANI, Y., FUKAGATA, K., ÖRLÜ, R. & SCHLATTER, P. 2015 Effect of uniform blowing/suction in a turbulent boundary layer at moderate Reynolds number. *Int. J. Heat Fluid Flow* **55**, 132–142.
- KASAGI, N., SUZUKI, Y. & FUKAGATA, K. 2009 Microelectromechanical systems-based feedback control of turbulence for skin friction reduction. *Annu. Rev. Fluid Mech.* **41**, 231–251.
- KLINE, S. J., REYNOLDS, W. C., SCHRAUB, F. A. & RUNSTADLER, P. W. 1967 The structure of turbulent boundary layers. *J. Fluid Mech.* **30**, 741–773.
- MAMORI, H., IWAMOTO, K. & MURATA, A. 2014 Effect of the parameters of traveling waves created by blowing and suction on the relaminarization phenomena in fully developed turbulent channel flow. *Phys. Fluids* **26**, 015101.
- MATSSON, O. J. E. & ALFREDSSON, P. H. 1990 Curvature- and rotation-induced instabilities in channel flow. *J. Fluid Mech.* **210**, 537–563.
- MIN, T., KANG, S. M., SPEYER, J. L. & KIM, J. 2006 Sustained sub-laminar drag in a fully developed channel flow. *J. Fluid Mech.* **558**, 309–318.
- MISHRA, M. & SKOTE, M. 2015 Drag reduction in turbulent boundary layers with half wave wall oscillations. *Math. Probl. Eng.* **2015**, 253249.
- MOREAU, E. 2007 Airflow control by non-thermal plasma actuators. *J. Phys. D. Appl. Phys.* **40**, 605–636.
- MOSER, R. D., KIM, J. & MANSOUR, N. N. 1999 Direct numerical simulation of turbulent channel flow up to  $Re_\tau = 590$ . *Phys. Fluids* **11**, 943–945.
- NAKANISHI, R., MAMORI, H. & FUKAGATA, K. 2012 Relaminarization of turbulent

- channel flow using traveling wave-like wall deformation. *Int. J. Heat Fluid Flow* **35**, 152–159.
- QUADRIOS, M., RICCO, P. & VIOTTI, C. 2009 Streamwise-traveling waves of spanwise wall velocity for turbulent drag reduction. *J. Fluid Mech.* **627**, 161–178.
- SCHOPPA, W. & HUSSAIN, F. 1998 A large-scale control strategy for drag reduction in turbulent boundary layers. *Phys. Fluids* **10**, 1049.
- SKOTE, M. 2014 Scaling of the velocity profile in strongly drag reduced turbulent flows over an oscillating wall. *Int. J. Heat Fluid Flow* **50**, 352–358.
- TROPEA, C., YARIN, A. L. & FOSS, J. F. 2007 *Springer Handbook of Experimental Fluid Mechanics*. Springer Science & Business Media.
- VANDERWEL, C. & GANAPATHISUBRAMANI, B. 2015 Effects of spanwise spacing on large-scale secondary flows in rough-wall turbulent boundary layers. *J. Fluid Mech.* **774**, R2.
- WICKS, M., THOMAS, F. O., CORKE, T. C., PATEL, M. & CAIN, A. B. 2015 Mechanism of vorticity generation in plasma streamwise vortex generators. *AIAA J.* **53**, 1–10.